High resolution double crystal X-ray diffractometry and topography of III-V semiconductor compounds

Cockerton, Simon

High resolution double crystal X-ray diffractometry and topography of III-V semiconductor compounds

by

Simon Cockerton B.Sc.

A Thesis submitted in partial fulfilment of the requirements for the degree of Doctor of Philosophy

The University of Durham
1991

Contents

Abstract

Double crystal diffractometry and topography are now routinely used in many laboratories for the inspection of epitaxially grown devices. However the trend towards thinner layers and more complex structures requires the continual development of novel approaches using these techniques. This thesis is concerned with the development of these approaches to study the structural uniformity of semiconductor materials. The uniformity of large single crystals of lithium niobate has been studied using synchrotron radiation and double crystal X-ray topography. This study has shown a variety of contrast features including low angle grain boundaries and non-uniform dislocation densities. The abruptness of an interface between a layer and the underlying substrate has been studied using glancing incidence asymmetric reflections. Comparisons to simulated structures revealed that a closer match was achieved by the inclusion of a highly mismatched interfacial layer. This study illustrates the need for careful comparison between experimental and simulated rocking curves as different structures may produce very similar rocking curves. A double crystal topographic study of a AlGaAs laser structure revealed X-ray interference fringes. These are shown to be produced from the interaction of two simultaneously diffracting layers separated by a thin layer. Possible formation mechanisms have been discussed showing that these fringes are capable of revealing changes in the active layer at the atomic level. A novel approach has also been developed using synchrotron radiation to study the non-stoichiometry of GaAs. This approach uses the quasi-forbidden reflections which are present in III-V semiconductors due to the differences in the atomic scattering factors. This study has also discussed the behaviour of strong and weak reflections in the region of absorption edges and modelled their behaviour using the anomalous dispersion corrections of Cromer and Liberman.

Acknowledgements

Financial support from the Science and Engineering Research Council is gratefully acknowledged.

I would also like to thank Professor A.W. Wolfendale for the provision of the departmental facilities of the Physics department at the University of Durham.

Thanks are also due to the staff at the Daresbury Synchrotron Source, particularly to Dr G.F. Clark for his assistance with the diffraction equipment.

I am very grateful to Professor B.K. Tanner for his supervision of this project and his continued support during the writing of this thesis. I am also very grateful to Dr G.S. Green for his advice, comments and help during many hours of data collection at the Daresbury laboratory. I would also like to thank Dr S.J. Miles for his help with the simulation program and assistance in the construction of the X-ray laboratory at Durham.

Thanks to Dr J. Tower of Spectrum Technologies for providing the LEC GaAs sample, MCP and McDonald Douglas for the InSb samples and Pilkington Electroptical Materials for the $LiNbO_3$ samples. I am also grateful to Professor M. Hart for the provision of a copy of the Cromer and Liberman program and his useful comments.

I would also like to thank the technical staff of the Department of Physics, especially Mr P. Foley, Mr D. Jobling, Mr T. Jackson, Mr G. Teasdale and Mr P. Armstrong.

Finally I would like to thank my wife Melanie, without her support and help this thesis would not have been completed.

Publications

Cockerton, S., Green, G.S. and Tanner, B.K. (1989) Mat. Res. Soc. Symp. Proc. 138, 65.

Cockerton, S., Miles, S.J., Green, G.S. and Tanner, B.K. (1990) J. Cryst. Growth 99, 1324.

Chapter I

Introduction

While it seems that silicon will always dominate the integrated circuit market the inability, as yet, of silicon devices efficiently to produce optical photons ensures large scale III-V device development. Semiconductor lasers coupled to optical fibres are now the basis of many long distance communication networks. Development to optimise performance and reliability is clearly fundamental as the demands of the communication industry increase. The basis of a III-V semiconductor device is the epitaxial growth of one semiconductor on another. These structures allow the electronic bandgaps to be tailored to the particular level necessary to emit light when a voltage is applied. To reduce defects associated with the growth of a layer of one semiconductor on another, the lattice parameters of the two materials should match within 0.1%. This restricts the range of emission wavelengths available to those in which the layer is lattice matched to the substrate or the layer thickness is small enough to prevent misfit dislocations.

To allow a wider range of emission wavelengths, ternary and quaternary compounds were developed. For example the band gap of GaAs is too small for light emission in the visible range, while AlAs emits in the green portion of the visible spectrum. Since AlAs has an indirect gap this material is an inefficient emitter but an alloy of GaAs and AlAs, of well chosen composition, can ensure that the direct gap of GaAs is maintained while the magnitude of the gap is suitably increased. The lattice constant versus energy gap for various III-V compounds is illustrated in figure 1.01. The solid lines, in this figure correspond to direct band gap material, the dashed lines to indirect band gap material. The shaded area shows the quaternary compound $Ga_xIn_{1-x}P_yAs_{1-y}$. By varying x and y the lattice constant may be matched to either InP or GaAs.

The development of particular devices was dictated by the wavelength dependent absorption of optical fibres. In the wavelength range from 800 to 900nm

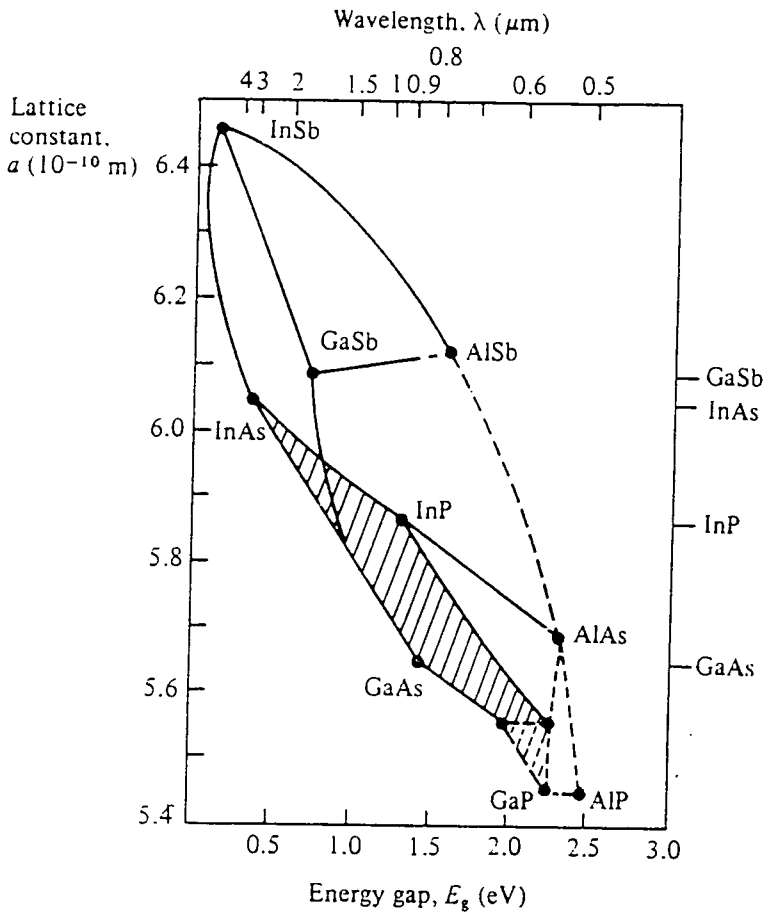

Figure 1.01 Illustrates the lattice constant versus energy gap of various III-V compounds. The shaded area corresponds to the quaternary alloy $Ga_xIn_{1-x}P_yAs_{1-y}$. This alloy is lattice matched to InP at x=0.8 and y=0.35. After Wilson and Hawkes (1983).

devices are generally those of GaAlAs while at slightly higher wavelengths (and generally lower absorption) the alloy InGaAsP is used.

Good quality substrate material is essential in the growth of a heterojunction device. While effort towards the improvement of substrate materials such as InP and GaAs is being made, current substrate quality is sufficient to support commercial production. Presently most of the material processed by industry is grown by the liquid encapsulated Czochralski (LEC) technique which is capable of producing wafers up to 4 inches in diameter with electrical properties homogenised by whole ingot annealing.

It has been known for some time that the threshold voltage variations measured in field effect transistor (FET) arrays are strongly correlated with the dislocation density distribution across the wafer (Nanishi et al, 1982). For lasers and light emitting diodes (LEDs) there is evidence that dislocations adversely affect performance, since dislocations present in the substrate are believed to propagate across the epilayer (Roedel et al, 1979). These defects act as non radiative recombination centres that decrease the light output. Dark line defects cause significant degradation in lasers and are also believed to arise from dislocations (Petroff and Hartman, 1973).

Improvement in device performance is directly related to the quality of the substrate material as well as the epitaxial layers. Stoichiometric substrate material is required to prevent large defect density populations such as in the defect labelled EL2 in GaAs (Holmes et al, 1982). As device structures become more complex and layers become thinner, adaptations of existing characterisation techniques are required. This necessitates the study of novel approaches as well as the refinement of existing methods.

1.1 Expitaxial growth of III-V materials

Expitaxial growth is the growth of a crystalline film on a crystalline substrate; the grown film reproduces the crystalline structure of the substrate. The development of sophisticated epitaxial techniques has been of major importance in the advancement of high quality electronic devices. The commonly used techniques are liquid phase epitaxy (LPE), vapour phase epitaxy (VPE) and molecular beam

epitaxy (MBE). The VPE technique is also known as chemical vapour deposition (CVD) and a modification of this is called metallo-organic chemical vapour phase decomposition (MOCVD) because this technique uses metal alkyls as a compound source.

1.1.1 Liquid phase epitaxy

In this technique a saturated solution of an alloy, such as GaAs, is cooled allowing precipitation. The phase diagram for GaAs is given in figure 1.02 where the point a is the starting point and points b and c are the beginning and end points of precipitation. LPE growth was first reported using a tipping system (Nelson, 1963) of the type illustrated in figure 1.03. In this method the substrate and solution are placed at opposite ends of a graphite boat which is placed inside a growth tube. The furnace can be tipped to elevate either end of the tube. Growth begins by heating the furnace with the substrate high and out of the solution. The melt is heated until uniform saturation is achieved, growth begins by tipping the furnace until the melt covers the substrate. An adaptation of this technique is the dipping technique (Rupprecht, 1967). For handling repeated layers both of these techniques are difficult to implement. To overcome this problem the sliding technique (Panish et al, 1969) was developed. In this technique, the substrate is held in a slider which can be slid under successive melts.

LPE has long been the preferred epitaxial growth method for optoelectronic device applications in III-V compounds, since this technique has proved to be extremely useful at preparing high quality relatively thick (greater than $0.5\mu m$) layers. Growth of thinner layers is difficult due to the inherent high growth rates of this technique. Growth of binary materials such as GaAs is aided by the near stoichiometric growth of this material; however ternary and quaternary alloys can suffer from a varying growth composition. The alloy may thus vary as the growth proceeds, depending on the initial composition of the melt and the growth temperature (Panish and Ilegems, 1972). A major problem with the growth of epitaxial layers using LPE is the poor surface morphology and the tendency of this technique to produce ridges on the surface introducing difficulties in subsequent processing of fine definition devices.

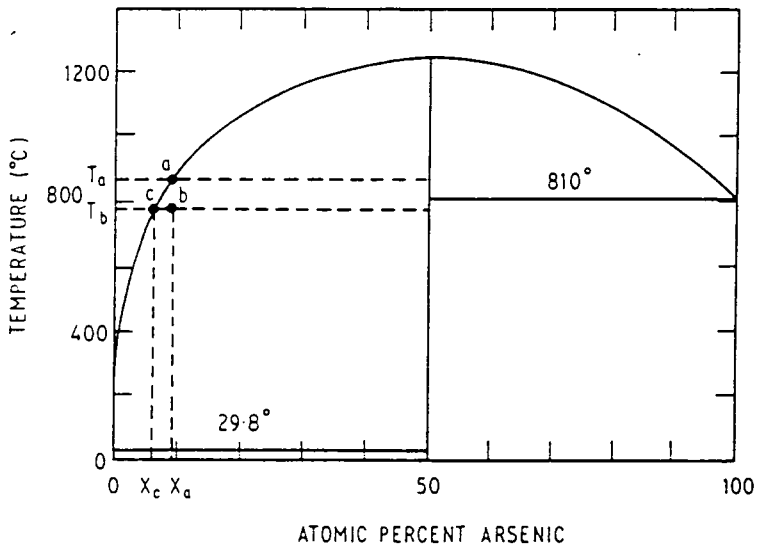

Figure 1.02 Schematic of Ga-As phase diagram. After Dorrity et al (1985).

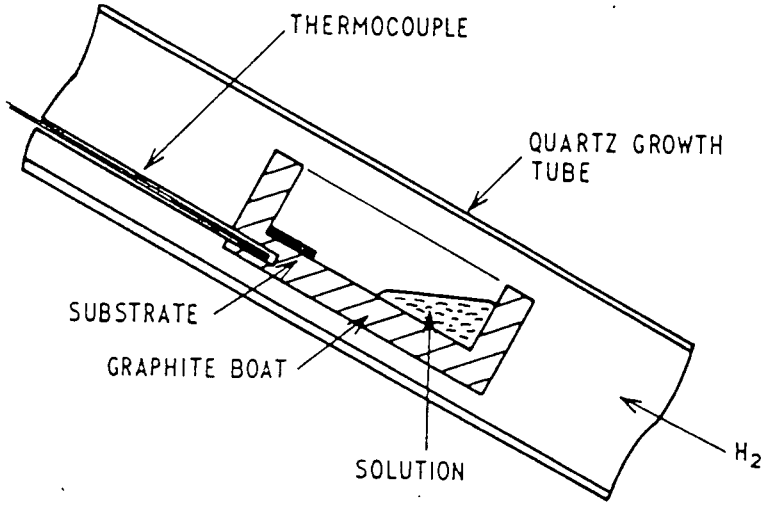

Figure 1.03 Schematic diagram of a tipping LPE system. After Dorrity et al (1985).

1.1.2 Vapour phase epitaxy

VPE is generally classified into one of two techniques; the chloride and hydride (Olsen and Zamerowski, 1979). In the chloride approach for the growth of GaAs, Ga is transported in the form of GaCl which is produced when a gallium source is reacted with arsenic chlorides. GaAs is formed at the substrate, this can be described by the following equations.

$$4AsCl_3 + 6H_2 \longrightarrow 12HCl + As_4$$

$$4GaAs + 4HCl \longrightarrow 4GaCl + As_4 + 2H_2$$

$$6GaCl + As_4 \longrightarrow 2GaCl_3 + 4GaAs$$

The source saturation is critical and it is vital that a flat temperature profile is maintained over the source, as failure to do so results in the partial dissolution of the GaAs. This leads to uncontrolled variations in the vapour composition which cause surface morphology problems and loss of growth rate control. The chloride approach has the advantage that the purity of the source materials is very high, material with sub parts per million impurities is readily available. Figure 1.04 shows the main features of a VPE reactor.

The hydride approach was developed to introduce a more controlled reaction for the growth of ternary and quaternary compounds. The growth of GaAs using this approach is described by the following equations.

$$2Ga + 2HCl \longrightarrow 2GaCl + H_2$$

$$4AsH_3 \longrightarrow As_4 + 6H_2$$

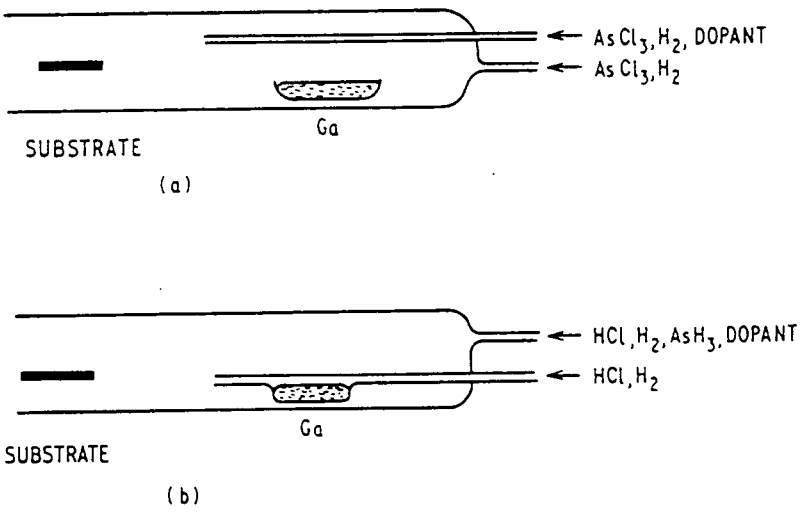

Figure 1.04 Schematic of the main features of GaAs VPE reactors. After Dorrity et al (1985).

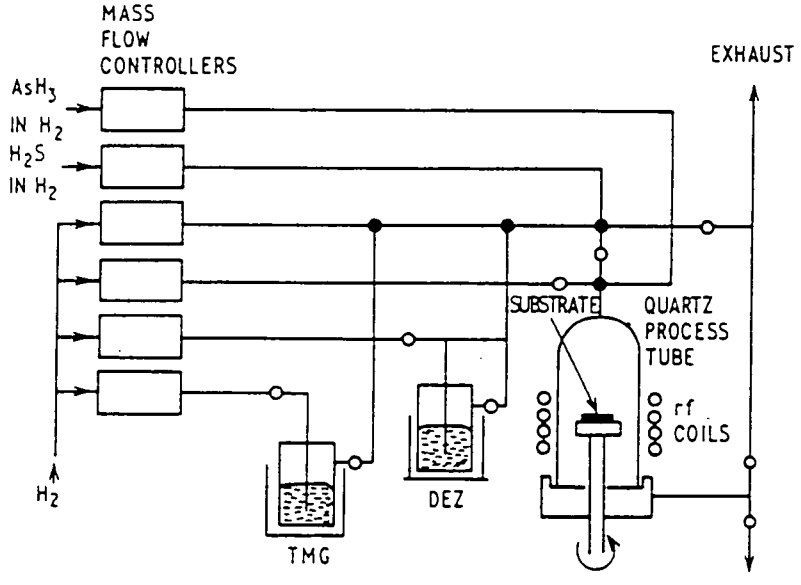

Figure 1.05 Schematic diagram of vertical MOCVD reactor for GaAs. After Dorrity et al (1985).

$$4GaCl + As_4 + 2H_2 \longrightarrow 4GaAs + 4HCl$$

From the above equations it can be seen that there are two independent sources of gallium and arsenic. A major disadvantage with VPE is that aluminium containing compounds can not be grown due to the reactivity of the aluminium.

1.1.3 Metallo-organic chemical vapour phase deposition

MOCVD is a variant of the VPE technique that uses metal alkyls as a source from which the epitaxial layers are grown. MOCVD has been extensively studied by Dapkus and co-workers (1981) using the AlGaAs system. Growth takes place in a cold walled quartz reactor in flowing hydrogen at atmospheric pressure. The substrate is heated to a temperature of between $600 - 800^oC$. Transport of the metal-organics to the substrate is achieved by bubbling hydrogen through the liquid sources. The growth of multilayer structures is achieved by changing the gas composition in the reactor. At high flow rates, this exchange can be accomplished rapidly so that atomically abrupt heterojunctions can be formed. Most of the III-V semiconductors can be grown by MOCVD, typical growth rates are in the range 2 to $4\mu m$ per hour and typical reagents for the growth of AlGaAs on GaAs are trimethylaluminum and trimethylgallium reacted with arsine. A typical MOCVD reactor is shown in figure 1.05.

1.1.4 Molecular beam epitaxy

MBE is the growth of alloy semiconductor films by the impingement of directed molecular beams on a crystalline surface under ultra high vacuum conditions. Widespread use of MBE for the growth of III-V materials has originated from the work of Cho and Arthur (Cho, 1979; Cho and Arthur, 1975). Modern MBE systems are generally multichannel apparatus comprising a fast entry load lock, a preparation chamber and a growth chamber, figure 1.06. A major attraction of MBE is that the ultra high vacuum enables the incorporation of high vacuum based analytical and diagnostic techniques such as RHEED (reflection high energy electron diffraction) and SIMS (secondary ion mass spectroscopy) to be used. The unidirectional nature of the flux in MBE is controlled by the source geometry and

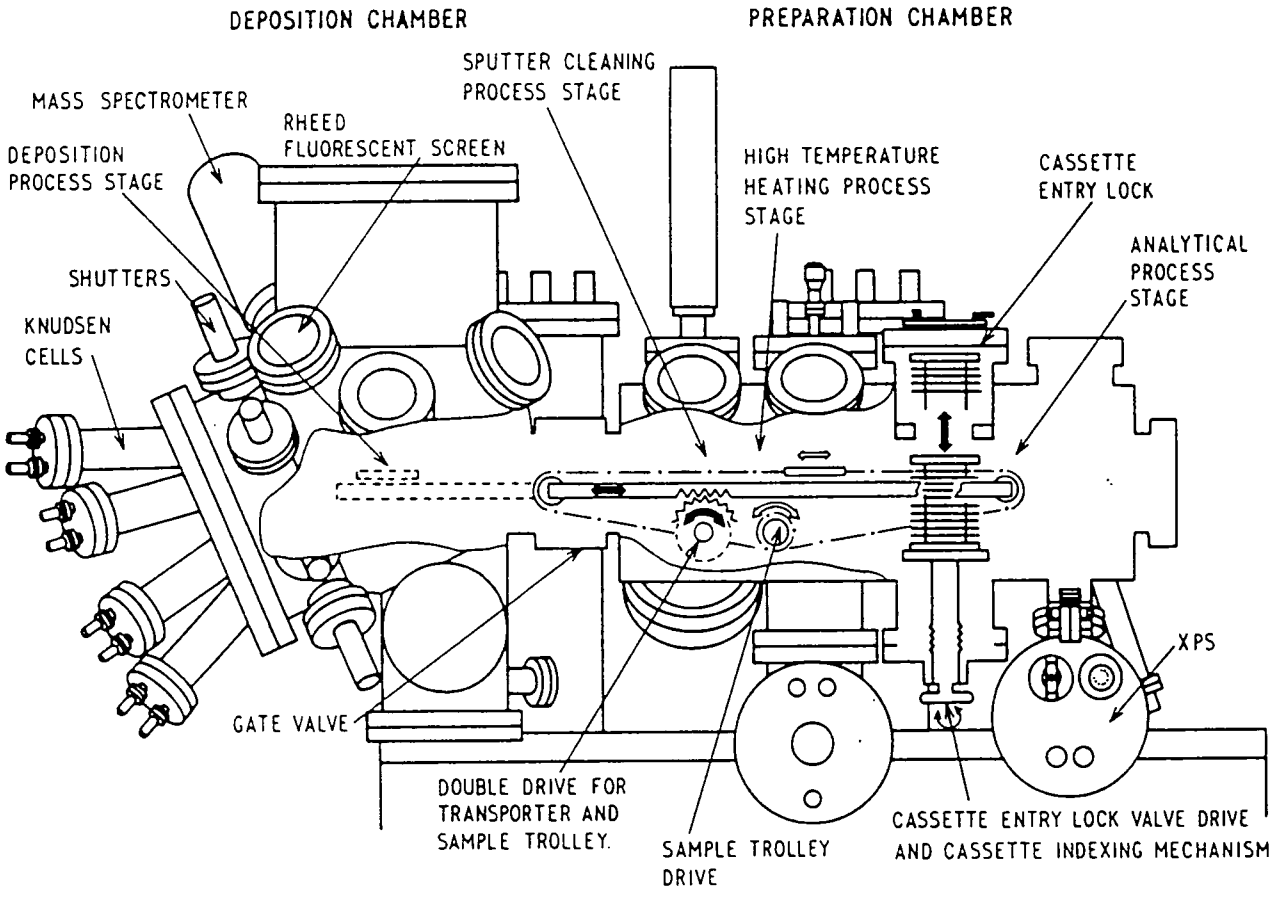

Figure 1.06 Typical multichamber MBE system. After Dorrity et al (1985).

this places limits on the size of the substrates that can be uniformly covered. Shutters are used to interrupt the flux of the various beams and to facilitate multi-layer growth. Because the flux from each source can be abruptly shuttered, abrupt transitions between layers of different dopants and composition can be achieved. The major attribute of MBE is its low growth rate allowing monolayers to be produced. This low growth rate becomes a liability when thick layers must be grown. The purity of MBE is controlled by the background vacuum, the purity of the starting materials and the source crucibles.

1.1.5 Comparison of expitaxial growth techniques

The major disadvantage of the LPE technique is that the surface morphology of the grown layers is inferior to that produced by MBE and VPE. Another problem is the restricted substrate size. However LPE offers the advantage of very simple apparatus capable of producing very high quality layers, particularly for use in electro-optical devices such as LEDs and lasers.

MBE and MOCVD are the preferred techniques for the growth of very thin layers. MOCVD is preferred for the growth of those compounds containing phosphorus because of the conflict between the high vapour pressure of phosphorus and the ultra-low vacuum requirements of MBE and the danger of ignition of the phosphorus.

MBE offers probably the most abrupt layers, with the capability of growing layers only a few $\mathring{A}$ in thickness, while MOCVD offers a high throughput of probably the best material due to the high purity of the starting material.

1.1.6 Crystal defects and non-uniformity

In general defects can be classified as volume, area, line or point defects. Volume defects are many atoms across in three dimensions and are the gross structural imperfections in crystals including orientation, structural and compositional variations. A volume differing in orientation only is called a grain and if the entire volume of the crystal consists of many such grains the material is said to be polycrystalline. If the variations of the grain orientations is less than about 1 degree then the material is said to be a single crystal with a lineage or mosaic structure.

A volume defect differing in only crystal structure is said to be an included grain while a volume differing in composition is said to be a precipitate. Area defects are one or a few atomic spaces in thickness but may be macroscopic in extent; most area defects are interfaces. Included in this classification are grain boundaries, twin boundaries, antiphase boundaries and stacking faults. Line defects are called dislocations and are specified by two vectors, one along the direction of the dislocation and the second (the Burgers vector) describing the energy as well as the orientation of the dislocation. Point defects are of atomic dimensions and are of three main types; impurity atoms, vacant lattice sites and interstitials.

1.1.7 Defects in epitaxial layers

As well as many of the defect types discussed above, epitaxial layers can suffer from compositional variations resulting in a mismatch from the substrate. In particular, ternary alloys are only lattice matched to binary alloys at one composition. Beyond or below this composition stress is introduced due to the compression or expansion of the layer (Olsen and Smith, 1975).

If a substrate and epilayer are lattice mismatched, the strain energy density of the layer increases directly with thickness (Osbourne, 1982). A critical thickness is reached when the strain energy exceeds the energy needed for defect nucleation. A number of models have been developed to describe and predict this transition, these include the Frank-van der Merwe model (1949), the Matthews model (1966) and the Bean model (1984).

The lattice parameter of a ternary layer is related to the lattice parameter of its constituents by Vegards Law, which states that the lattice parameter is a linear function of the composition (Fukui, 1984). In the case of GaAlAs this can be written as

$$a_{Ga_{1-x}Al_xAs} = xa_{AlAs} + (1-x)a_{GaAs}$$

The lattice parameter of quaternary compounds is more complex as for example, the quaternary $Ga_xIn_{1-x}As_yP_{1-y}$ in which there are two variable compositions. From Hill (1985) if one considers the change in lattice parameter with both the x and y composition then one can obtain the lattice matched relationship to InP as,

$$x = \frac{0.4526y}{1 - 0.031y}$$

and using the empirical relationship between band gap and composition the quantities x and ŷ can then be determined (Nahory et al, 1978).

1.1.8 Characterisation techniques

In applying characterisation techniques, information from one method often complements another and multiple analyses often solve problems left unsolved by a single technique alone. Excellent reviews of modern characterisation techniques for semiconductor materials have been presented elsewhere (Shaffner, 1986; Halliwell et al, 1985; Davies and Andrews, 1985; Ambridge and Wakefield, 1985). Table 1.1 compares various characterisation techniques for semiconductors, sub divided under the headings of optical, electron, X-ray and particle beams. Complementary techniques to X-ray diffraction include photoluminescence (PL), Raman scattering and transmission electron microscopy (TEM).

Photoluminescence is useful in characterizing epilayers, but only has a limited sampling depth of about 1 micron. Incident light of a greater energy than the band gap of a material is incident on the sample, some of this light is then absorbed to create an electron hole pair which then recombines to emit light which is characteristic of the material. Photoluminescence gives information on impurity concentrations down to 1×10^{13} per cm^3 (Andrews et al, 1986) and enables an estimate to be made of the abruptness of the interfaces (Scott et al, 1988; Goetz et al, 1983; Skolnick et al, 1986).

Raman spectroscopy is particularly useful in the characterisation of superlattice structures (Davey et al, 1987; Diebold et al, 1989). In this technique optical phonons are scattered whose energy is characteristic of the composition of the alloy and also the strain present. This technique allows superlattice periods to be measured to an accuracy of 0.5nm, and composition of 1%, as well as giving an indication of the relaxation in strained materials.

Transmission electron microscopy and X-ray diffraction topography are complementary techniques and can be thought of as providing a two dimensional map

of the scattering of a particular Bragg reflection. TEM has a resolution at the atomic level whereas X-ray topography is limited by the width of the defects as determined by the weak scattering of X-rays and the photoelectron track length in the emulsion. Magnification in the X-ray case may only be achieved by the use of asymmetric geometries, whereas electrons may be readily focused. Electrons have a high absorption in semiconductor materials compared to X-rays which leads to inspection depths of less than $1\mu m$ and areas of many square microns whereas X-rays can readily image whole wafers several inches in diameter and penetrate several millimetres of low atomic number materials. As a consequence X-ray topography is highly applicable to the study of materials with dislocation densities of less than 1×10^4 per cm^2 where electron microscopy becomes impracticable because of the small field of view (Tanner, 1990). TEM requires lengthy sample preparation often requiring thinning to a few hundred atomic layers; this technique is therefore destructive in the sample preparation stage. This preparation also means that TEM can not be carried out as an intermediate technique between various sample preparation stages unlike X-ray topography which requires little or no sample preparation.

X-ray diffraction, in the context of analytical techniques, can be split into diffractometry and the imaging technique of topography. Diffractometry is concerned with the recording of the auto correlation function of the perfect crystal reflecting ranges while X-ray topography is the imaging of the point to point variation in intensity or direction. Both techniques are governed by Braggs law,

$$\lambda = 2d_{hkl}sin\theta$$

where λ is the wavelength, d_{hkl} is the Bragg plane spacing and θ is the Bragg angle.

Table 1.1 These tables describe some of the main characterization techniques subdivided into the four probing radiations. After Shaffner (1986).

	Scanning Electron Microscopy (SEM)	Auger Electron Spectroscopy (AES)	Scanning Auger Microprobe (SAM)	Electron Microprobe (EMP)	Analytical Electron Microscopy (AEM)	High Voltage TEM (HVTEM)
Depth Analyzed	~ 1000 Å	20 Å	20 Å	1 μm	< 1000 Å	< 1000 Å
Diameter of Analysis Region	50 Å – 5 mm	100 μm	1000 Å	1 μm	10 μm	10 μm
Detection Limit (atoms/cm^3)	surface image	$5x10^{19}$	$1x10^{21}$	$5x10^{19}$	defect imaging	lattice imaging
Detection Limit (ppm)	surface image	1.000	20.000	1000	defect imaging	lattice imaging
In-Depth Profiling Resolution	stereo microscopy	20 Å	20 Å	none	stereo microscopy	none
Time for Analysis	< 1 hour	< 1 hour	< 1 hour	< 1 hour	1-3 days	1-3 days
Comments	In-depth profiling achieved by angle-lap cross section	Profiling achieved by argon sputtering	Profiling achieved by argon sputtering	Wave-length & energy dispersive analysis	sample preparation requires specialized techniques and is time consuming	

(a) Electron beams

	Optical Micro-scopy	Fourier Transform Infrared (FTIR)	Photo Lumines-cence (PL)	Infrared and Ultra-Violet (IR & UV)	Raman Micro-Probe	Photo-Neutron Activation
Depth Analyzed	> 1-3 μm	1-10 mm	1-3 μm	1 mm IR 1 μm UV	1 μm	0.5 cm
Diameter of Analysis Region	~ 1 cm	2 mm	> 5 μm	1 mm	2 μm	0.5 cm
Detection Limit (atoms/cm^3)	visual inspect	$1x10^{11}$	$1x10^{11}$	$5x10^{18}$	$5x10^{19}$	$5x10^{15}$
Detection Limit (ppm)	visual inspect	$2x10^{-6}$	$2x10^{-6}$	100	1000	0.1
In-depth profiling resolution	none	none	none	none	none	none
Time for Analysis	< 1 hour	2 hours	2 hours	< 1 hour	< 1 hour	2 hours
Comments	In-depth profiling achieved by angle-lap cross section	Performed at 10-15°K tempera-tures	Performed at 4°K tempera-tures	Performed at room tempera-ture		Bulk measure-ment only

(b) Optical probes

	Powder X-ray Diffraction (XRD)	Thin Film Analysis (Seeman-Bohlin)	Lang X-ray Topography (Lang)	Double Crystal Topography (DCT)	X-ray Fluorescence (XRF)	X-ray Photo-electron Spectro-scopy (XPS,ESCA)
Depth Analyzed	10-50 μm	100 Å - 1 μm	500 μm	5-100 μm	1-3 μm	20 Å
Diameter of Analysis Region	> 1 mm	1x5 mm	> 1 cm	> 1 cm	> 5 mm	5 mm
Detection Limit (atoms/cm^3)	$5x10^{19}$	$5x10^{19}$	$1x10^{-3}$ in $\Delta d/d$	$1x10^{-7}$ in $\Delta d/d$	$1x10^{19}$	$5x10^{19}$
Detection Limit (ppm)	1000	1000	—	—	200	1000
In-depth Profiling Resolution	none	none	stereo topography	none	none	20 Å
Time for Analysis	< 1 hour	2 hours	1 hour	4 hours	10 min	<1 hour
Comments	sample cannot be amorphous	grazing incidence beam used	whole slice survey	whole slice survey	rapid & quanti-tative	In-depth profiling by argon sputtering

(c) X-ray probes

	Rutherford Backscattering Spectroscopy (RBS)	Neutron Activation Analysis (NAA)	Ion Microscope (IMS,SIMS)	High Energy Ion Channeling	Charged Particle Activation Analysis (CPA)
Depth Analyzed	200 Å - 1 μm	1 μm	50 Å	100 Å	300 μm
Diameter of Analysis Region	2 mm	> 1 cm	> 5 mm	1 mm	5 mm
Detection Limit (atoms/cm^3)	$5x10^{19}$	$5x10^{11}$ - $5x10^{18}$	$5x10^{15}$ - $5x10^{18}$	$5x10^{16}$	$5x10^{13}$
Detection Limit (ppm)	1000	0.00001 - 100	0.1 - 100	1.0	0.001
In-depth Profiling Resolution	200 Å	1 μm	50 Å	surface technique	25 μm
Time for Analysis	1 hour	2-5 days	1 hour	2 hours	2 hours
Comments	No standards needed	In-depth profiling by chemical etching	Spatial Resolution near 1 μm	crystal-line substrate required	In-depth profiling by chemical etching

(d) Particle beams

Chapter II

X-ray diffraction theory

2.1 Introduction

There are two widely accepted theories of X-ray diffraction, the kinematical theory and the dynamical theory. Using the kinematical theory diffracted intensities are calculated assuming no interaction between the incident and scattered radiation and that each wavelet is scattered only once. Since the probability of multiple scattering events increases with increasing perfect crystal size, only small crystals or highly mosaic crystals are described adequately by this approach. Excellent reviews of the kinematical theory may be found in James (1948) and Warren (1969). In contrast to the kinematical theory, the dynamical theory considers diffraction in materials where the probability of multiple scattering is appreciable. That is, the interaction between components in the wave field produce a coherent coupling between the scattered and incident beam.

The development of the dynamical theory is achieved by considering the electromagnetic properties at each point in the crystal to be described by the simultaneous solutions of Maxwell's equations and the Laue equation, in the environment of a triply periodic complex susceptibility.

2.1.1 Susceptibility and the complex refractive index.

An electron excited by an incident X-ray will oscillate becoming an emitting dipole and due to the electric moment of all the electrons the medium becomes polarised. If ρ is the electron density, the electric polarisation can be described by,

$$\underline{P} = \frac{-e^2 \rho \underline{E}}{4m\pi^2\nu^2} \tag{2.01}$$

where $\underline{P}$ is the electric polarisation vector, -e is the charge on an electron, $\underline{E}$ is the electric field vector, m is the mass of an electron and ν is the frequency of incident

radiation. The electric polarization vector and the electric field vector are related by $\underline{P} = \chi \underline{E}$, where χ is the electric susceptibility and is given by,

$$\chi = -\frac{e^2}{mc^2}\frac{\lambda^2 \rho}{4\pi^2 \epsilon_0} \tag{2.02}$$

which may be written as

$$\chi = -\frac{R\lambda^2 \rho}{\pi} \tag{2.03}$$

where R is the classical radius of an electron. Since the electron density in a crystal is triply periodic, the susceptibility may be expanded as a Fourier series, this gives

$$\chi = \sum_h \chi_h e^{-2\pi i \underline{h}.\underline{r}} \tag{2.04}$$

where,

$$\chi_h = -\frac{R\lambda^2}{\pi V} F_h \tag{2.05}$$

and where $\underline{h}$ is the reciprocal lattice vector, F_h is the structure factor and is given by,

$$F_h = \sum_{unit} \sum_{cell} f_i exp(2\pi i \underline{h}.\underline{r}_i) \tag{2.06}$$

V is the volume of the unit cell and λ is the wavelength of the incident radiation. Absorption is taken into account by considering the susceptibility to be complex and described by,

$$\chi = \chi^r + i\chi^i \tag{2.07}$$

where the superscripts r and i are the real and imaginary contributions. The imaginary part is also triply periodic and can be expanded as a Fourier series giving,

$$\chi^i = \sum_h \chi^i_o e^{-2\pi i \underline{h}.\underline{r}} \tag{2.08}$$

where

$$\chi^i_0 = -\frac{\mu}{2\pi k} \tag{2.09}$$

and μ is the linear absorption coefficient.

2.1.2 Maxwell's equations

Assuming that the electric conductivity is zero and the magnetic permeability is unity, Maxwells equations reduce to

$$curl \quad curl \quad (1-\chi)\underline{D} = -\frac{1}{c^2}(\frac{\partial^2 \underline{D}}{\partial t^2}) \tag{2.10}$$

where $\underline{D}$ is the electric displacement amplitude.

Since the susceptibility is triply periodic, the solution must reflect this periodicity. A solution called a "Bloch-wave" is tried in which the wave field is considered to consist of an infinite number of plane-waves. Although these waves are a convenient mathematical expression, they have also been shown to be a physical reality by the existence of Pendellosung fringes and the Bormann effect. In the case of X- rays, the number of plane waves making up a Bloch wave is finite, usually 2, but sometimes 3. All the wave vectors of a given field drawn from the various reciprocal lattice points define a point characteristic of the wave field, figure 2.01.

If only one reciprocal lattice point lies sufficiently close to the Ewald sphere to produce a diffracted beam of appreciable intensity, then only the forward diffracted and Bragg diffracted components of the total wave field need to be considered. Using a Bloch wave of the form,

$$\underline{D} = \sum_g \underline{D}_g e^{-2\pi i \underline{k}_g \cdot \underline{r}} e^{i\omega t} \tag{2.11}$$

and a Fourier series to represent the susceptibility, the wave equation reduces to

$$k^2 C \chi_{\bar{g}} \underline{D}_g + [k^2(1+\chi_o) - \underline{K}_o \cdot \underline{K}_o]\underline{D}_o = 0 \tag{2.12}$$

$$[k^2(1+\chi_o) - \underline{K}_g \cdot \underline{K}_g]\underline{D}_g + k^2 C \chi_g \underline{D}_0 = 0 \tag{2.13}$$

where $\underline{k}$ is the incident wave vector in free space and C is the polarisation factor. This has the value of unity when the electric field vector is perpendicular to a plane

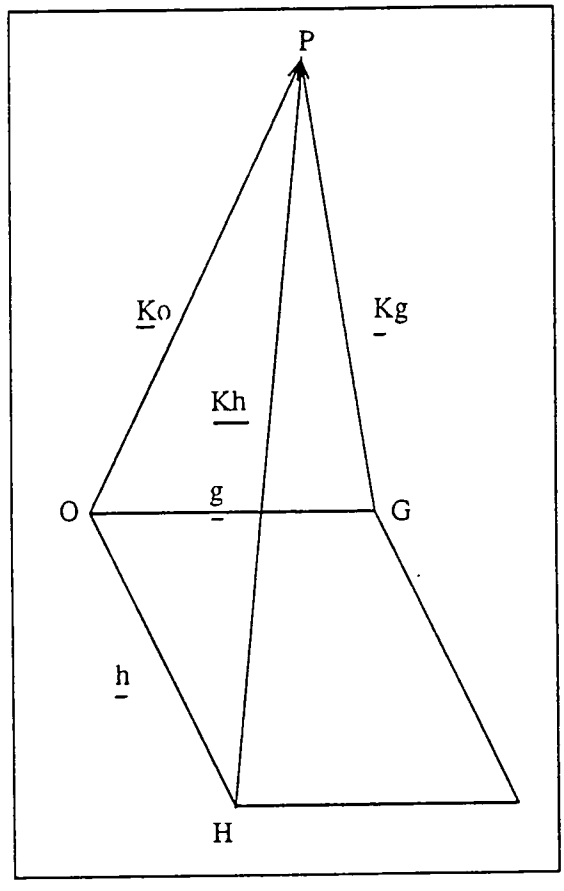

Figure 2.01 illustrates a tie point P characterising a given wave-field, excited by an incident wave vector K_o from a reciprocal lattice vector g.

defined by, the internal wave vector $\underline{K}_0$ and diffracted wave vector $\underline{K}_g$ and equal to $cos2\theta$ when the field vector lies in this plane. $\underline{K}_g$ is the Bragg diffracted wave vector and $\underline{K}_o$ is the forward diffracted wave. These equations require that for a non-trivial solution the determinant of the coefficients be zero. That is

$$\begin{vmatrix} k^2 C\chi_{\bar{g}} & k^2(1+\chi) - \underline{K}_o.\underline{K}_o \\ k^2(1+\chi_o) - \underline{K}_g.\underline{K}_g & k^2 C\chi_g \end{vmatrix} = 0 \tag{2.14}$$

writing

$$\alpha_o = \frac{(\underline{K}_o.\underline{K}_o - k^2(1+\chi_o))}{2\underline{k}} \tag{2.15}$$

and

$$\alpha_g = \frac{(\underline{K}_g.\underline{K}_g - k^2(1+\chi_o))}{2\underline{k}} \tag{2.16}$$

a solution can be obtained in the form

$$\alpha_o\alpha_g = \frac{1}{4}k^2C^2\chi_g\chi_{\bar{g}} \tag{2.17}$$

This equation represents the fundamental solution of the dynamical approach, describing a surface of possible solutions called a 'dispersion surface'.

2.1.3 The dispersion surface.

The dispersion surface is a graphic illustration of equation (2.17) and can be obtained by considering the two reciprocal lattice points O and H. About these points draw spheres of radius k, only close to the intersection of these spheres will strong diffraction take place, figure 2.02a. Far from the Bragg condition the wavevector in the crystal is given by,

$$|k_0| \simeq k(1 + \frac{\chi_o}{2}) \tag{2.18}$$

Close to the Laue point degeneracy is removed and equations 2.15, 2.16 and 2.17 apply, described a hyperboid of revolution, figure 2.02b.

Since the refractive index is very small the spheres may be approximated to planes about the Laue point. By considering a particular tie point P the values

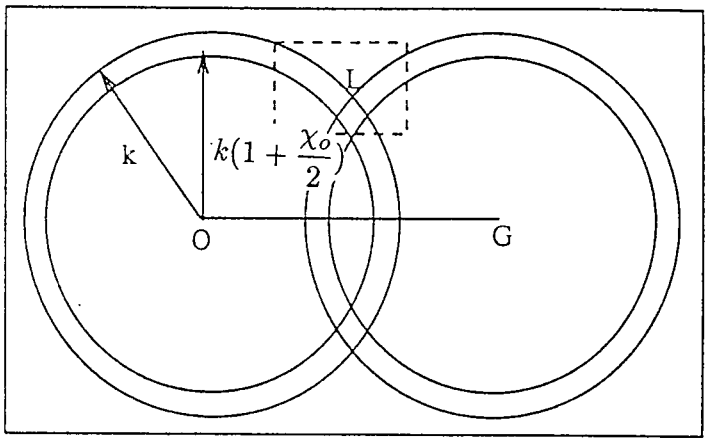

Figure 2.02a shows spheres in reciprocal lattice space about the lattice points O and G, the position of the Laue point is indicated by L.

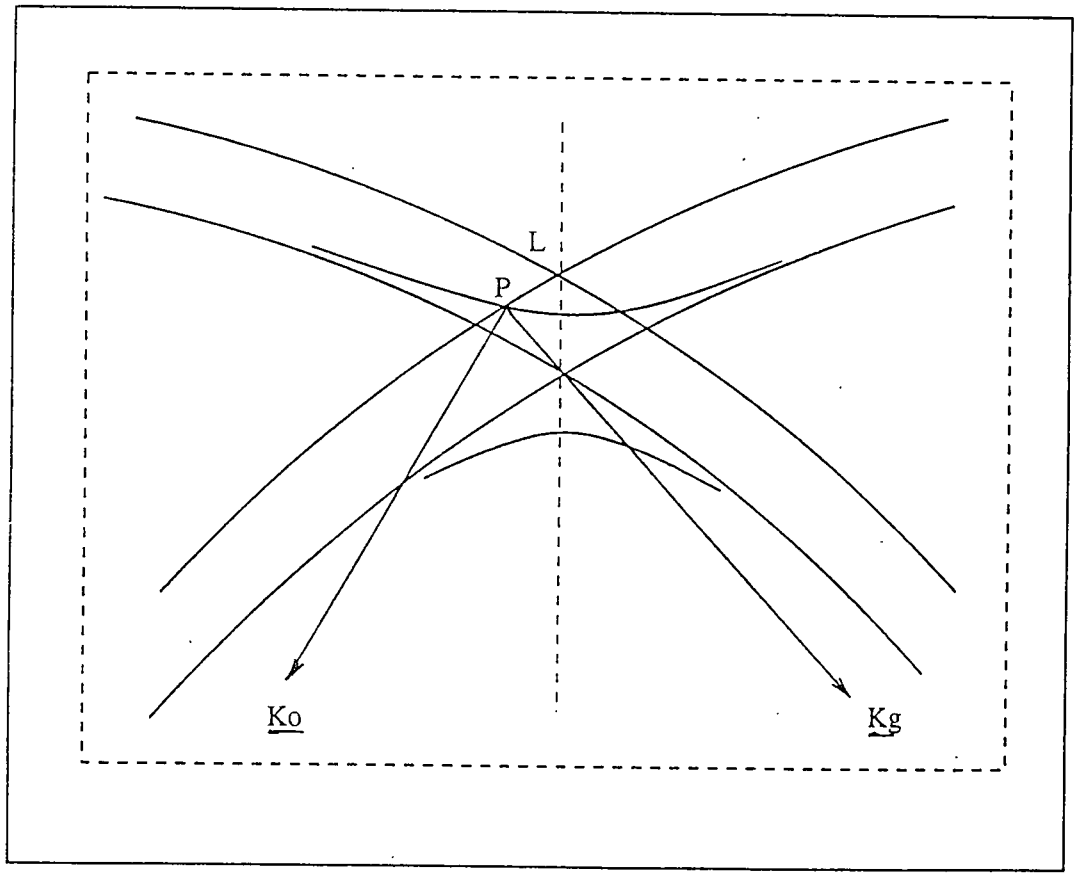

Figure 2.02b. This figure shows the dispersion surface construction magnified about the Laue point, L. The tie point P is marked, which is selected from the incident wave vector K_o and the diffracted wave vector K_g

of α_o and α_h are represented by the perpendicular distances from this point to the sphere of radius k. Positive values α_o and α_h are obtained from branch 1 and negative values from branch 2. These two branches are further divided into two polarisation states σ and π.

2.1.4 Boundary conditions.

The dispersion surface allows the wave fields propagating in a crystal to be determined while the boundary conditions for the wave vector show which particular wave fields are excited in any given problem. The matching conditions for electromagnetic waves apply constraint on frequency, amplitude, and wave vector. The requirement of the continuity of frequency does not explicitly concern us, but the continuity of wave vector has important consequences. The boundary condition for the wave vector is the continuity of the tangential components, that is for a plane wave of amplitude

$$\underline{D} = \underline{D}_i e^{(-2\pi i \underline{k}.\underline{r})} \tag{2.19}$$

incident on the upper surface of the crystal,

$$e^{(-2\pi i \underline{k}.\underline{t})} = e^{(-2\pi i \underline{K}_o.\underline{t})} \tag{2.20}$$

where $\underline{t}$ is a unit vector in the surface. This is equivalent to stating that the tangential components on either side of the boundary must be equal. This may be written as

$$\underline{K}_{oi} - \underline{k} = \underline{K}_{g1} - \underline{K} = \delta \underline{n} \tag{2.21}$$

where $\underline{k}$ is the wave vector outside the crystal, $\underline{k}_{oi}$ is the incident wave vector in the crystal while $\underline{K}_{g1}$ is the excited wave vector and $\underline{n}$ is a unit wave vector normal to the crystal surface. These constraints mean that the incident and diffracted wave vectors may only differ by a vector normal to the crystal surface. This condition then allows a graphical interpretation to be made of how the points are selected. In figure 2.03, which illustrates the Laue case, it can be seen that a normal from the crystal surface cuts the dispersion surface at the points P and Q when drawn from the tail of the incident wave vector. This implies that, in the Laue case two

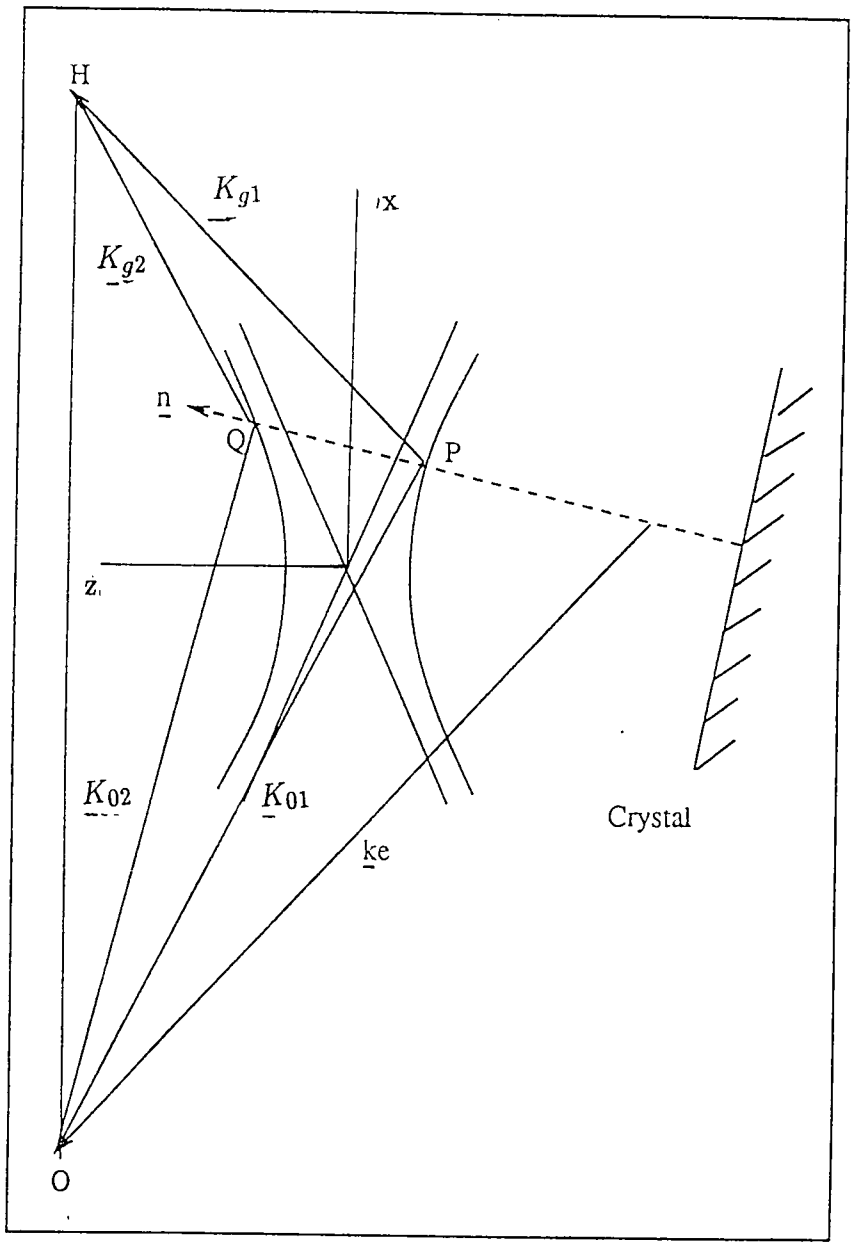

Figure 2.03. This figure shows the Laue case dispersion surface construction. The tie points P and Q are also shown being determined from the interception of the normal from the crystal surface and the tail of the incident wave vector $\underline{k}_e$

Bloch waves are excited from each branch of the dispersion surface, one for each polarization state. The interception of the normal with the dispersion surface may be described by considering the deviation from the Laue point.

In the coordinate system Ox, Oz in figure 2.03 the equation of the dispersion surface is

$$z^2 = \frac{1}{4}\Lambda_o^2 + x^2 tan^2\theta_b \tag{2.22}$$

where Λ_o is the diameter of the dispersion surface and θ_b is the Bragg angle. The angle Θ between the normal to the dispersion and the 0_z axis is given by

$$tan\Theta = \frac{dz}{dx} = \frac{x tan^2\theta_b}{z} \tag{2.23}$$

The deviation of the tie points from the exact Bragg condition, in the symmetric case, is expressed in terms of a parameter η. This is defined as

$$\eta = \frac{2x tan\theta_b}{\Lambda_o} \tag{2.24}$$

The angular deviation from the exact Bragg condition is given by

$$\Delta\theta = \frac{x sec\theta_b}{k} \tag{2.25}$$

It can then be seen that the deviation parameter is proportional to the angular deviation from the exact Bragg condition, since substitution into equation 2.22 gives

$$z = \frac{\pm\Lambda_o(1+\eta^2)^{\frac{1}{2}}}{2} \tag{2.26}$$

It can then be shown that the direction of propagation of the diffracted wave is normal to the dispersion surface (Tanner, 1976).

The boundary condition for the wave amplitudes may be taken as

$$\underline{D}_i = \underline{D}_{o1} + \underline{D}_{o2} \tag{2.27}$$

and

$$0 = \underline{D}_{g1} + \underline{D}_{g2} \tag{2.28}$$

This allows expressions for the amplitude ratio, R, given by $R = \frac{D_o}{D_g}$ to be calculated from the dispersion surface equation in terms of the deviation parameter η. This then gives in the Laue case

$$R = \eta \pm (1 + \eta^2)^{\frac{1}{2}} \tag{2.29}$$

where the + sign refers to branch 1 and the - sign to branch 2. The intensity of the diffracted and transmitted beams at a depth t below the surface may then be calculated by applying the boundary conditions of equations 2.27 and 2.28 to the exit beams. This then gives expressions for the diffracted intensity as,

$$I_g = \frac{sin^2 \pi \Lambda_o t (1 + \eta^2)^{\frac{1}{2}}}{1 + \eta^2} \tag{2.30}$$

$$I_o = 1 - \frac{sin^2 \pi \Lambda_o t (1 + \eta^2)^{\frac{1}{2}}}{1 + \eta^2} \tag{2.31}$$

Once the Bloch waves from each tie point have been excited they become spatially separated in thick crystals and act independently, as they have different wave vectors. This therefore gives rise to interference and by considering the boundary conditions it can be shown that both the diffracted and transmitted beams display a periodic variation in intensity with thickness. This period is the same for both beams and is given by a depth $[\Lambda_o(1 + \eta^2)^{\frac{1}{2}}]^{-1}$. This has a maximum value at $\eta = 0$ which corresponds to the exact Bragg condition. The depth corresponding to one period is known as the extinction distance η_g and is given by, $(\Lambda)^{-1}$

$$\eta_g = \Lambda_o^{-1} = [\frac{\pi V_c cos\theta_b}{R\lambda C(F_g F_{\bar{g}})^{\frac{1}{2}}}] \tag{2.32}$$

In the Bragg case the normal from the entrance surface, drawn from the tail of the incident wave vector, cuts the dispersion surface in two points both on the

same branch. Since the propagation direction of energy is normal to the dispersion surface this implies that at one intersection the energy is directed into the crystal, while at the other point it is directed outwards. Since energy flow is attenuated by photoelectric absorption in thick crystals only the point which directs energy into the crystal is realistic. This corresponds to points excited on the low angle side of branch 1 and the high angle side of branch 2, figure 2.04. In thin crystals the intensity of the diffracted beam shows interference effects because both Bloch waves are present and is calculated assuming similar boundary conditions to the Laue case. However in thick crystals the intensity of the diffracted beam may be calculated assuming only one tie point contributes to the wave field this then gives the intensity as,

$$I_g^{\eta} = (1 + \eta^2)^{-1} \tag{2.33}$$

As the crystal is rotated through the Bragg condition the intensity varies as a function of η. The intensity of the curve drops to half its value when $\eta = \pm 1$. By reference to equation 2.33 this gives the half width of the reflection as

$$\Delta\theta_{\frac{1}{2}} = \frac{2}{g\xi_g} \tag{2.34}$$

In the region, $|\eta| = 1$ no wave fields are excited and total reflection occurs. When absorption is considered the curve becomes asymmetric. In the case of a thin crystal then the interference effects referred to earlier are visible in the tails of the rocking curve.

Upon substitution of approximate numbers we find that plane wave rocking curves are of the order of a few seconds in width and ξ_g and η rise with the increasing order of the reflection. High order and weak reflections have extremely narrow rocking curves.

However to describe fully the scattered intensity as a function of wavelength in real crystals it is necessary to consider the wavelength dependent absorption, commonly referred to as anomalous scattering, particularly in the region of an absorption edge. A discussion of the anomalous dispersion correction factors is included in appendix B.

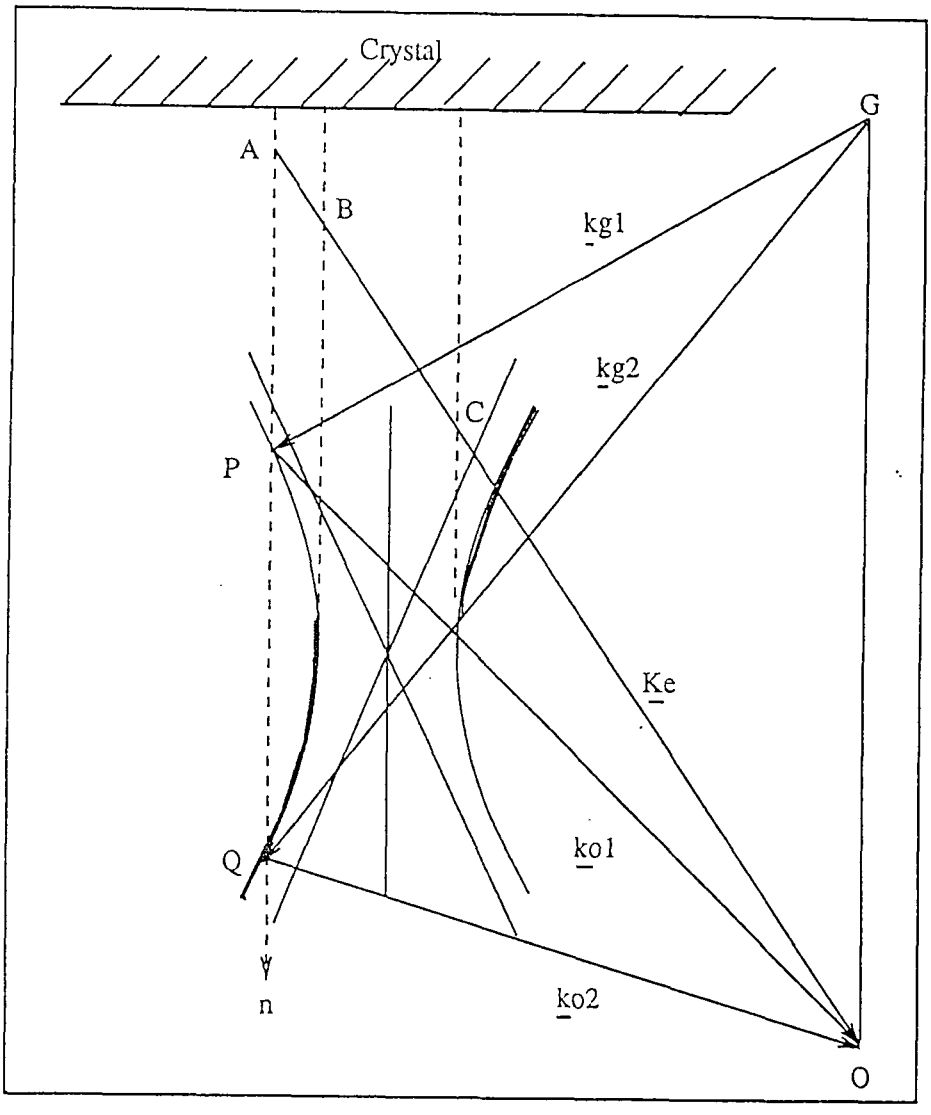

Figure 2.04. This figure shows the dispersion surface construction of the Bragg case.

Chapter III

Multiple crystal X-ray diffraction

3.1 Introduction

The use of multiple reflections allow the study of small variations in long range strains (up to 1×10^{-8}) associated with the growth of epitaxial layers (Bond and Andrus, 1952; Bonse and Kappler, 1958). The principle of using a first crystal to produce a monochromatic beam of X-rays was first demonstrated in the late 1920s by Compton (Compton, 1931) while studying calcite crystals. This was later developed by Schwarzschild (1928), Compton and Allison (1936) and DuMond (1937) who discussed the dependence of the rocking curve on the spectral and angular characteristics of the source and the number and type of reflections taking place. It was not until the sixties that highly perfect single crystals became widely available and the use of this technique much more widespread. In the case of a single crystal rocking curve, the width of the peak is dominated by the divergence of the source, this is illustrated in figure 3.01 where the size of the collimating slits defines the angular range incident on the sample. The double crystal diffractometer uses a first crystal which is rocked to obtain the centre of the reflecting range and then fixed in position. This provides an incident beam on the second crystal with a much reduced angular range defined only by the quality and curvature of the crystal, rather than the divergence of the source.

3.2 Theory of the double crystal diffractometer

Double crystal diffractometry uses two crystals aligned at the Bragg condition, figure 3.02 illustrates the three general arrangements for double crystal diffraction to take place. The (n,+n) geometry corresponds to the two outward normals pointing in the same direction, while the (n,-n) geometry corresponds to the two outward normals pointing towards one another. The (n,+n) geometry is dispersive in wavelength, while the (n,-n) geometry may be either non-dispersive or dispersive in wavelength depending on the crystals and Bragg planes used. To understand

the way in which these arrangements differ consider figure 3.03 which illustrates the (n,-n) arrangement. In this figure the first crystal A has a range of incident radiation of horizontal divergence given by the angle α and vertical divergence given by the angle ϕ. The horizontal divergence is defined as the angle made with its projection on a vertical plane containing the incident beam. The vertical divergence is defined as the angle made with its projection on a horizontal plane containing the incident beam. The crystal is aligned so that diffraction is taking place in the centre of the Bragg peak defined by the incident angle of $\theta(\lambda_0, n_a)$, where n is the order of diffraction from crystal a. The glancing angle of an arbitary ray on the crystal is given by,

$$\theta(\lambda_0, n_a) + \alpha - \frac{1}{2}\phi^2 tan\theta(\lambda_0, n_a) \tag{3.01}$$

and since

$$\theta(\lambda, n_a) = \theta(\lambda_0, n_a) + (\lambda - \lambda_0)\frac{\partial\theta}{\partial\lambda_0}\theta(\lambda_0, n_a) \tag{3.02}$$

the deviation of the ray from the central position is given by

$$\alpha - \frac{1}{2}\phi^2 tan\theta(\lambda_0, n_a) - (\lambda - \lambda_0)\frac{\partial\theta}{\partial\lambda_0}(\lambda_0, n_a) = 0 \tag{3.03}$$

The first term in the above equation corresponds to the reduction in the Bragg angle by the horizontal divergence, while the second term corresponds to the reduction from vertical divergence and the third term to the reduction from the wavelength deviation of the ray. Unlike the first crystal, the second crystal is moving and the deviation from the exact Bragg condition is given by the angle β, hence a similar expression may be written as

$$\pm\beta \pm \alpha - \frac{1}{2}\phi^2 tan\theta(\lambda_0, n_b) - (\lambda - \lambda_0)\frac{\partial\theta}{\partial\lambda_0}(\lambda_0, n_b) = 0 \tag{3.04}$$

To obtain the reflected power from crystal B the power reflected from crystal A needs to be considered first. This can be achieved by considering the element of power present within the wavelength increment $\lambda + d\lambda$ and the horizontal and vertical divergence increments $\alpha + d\alpha$ and $\phi + d\phi$. This elemental power can be described by the relation

$$G(\alpha, \phi)J(\lambda - \lambda_0)d\alpha d\lambda d\phi \tag{3.05}$$

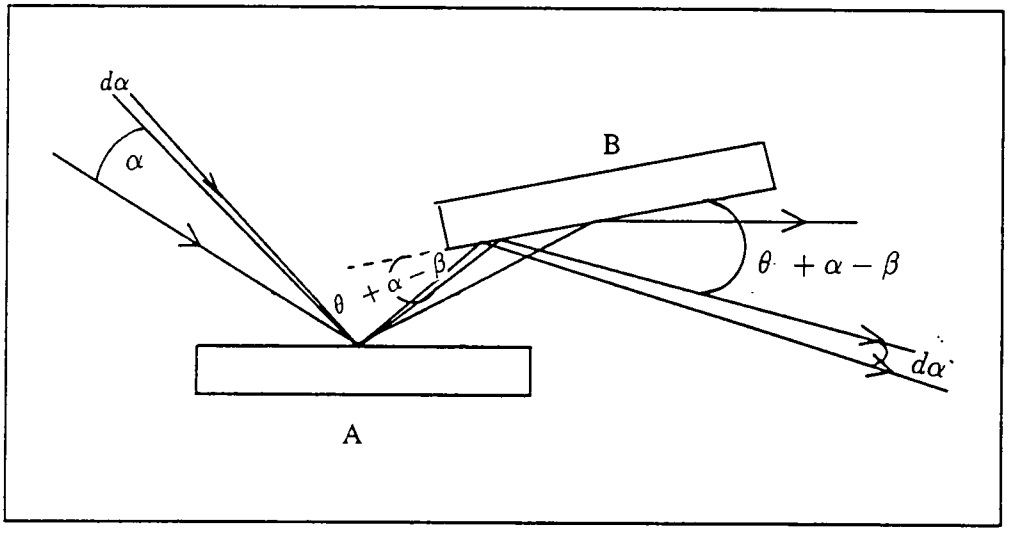

Figure 3.03. This figure illustrates a general double crystal arrangement with horizontal divergence α, vertical divergence ϕ and incident angle θ at the first crystal and β at the second crystal.

where J is the energy distribution of the incident spectrum and the function G is a term which represents the geometry of the instrument. The power reflected from crystal A depends on the deviation of the incident ray, from the angle $\theta(\lambda, n_a)$. This is given by the single crystal diffraction function C_a which is a function of equation 3.03. Similarly the power reflected from crystal B is dependent on the deviation of the glancing angle on B from $\theta(\lambda, n_b)$ and the deviation may be described by the function C_b which is a function of equation 3.04.

The total intensity reflected from crystal B is obtained by considering the product of the two crystal expressions integrated over the ranges of vertical and horizontal divergence as well as the characteristic wavelength spread.

$$P(\beta) = \int_{\phi_{min}}^{\phi_{max}} \int_{\lambda_{min}}^{\lambda_{max}} \int_{\alpha_{min}}^{\alpha_{max}} G(\alpha, \phi) J(\lambda - \lambda_0) C_a[\alpha - \frac{1}{2}\phi^2 tan\theta(\lambda_0, n_a)$$

$$-(\lambda - \lambda_0)\frac{\partial\theta}{\partial\lambda_0}(\lambda_0, n_a)]$$

$$\times C_b[\pm\beta \pm \alpha - \frac{1}{2}\phi^2 tan\theta(\lambda_0, n_b) - (\lambda - \lambda_0)\frac{\partial\theta}{\partial\lambda_0}(\lambda_0, n_a)]d\alpha d\lambda d\phi \qquad (3.06)$$

This expression can be simplified by considering a number of practical constraints. Firstly the effective value of C_a and C_b is negligible unless the value of its argument is very nearly zero. This allows the function G to be expressed as,

$$G(\alpha, \phi) = G_1(\alpha) G_2(\phi) \qquad (3.07)$$

A further simplification may be made by considering the vertical divergence to be small, the two crystals to be the same and the power distribution of the source to be constant over the reflecting range of the crystal. This then enables the expression to be simplified to

$$P(\beta) = K \int_{-\infty}^{\infty} C(\alpha) C(\alpha - \beta) d\alpha \qquad (3.08)$$

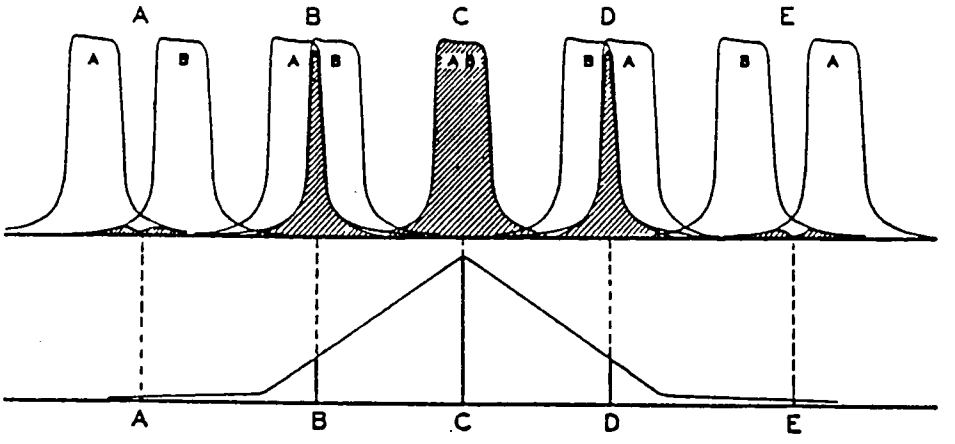

Figure 3.04 Illustrates the variation of the reflected intensity with various degrees of overlapping of the diffraction patterns of crystals A and B as the crystals are rocked through the parallel position. The values of the product integral plotted as the ordinates in the lower curve correspond to the total superimposed transparency area. After DuMond (1935).

where K represents the functions G_1, G_2 and J.

This expression can be visualised by allowing the function C to be described by a normal distribution. The integral is evaluated by taking the product of the ordinates as a function of α for each value of β. Varying β then gives additional values of the function, in this way the two functions effectively cross over one another and form a function which is the correlation of the two crystal reflecting ranges, figure 3.04.

3.2.1 Dispersion for the double crystal arrangement

The dispersion of the double crystal arrangement can be deduced by considering the range of diffraction to be small, which allows the arguments of equation 3.03 to be equal to zero. That is,

$$\alpha - \frac{1}{2}\phi^2 tan\theta(\lambda_0, n_a) - (\lambda - \lambda_0)\frac{\partial\theta}{\partial\lambda_0}(\lambda_0, n_a) = 0 \tag{3.09}$$

and

$$\pm\beta \pm \alpha - \frac{1}{2}\phi^2 tan(\lambda_0, n_b) - (\lambda - \lambda_0)\frac{\partial\theta}{\partial\lambda^0}(\lambda_0, n_b) = 0. \tag{3.10}$$

thus,

$$\beta - \frac{1}{2}\phi^2[tan(\lambda_0, n_a) \pm tan\theta(\lambda_0, n_b)]$$

$$-(\lambda - \lambda_0)\frac{[\partial\theta(\lambda_0, n_a)}{\partial\lambda_0} \pm \frac{\partial\theta(\lambda_0, n_b)}{\partial\lambda_0}] = 0. \tag{3.11}$$

defining D as

$$D = \frac{\partial\theta(\lambda_0, n_a)}{\partial\lambda_0} \pm \frac{\partial\theta(\lambda_0, n_b)}{\partial\lambda_0}, \tag{3.12}$$

where the upper sign is for (n,+n) setting and the lower is for the (n,-n) setting, and using the differential of Braggs law gives,

$$D = \frac{1}{\lambda_0}[tan\theta(\lambda_0, n_a) \pm tan\theta(\lambda_0 n_b)]. \tag{3.13}$$

This allows equation (3.12) to be written as,

$$\beta - \frac{1}{2}\phi^2 D\lambda_0 - (\lambda - \lambda_0)D = 0 \tag{3.14}$$

or

$$\beta = \frac{1}{2}D\lambda_0\phi^2 + D(\lambda - \lambda_0) \tag{3.15}$$

The differential of this expression gives

$$\frac{\partial\beta}{\partial\theta} = D \tag{3.16}$$

which clearly shows that in the case of the (n,-n) setting if the reference and sample crystals are the same then the dispersion is zero.

3.2.2 DuMond diagrams

DuMond diagrams represent Braggs law by plotting wavelength against angle and demonstrate multiple crystal diffraction by overlaying the curves for successive reflections.

To illustrate the usefulness of the DuMond diagram consider the situation where two wavelengths are close enough together and of comparable intensity so that they are simultaneously diffracted from the first crystal, due to the source divergence. This is the case for the K line of copper which consists of a $K_{\alpha 1}$ and a $K_{\alpha 2}$ doublet separated by $0.00383\mathring{A}$. Since the divergence of the source allows diffraction of these two wavelengths simultaneously, these wavelengths are also incident on the second crystal. Only when the second crystal is identical and parallel to the first will both wavelengths again be diffracted at the same angle. Therefore this arrangement is non-dispersive in wavelength, but dispersive in angle. The DuMond diagram corresponding to the (n,-n) arrangement is illustrated in figure (3.05) which shows the two single crystal ranges superimposed on one another with diffraction taking place simultaneously at all wavelengths. Any shift in the angle between the crystals greater than the reflecting ranges ($\Delta\theta_1$, $\Delta\theta_2$) results in loss of diffraction from the second crystal. If one now considers the (n,+n) geometry then diffraction occurs over only a narrow region of overlap, hence this geometry is dispersive in wavelength and may be described by figure 3.06. Additional crystal arrangements can also be readily described by the use of a DuMond diagram

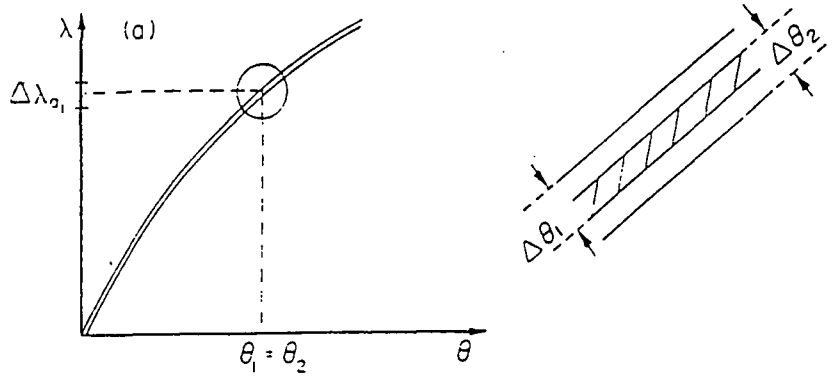

Figure 3.05 This shows the DuMond diagram for the (n,-n) geometry which is non-dispersive is wavelength but dispersive in angle.

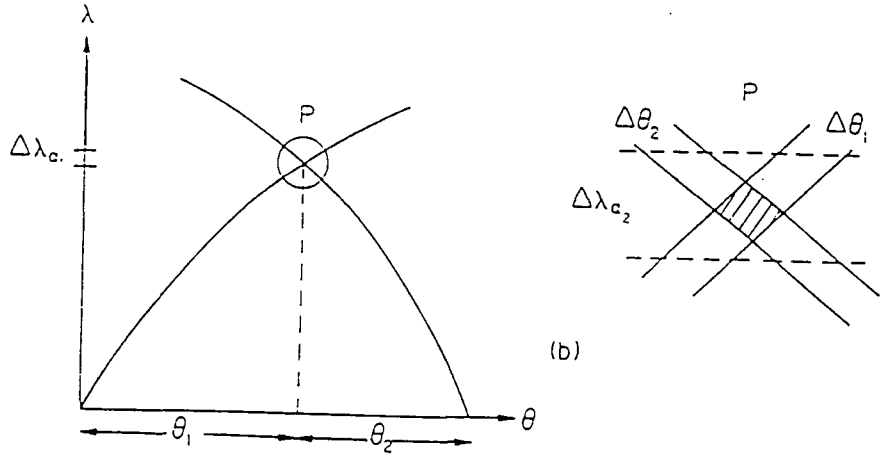

Figure 3.06 This shows the DuMond diagram for the (n,+n), geometry which is dispersive in wavelength but non -dispersive in angle.

and figure 3.07 illustrates the (n, -n, -n, n) geometry in which the first pair of crystals is angular dispersive while the third crystal is wavelength dispersive. This arrangement provides a rocking curve conditioned in both angle and wavelength.

3.3 Vertical beam divergence

The effect of vertical divergence and tilt has been considered by a number of authors (for example Yoshimura, 1984). Two graphs describing this effect are given in figures 3.08a and 3.08b and show the change in Bragg angle θ_b associated with a vertical divergence φ and a tilt angle χ at positions corresponding to the centre of the rocking curve, W=0 and at positions W=$\pm$1 corresponding to the full width half maximum (FWHM) positions. The graphs also illustrate the case when diffraction is taking place at a range of angles slightly off the Bragg peak. Figure 3.08a illustrates the parallel (n,-n) setting of two Si(333) reflections. In the case of a tilt angle of 1.55 secs (which in the figure corresponds to the dashed line curves) with diffraction taking place at the exact Bragg condition (corresponding to W=0), increasing the vertical divergence from -0.5 secs to 0.5 sec on the figure results in a change in the Bragg angle of approximately 1 secs. If there is no tilt (that is $\chi = 0$) and the crystal is at the exact Bragg condition then the effect of vertical divergence is negligible on the intensity. The curve for the non-parallel (n,-n) arrangement, with Si(111) and Si(220) reflections, is shown in figure 3.08b. The effect of increasing vertical divergence with the parameter W=0 causes a large movement in the Bragg angle required for diffraction. Yoshimura (1984) has shown that the half width of a rocking curve, ω', is related to the half width of a rocking curve at zero vertical divergence, ω, by

$$\omega' \simeq \frac{\omega}{[1 - \varphi^2/cos^2\theta_b]^{\frac{1}{2}}} \tag{3.17}$$

if the two reflection curves are assumed to be gaussian.

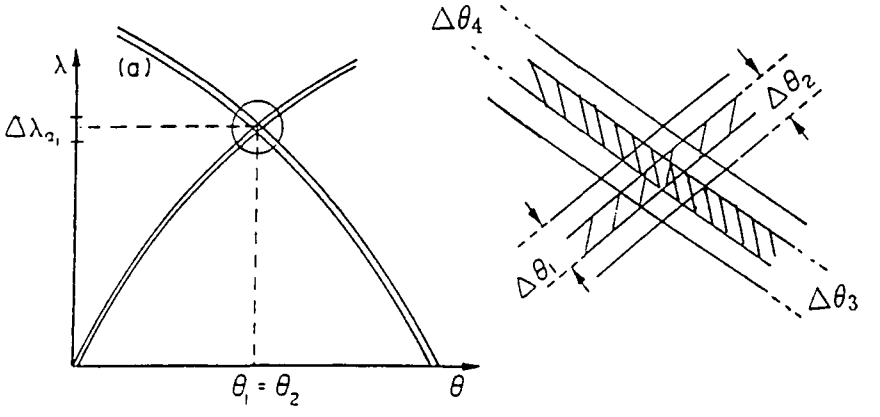

Figure 3.07 This shows the 4 crystal arrangement (n,-n,-n, n). The first two crystals are dispersive in angle while the second and third are dispersive in wavelength.

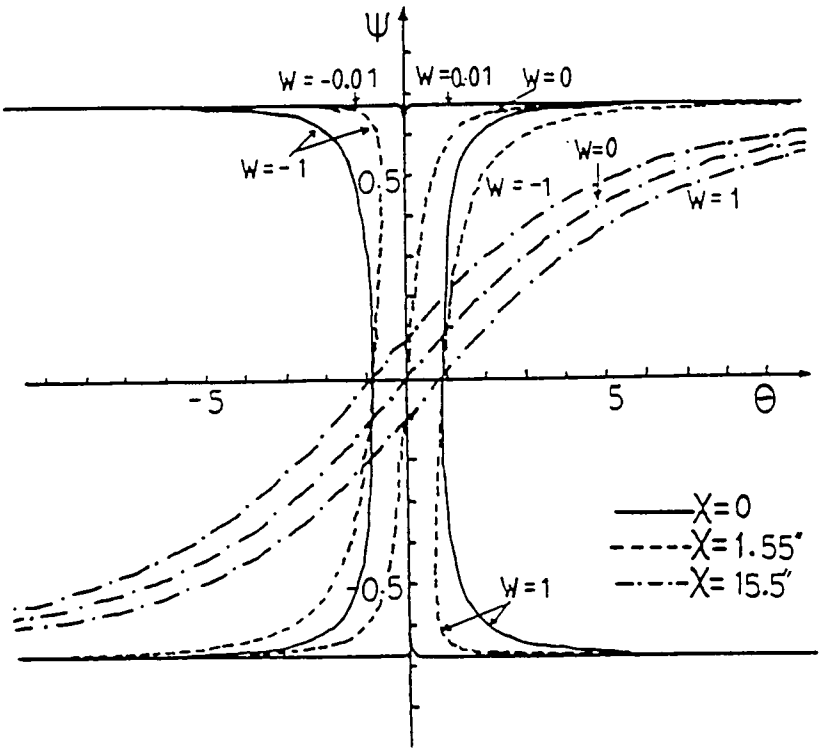

Figure 3.08a The change in crystal angle (θ) required to diffract a beam with value W as a function of ψ, the position of the incident beam on the first crystal, for a parallel $(+,-)$ setting with two silicon (333) reflections and CuK_{α_1} radiation, for varying values of χ the tilt angle. After Yoshimura (1984).

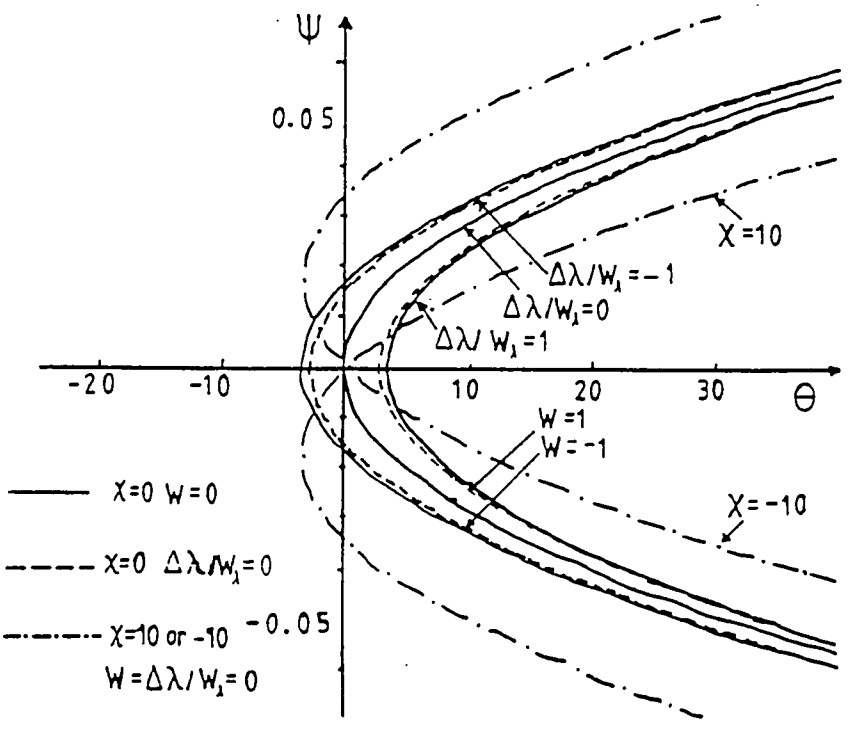

Figure 3.08b Curve of ψ vs (θ) for a non- parallel $(+,-)$ setting with $Si(111)$ and $Si(220)$ reflections. CuK_{α_1} radiation with the abscissa scaled in units of 1.55 arc seconds. After Yoshimura (1984).

Chapter IV

Experimental techniques and use of synchrotron radiation

4.1 The study of heteroepitaxial layers

Double crystal diffractometry is now widely accepted as an effective technique for the non-destructive measurement of structural parameters of semiconductor devices (Bartels and Nijman, 1978; Tapfer and Ploog, 1986; Halliwell et al, 1984; Baumbach et al, 1988). The most common application of this technique is in the determination of the effective mismatch relative to the substrate and layer thickness (Estrop et al, 1976). Interference effects present in the rocking curve can also give information on a number of other structural defects such as compositional grading, roughness and inter-diffusion at interfaces (Ryan et al, 1987). Refinements of the double crystal technique are now able to detect nanometer layer thicknesses and compositional variations of a few ppm (Tanner and Halliwell 1988; Tanner, 1990).

For thick single layers of uniform composition the lattice mismatch can be determined directly from the separation of the rocking curve peaks, the ratio of the areas under the peaks gives a measure of the thickness, while the widths allow an estimate of the quality of the layer to be made (Bartels and Nijman, 1978; Macrander et al, 1986). Halliwell (1981) has shown that the measurement of mismatch using double crystal rocking curve analysis is accurate to 20ppm when using a combination of asymmetric and symmetric reflections on samples of InGaAs and InGaAsP on InP. For highly mismatched layers, asymmetric reflections have been used to determine the degree of relaxation at growth interfaces (Wang et al, 1988). When the layer composition varies with depth, the lattice parameter profile can be determined by fitting simulated and experimental rocking curves (Hill et al, 1985; Macrander et al, 1986; Tapfer and Ploog, 1986; Bowen et al, 1987).

Fleming et al (1980) and Halliwell et al (1983) have shown how compositional grading as a result of a time dependent MBE flux in the growth of GaAlAs layers can be determined by rocking curve analysis. Burgeat et al (1981) have also shown,

using double crystal rocking curve analysis, how the growth of several microns thick layers of GaInAsP on InP by LPE can lead to a sublayer structure. Lyons (1989) has discussed the effect of compositional grading at interfaces and has shown that X-ray diffraction techniques are more sensitive to strained interfacial regions than TEM. Bass et al (1986) illustrated the use of X-ray diffraction as a complementary technique to TEM in the study of InGaAs on GaAs and found that a loss in the optical properties believed to be associated with carbon impurities, determined from photoluminescence, was in fact a structural effect. Double crystal techniques have also shown that substrate rotation during the growth of MBE layers greatly improves the uniformity of layer thickness (Alavi et al, 1983). Several workers have shown how the effect of ion bombardment can lead to a damaged region which can be detected as having a slightly different lattice parameter (Burgeat and Colella, 1969; Fukuhara and Takano, 1977; Larson and Barhorst, 1980). Macrander and Strege (1986) showed how the VPE growth technique requires careful monitoring of the gas stoichiometry to achieve lattice matched layers of InGaAsP on InP and also studied the layer uniformity across wafers. Chu and Tanner (1986; 1987) and Wie (1989) have shown how structures consisting of a sandwich of a thin layer between two relatively thick layers, commonly found in optical laser structures, can be characterised. These thin layers can not be characterised directly from a diffraction peak associated with the layer, but structure present on the confining layer peak has been shown to allow thickness characterisation to 100 $\AA$. Multiple quantum well (MQW) structures which are an example of bandgap engineering have also been studied using double crystal techniques (Halliwell et al, 1984; Bartels et al, 1986). These structures give the crystal grower a further degree of freedom allowing layer growth even if the lattice parameter of the material does not match that of the substrate. The strain in turn modifies the band gap and hence the electronic and optical properties of the device. These layers only remain coherent if the thickness is maintained below the critical thickness value preventing the onset of relaxation resulting in dislocation formation (Matthews, 1966; Bean et al, 1984).

4.1.1 Lattice mismatch

In the growth of structures only several microns thick, the substrate is considered to be elastically rigid while the overlayers are subjected to an isotropic

stress. Assuming pseudomorphic growth, the layers grow in a way as to match the in-plane lattice parameter of the substrate and are therefore tetragonally distorted, figure 4.01. The mismatch is defined

$$m = \frac{a_r - a_0}{a_0} \tag{4.01}$$

where a_r is the lattice parameter of the unit cell of the relaxed layer material and a_0 is the lattice parameter of the substrate material. Layer growth results in the lattice parameter perpendicular to the interface adopting a value dependent on the degree of mismatch, and it is this lattice parameter which is determined in the case of surface symmetric reflections.

The relationship between the relaxed mismatch and the measured mismatch is given by

$$m^* = \frac{(1-\nu)}{(1+\nu)}m \tag{4.02}$$

The relationship between the peak separation and the measured mismatch is given by,

$$m^* = -cot\theta_B(\delta\theta) \tag{4.03}$$

for surface symmetric reflections, where $\delta\theta$ is the separation of the peaks and θ the Bragg angle of the substrate.

In the case of surface asymmetric reflections there is now a second contribution to the layer-substrate peak separation, that associated with a rotational component of the reflecting planes. This can be visualised by considering the distorted layer lattice parameter perpendicular to the surface as having a larger or smaller lattice parameter than that associated with the substrate, figure 4.02. Thus the layer substrate-peak splitting is made up of two components, the first $\delta\theta$, is directly related to the fractional change in the lattice parameter and the second, $\delta\phi$, is the difference in the rotation of the reflecting planes to those planes in the substrate. Hornstra and Bartels (1978) have derived general expressions for these parameters relative to the experimental mismatch,

$$\frac{\delta d}{d} = m^* cos^2(\phi) \tag{4.04}$$

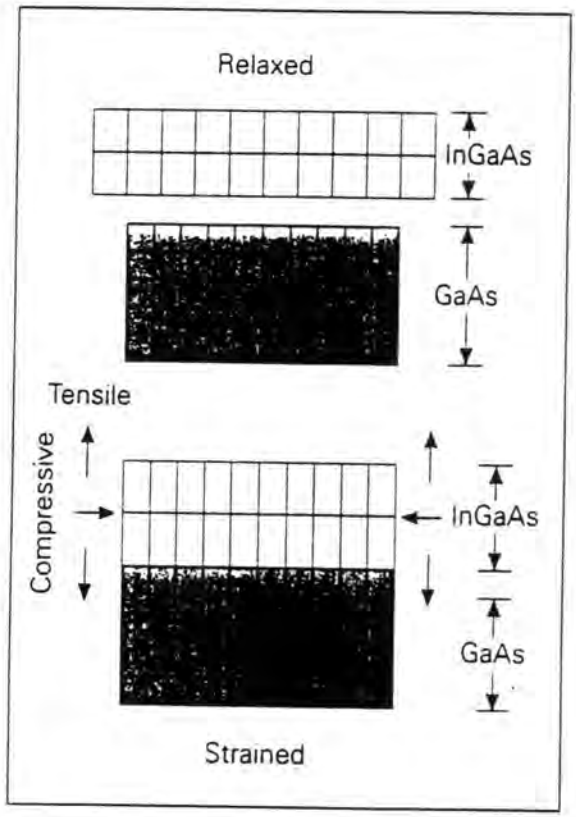

Figure 4.01. This figure shows a block diagram representing tetragonal distortion produced when a layer of InGaAs is grown on a substrate of GaAs.

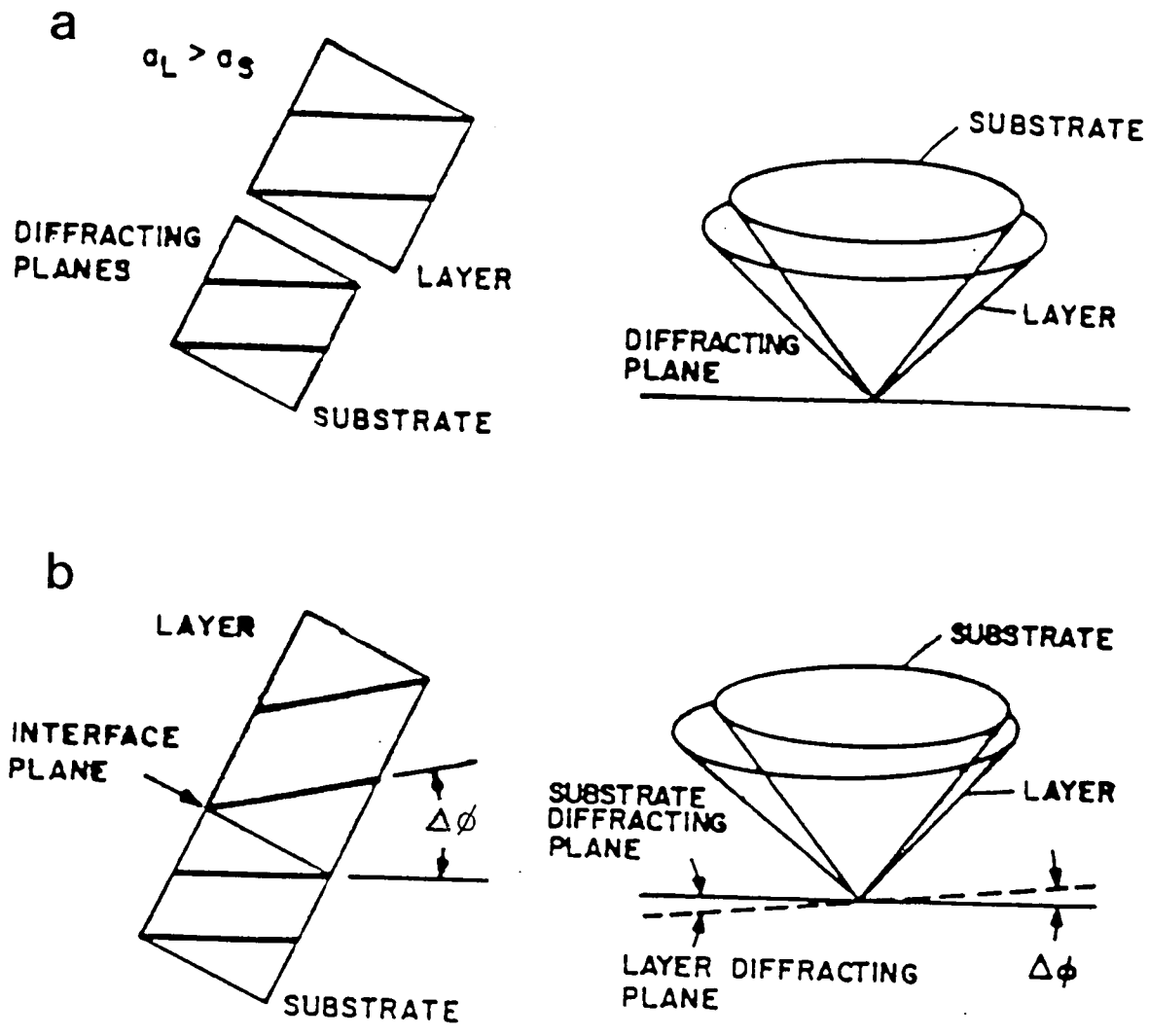

Figure 4.02. This figure shows the rotational component of the layer-peak mismatch in the asymmetric case. Diagram (a), where the layer is incoherent, shows the diffracting planes horizontal and the cone of reflection for the layer placed central to the substrate diffracting cone. In diagram (b) the layer material is now tetragonally distorted with the diffracting cone situated non central to the layer cone.

$$\delta\phi = m^* cos(\phi) sin(\phi) \tag{4.05}$$

Therefore in order to describe the strain in an epitaxial layer one needs to know both $\delta\theta$ and $\delta\phi$. This can be measured experimentally by considering one asymmetric reflection in both glancing incidence and glancing exit geometries. Defining $\delta\omega_A$ as the separation of the substrate and layer peaks on glancing incidence and $\delta\omega_B$ as the peak separation on glancing exit then;

$$\delta\omega_A = (\theta_s - \theta_l) + (\phi_s - \phi_l) \tag{4.06}$$

$$\delta\omega_B = (\theta_s - \theta_l) - (\phi_s - \phi_l) \tag{4.07}$$

substituting and subtracting gives

$$\theta_s - \theta_l = \frac{1}{2}(\delta\omega_A + \delta\omega_B) \tag{4.08}$$

$$\phi_s - \phi_l = \frac{1}{2}(\delta\omega_A - \delta\omega_B) \tag{4.09}$$

and

$$\delta\phi = \phi_l - \phi_s = \frac{1}{2}(\delta\omega_B - \delta\omega_A) \tag{4.10}$$

4.2 Synchrotron radiation

A source of high brilliance is required for X-ray topography. High power is needed to reduce exposure times and a small beam size is required to give good spatial resolution. The production of X-rays is achieved in sealed tubes by the bombardment of electrons onto a target material. This produces a compromise between the X-ray power output and the spatial resolution. A typical sealed fine focus source has a focal spot of 10mm × 0.4mm which can be viewed from two orthogonal directions, usually with a take off angle of 6 degrees from the anode surface. Wavelength range extends from 0.599 - 2.289Å. In recent years the development of rotating anode sources has improved the brilliances by an order of

magnitude, but even with their improved reliability rotating anode sources still require more maintenance.

The limitations of a conventional X-ray source apply practical constraints on the range and number of experiments which can be performed. The major limitations include the need for lengthy exposures times for topography (ranging from several hours to several days for weaker reflections) and the limitation imposed by the source size. Major advantages of synchrotron radiation include; typically three orders of magnitude more usable flux, a high degree of collimation as a result of a low natural divergence of radiation emitted from fast electrons, tunability and a polarization approaching 100% in the horizontal plane. This then allows exposure times to be reduced to several minutes while irradiating samples tens of centimeters in size at a range of wavelengths.

Synchrotron radiation is produced in a manner analogous to bremsstrahlung (braking) radiation emitted when electrons are incident on a target material in a conventional X-ray generator. Charged particles, typically in the energy range 1.5-10GeV, are constrained to move in a circular orbit emitting radiation. The storage ring is a closed toroidal tube which is evacuated to ultra-high vacuum, the toroid is not circular but polygonal with bending magnets at the apex of each section providing the accelerating field. Beam lines extend from the storage ring tangentially outwards and are typically 10-500m in length. The emission spectrum for the SRS source at Daresbury is given in figure 4.03, with the total emitted intensity being proportional to $\frac{E}{m^4}$ where E is the particle energy and m the particle mass. The spectrum is continuous with a broad maximum in the number of emitted photons close to a wavelength in $\mathring{A}$ given by,

$$\lambda_{max} = \frac{5.6R}{E^3} \qquad (4.11)$$

where R is the bending radius of the magnet in metres and E is the kinetic energy of the accelerated particles expressed in GeV. This critical wavelength may be reduced by the use of wigglers or undulators. These devices consist of magnets placed along straight sections of beam line resulting in perturbations of the electron path. This can have the effect of reducing the characteristic wavelength

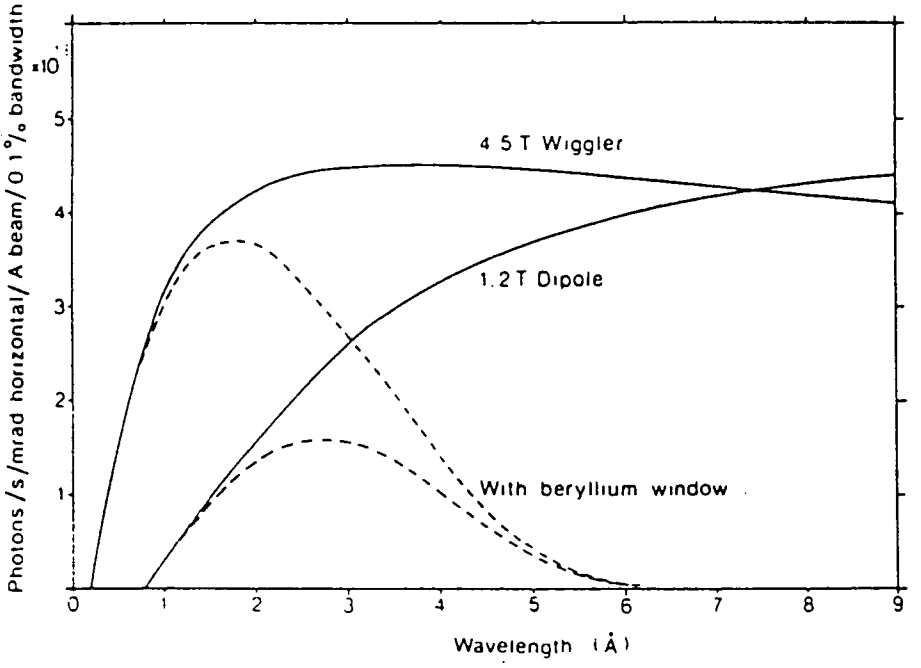

Figure 4.03 Synchrotron X-ray radiation intensities from the SRS, and effect of beryllium window transmission. Solid curves refer to intensities produced in wiggler (4.5T) and standard dipole magnet (1.2T) with the SRS operating at 2 GeV. Dashed curves show corresponding fluxes after passage through a beryllium window of thickness 381μm.

and increasing the overall intensity at the reduced wavelengths. The beam lines are terminated by beryllium windows, this introduces a high wavelength cut off around 6 $\AA$, corresponding to the K absorption edge of beryllium. The emission spectrum is given by,

$$N(\lambda) = 2.46 \times 10^{10}[\frac{\lambda}{\lambda_c}]^2 EG\{\frac{\lambda}{\lambda_c}\} \tag{4.12}$$

where λ_c is the critical wavelength in $\AA$ngstroms and G is the Bessel function given by:

$$G\{\frac{\lambda}{\lambda_c}\} = \{\frac{\lambda_c}{\lambda}\}^3 \int_{\frac{\lambda}{\lambda_c}}^{\infty} K_{\frac{5}{3}}(u)du \tag{4.13}$$

where $K_{\frac{5}{3}}$ is a modified Bessel function and $N(\lambda)$ is the number of photons s^{-1} mrad $^{-1}$ mA^{-1} in a 0.1% bandwidth over the full height of the beam. The use of synchrotron radiation allows white beam topography to be performed. This technique produces white beam Laue patterns of a crystal with each point forming an image at a different wavelength. The applicability of white radiation topography or multiple crystal topography essentially depends on the strain sensitivity that is required. The white radiation methods are sensitive to the order of $10^{-4} - 10^{-5}$ and are suitable for characterising materials in the early stages of development. Multiple crystal methods are sensitive to strains as low as 10^{-8} and can reveal strain related defects in high quality crystals. Image contrast is different from the contrast observed by the use of characteristic line sources as contrast arises from overlap or divergence of the reflected beams. The effect of a grain boundary is simply that a suitable wavelength is selected to undertake diffraction. Synchrotron radiation also has the significant advantage that the photographic plate may be placed several centimetres away from the sample without an appreciable loss in resolution.

In order to improve the strain sensitivity multiple crystal techniques are required and with the use of asymmetric reflections low geometrical distortion may be obtained. Synchrotron radiation also allows tuning of the wavelength to enable

higher contrast from defects as a function of depth in the sample to be obtained (Tanner, 1990).

4.3 Experimental alignment and instrumentation

The majority of the experiments undertaken were performed at the Daresbury synchrotron radiation source on topography stations 7.6 and 9.4. A detailed description of the double crystal camera design can be found in Bowen and Davis (1983). Both stations are equipped with similar double crystal cameras enclosed in radiation proof hutches which are safety interlocked. Station 7.6 is located 80m from the tangent point of the ring while station 9.4 which is a wiggler line located 30m away. The beam line is terminated in the hutch by beryllium windows which impose a long wavelength cut off of approximately $6\mathring{A}$. Immediately in front of the windows are a number of sets of slits which are used primarily to define the source size but also act as radiation shielding. To allow timed exposures which may be as short as 0.1secs both stations are also equipped with fast shutters. The first set of slits is located outside the hutch, these are DC motor driven slits rather than stepper motor driven, and are intended to be used as the beam defining slits. This is because these slits are heavy duty and absorb most of the heat. This approach is also sensible from the shielding view point as the scattering from the first set of slits may be shielded by another set. There are two more sets of slits located inside the hutch, these are referred to as the large and small slits.

The accurate alignment of the double crystal camera with the beam is necessary to ensure not only good results but also the efficient use of available time. To begin the alignment all sets of slits are opened fully. The large DC motor driven slits are then closed to the beam size required. To align the subsequent sets of slits each slit is closed in turn until it just cuts the beam. Once both sets of slits have been aligned the outer slits are then opened slightly to act as scatter shields and not introduce any further scatter.

The double crystal camera is mounted on an assembly which enables rotation about the beam to allow either a horizontal or vertical dispersion to be achieved. Since synchrotron radiation is almost completely horizontally plane polarized, a vertical dispersion geometry is almost always used. The first alignment procedure for the camera is to ensure that the beam passes accurately through the centre of

both the first and second axes. This may be achieved by taking a film of the beam with pointers located in the axes. It is important to realise that an error of 1mm may be too large when adopting glancing incident geometries, so careful alignment is essential. The first crystal is aligned by placing the surface of the crystal on the first axis and taking a film with the crystal parallel to the beam and aligned so that the crystal surface cuts the beam in two. Rotation of the goniometer by $2\theta_b$ is then required and the sample is aligned in a similar way.

Shielding the whole apparatus is essential, especially on station 9.4, as the noise level unless extremely well shielded will exceed the signal. This is usually achieved by placing the first crystal in a lead box with only the smallest possible aperture for the exit beam. The use of a slit over the detector is also useful.

The camera design is based on the earlier instrument of Hart (1980) with a resolution of 0.2arc secs on each axis. The detector is mounted on an axis which is concentric with the second axis and is free to rotate 180 degrees.

The experiments performed at Durham were undertaken using a prototype of the Bede 150 double crystal camera, based on the earlier design of Hart (1980). The detector used was a Nuclear Instruments DM1-1 sodium iodide thallium activated scintillation counter. All the experiments were performed on a sealed fine focus 1.5KW tube driven by a Hiltonbrooks generator.

The double crystal camera alignment is essentially the same as the Daresbury procedure except that the intensity of the source is considerably less and the slitting and shielding requirements are not as important. Again good results may only be obtained if the camera is aligned accurately.

Chapter V

Structural uniformity and the use of double crystal X-ray topography and diffractometry

X-ray diffraction topography is complementary to transmission electron microscopy, (TEM), since TEM images defects with a higher spatial resolution but lower strain sensitivity than X-ray topography. This is because of the much stronger interaction of electrons with atoms than X-rays and atoms. Electrons are rapidly scattered and absorbed on entering a sample. This means that only thin samples (up to 1 μm thick) can be examined. In contrast X-ray topography can study material of any thickness in the Bragg geometry and up to several millimeters in transmission. A second significant difference between X-ray and electron diffraction is that electrons can be readily focused using electromagnetic lenses whereas no lenses exist for focusing X-rays. Thus the spatial resolution obtained in electron diffraction imaging techniques can be directly recorded at increased magnification, whereas X-ray diffraction data is recorded at unit magnification and subsequently magnified using optical techniques.

Image contrast in non-dispersive double crystal topography is dominated by differences in orientation of the first crystal and the specimen. This is because the rocking curves are very narrow and the flanks very steep, compared to rocking curves from single crystal diffractometers. Strain contrast and orientation contrast relate to a change in intensity by (Bonse, 1962)

$$\frac{\Delta I}{I} = k\{tan\theta_b \frac{\partial d}{d} + \underline{n}_t . \underline{n}_g \partial\theta\}$$

where k is the rocking curve slope, θ_b is the Bragg angle, $\frac{\partial d}{d}$ is the fractional change in the Bragg spacing, $\partial\theta$ is the tilt angle, $\underline{n}_g$ is the unit vector parallel to the goniometer axis and $\underline{n}_t$ is the unit vector parallel to the tilt axis. To distinguish between tilt contrast and dilation contrast two topographs may be taken 180 degrees apart about the surface normal. In the vicinity of a crystalline defect the Bragg planes are distorted. If these distortions require a change in the

incident Bragg angle greater than about $\Delta\Theta$, (where $\Delta\Theta$ is the perfect crystal reflecting range) then diffraction will not occur and no intensity will reach the recording medium. X-ray topography using conventional sealed tube sources has two major disadvantages, as discussed previously, those of lengthy exposure times and critical adjustments when setting up the crystals. Unlike the laboratory source the synchrotron radiation is highly collimated and white; a first crystal placed in the beam acts as a monochromator selecting discrete wavelengths defined by the incident and exit angle. If a film is placed behind a crystal a Laue pattern results with each set of reflecting planes selecting its own wavelength and each spot is then an image of the crystal (Tuomi et al, 1974; Hart, 1975). Since primary extinction is lower in regions of distortion, in white radiation topographs dislocations will diffract more than perfect regions (Halliwell et al, 1972).

In order to allow separation of the image produced from substrate and an epi-layer and also to obtain higher strain sensitivity, multiple crystal reflections are required. One of the earliest double crystal synchrotron topography studies of semiconductors was undertaken by Riglet et al (1980) on the contrast of misfit dislocations in GaAlAsP on GaAs. These experiments employed a multiple reflection beam conditioner developed by Hashizume et al (1975) providing a plane wave of low angular divergence.

5.1 Double crystal topographic study of lithium niobate

5.1.1 Introduction

To illustrate some of the features of double crystal synchrotron topography discussed previously this technique was applied to a lithium niobate. This work was carried out in collaboration with Pilkingtons Electro-Optical materials division U.K. who supplied the sample used and the topographs were taken at Daresbury SRS.

The importance of lithium niobate ($LiNbO_3$) single crystals in optical applications, such as a second harmonic generator and electro-optical modulators of laser beams, has been increased and needs for high quality crystals have been created. The most serious problem concerning the quality is the spatial variation in the birefringence, which is considered to be related to the thermal stresses

and compositional variations during crystal growth. Single crystal X-ray diffraction techniques have shown a variety of defects including dislocations, subgrain boundaries, and gross imperfections at ferroelectric domain boundaries. Typical dislocation densities have be found to be 10^4 per cm^2 with grain boundaries in the angular range 5-15 minutes of arc (Sugii et al, 1973).

The purpose of the present study was to attempt to study small(between 1 part in 10^5 and 1 part in 10^6)long range strains induced by periodic variations in the lattice parameter using double crystal synchrotron topography.

The sample studied consisted of a 5mm thick slice of single crystal approximately 50mm × 30mm orientated so that the surface normal lies along the [010] direction. The stereographic projection for the (001) surface of $LiNbO_3$ is given in figure 5.01, indicating the electo-optical axes X,Y and Z as lying along the [210], the [010] and the [001] directions respectively. The [010] direction is also the growth axis. Since $LiNbO_3$ is a hexagonal material there are four reference indices h, i, k, and l. These are derived by using the intercepts on four axes, three in a basal plane lying at 120^o to each other and the forth one normal to the basal plane.

5.1.2 Results

The topographs were taken on station 7.6 at the Daresbury synchrotron source using 1.5 $\AA$ radiation and a large silicon monochromator. The alignment of the camera and the experimental technique employed is as described previously. Plate 5.01 shows the surface symmetric $03\bar{3}0$ topograph taken using a 333 first crystal reflection. Plate 5.02 shows the surface asymmetric $11\bar{2}12$ topograph again taken using a 333 first crystal reflection. The $03\bar{3}0$ reflection was chosen as it allows variations in the lattice parameter parallel to the growth direction to be observed, while the $11\bar{2}12$ plane lying in a zone 30 degrees from the surface zone allows variations in the lattice parameter perpendicular to the growth direction to be observed.

Growth bands are due to periodic variations in the lattice parameter and lie normal to the growth front. The growth bands therefore disappear when the diffraction vector lies normal to the growth band. That is growth bands are invisible when,

$$\underline{g}.\underline{n} = 0 \qquad (5.01)$$

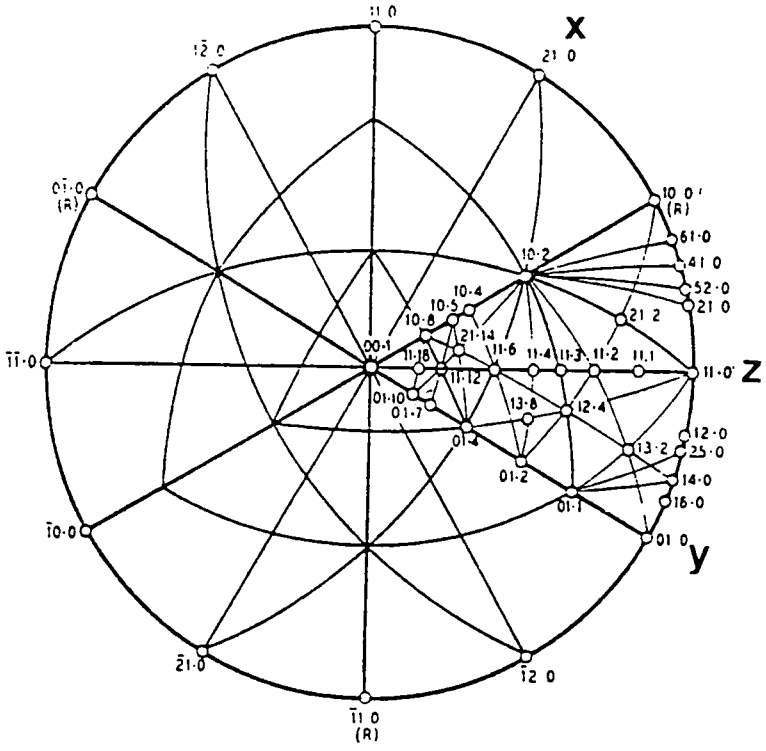

Figure 5.01 shows the stereographic projection of $LiNbO_3$ in terms of the hexagonal parameters hkil, ignoring the rhombohedral requirements -h+k+l=3N. After Nassau et al (1966).

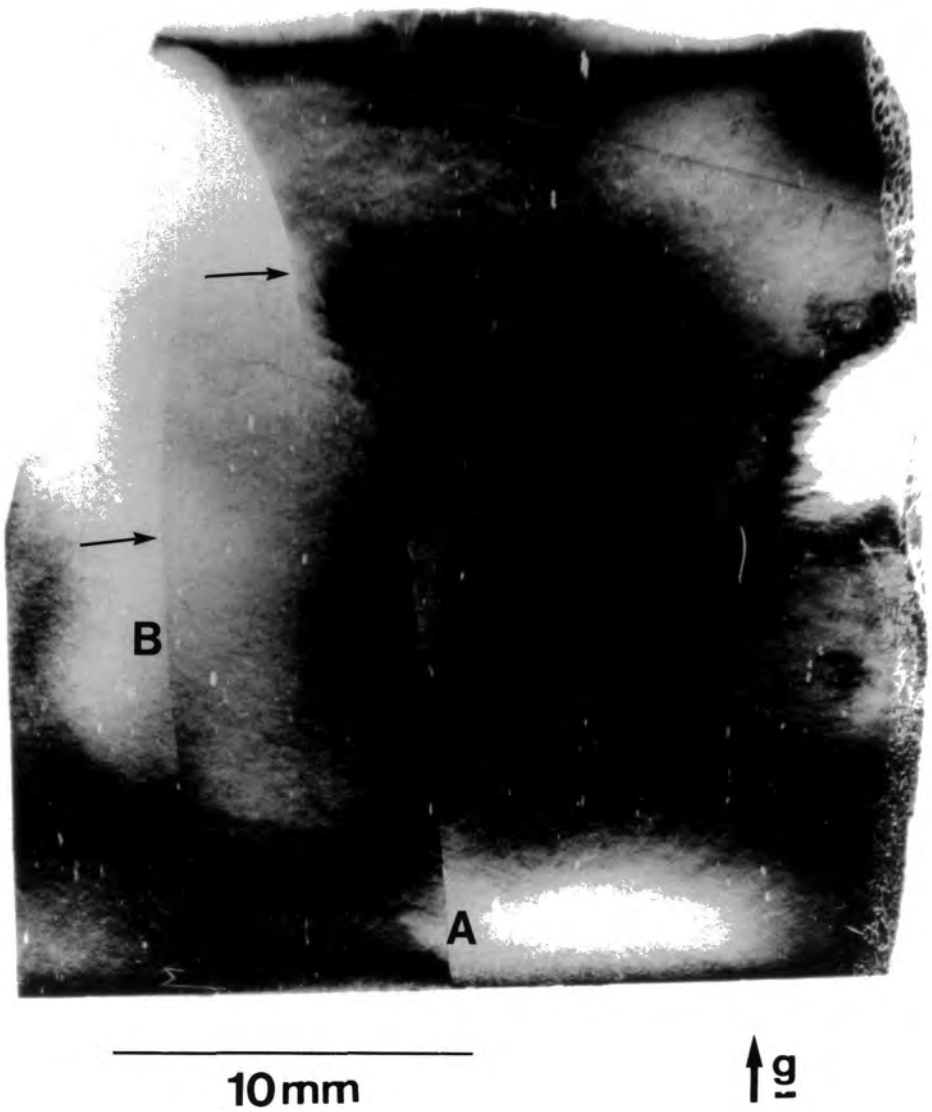

Plate 5.01. This plate shows the $03\bar{3}0$ topograph of the lithium niobate sample.

Plate 5.02. This plate shows the $11\bar{2}\,12$ topograph of the lithium niobate sample.

where n is a unit vector parallel to the growth direction. The contrast observed in both topographs is non uniform consisting of areas of light and dark contrast associated with a highly strained granular structure. Those areas with lattice distortions greater than the rocking curve width are not imaged since diffraction will not occur. In the $03\bar{3}0$ topograph there are grain boundaries running from the top of the topograph to the bottom, of angular rotation less than 12 arc seconds, given by the FWHM of the rocking curve. These boundaries are considerably lower in angle than those reported previously by Sugii et al (1973) illustrating the greater sensitivity of this technique to small long range strain. Further contrast observed on the $03\bar{3}0$ topograph includes a line running across the top right hand corner, this is believed to be a scratch on the emulsion as the contrast is uniform on both sides and the mottled contrast observed on the left of the plate is believed to be due to surface damage. The general non uniform dislocation density indicates a structurally poor crystal with particularly high densities in the centre and at the edges of the crystal. The sharp transition from areas on either side of the grain boundaries in the area A is contrasted with the more gradual transition in area B.

The $11\bar{2}12$ topograph has a significantly different appearance than the $03\bar{3}0$, this is principally due to the weaker nature of this reflection. Noticeable differences in the topographs include the sharper contour lines associated with the narrower rocking curve at grain boundaries and the more pronounced Bragg contour resulting from geometrical distortion in the crystal. In contrast to the $03\bar{3}0$ significantly less area of the sample is imaged, associated with grains being misorientated by more than the rocking curve width. This can be clearly seen in the top area of the topograph where the Bragg contours stop at a grain boundary. No periodic variations in contrast are observed associated with lattice parameter fluctuations normal to the growth front. This indicates that growth bands if present have lattice parameter changes smaller than $\frac{\Delta d}{d} \leq 1 \times 10^{-6}$ since typical rocking curve halfwidth were of the order of 20 arc seconds.

5.2 Diffractometry and interfacial layers

5.2.1 Introduction

The presence of non-abrupt interfacial layers in hetero-epitaxial device struc-

tures can have a considerable influence on the properties of the devices, (Jusserand; 1985). This is particularly so in the case of multi -quantum-well and superlattice structures where, because of the small dimensions of the layers, even narrow interfacial regions only a few monolayers thick may represent a significant fraction of the well thickness. In attempting to characterize rocking curves accurately, as stated previously, the importance of theoretical simulation based on the use of differential equations calculating the scattered intensity from a model can not be over stated. Although no detailed discussion of the simulation program is given, the reader is referred to the work of Takagi (1962; 1969) and Taupin (1964) which has been reviewed in Pinsker (1978). The development of the program used here was originally carried out by Hill (1985) with recent modifications by Miles (1989). Examples of early work using the simulation program can be seen in Halliwell et al (1984) and Hill et al (1985). In essence, the program calculates the values of the amplitude ratio of the diffracted and transmitted beams in the substrate using the equations of dynamical theory. These values are then used as the input values into the Takagi-Taupin equations which calculate the amplitude ratio as the beam passes through the crystal. The crystal is divided into lamina of constant composition and the reflectivity of each laminae is calculated. The complex amplitude ratios at each interface are then matched and the reflectivity is calculated at the exit surface.

To illustrate the application of double crystal diffractometry and the simulation program a single thin layer of GaInAsP on InP was studied using the 044 highly asymmetric reflection. This sample was grown by MOVPE, a technique thought to give rise to thin highly mismatched interfacial regions, which have a detrimental effect on device performance (Lyons, 1989). The results of this study have been recently published (Cockerton et al, 1990).

For layers greater than about half a micron the effective mismatch can be determined as described previously. However it has been recently shown by Fewster and Curling (1987) both by experiment and simulation that the position of the Bragg peak maximum shifts as the epitaxial layer thickness is reduced. It then becomes necessary to match the experimental rocking curves with simulated curves to determine the effective mismatch.

As an epitaxial layer becomes thinner, the width of the layer peak increases and the peak height decreases, making the determination of the mismatch difficult and even impossible for near lattice-matched layers. Use of highly asymmetric reflections reduces the depth from which data is taken due to an increased path length and reduced extinction distance. This reduction in the extinction distance results in an increased scattering from the layer and a narrow peak half width. As a result, the study of surface layers down to a few tens of nanometers can be made (Bates et al, 1988).

In the present study a (001) sample was studied using both experiment and simulation using the asymmetric 044 reflection. This sample consisted of a single layer of 175nm GaInAsP on InP. The experiments were performed at Durham using a prototype of the Bede 150 double crystal camera. The experimental procedure is described in the previous chapter. Rocking curves were recorded in both glancing incidence and glancing exit geometries and no layer tilt was detected. Upon matching the measured peak height and position with simulation, a satisfactory fit could not be obtained. It became clear that the inclusion of an intermediate layer at the substrate-layer interface in the simulations gave a closer fit to the Bragg peak.

5.2.2 Results

Figure 5.02 illustrates how the parameters of a single layer can be varied to match the peak position and height but it is not until the intermediate layer is included that a close fit to the peak width is obtained. It can be seen that the intermediate layer has a strong effect on the asymmetry of the peak and particularly at the high angle shoulder. As a result of many simulations it was discovered that the thickness of such an intermediate layer, while having an effect on the peak width and high angle shoulder, also had a major effect on the layer peak position. Indeed for a total layer thickness of 200nm, with a mismatch of -500ppm and the intermediate layer varying in thickness from zero to 50nm with a mismatch of -1200ppm, the layer position moves by 45 arcsecs, figure 5.03. For a fixed interface layer of thickness 50nm and a varying range of mismatch this function is an oscillatory function, making the fitting of a unique solution very difficult, figure 5.04. Figure 5.05 illustrates the example of two almost identical rocking

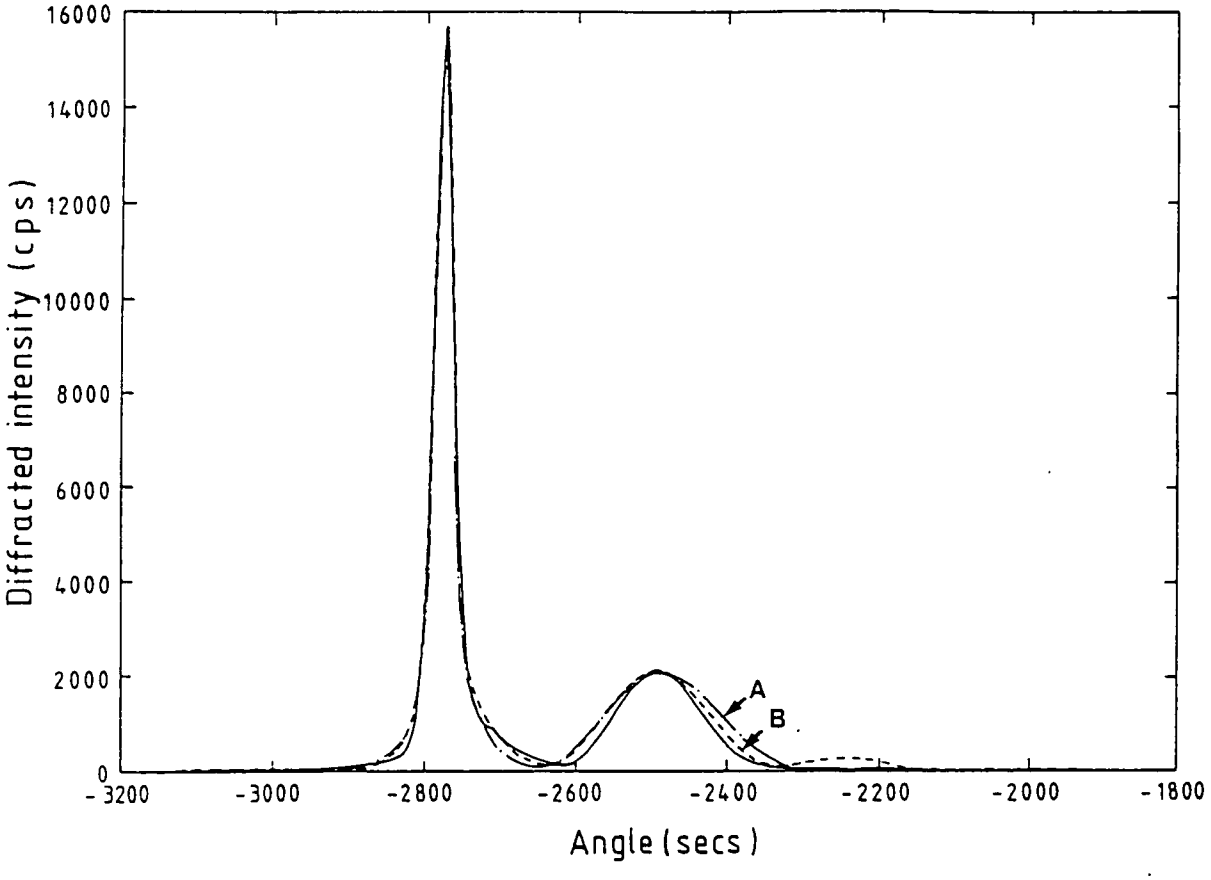

Figure 5.02 Experimental (solid line) and simulated (broken lines) 044 CuKα, (+,-) parallel, rocking curves of what is nominally a single GaInAsP layer on InP. Curve A (dot-dashed) is for a simulation using a single layer 173nm thick and a mismatch of -720ppm. Curve B (dashed) is for a layer 116nm thick, mismatch of -540ppm and 65nm thick interface layer mismatch =-1050ppm.

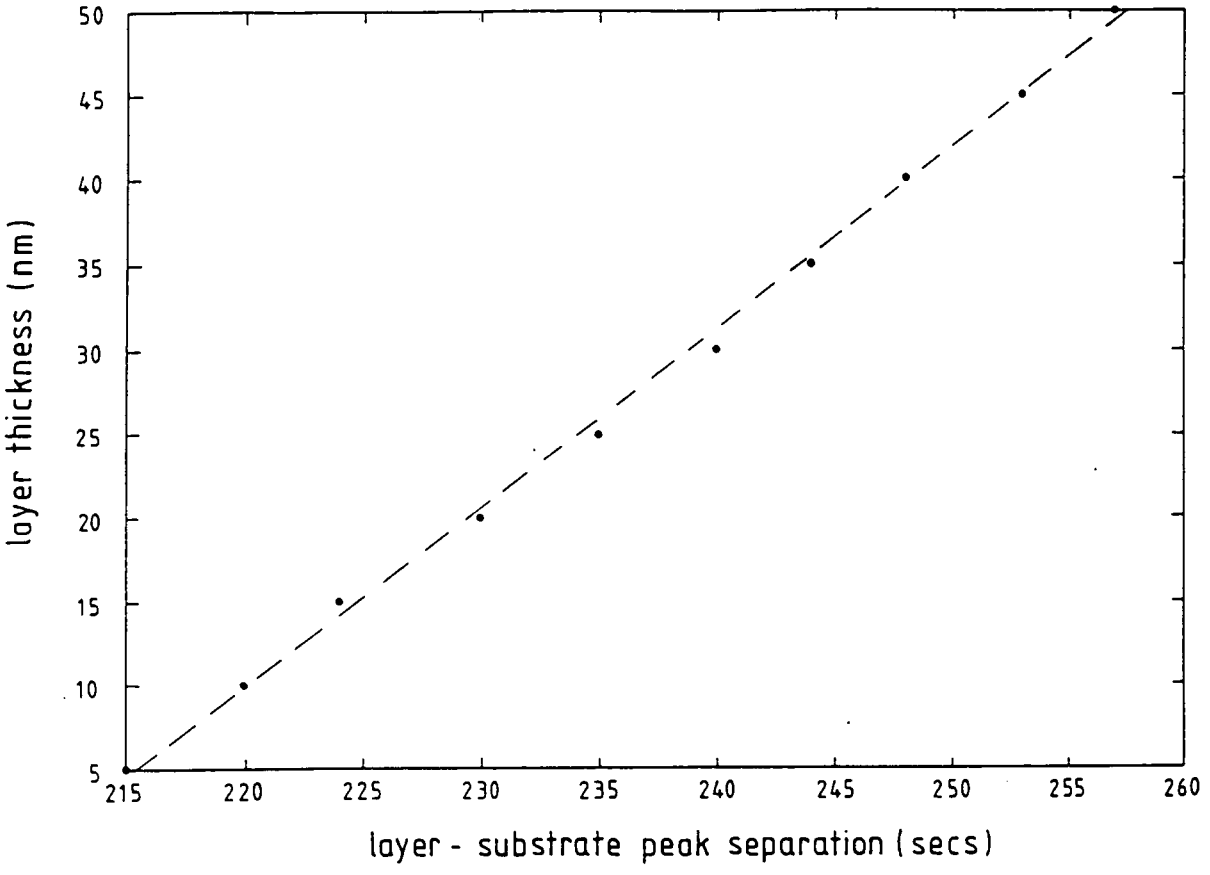

Figure 5.03 illustrates the variation in the main layer peak separation from the substrate as the intermediary layer thickness is changed between 5-50nm. The total epilayer thickness is held constant at 200nm.

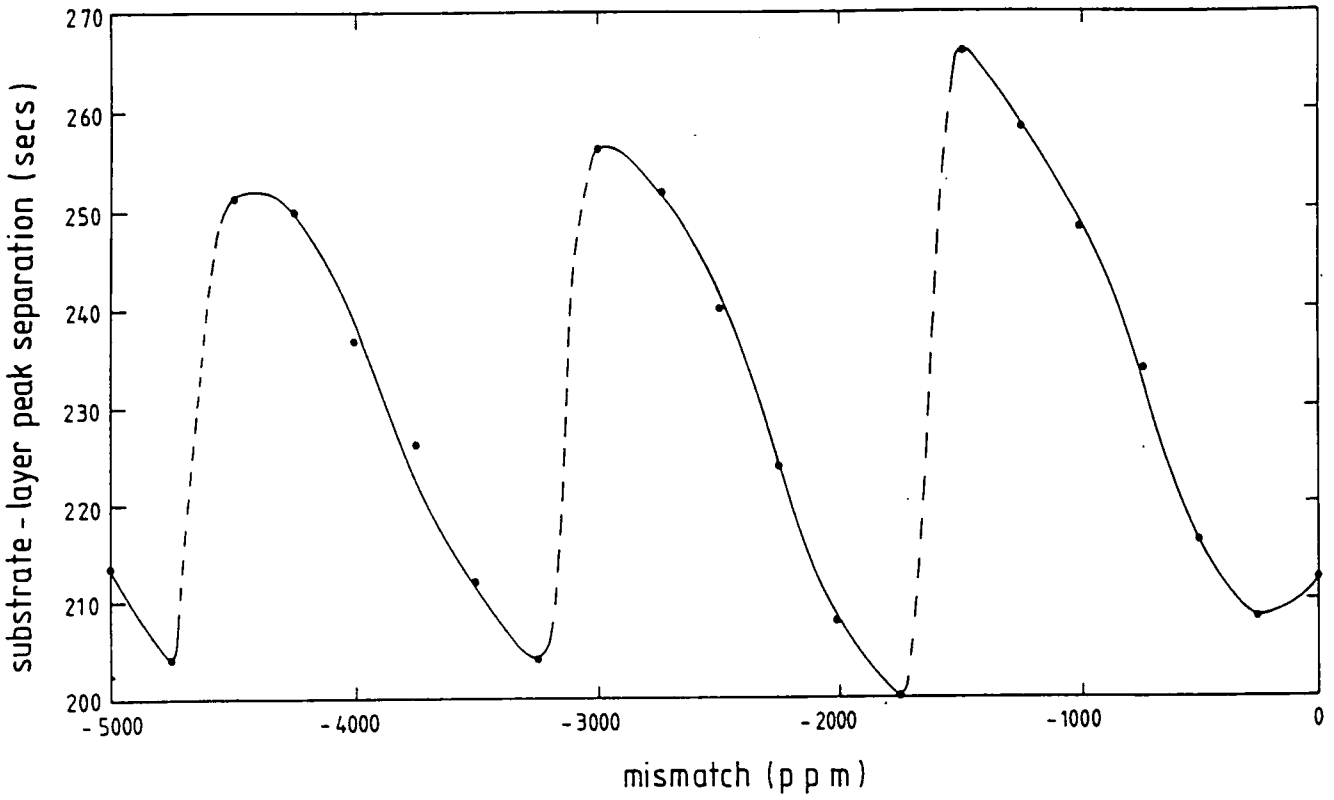

Figure 5.04 shows the variation of the substrate and layer peak separation with a change in the mismatch of an intermediary layer of thickness 50nm. The main layer thickness was 200nm with a mismatch of -550ppm.

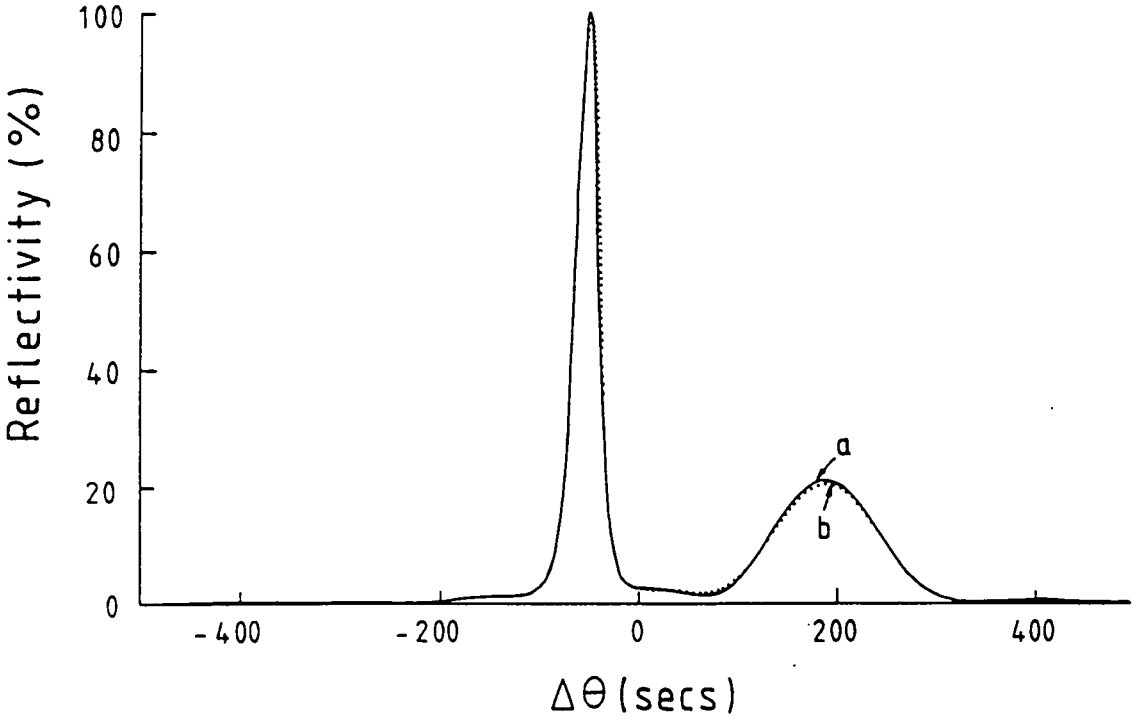

Figure 5.05 illustrates two rocking curves obtained from very different structure; these rocking curves are remarkably similar. These curves are for a total layer of thickness 200nm and mismatch -550ppm with an interfacial layer of thickness 50nm and mismatches of (a) -2500ppm and (b) -4000ppm.

curves calculated with very different intermediate layer mismatches of -2500ppm and -4000ppm. It is clear that these rocking curves are also very similar when plotted on a semilog scale, as is the case in figure 5.06. However the total thickness is the same, the pendellosung fringes clearly visible in the simulations are of differing frequencies due to the intermediate layer providing its own pendellosung frequency which will add and subtract to that of the layer. It is therefore necessary to take high quality data with a signal to noise ratio better than 1×10^4 inorder to distinguish the two cases.

5.2.3 Conclusion

These studies have demonstrated the usefulness of both double crystal topography and diffractometry for the characterisation of structural uniformity in substrate and epitaxially grown material. Topography using synchrotron radiation has been shown to be an extremely powerful tool enabling a large area of crystal to be imaged in one exposure, while diffractometry has been shown capable of studying interface layers . . The dislocation density of the lithium niobate crystal showed large variations across the slice there being a number of grain and subgrain boundaries and large areas of imperfection. The use of the $11\bar{2}12$ reflection has shown that growth bands are not observed normal to the growth front at the detection limit of this reflection.

In matching the experimental and simulated rocking curves from the GaInAsP structure it was shown that scattering far from the Bragg peak is extremely important in distinguishing between rival structures. In order that this can be achieved, lengthy data collection times are required and care must be taken in shielding the detector from scattered radiation, a low background detector is also vital. This work is of significance since the presence of non-abrupt interfaces in hetero-epitaxial layers is becoming increasingly important, particularly in devices only a few monolayers in thickness.

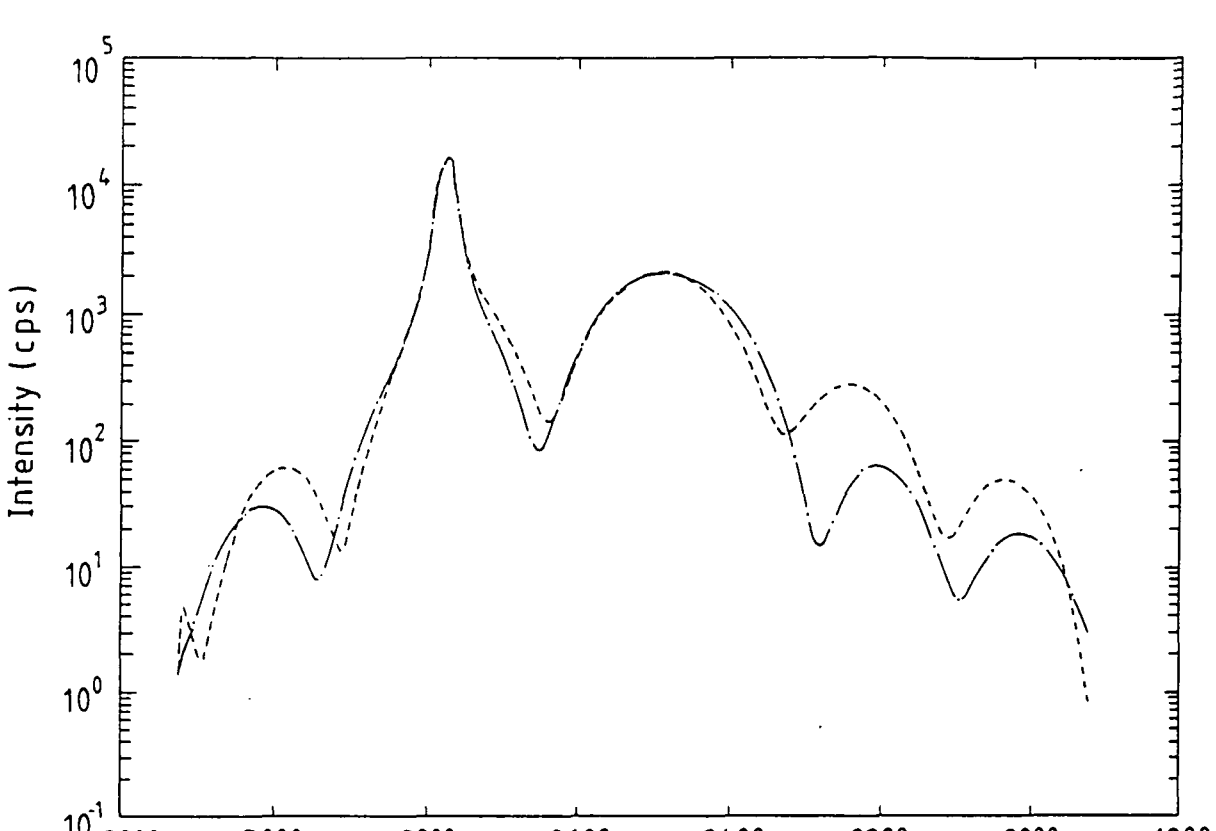

Figure 5.06. This figure shows two similar rocking curves of the previous figure on a semilog scale.

Chapter VI

Interference fringes produced from thin buried layers

6.1 Introduction

There are considerable difficulties in characterising thin (less than 0.01 μm) epitaxially grown layers using conventional double crystal techniques. This is because the peak associated with a thin layer becomes broad and low in intensity and may, in the case of small mismatches, become indistinguishable from the tails of the substrate peak (Estrop et al, 1976; Bartels, 1983; Fewster, 1986; Fewster and Curling, 1987; Tanner and Hill, 1986). To illustrate the effect of reducing layer thickness, figure 6.01 shows the simulated rocking curves obtained for the symmetric 004 and asymmetric 044 reflections from a single layer of AlGaAs with a range of thicknesses. It can be seen that by using the 044 reflection the intensity scattered by the layer is increased. This is due to an increased path length through the layer relative to the substrate (Bruhl et al, 1988; Hartwig, 1978; Lucas et al, 1988; Tanner and Hill, 1986). Glancing incidence or glancing exit diffraction geometries may be used, however care should be taken when selecting either geometry as they may differ in their sensitivity (Capano, 1989; Ryan, 1989). Refinement of the asymmetric geometry is made by shallow angle rocking curve analysis (SARCA), this has been shown capable of inspecting surface layers down to 100 $\AA$ (Miles et al, 1989).

At present the measurement of thin buried layers can not be made directly from a peak associated with the layer, but must be measured by modelling interference effects on the rocking curve (Fewster and Curling, 1987; Jeong et al, 1988; Tanner and Halliwell, 1988). Interference effects such as pendellosung fringes are produced in thin layers due to interference between the two excited wave fields on the same branch of the dispersion surface. In relatively thick crystals these fringes are not seen as the more strongly attenuated wave field, following reflection, is greatly deminished. Pendellosung fringes may be observed in the tails of the rocking curve

Figure 6.01a. Simulated 044 rocking curves from a layer $1.0\mu m$(solid line)$0.5\mu m$(dashed) and $0.1\mu m$(dotted).

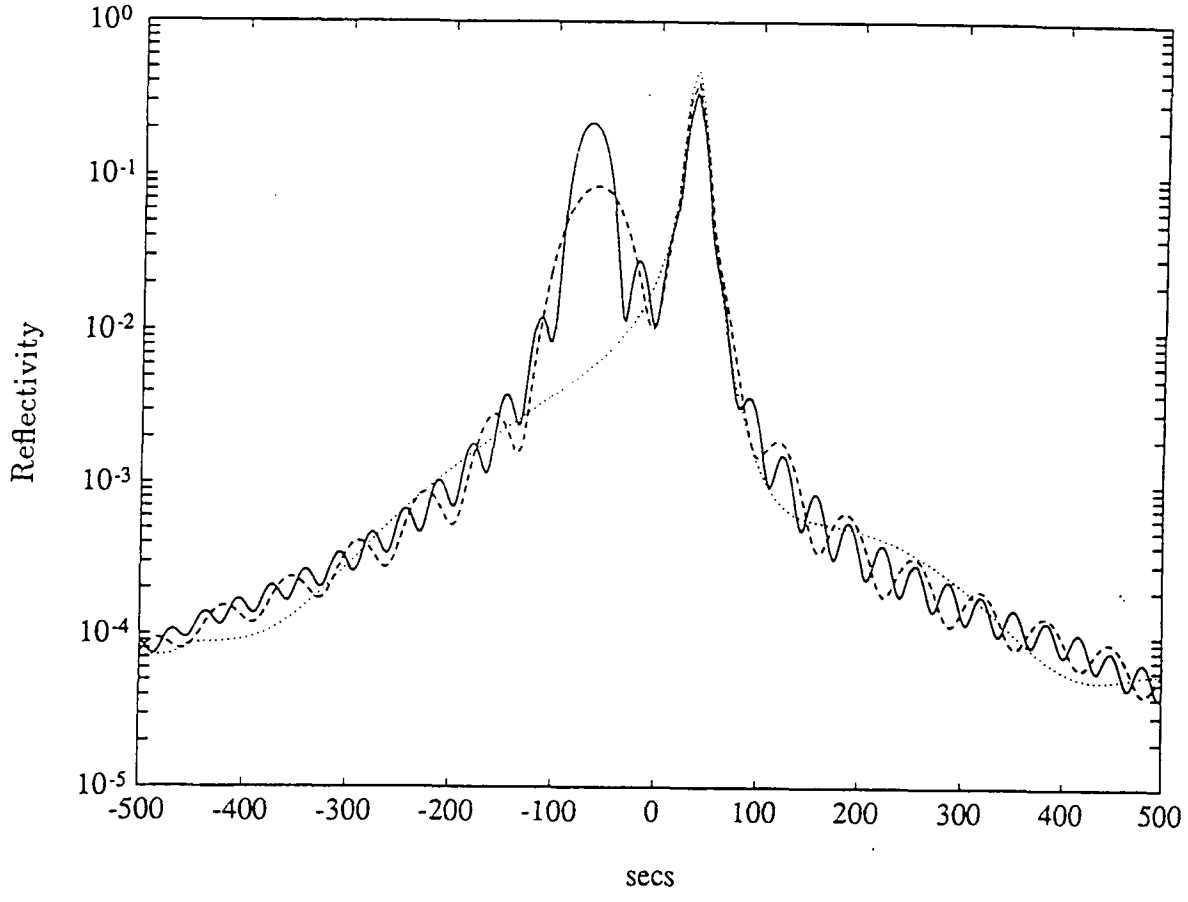

Figure 6.01b Simulated 004 rocking curves from a layer $1.0\mu m$(solid line)$0.5\mu m$(dashed) and $0.1\mu m$(dotted).

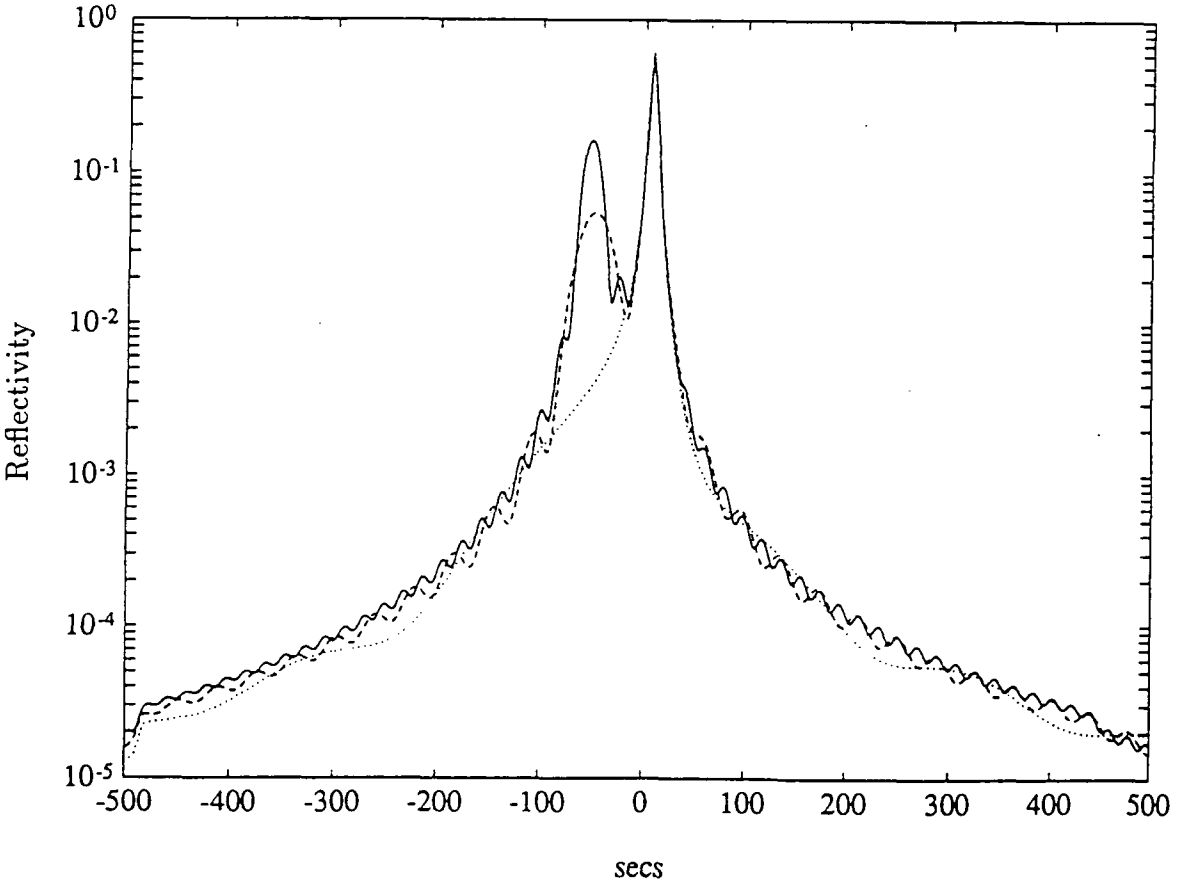

and have intensities oscillating between 0.01% and 1.0% of that of the Bragg peak. The frequency of these oscillations is associated with the thickness of the layer by,

$$\delta\theta = \frac{\lambda sin(\theta_b + \phi)}{t sin 2\theta_b} \tag{6.01}$$

where $\delta\theta$ is the angular spacing of the fringes, t is the layer thickness and ϕ is the angle between the surface normal and the diffracting planes.

In structures consisting of more than one layer the rocking curve shows the superposition of multiple frequencies, one for each layer. Problems caused by sample curvature together with grading in the layer and often insufficient counting times produce a limit to the number of layers that can be resolved experimentally (Jeong et al, 1988; Bensoussan et al, 1987; Macrander et al, 1988).

At present there is particular interest in characterising injection laser structures. These consist of a thin active layer, B, sandwiched between two confining layers, A, of identical composition. In this structure it has been shown that interference effects produced on the Bragg peak associated with the confining layer are extremely sensitive to variations in the active layer thickness and composition. In 1987 Chu and Tanner, using a combination of experiments matched with simulation, showed that in a typical laser structure variations in the active layer thickness could be detected to 200 $\mathring{A}$. Later work by Wie (1989) showed that, in a multiple quantum well structure, the active layer thickness could be monitored to within a few atomic layers.

6.2 Bragg case Moire fringes

X-ray Moire fringes have been observed in a number of situations using transmission X-ray topography and TEM studies. However these fringes have not yet been reported using reflection or Bragg case X-ray topography. Moire fringes have been reported in transmission X-ray topographs and are produced where wave fields diffracted from two crystals of slightly differing lattice parameter or orientation overlap. Chikawa (1965) observed Moire fringes in X-ray transmission topographs from a cadmium sulphide crystal grown epitaxially on another, these fringes allowed the observation of edge dislocations to be made. Moire fringes have

also been observed from cracks where the lattice planes on either side of the crack are slightly misorientated (Lang and Muiskov, 1965), and in crystals consisting of two coherent layers separated by a damaged layer (Lang and Muiskov, 1965). The most common example of transmission case Moire fringes is in the three crystal monolithic interferometer originally designed by Bonse and Hart in the 1960s (Bonse and Hart, 1965; Hart, 1972, 1975). This instrument allows interfering wave fields produced by diffraction from two separated blades to intersect on a third analysing blade. Since the periodicity of the analysing blade is identical to the period of the interfering beams, small displacements in the analysing crystal produce large changes in transmitted intensity. If the analysing blade is slightly misaligned with respect to the two fixed blades, this results in Moire fringes. Figure 6.02 illustrates the three blades together with the diffracted beams while figure 6.03 attempts to illustrate the formation of Moire fringes using two ruled gratings. In the latter figure it can be seen that when the two grids are slightly rotated with respect to one another, horizontal Moire fringes are produced while a slight difference in interplanar spacing in one grid with respect to the other produces vertical fringes. Hence a combination of rotation and dilation results in a Moire fringe at an angle determined by the ratio of the two contributions.

6.3 The formation of Moire fringes in laser structures

6.3.1 Introduction

In 1987 Chu and Tanner observed interference fringes, thought to be Bragg case Moire, from an AlGaAs laser structure. The experiments were carried out using a standard sealed tube X-ray source. The purpose of the present study is to investigate these fringes using synchrotron radiation enabling more of the sample to be imaged and a variety of wavelengths to be used. Attempts are also reported at observing these fringes from an InGaAs laser structure.

The production of fringes is due to interference between two diffracted beams, one from each of the confining layers. In these structures the confining layers are of near identical composition, this implies that diffraction from each layer should occur at exactly the same Bragg angle. Diffraction from both confining layers

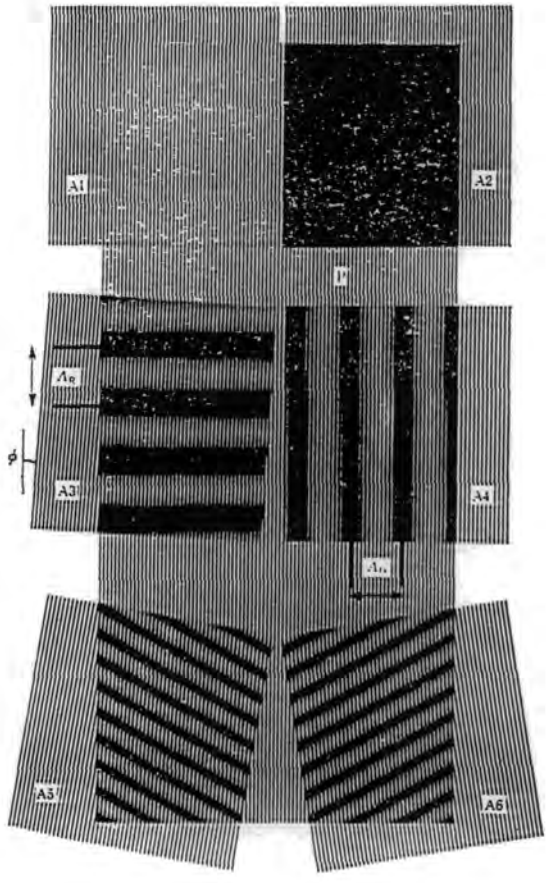

Figure 6.03. This figure shows a schematic of the formation of Moire fringes from two ruled gratings. When both gratings are aligned, A1, bright contrast is observed. If one grating is displaced by the width of one line then dark contrast is observed, A2. Rotation of one relative to the other, A3, produces horizontal fringes, while a difference in the size of the gratings produces a vertical Moire, A4. A combination of both a rotational and dilational effect produces fringes at an angle dependant on the individual contributions, after Hart (1968).

requires that the variation in composition of these layers is small enough so that the peak from each individual layer cannot be resolved.

6.3.2 Theory

To model the formation of Moire fringes consider figure 6.04 in which the diffracting planes are horizontal and let the wave field diffracted from layer 1 and layer 2 be described by

$$\underline{E}_1(r) = \underline{E}_{01} exp[2\pi i(\underline{k}_0 + \underline{g}_1).\underline{r} + \phi_1] \tag{6.02}$$

and

$$\underline{E}_2(r) = \underline{E}_{02} exp[2\pi i(\underline{k}_0 + \underline{g}_2).\underline{r} + \phi_2] \tag{6.03}$$

the magnitude of the combining wave vectors is given by

$$\underline{E} = \underline{E}_1 + \underline{E}_2 \tag{6.04}$$

$$\underline{E} = \underline{E}_{01} exp[2\pi i(\underline{k}_0 + \underline{g}_1).\underline{r} + \phi_1] + \underline{E}_{02} exp[2\pi i(\underline{k}_0 + \underline{g}_2).\underline{r} + \phi_2] \tag{6.05}$$

which can be written using,

$$e^{i\theta} = cos\theta + isin\theta \tag{6.06}$$

and

$$I = \underline{E}.\underline{E}^* \tag{6.07}$$

the intensity is given by

$$I = |\underline{E}_1|^2 + |\underline{E}_2|^2 + 2|\underline{E}_{01}||\underline{E}_{02}[cos2\pi(\Delta\underline{g}.\underline{r} + \Delta\phi)] \tag{6.08}$$

where

$$\Delta\underline{g} = \underline{g}_1 - \underline{g}_2 \tag{6.09}$$

$$\Delta\phi = \phi_1 - \phi_2 \tag{6.10}$$

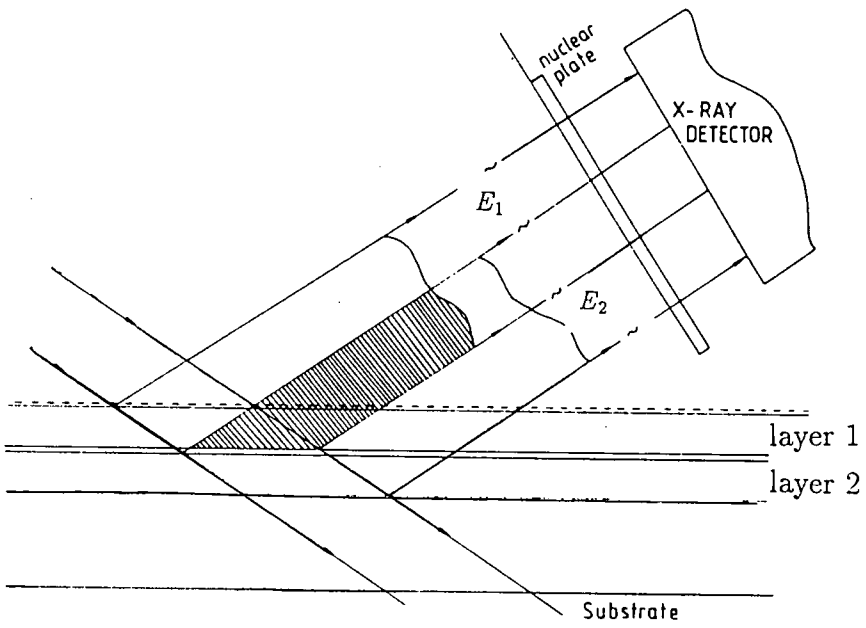

Figure 6.04. Schematic diagram of the formation of Moire fringes from the interference of two diffracted beams, one from each of the confining layers of an ABA type laser structure.

From the above expression it can be seen that the intensity of the combined wave is modulated by a cosine term. The period of the spacing is given by the values of $\Delta\underline{g}$ and $\Delta\underline{r}$ by,

$$cos(2\pi\Delta\underline{g}.\underline{r}) = cos(2\pi) \tag{6.11}$$

that is,

$$\Delta\underline{g}.\underline{r} = 1 \tag{6.12}$$

which is equal to,

$$|\Delta\underline{g}|rcos\alpha = 1 \tag{6.13}$$

where the angle α is the angle between $\Delta\underline{g}$ and the vector $\underline{r}$. When α is equal to 90 degrees this corresponds to the perpendicular fringe spacing and may be represented by,

$$\Lambda = \frac{1}{|\Delta\underline{g}|} \tag{6.14}$$

The two cases in which $\Delta\underline{g}$ is in a direction along the diffraction vector, ie a dilation, and $\Delta\underline{g}$ is perpendicular to the diffraction vector, a tilt, can be described by considering figure 6.05.

Since

$$d = \frac{1}{\underline{g}} \tag{6.15}$$

then in the case of a dilation

$$\Delta g_D = \frac{-\Delta d}{d^2} \tag{6.16}$$

then spacing is given by

$$\Lambda = -\frac{d^2}{\Delta d} \tag{6.17}$$

This corresponds to fringes which are perpendicular to the Bragg plane normal and the incident plane. In a similar manner one can consider the case in which one layer is slightly rotated with respect to the other by an angle $\Delta\theta$. In this case

$$\Delta g = g\Delta\theta \tag{6.18}$$

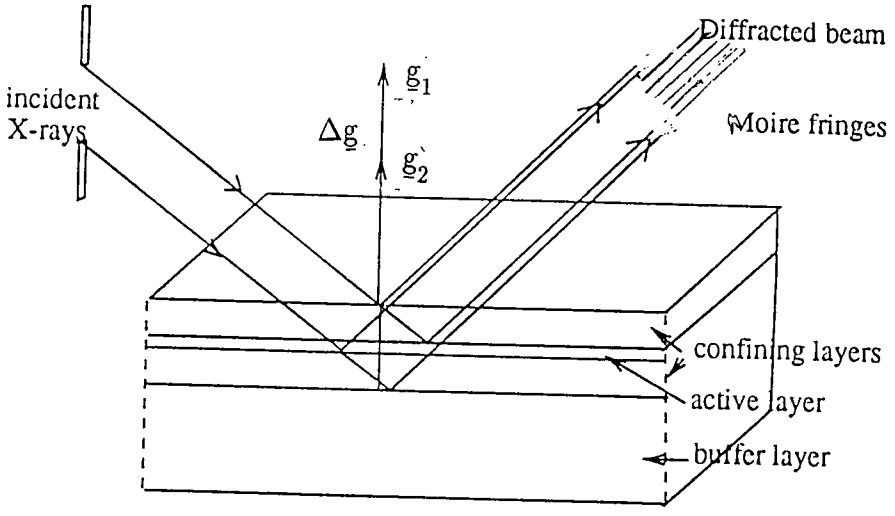

Figure 6.05a. Schematic diagram of the formation of Moire fringes due to a dilation of one confining layer relative to another. This corresponds to a slight variation in the composition of one of the layers.

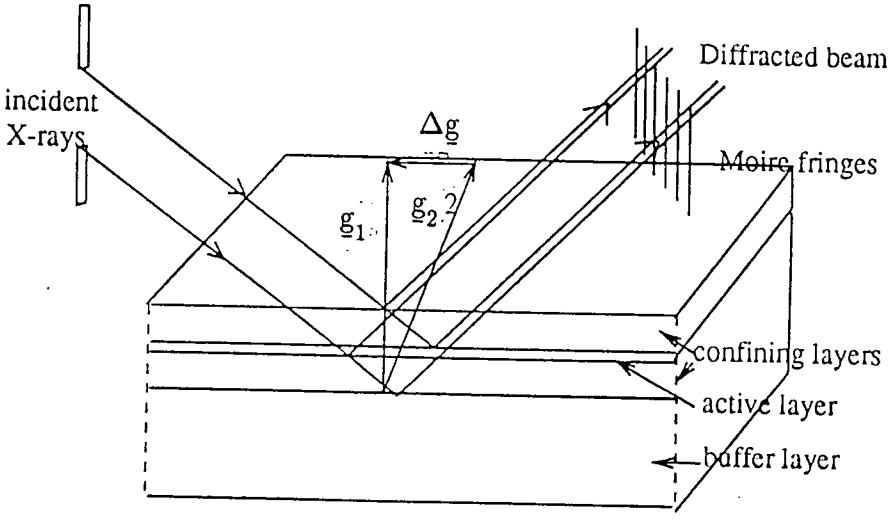

Figure 6.05b. Schematic diagram of the formation of Moire fringes due to a rotation of one of the layers relative to another.

then the spacing is,

$$\Lambda = \frac{d}{\Delta\theta} \tag{6.19}$$

which corresponds to fringes which are parallel to the Bragg plane normal. The Moire fringes spacing is sensitive to the order of the reflection but not the wavelength of the radiation used and the spacing is also sensitive to different Bragg reflections since each reflection is sensitive to different components of the rotation and tilt components. From the equations above it may also be seen that a Moire fringe spacing of $100\mu m$ will be produced by a difference in the lattice parameter of 1ppm or a rotation of 2 arc seconds. These values are small enough not to be detected in the double crystal rocking curve.

If the active layer has a uniform variation in thickness or mismatch then it is also possible that thickness or pendellosung fringes could be produced. In this case the mechanism of fringe formation is shown in figure 6.06.

In this figure it can be seen that at one fringe position

$$2Dsin\theta_B = \lambda n \tag{6.20}$$

and at the next fringe

$$2D'sin\theta_B = \lambda(n+1) \tag{6.21}$$

where D is the thickness at one fringe maximum and D' is the thickness at the next. This corresponds to a phase difference of 2π across the active layer. Combining these two equations and taking a thickness variation produced by a wedge of angle ϕ gives

$$2sin\theta_B(D' - D) = \lambda \tag{6.22}$$

and

$$sin\phi = \frac{(D' - D)}{R} \tag{6.23}$$

where R is the fringe spacing. Thus,

$$R = \frac{\lambda}{2sin\theta_B sin\phi} \tag{6.24}$$

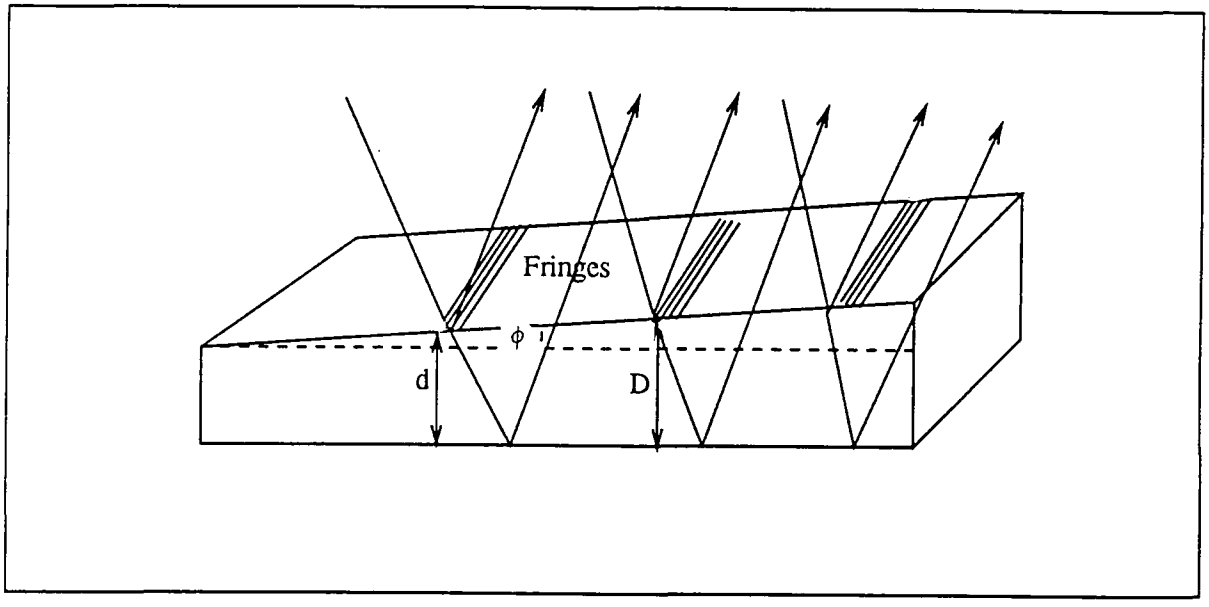

Figure 6.06. Schematic diagram of the formation of fringes due to a constant variation in the active layer thickness or composition. Fringes occur when the difference in the phase of the combining waves is an integral multiple of wavelengths.

Clearly these fringes are fixed in position defined by the angle of the wedge. The formation of fringes of this type is sensitive to thickness or mismatch variations at the monolayer level, since a fringe is produced at each integral number of wavelengths.

6.4 Experimental results

Two samples were studied consisting of an AlGaAs structure illustrated in figure 6.07 and an InGaAs structure shown in figure 6.08. The AlGaAs structure consists of an active layer and two confining layers of identical composition and thickness, whereas the InGaAs structure consists of an active layer and two confining layers of different thicknesses but of identical composition. It can also be seen that the AlGaAs structure has two more layers than the InGaAs structure (a buffer layer and a capping layer) but these layers are not thought to affect the confining layer peak. The values of the layer thicknesses and mismatches shown in the two previous figures are those deduced from experimental comparison to simulations. Figure 6.09 shows the symmetric 004 rocking curve taken from the AlGaAs structure together with the best fit simulation. There are three peaks, the high angle peak being the substrate peak. The remaining two peaks are from the buffer layer and the confining layers. Figure 6.10 shows the experimental and simulated rocking curves for the InGaAs structure using the 004. Unlike the AlGaAs structure the active layer thickness is sufficient to give a small peak, which is located at the low angle side of the rocking curve.

The interference effects produced as a result of a dilation or a tilt between the confining layers should produce fringes present only on the confining layer peak. This condition is significant as it allows the elimination of defects or surface effects since contrast produced from defects or the surface of the sample should be present on all three peaks.

Double crystal X-ray topography of structures with a combined thickness of several microns often reveals the bending of the substrate in either a convex or concave manner. Materials such as AlGaAs, having a larger lattice parameter than GaAs, produce a convex bending while InGaAs may produce bending in either sense. This effect is of little significance to the device but does affect the ability to image large areas of the sample. Hence in the topographs to follow often

	GaAs	cap	0.17μm
526ppm	GaAlAs	confining layer	1.28μm
137ppm		active layer	0.19μm
526ppm	GaAlAs	confining layer	1.28μm
233ppm	GaAlAs	Buffer layer	3.5μm
	GaAs (001)	Substrate	

Figure 6.07. The AlGaAs structure. The layer thicknesses and mismatches are those determined from the best fit simulated data to the experimental rocking curves.

-1100ppm	InGaAs	confining layer	0.78μm
600ppm	InGaAs	active layer	0.245μm
-1100ppm	InGaAs	confining layer	0.213μm
	InP (001)	Substrate	

Figure 6.08. The InGaAs structure. The layer thicknesses and mismatches as determined from best fit simulation to the experimental rocking curves.

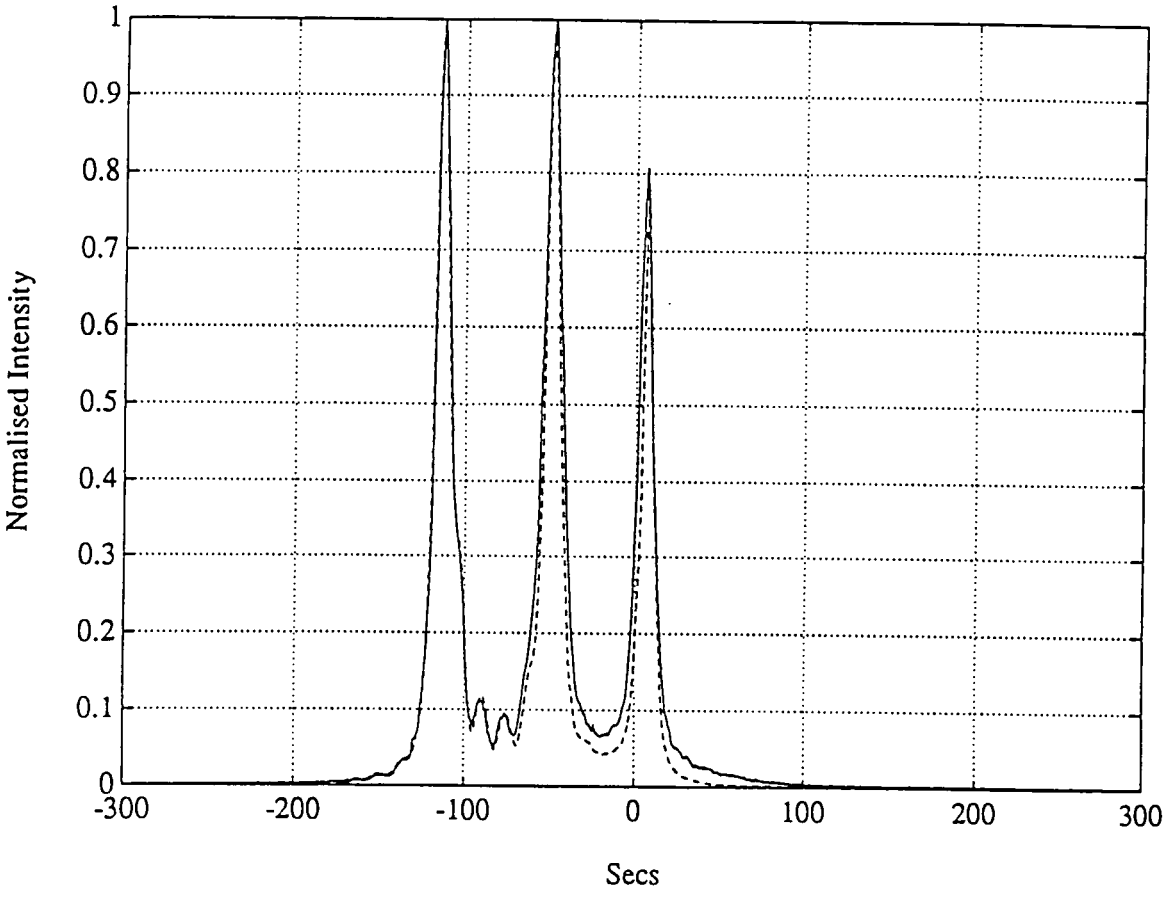

Figure 6.09. The experimental 004 (solid line) rocking curve together with the best fit simulation(dashed line). These parameters correspond to those given in figure 6.07.

Figure 6.10. The experimental 004 reflection from the InGaAs structure, together with the best fit simulation using the parameters given in figure 6.08.

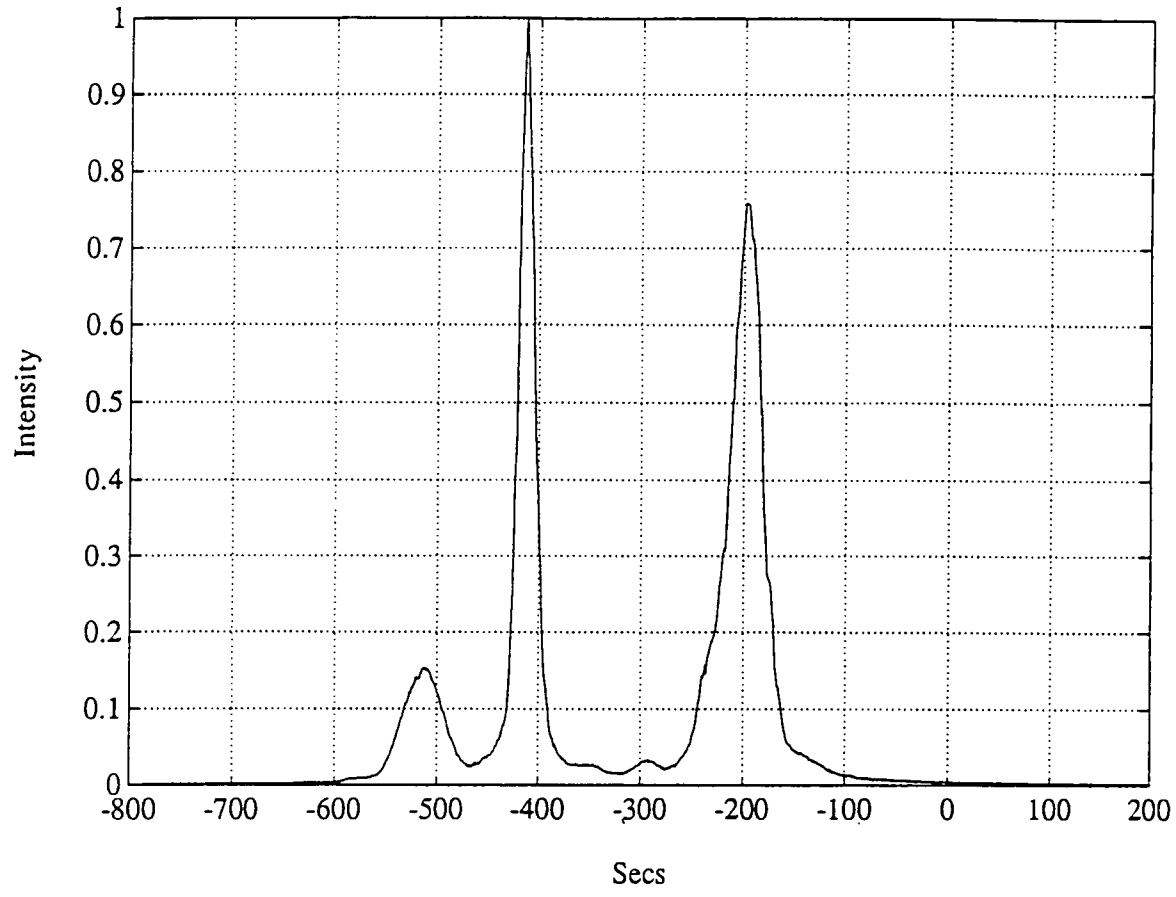

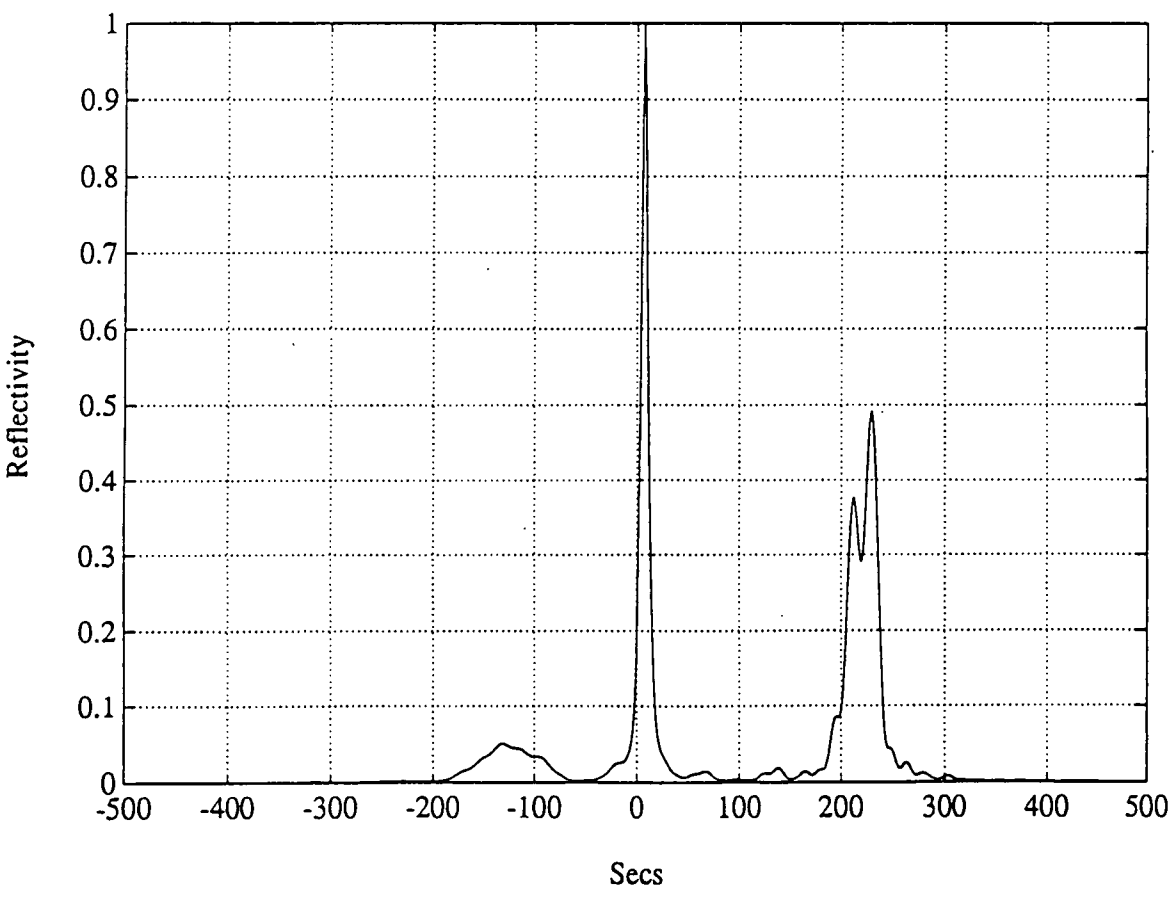

more than one Bragg peak can be observed; each peak then represents a contour of constant curvature. If the sample is flat, then the whole sample is imaged by diffraction from only one peak.

Plate 6.01 shows the 004 topograph obtained from the AlGaAs sample using radiation of 1.5$\mathring{A}$ while at the Bragg angle for the maximum of the confining layer peak. This topograph has imaged the whole of the sample with the edges of the topograph being the edges of the sample. A variety of contrast features are present, including a region of damage located at the bottom end of the sample. This is a region of the sample that had cracked and is slightly misorientated from the rest of the sample. Most noticeable are the two dark bands running vertically, these bands correspond to the Bragg contours of the confining layer and buffer layer peaks, labelled cl and bl. The presence of these two bands indicates that the sample is curved allowing different Bragg angles to be satisfied over the sample surface. It can also be seen that there are subsidiary vertical bands corresponding to the subsidiary peaks clearly visible between the confining and buffer layer peaks, in figure 6.09. Plate 6.02 is an enlarged region around the confining layer peak. It can be seen that there are periodic variations in the contrast running along the Bragg peak associated with the confining layer, as well as the subsidiary peaks. These periodic variations in contrast were only present on the confining layer peak and not on either the buffer layer or substrate peaks. This observation is significant since it implies the observed contrast is not from surface damage.

Plate 6.03 shows the 004 topograph obtained at 1.5 $\mathring{A}$ from the InGaAs sample while at the confining layer peak maximum position. This plate again shows the whole sample with a variety of contrast features. The curved line running around the top section of the sample corresponds to the edges of the grown layers. Bands of constant curvature are again clearly visible however it is not clear which bands correspond to which diffraction peaks, apart from the darkest band which is the confining layer peak. Following enlargement and repeated exposures no fringes could be observed.

To determine the origin of the fringes produced from the AlGaAs sample, the following series of experiments were performed.

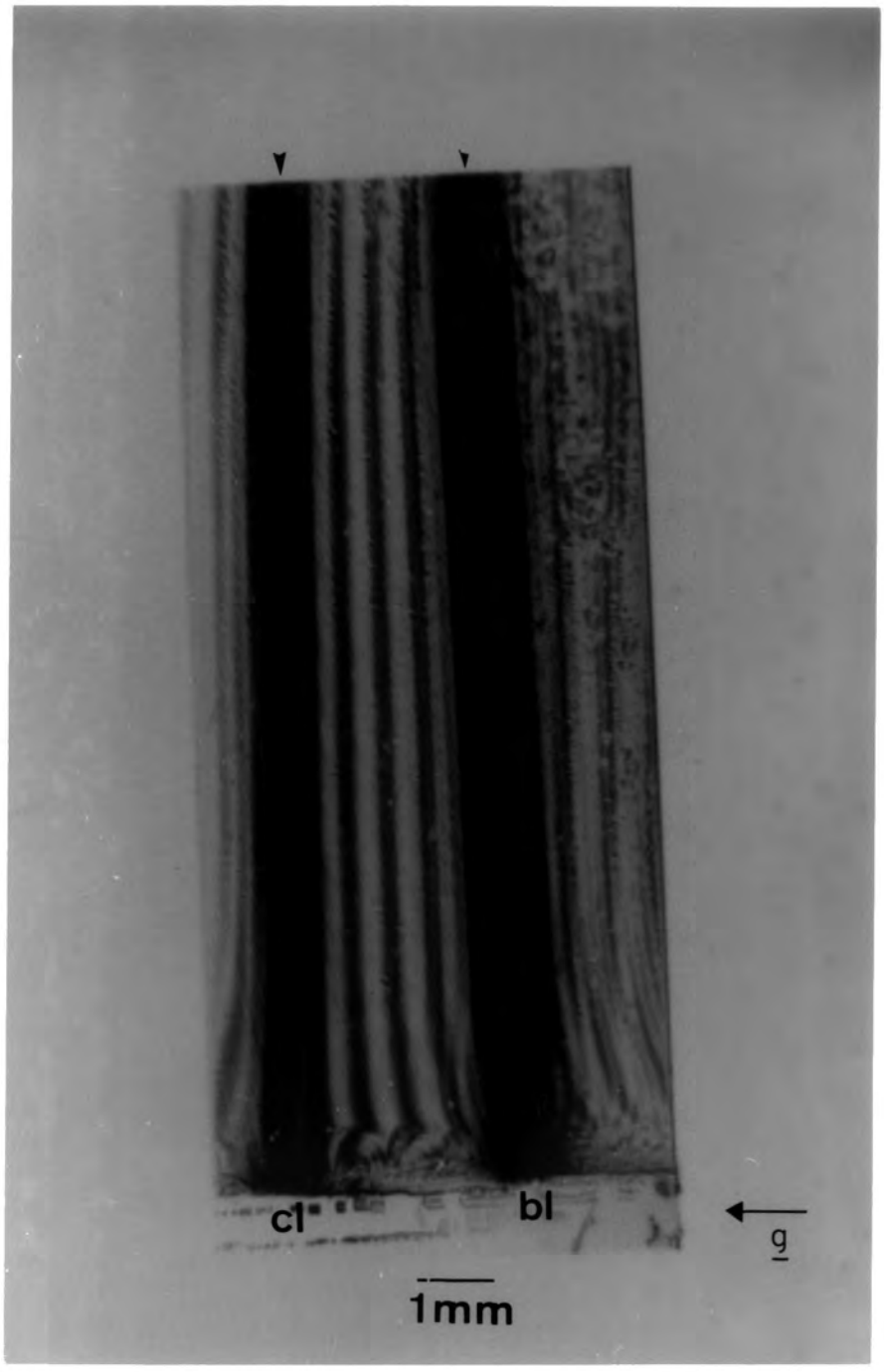

Plate 6.01. An 004 topograph at 1.5 $\mathring{A}$ from the AlGaAs sample. Note the two main dark bands are those from the confining layers (cl) and the buffer layer (bl), due to curvature of the sample. The subsidiary peaks between these two bands are pendellosung fringes.

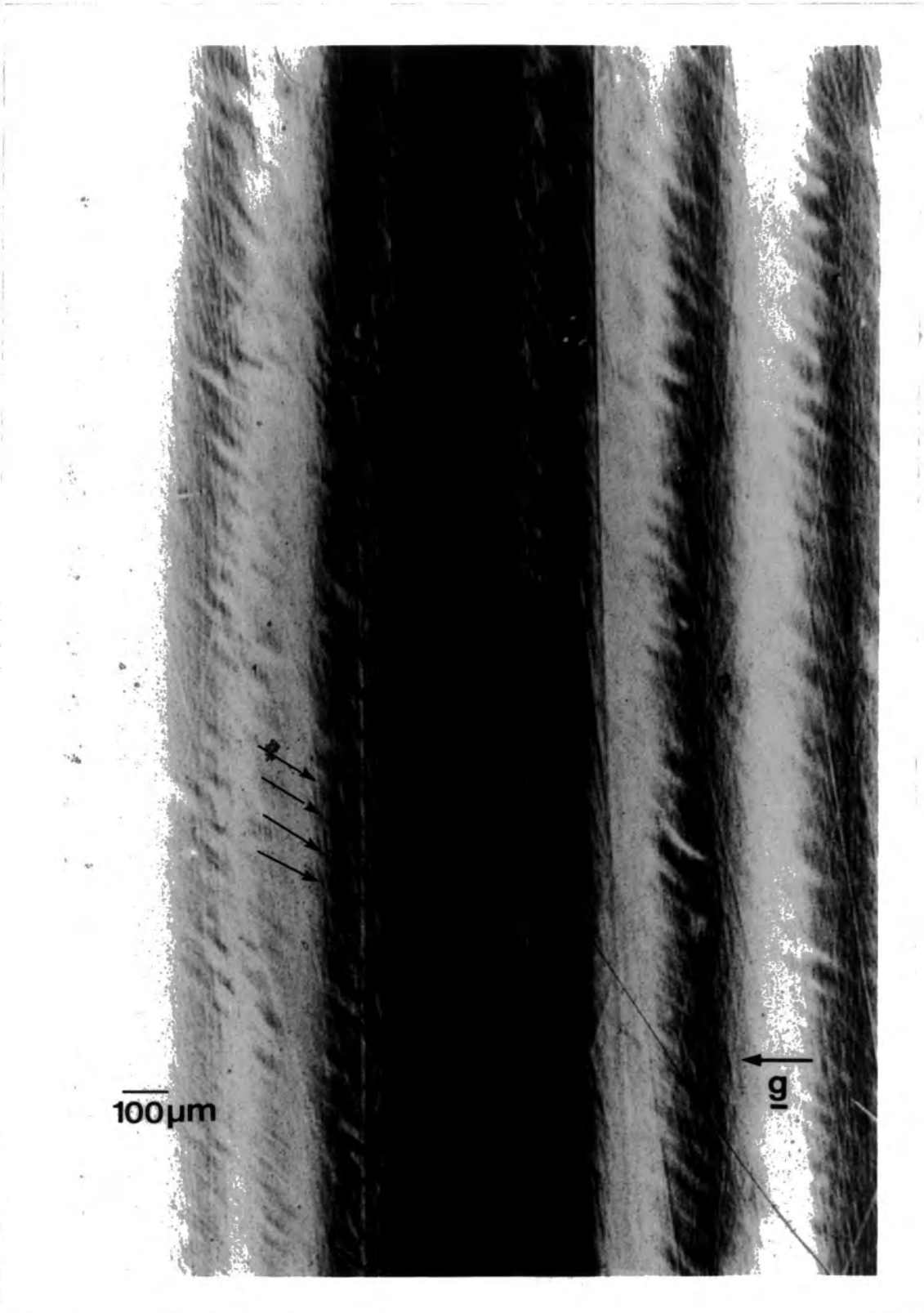

Plate 6.02. This plate shows an enlarged region around the confining layer peak.

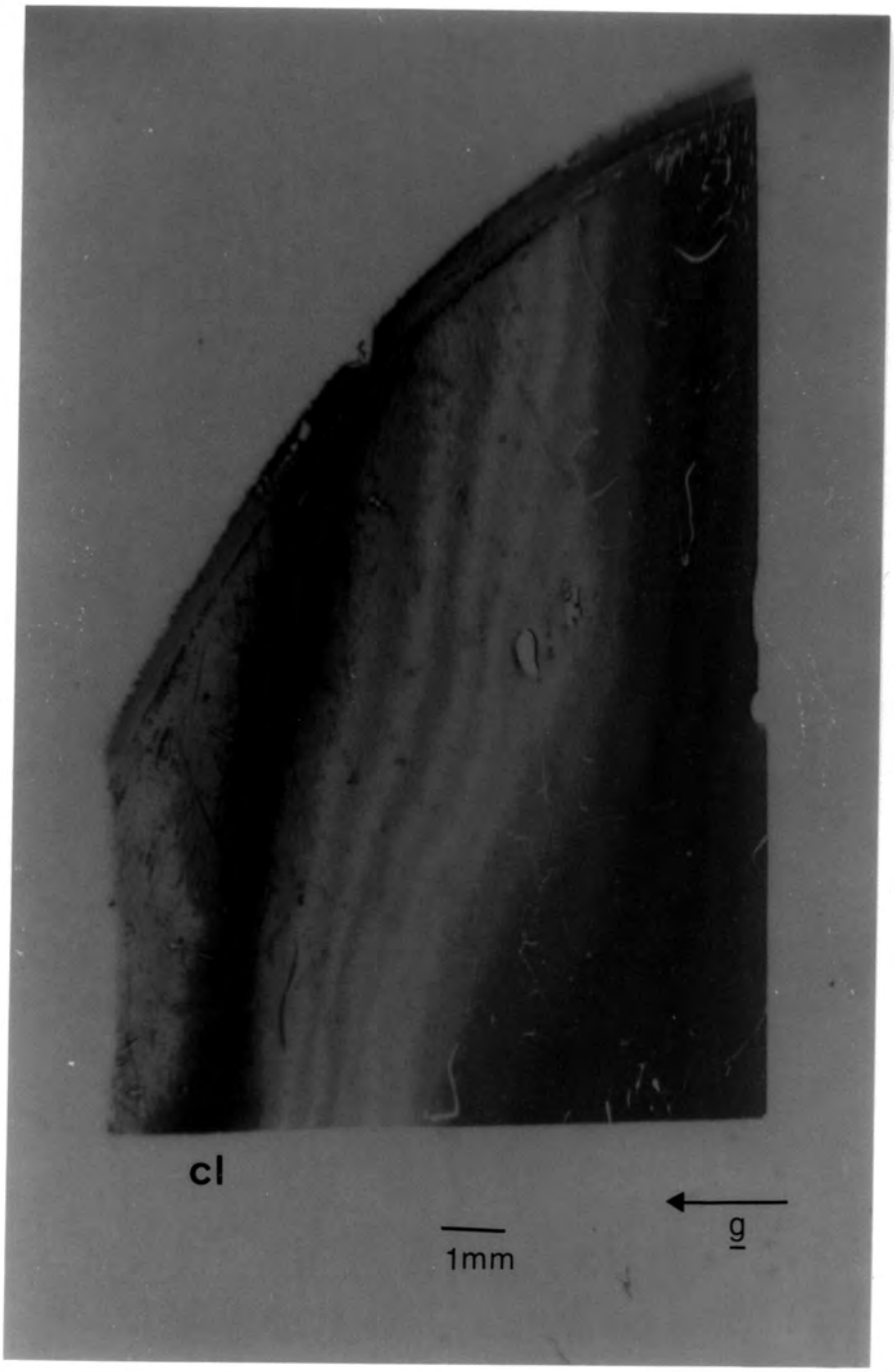

Plate 6.03. This plate shows the 004 topograph of the InGaP sample with the confining layer peak marked.

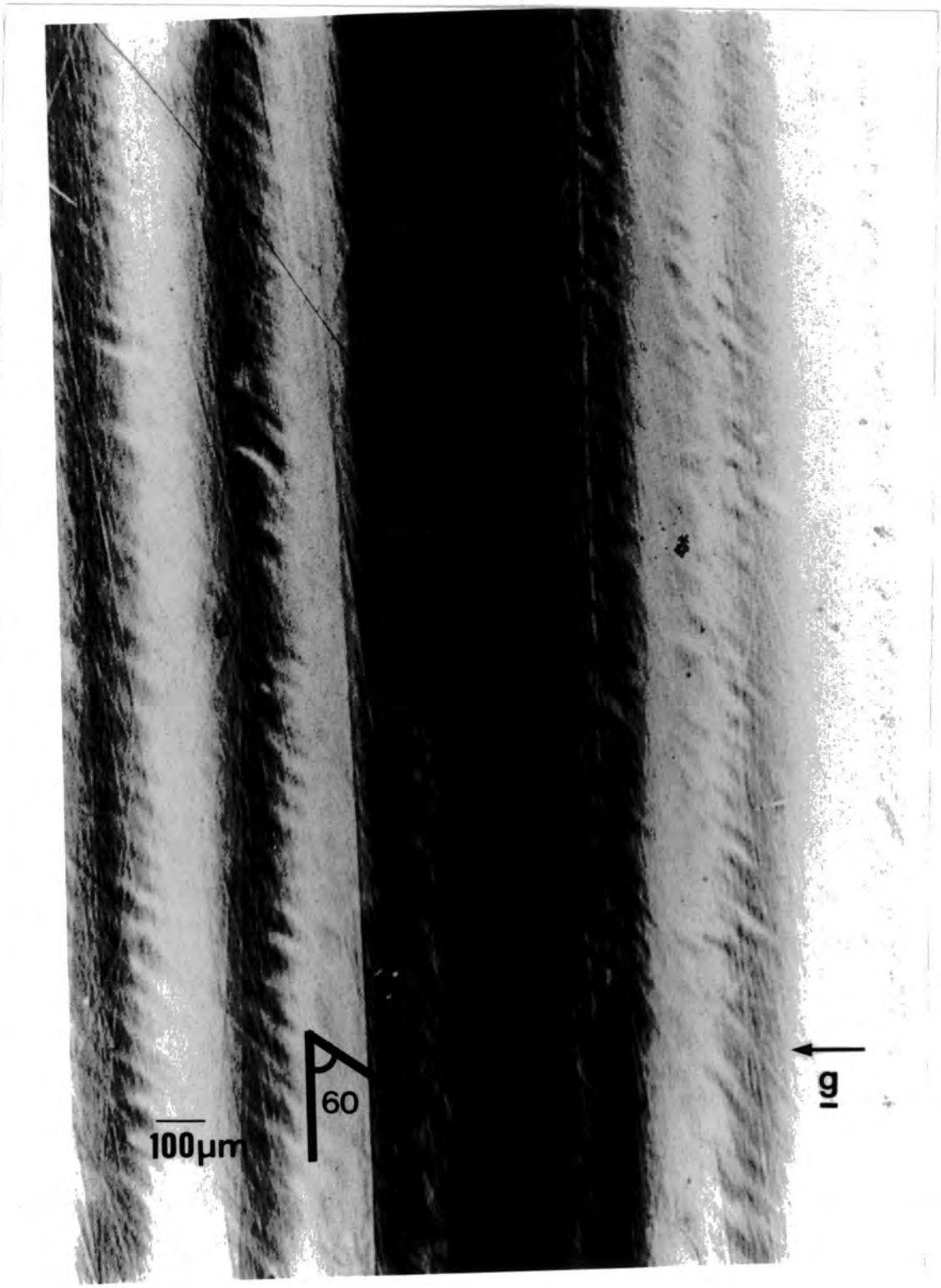

Plate 6.04. This plate shows an enlarged region around the confining layer peak of the AlGaAs sample with nominally 0 degree rotation. The fringes are inclined at an angle of approximately 60^{o} to the normal from the confining layer band, as shown.

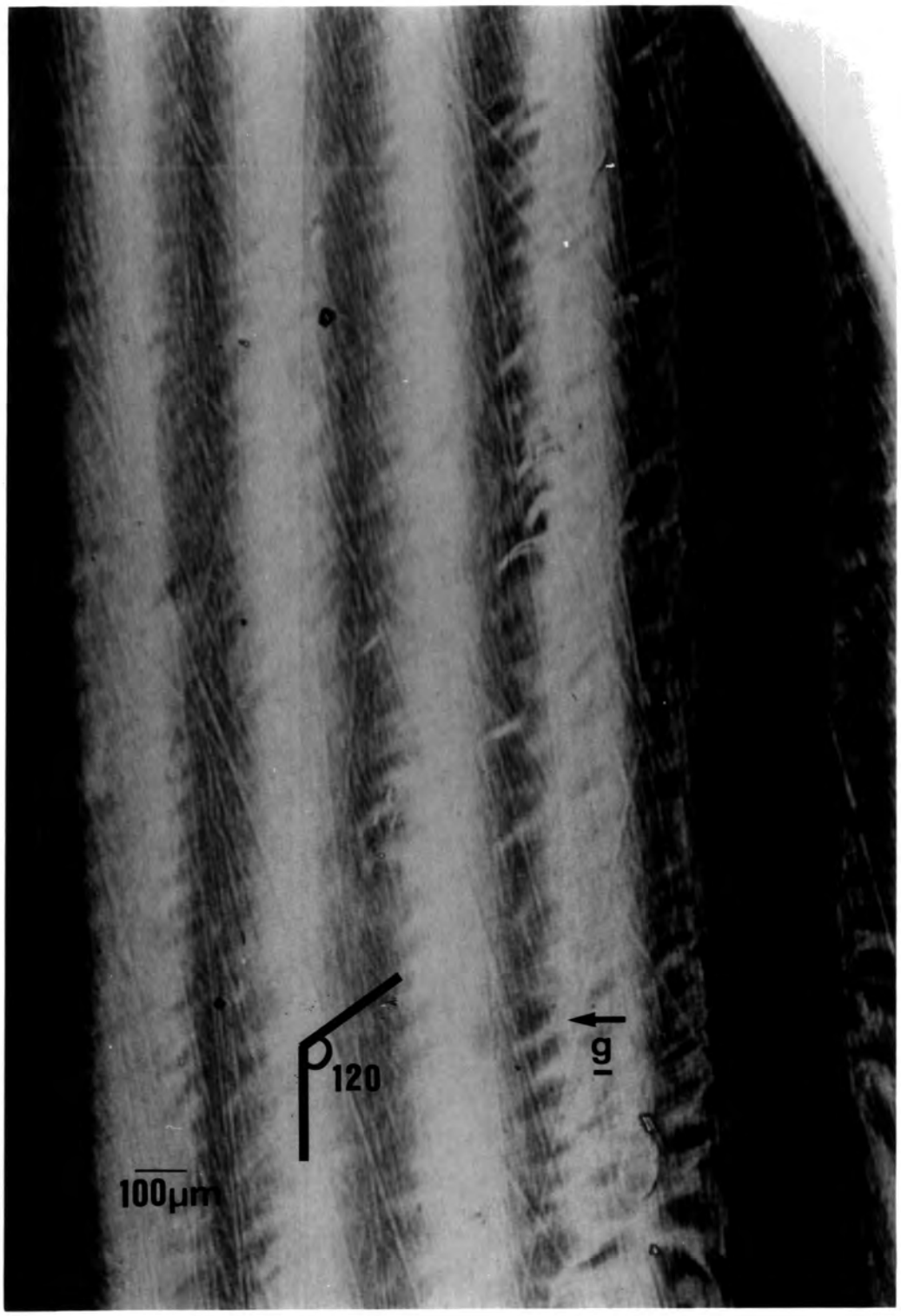

Plate 6.05. This plate shows an enlarged region around the confining layer peak of the AlGaAs sample with a 45° degree rotation about a normal to the sample surface. The fringes are inclined at an angle of approximately 120°.

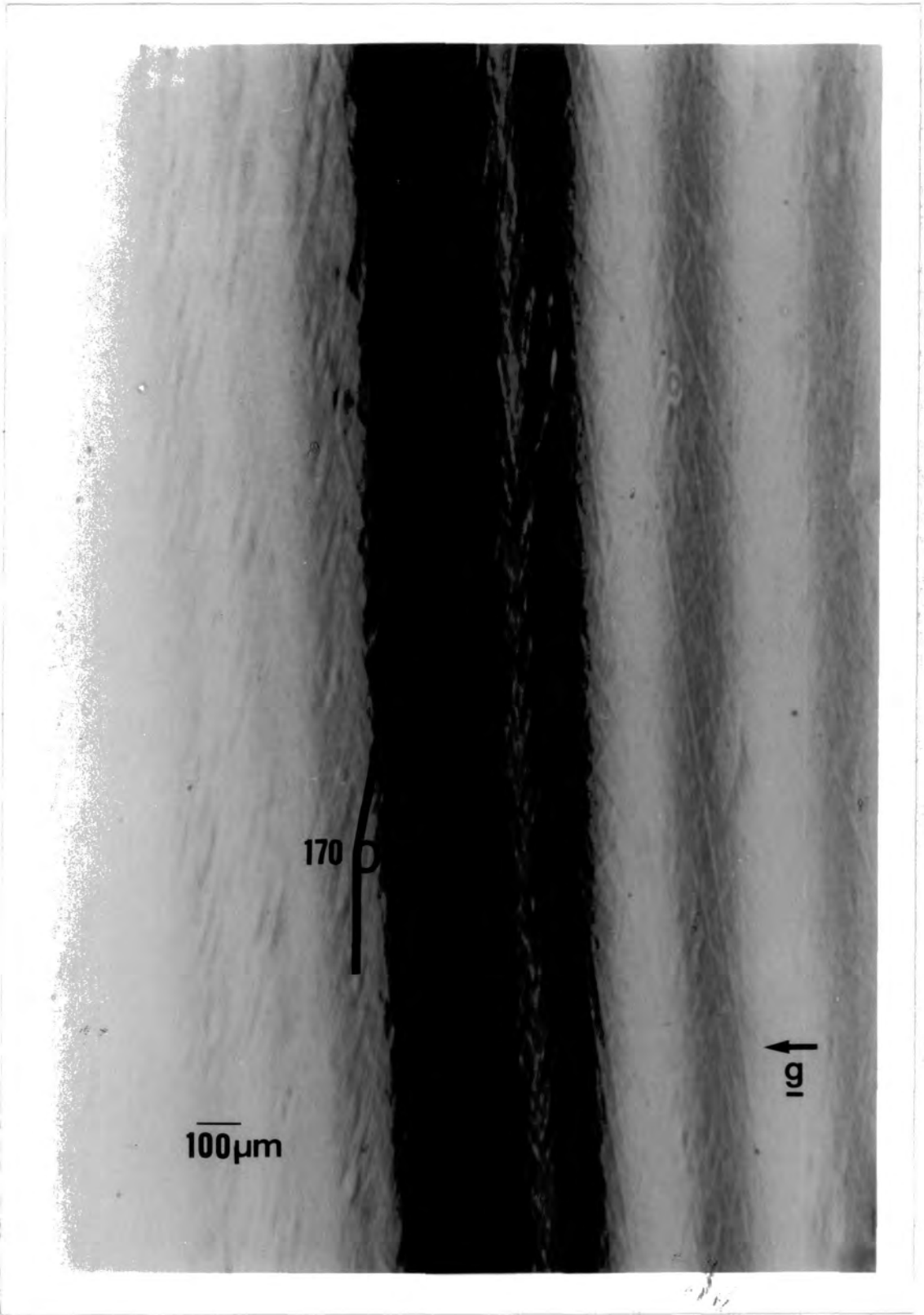

Plate 6.06. This plate shows an enlarged region around the confining layer peak of the AlGaAs sample with a 90° degree rotation about a normal to the sample surface. The fringes are inclined at an angle of approximately 70°.

Rotation Angle	Fringe Spacing	Angle on Plate
0^o	$60\mu m$	$60^o \pm 5^o$
45^o	$80\mu m$	$120^o \pm 5^o$
90^o	$60\mu m$	$170^o \pm 5^o$

Table 6.01. This shows the rotation angle measured on the plates for the 0, 45 90 degree rotations.

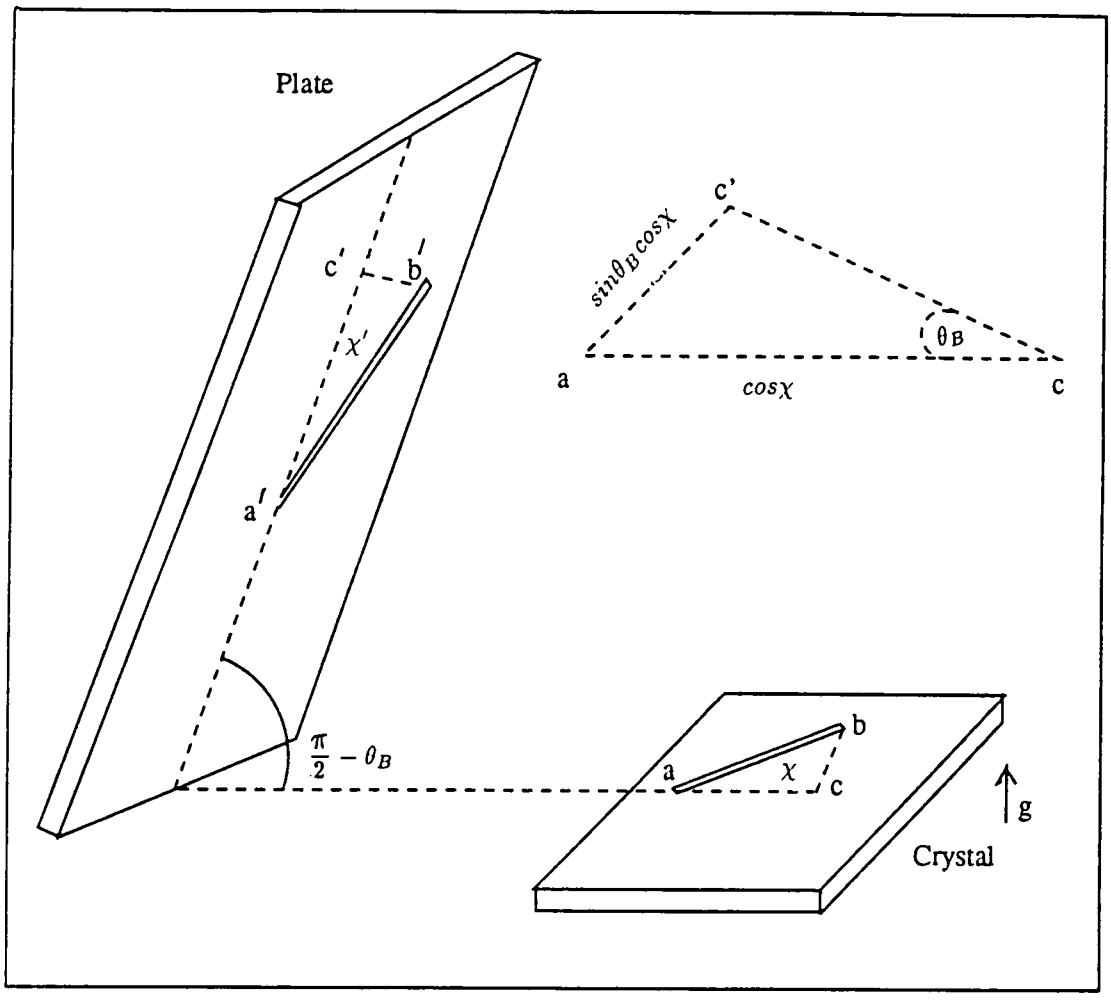

Figure 6.11. Schematic diagram showing the diffracting crystal lying horizontally and the plate at an angle of $\frac{\pi}{2} - \theta_B$. The angle χ describes the rotation of the fringe on the crystal, as shown. The projection angle χ' is obtained by considering the triangle ac'c.

Then if we set ab=1, as b'c'=bc,

$$tan\chi' = \frac{sin\chi}{sin\theta_b cos\chi} \tag{6.27}$$

hence

$$tan\chi' = \frac{tan\chi}{sin\theta_b} \tag{6.28}$$

The spacing of the fringes on the crystal is given by taking the magnitude of the dilation and tilt components. Then the spacing Λ is given by,

$$\Lambda = \frac{1}{\sqrt{\Delta g_D^2 + \Delta g_T^2}} \tag{6.29}$$

and the angle χbetween the fringes and the intersection of the incident plane on the crystal is given by

$$tan\chi = \frac{d\Delta\theta}{\Delta d} \tag{6.30}$$

The errors in measuring the spacing were principally the difficulty in determining the center of each fringe and the variation in fringe spacing over the area of topography. These errors were reduced by taking repeated measurements over 10 fringes and recording the average value.

From the previous discussion it can be seen that a fringe inclined at an angle χ in the crystal surface will be at a different angle χ' on the surface of the plate. A rotation of the crystal about the surface normal by 45 degrees produces a projected rotation angle of 61 degrees at the plate. From table 6.01 the difference in angle between the 0 and 45 and the 45 and 90 degree rotation corresponds well to 61 ± 5 degrees. Therefore it may be concluded that the fringes are fixed with respect to the sample surface which is consistent with them being either Moire type fringes or thickness type fringes.

6.4.2 Topography as a function of wavelength and beam geometry.

In this study the 004 reflection using $1.0\mathring{A}$ radiation and the 224 reflection using $1.5\mathring{A}$ radiation was used to investigate whether the fringe spacing changed as a function of diffraction geometry. Plate 6.07 illustrates the 004 topograph of

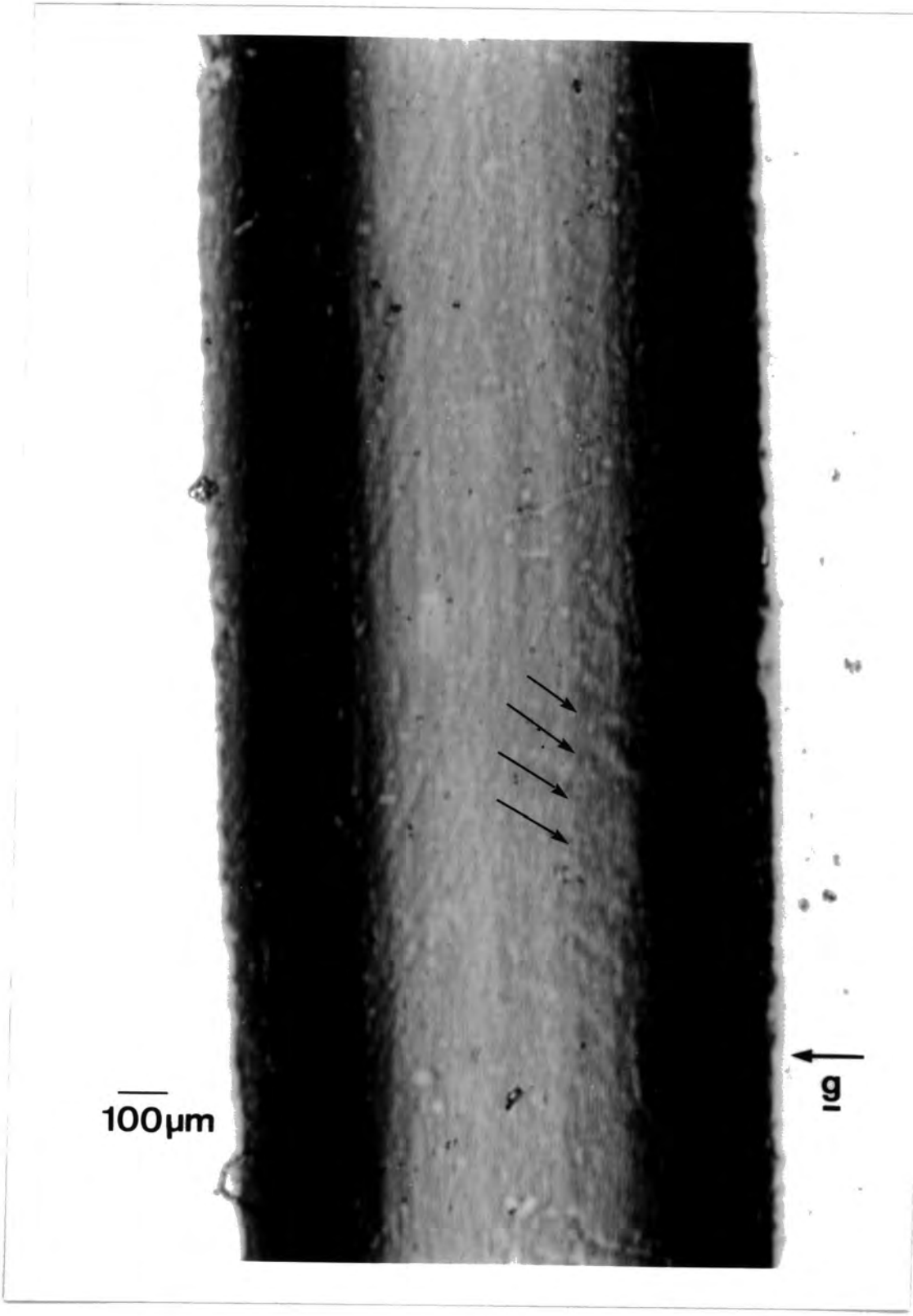

Plate 6.07. This plate shows an enlarged region around the confining layer peak of the AlGaAs sample taken with the 004 reflection at 1.0$\mathring{A}$. The fringe spacing is approximately $60 \pm 10 \mu m$.

an enlarged region around the confining layer peak. Fringes are no longer clearly visible, however fringes can still be observed and these are marked with arrows running along the confining layer peak. These fringes have a spacing of $60\mu m \pm 10\mu m$ which is very similar to those found previously using the 004 reflection at 1.54 $\AA$. This implies that the fringe spacing also appears to be independent of the incident angle which illiminates the possibility of the fringes being produced from a uniform variation in thickness or mismatch. Plate 6.08 illustrates the 224 topograph around the confining layer peak. This plate shows considerably different contrast than the previous topographs taken using the symmetric 004 reflection. To account for the contrast observed one needs to consider the greatly reduced incident angle of the X-ray beam to the surface. A lower angle of incidence to the surface increases the perpendicular acceptance of the incoming beam. Therefore a larger angular range is covered resulting is a larger area imaged. However because of the lower angle of incidence only a small region of the crystal close to the surface now diffract and defect contrast goes up. Scattering from the surface region becomes comparable to scattering from the bulk crystal hence defects in the surface become prominant. This does not explain the loss in contrast of the fringes, though if you increase defect contrast in the surface layer the fringe contrast goes down.

A second possibility for reduced fringe contrast is absorption in the upper layers stopping the beam from reaching the lower confining layer and therefore reducing contrast. However the extinction distance for the 224 reflection at $1.54\AA$ is $13\mu m$.

6.4.3 Rocking curve scans using the 004 reflection

To attempt to obtain futher evidence that the contrast is not from thickness fringes rocking curves have been taken from different points on the crystal. As mentioned in the introduction, Chu and Tanner (1986) and later Wie (1989) showed that interference effects on the confining layer peak are extremely sensitive to variations in the active layer thickness or composition. To illustrate the effect on the rocking curves of changing layer thickness and mismatches figure 6.12 illustrates the effect of varying the active layer thickness, while figure 6.13 shows the effect of changing the active layer composition. Figure 6.14 shows the effect of varying one of the confining layer peak thicknesses. It is clear that the structure noticeable on the low angle side of the confining layer peak is strongly affected by the active

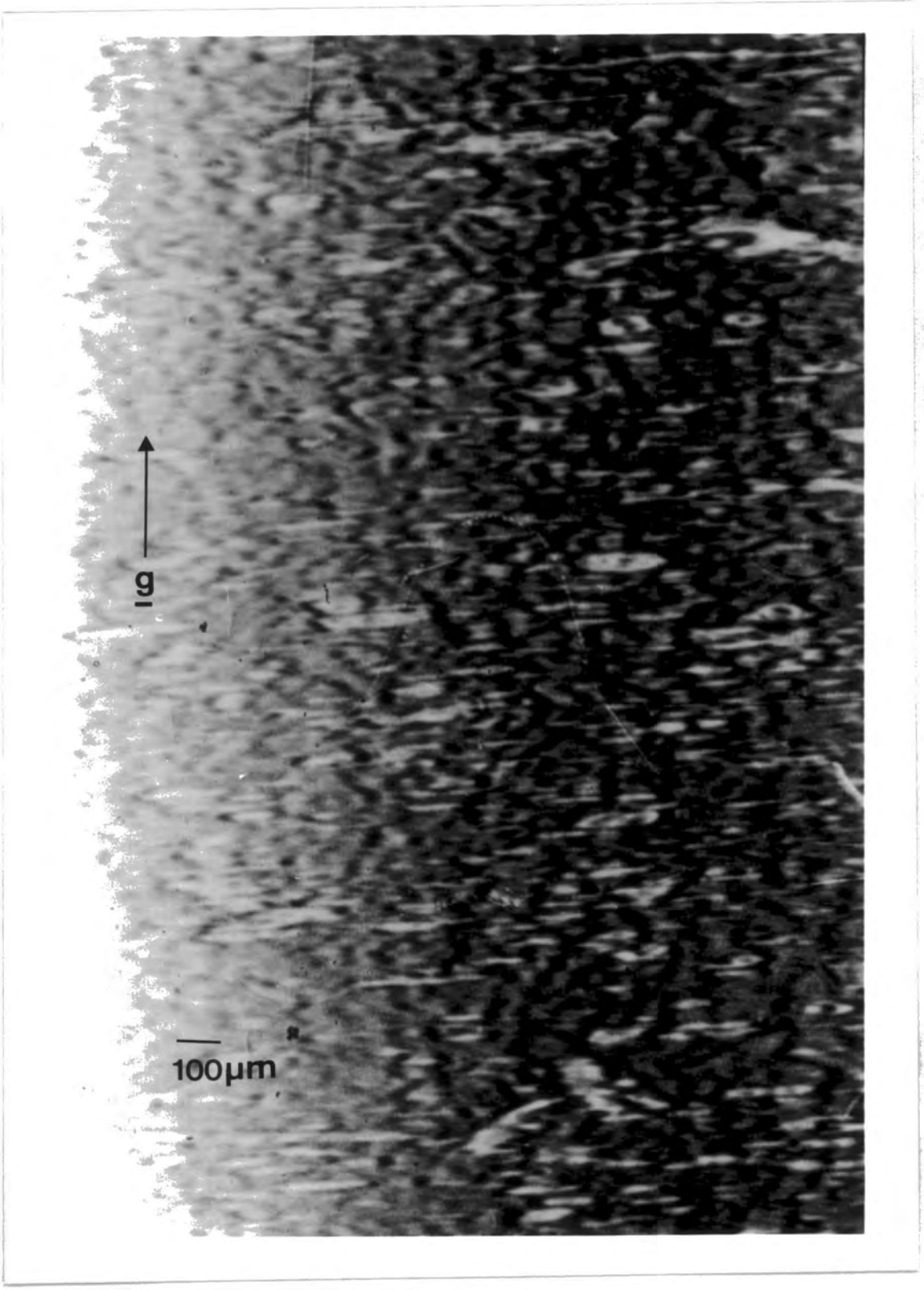

Plate 6.08. This plate shows an enlarged region around the confining layer peak of the 224 reflection taken at 1.54Å. No fringes are visible.

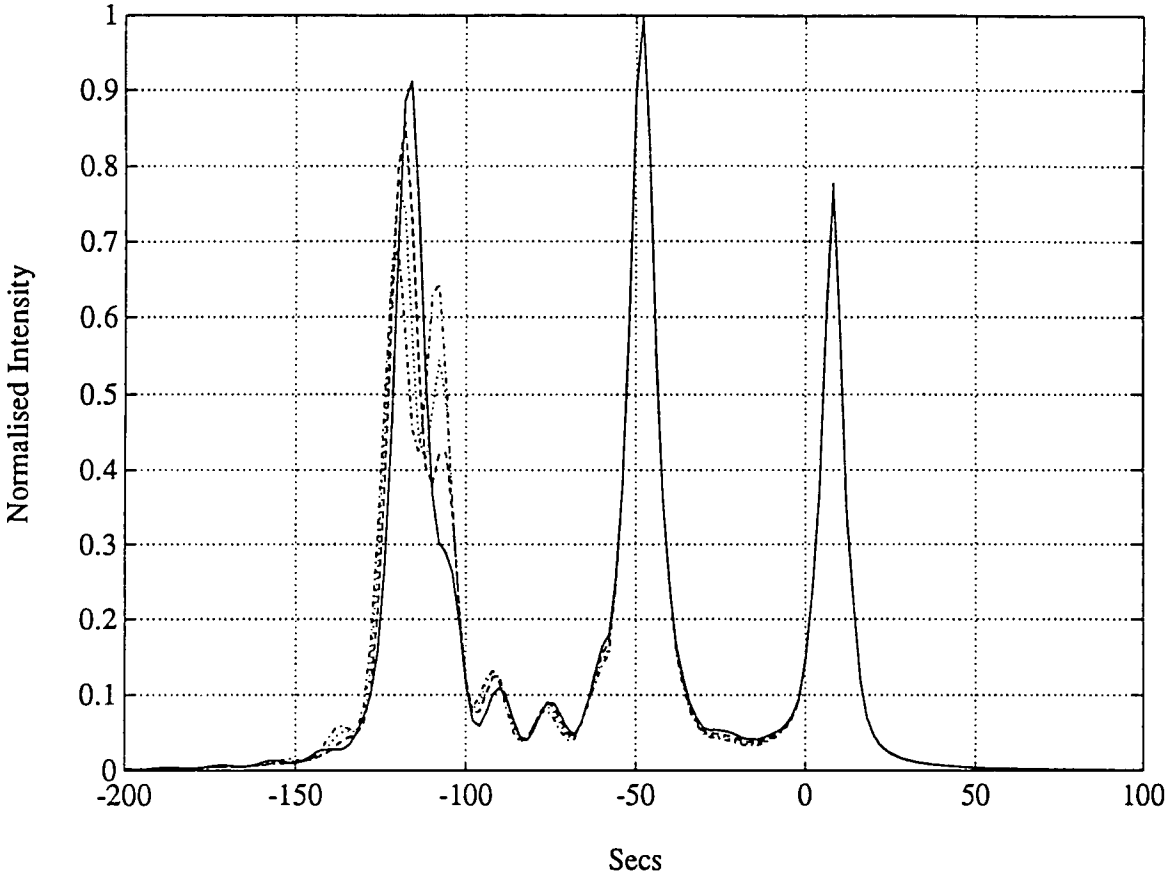

Figure 6.12. This figure illustrates the effect of changing only the active layer thickness: solid line, $0.19\mu m$; dashed line, $0.16\mu m$; dotted line $0.14\mu m$; dashed-dot, $0.12\mu m$, of the AlGaAs sample using the 004 reflection. The other layer parameters are those in figure 6.07.

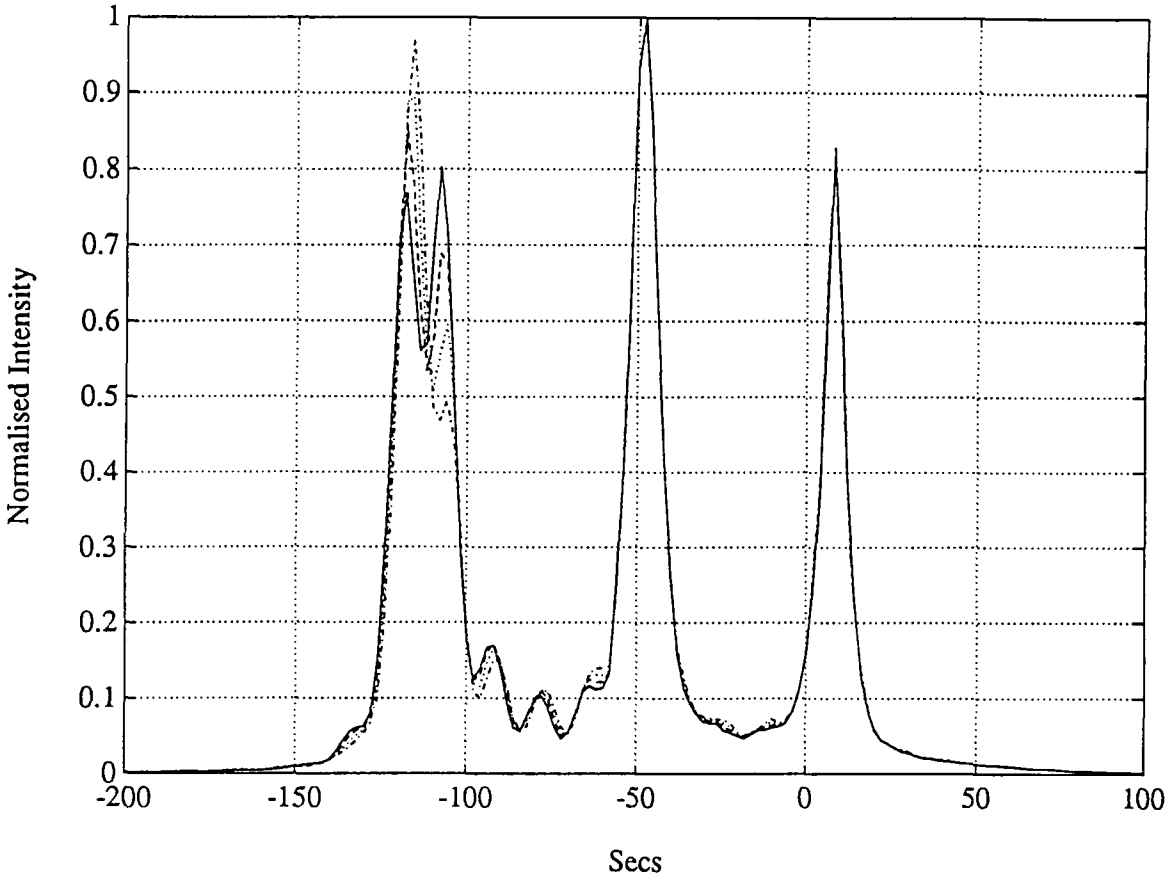

Figure 6.13. This figure illustrates the effect of changing only the active layer composition: dashed-dot, 12.0%Al; dotted line,14.0%Al; dashed line, 16.0%Al; solid line,18.0%Al. The other layer parameters are those in figure 6.07.

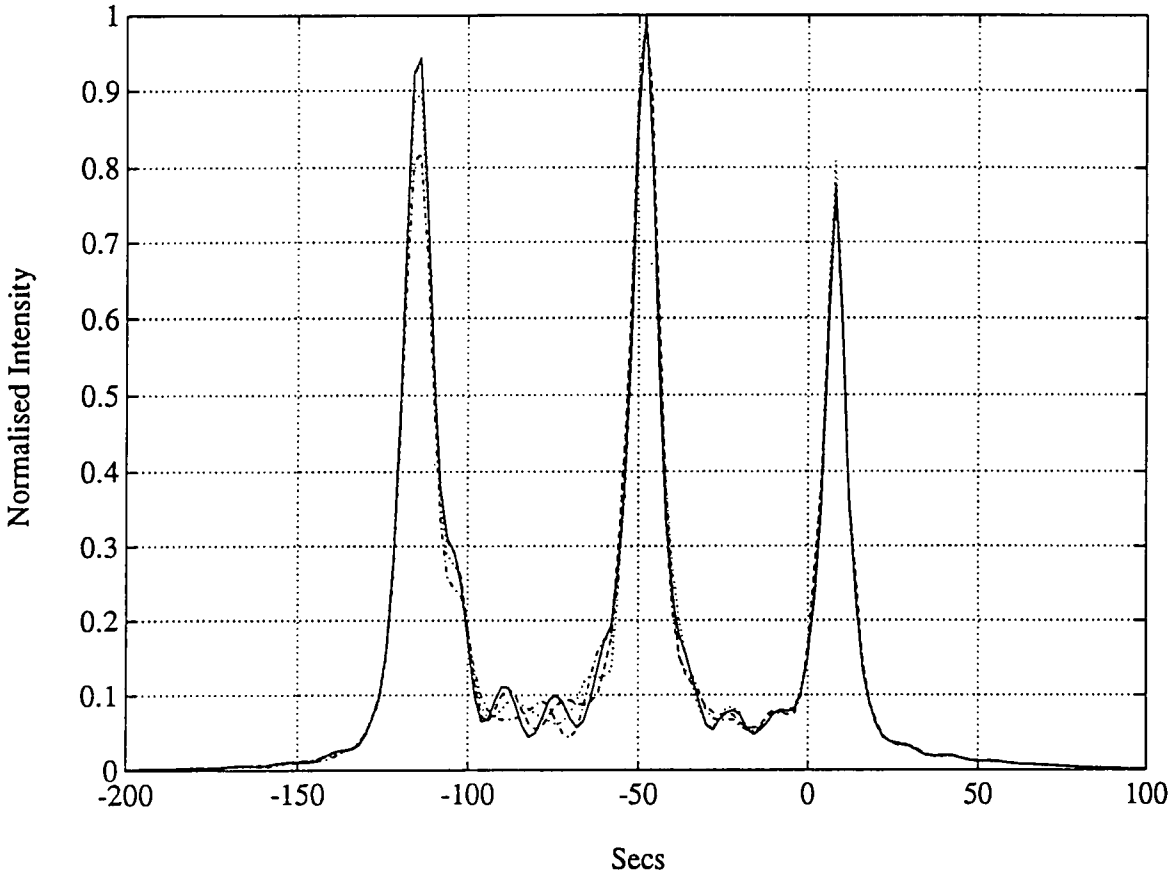

Figure 6.14. This figure illustrates the effect of changing only one of the confining layer thickness: solid line, $1.18\mu m$; dotted line,$1.08\mu m$; dashed -dot line, $0.98\mu m$; dashed line $0.88\mu m$. Note there is very little change to the asymmetry on the confining layer peak, but the pendellosung fringes change phase.

layer composition or thickness, yet it is weakly influenced by variations in the confining layer. The confining layer thickness or composition seems to have a much stronger effect on the phase of the pendellosung fringes located between the confining layer and buffer layer peaks. Experimental rocking curves were recorded at Durham using the Bede model 150 prototype double crystal camera with a GaAs first crystal in a line 2, 4, 6 and 8mm from one edge. Each of these rocking curves were also recorded again following a 180 degree rotation about the surface normal. There were no detectable differences in each pair of rocking curves indicating no layer tilt was present.

The experimental rocking curves are shown in figures 6.15, 6.16, 6.17 and 6.18 (solid lines) together with the best fit simulations (dashed lines) obtained by only changing the active layer thickness.

It can be seen that a fairly good match to the experimental data can be obtained simply by changing the active layer thickness. However the simulated match is not perfect and therefore care must be taken in concluding a variation in thickness or mismatch across the sample. The simulations suggest that a variation in thickness or mismatch of the active layer is present of $0.07 \pm 0.01 \mu m$ or $4\% Al$. If one assumed that this variation was constant across the active layer and the fringes are produced at every integral number of wavelength this would produce a fringe spacing of $27 \pm 5 \mu m$. Clearly this figure is subject to the errors involved in matching the simulated and the experimental rocking curves, which are clearly not exact matches, and also the assumption of a uniform variation in the layer. However this variation does not agree with the spacing of the fringes on the topograph and is therefore consistent with the fringes not being produced from a uniform thickness variation.

6.4.4 Feasibility study into the use of Pendellosung fringes

In order to attempt to improve the measurement of layer thickness attempts at using fourier transforms were made. This technique allows the layer thickness to be measured from detecting the pendellosung fringe frequency which can then be related to the layer thickness. The observation of pendellosung fringes was first reported by Batterman and Cole (1968), who described the formation of these fringes in terms of interference between two waves excited on the same branch of

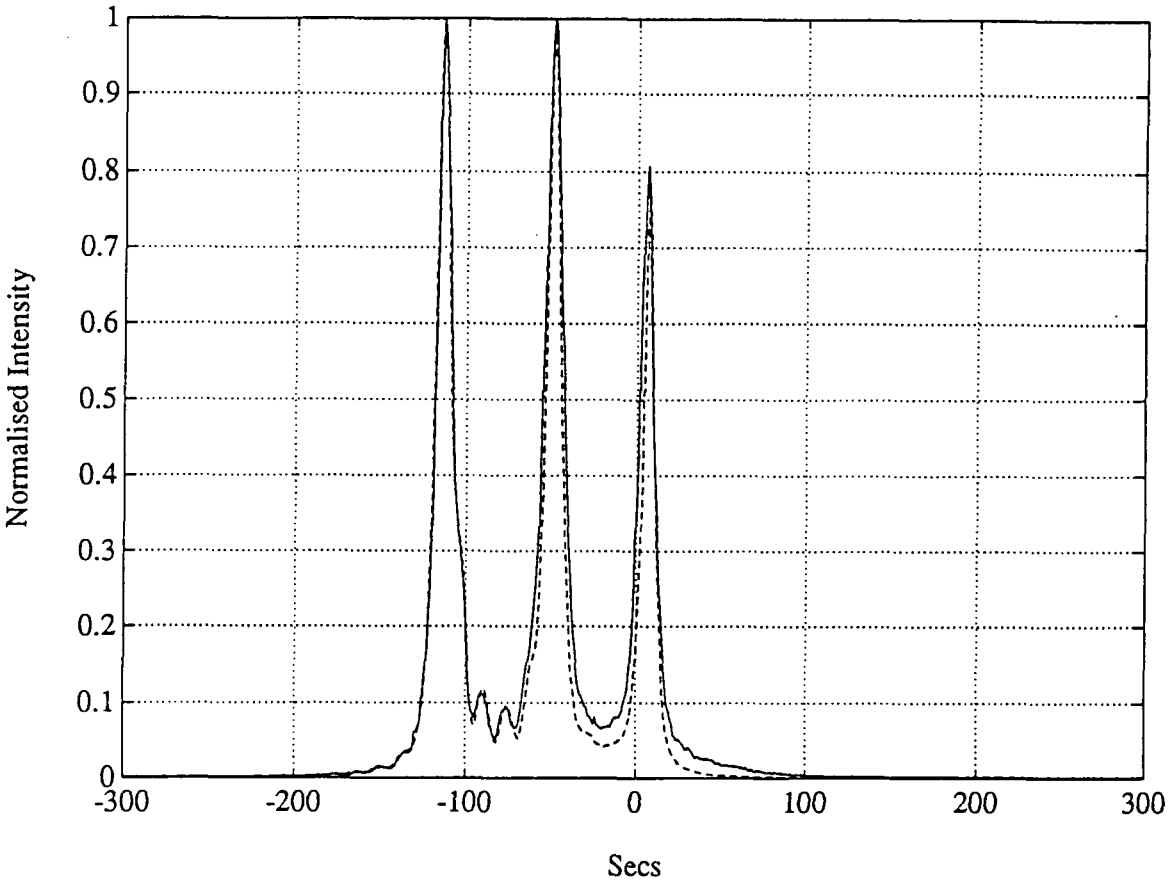

Figure 6.15. Shows the experimental 004 reflection taken at +2mm from the damaged edge (see topgraphy plate 5.01), together with the best fit simulation obtained with the same parameters as in figure 6.07 except for the active layer being $0.195\mu m$. Solid line experimental, dashed line simulation.

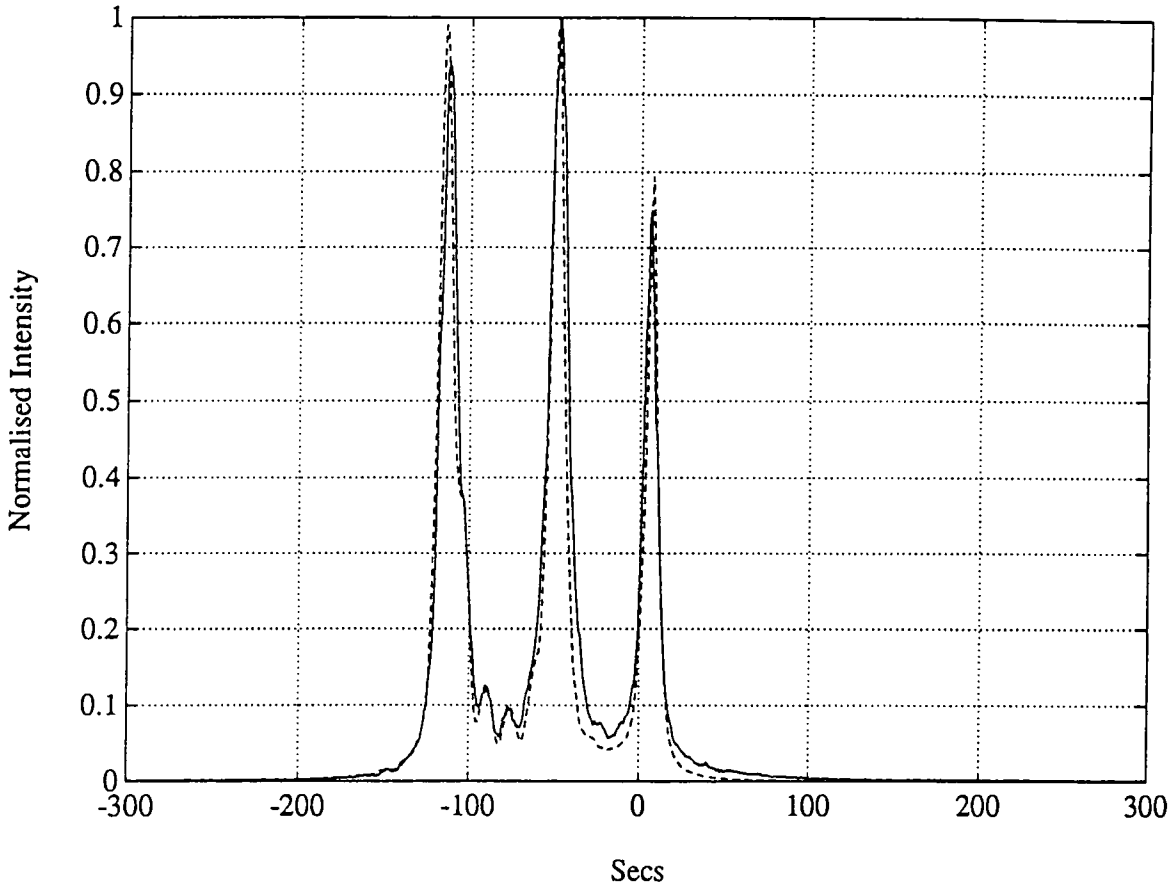

Figure 6.16. Shows the experimental 004 reflection taken at +4mm position. The best simulation was obtained solely by varying the active layer to $0.185\mu m$, in an attempt to fit the asymmetric shoulder on the low angle side of the confining layer peak. Solid line experimental, dashed line simulation.

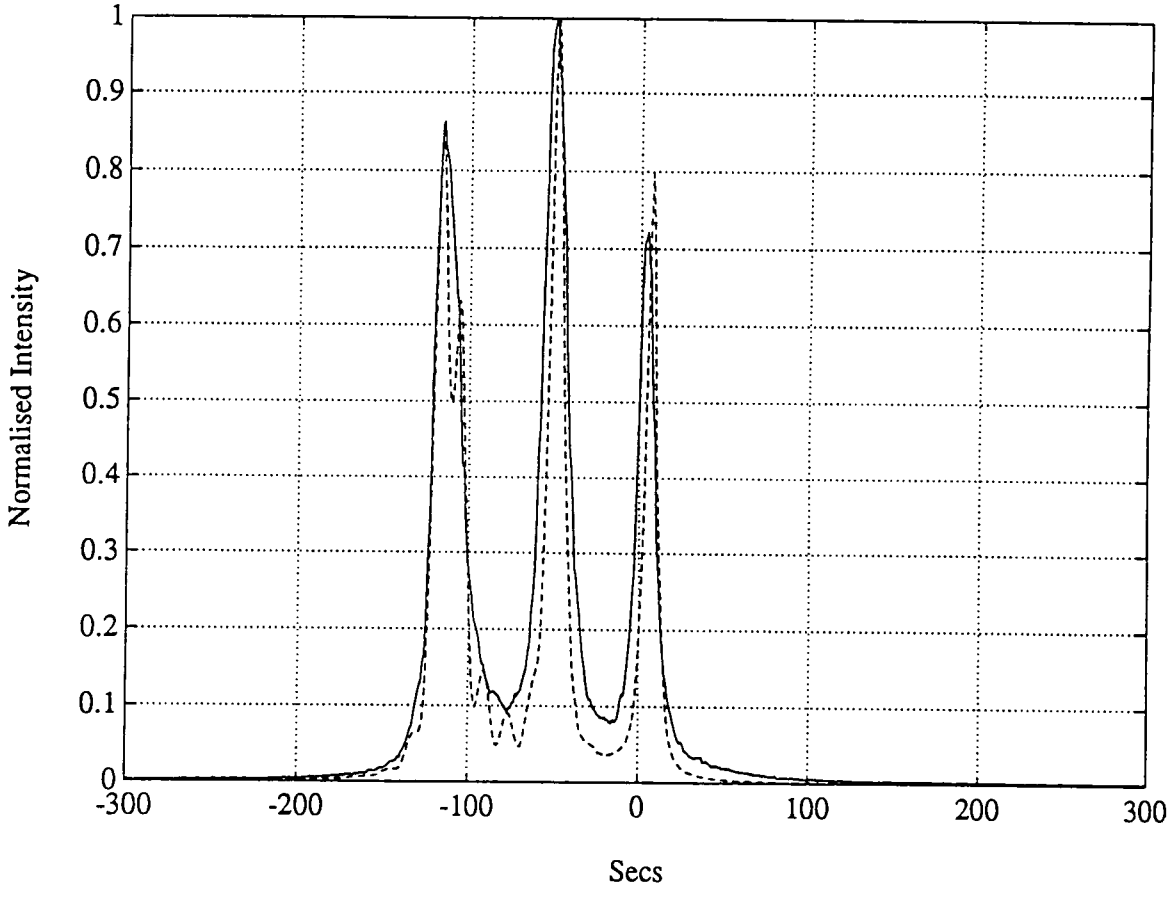

Figure 6.17. Shows the experimental 004 reflection taken at +6mm position. The best simulation was obtained solely by varying the active layer to $0.165\mu m$, in an attempt to fit the asymmetric shoulder on the low angle side of the confining layer peak. Solid line experimental, dashed line simulation.

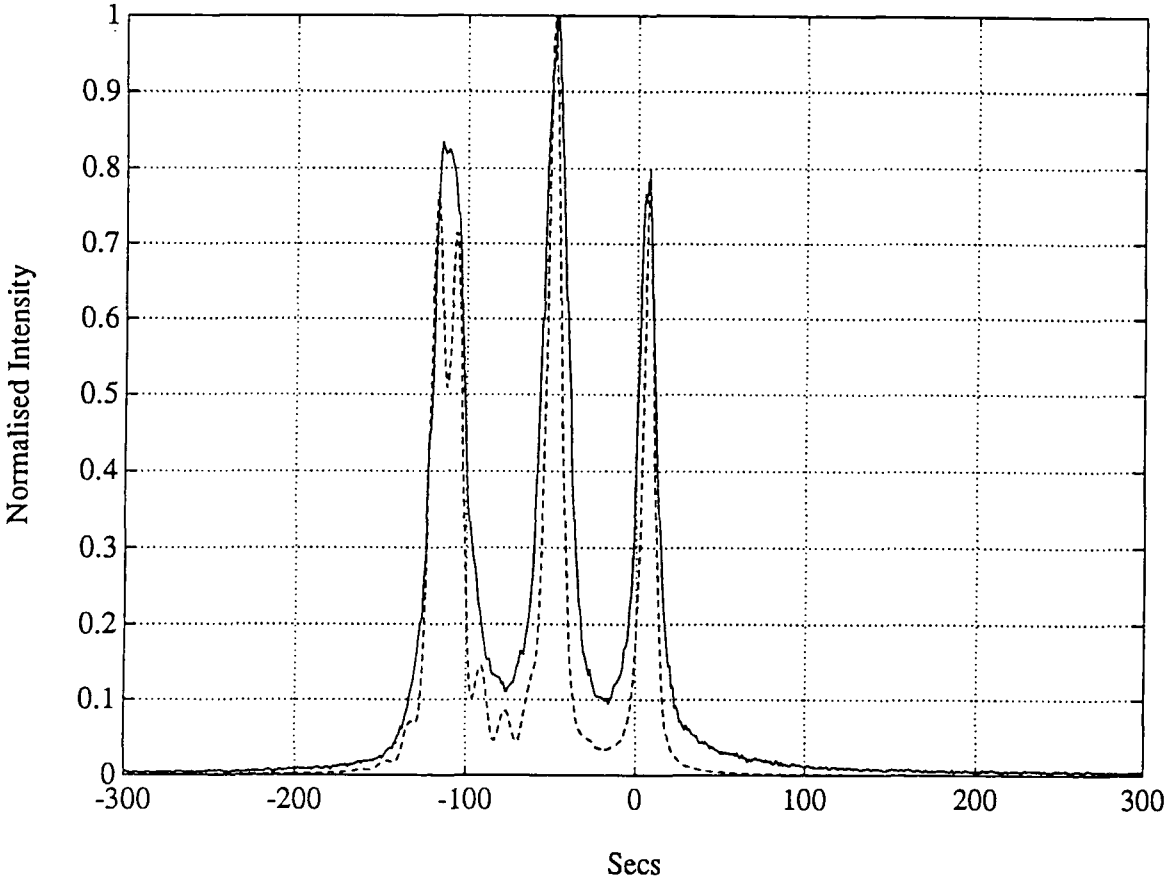

Figure 6.18. Shows the experimental 004 reflection taken at +8mm position. The best simulation was obtained solely by varying the active layer to $0.125\mu m$, in an attempt to fit the asymmetric shoulder on the low angle side of the confining layer peak. Solid line experimental, dashed line simulation.

the dispersion surface. The angular spacing of the fringes can be used to give a value of the layer thickness. The fringe spacing is related to the layer thickness through the relation stated previously.

Pendellosung fringe analysis can only accurately be undertaken by taking the fourier transform of the experimental rocking curve. This is because the effect of the superposition of harmonics and fundamental frequencies can often lead to misleading frequency determination if the peak separations are measured (Miles, 1989).

To investigate the pendellosung frequencies present in structures of this type, and attempt a direct confirmation of the results obtained in the line scan study, a series of simulations were performed, together with their fourier transforms. The simulated 004 rocking curves, together with their fourier transforms, for the InGaAs sample are given in figure 6.19 with all the layers present, figure 6.20 for the top layer removed and figure 6.21 for the top two layers removed. In all the fourier transforms the x axis gives the value of the pendellosung fringe spacing. The peaks corresponding to harmonics and subharmonics of layer thickness are indicated. The fourier transform can be seen to be symmetrical about the centre, this feature is a function of the transform used. Figure 6.22 shows the experimental 004 rocking curve obtained from the InGaAs sample together with its fourier transform.

In the study carried out above it has been shown that it should in principle be possible to measure the thickness of the layer using the fourier transform technique. However in practice fringes are often located below the level of the noise encountered in the experiment and the resulting fourier transform can not reveal the layer thicknesses. The ratio of the signal to noise can be improved by using very long counting times and a low noise level counter, such as a proportional counter.

It can be seen that the fourier transforms do show some peaks which have been labelled with the calculated layers, however the presence of many additional peaks makes a determination of layer thickness unreliable.

Figure 6.19. Shows the simulated 004 reflection from the InGaAs sample with all three layers present, together with its fourier transform. Peaks are marked where their position corresponds to a multiple of the layer thicknesses.

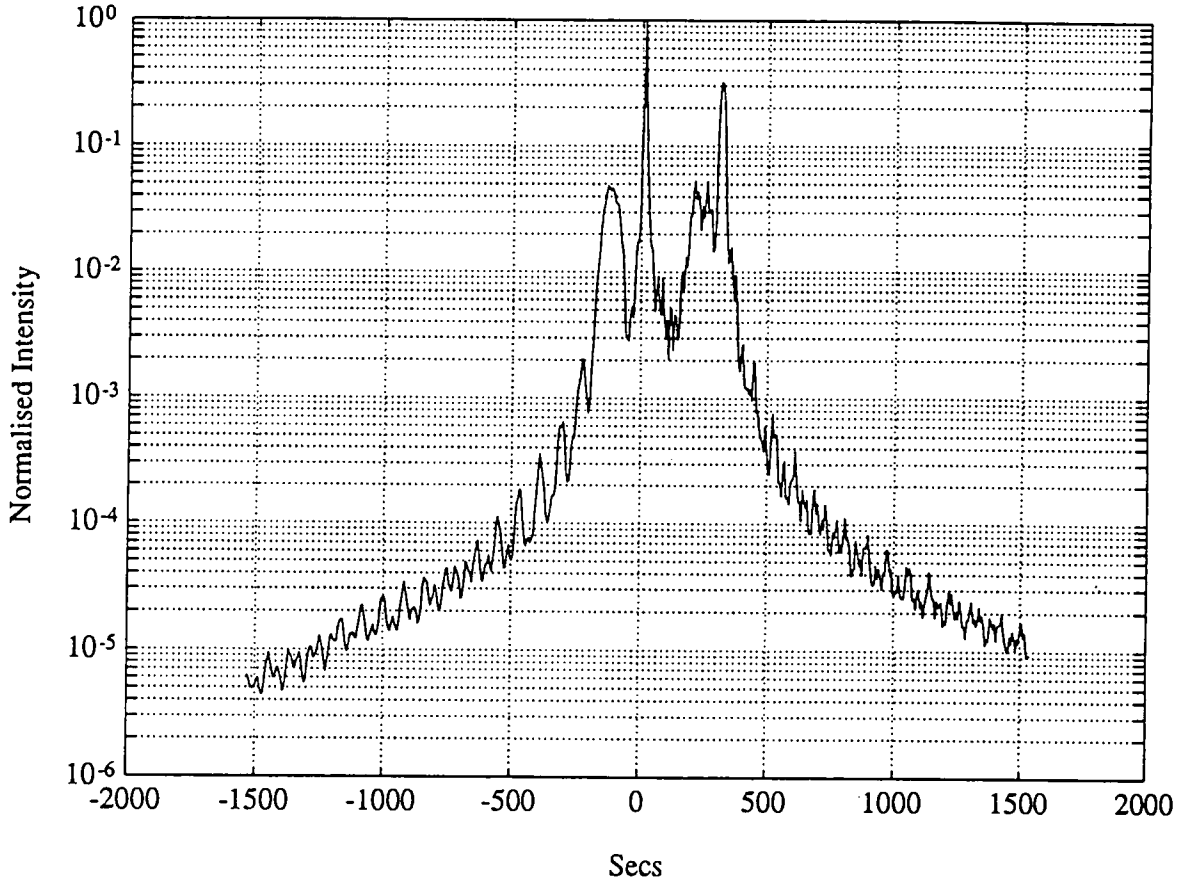

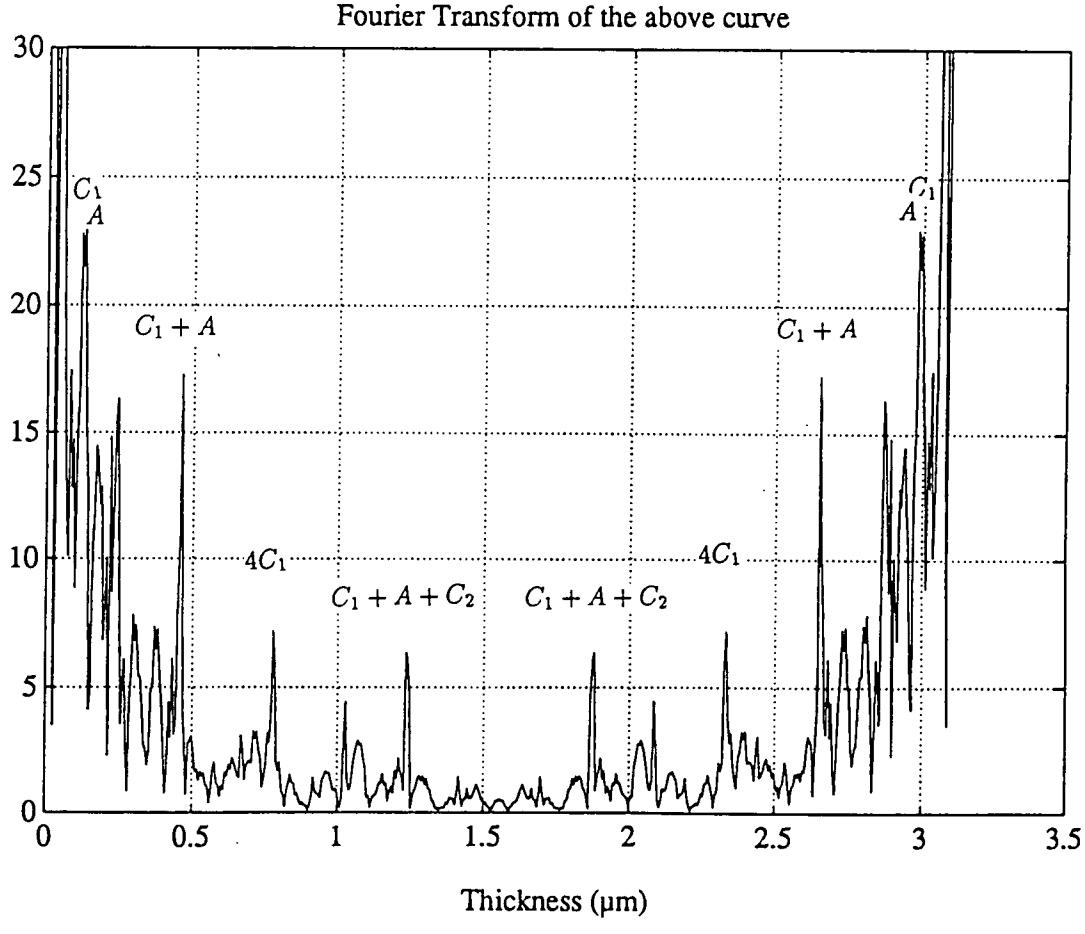

Figure 6.20. Shows the simulated 004 reflection from the InGaAs sample with the top layer removed, together with its fourier transform.

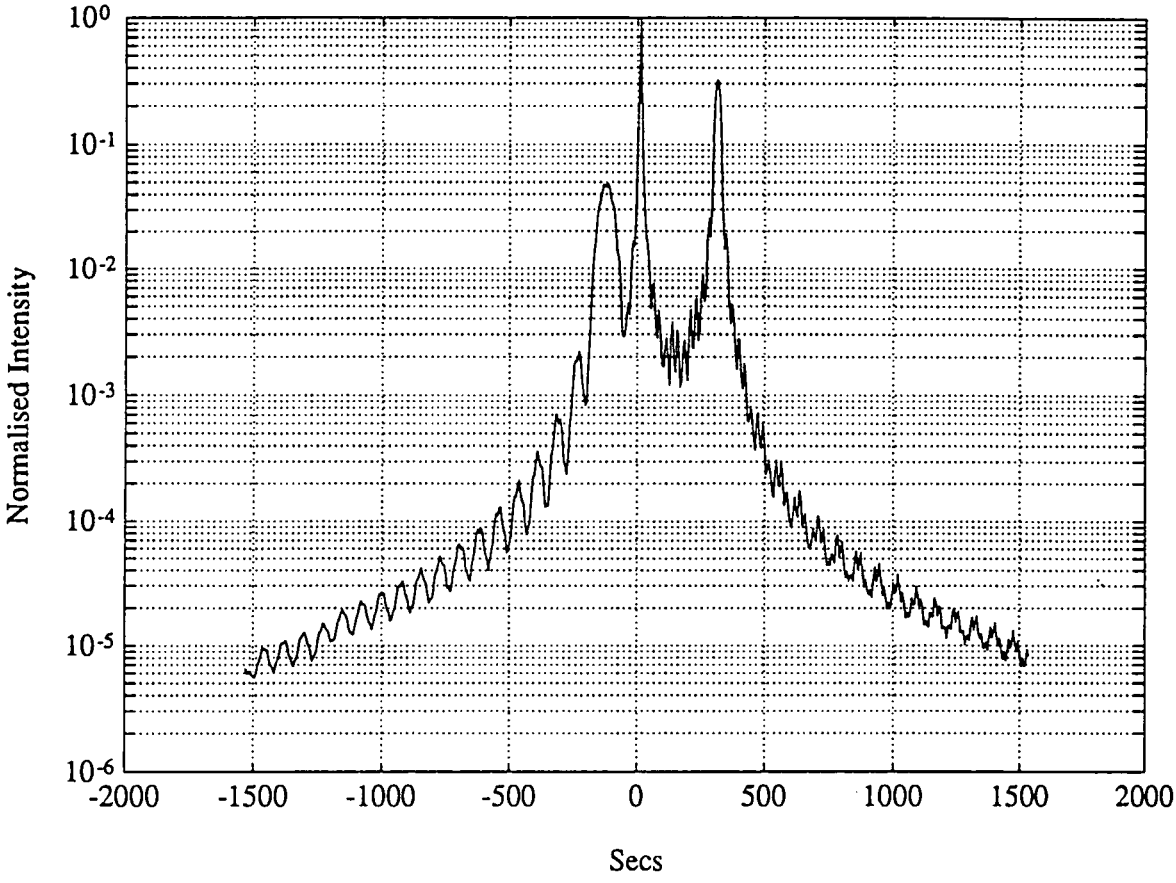

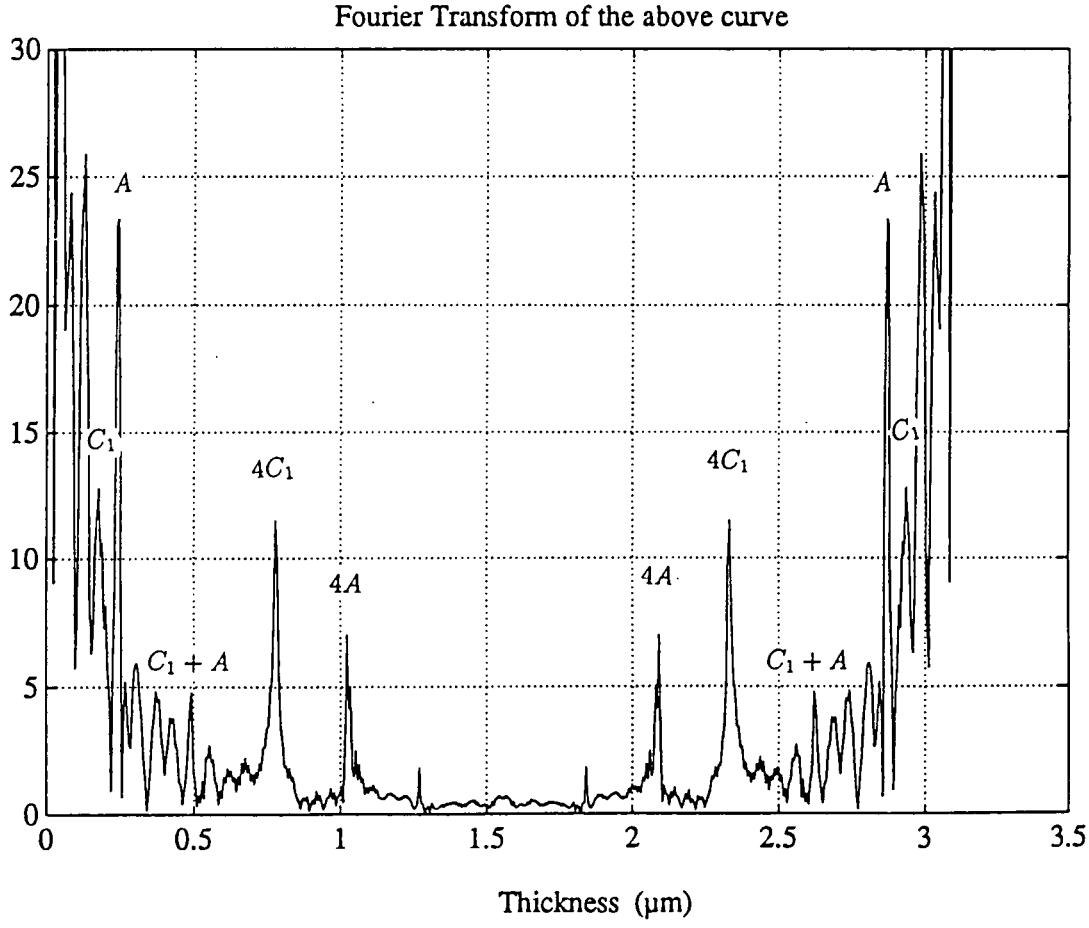

Figure 6.21. Shows the simulated 004 reflection from the InGaAs sample with the top two layers removed, together with its fourier transform.

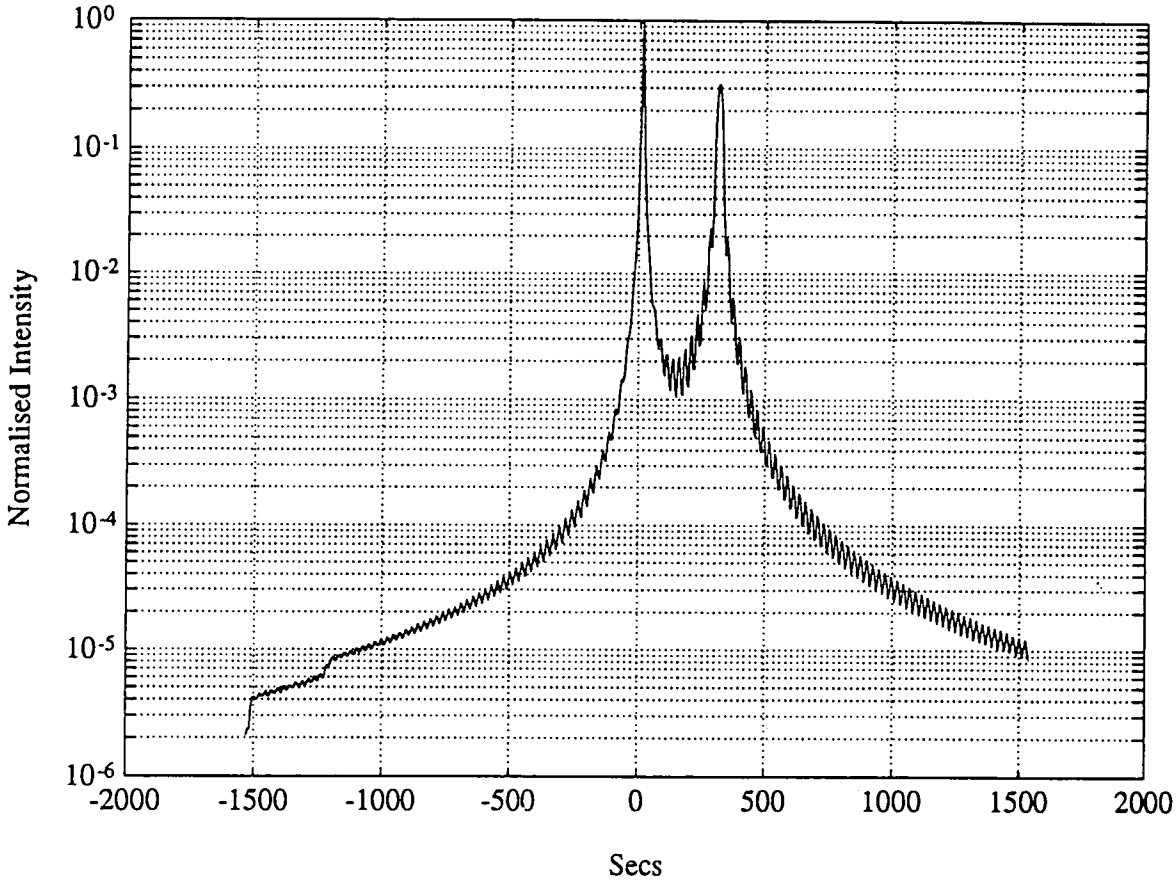

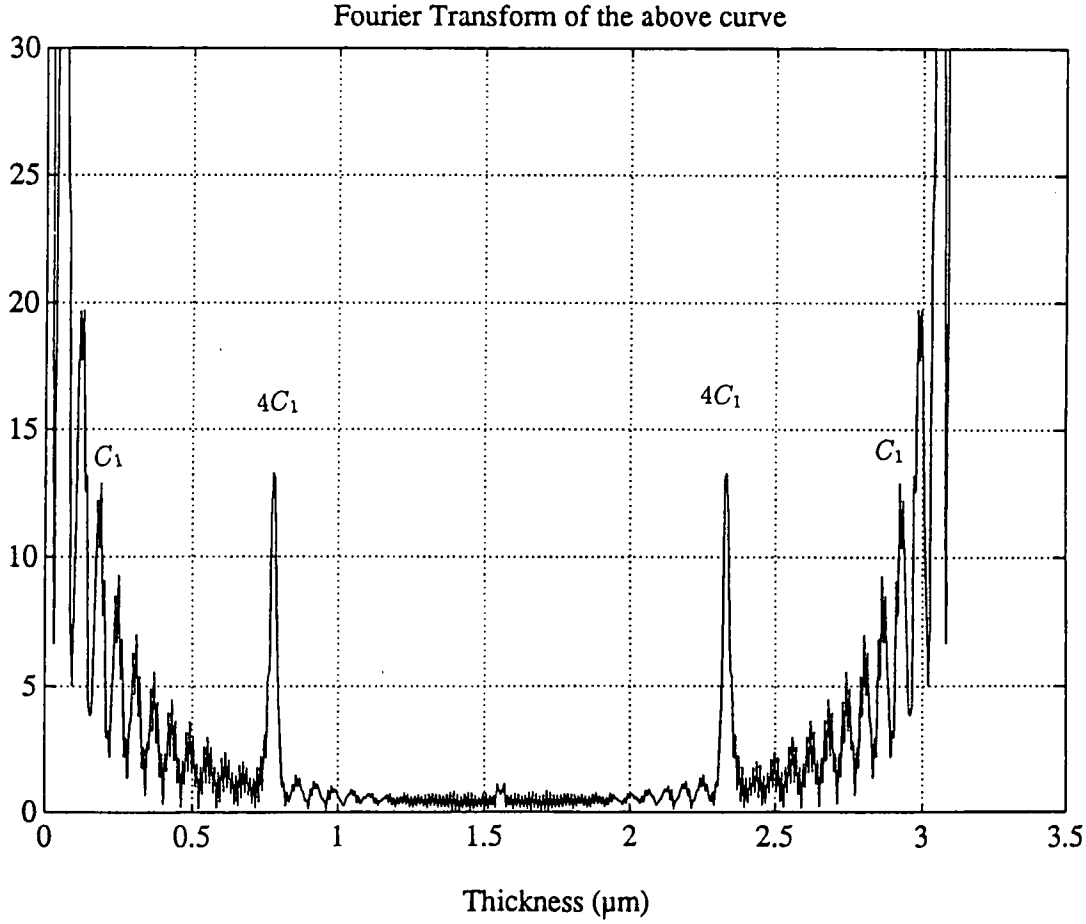

Figure 6.22. Shows the experimental 004 reflection from the InGaAs sample, together with its fourier transform.

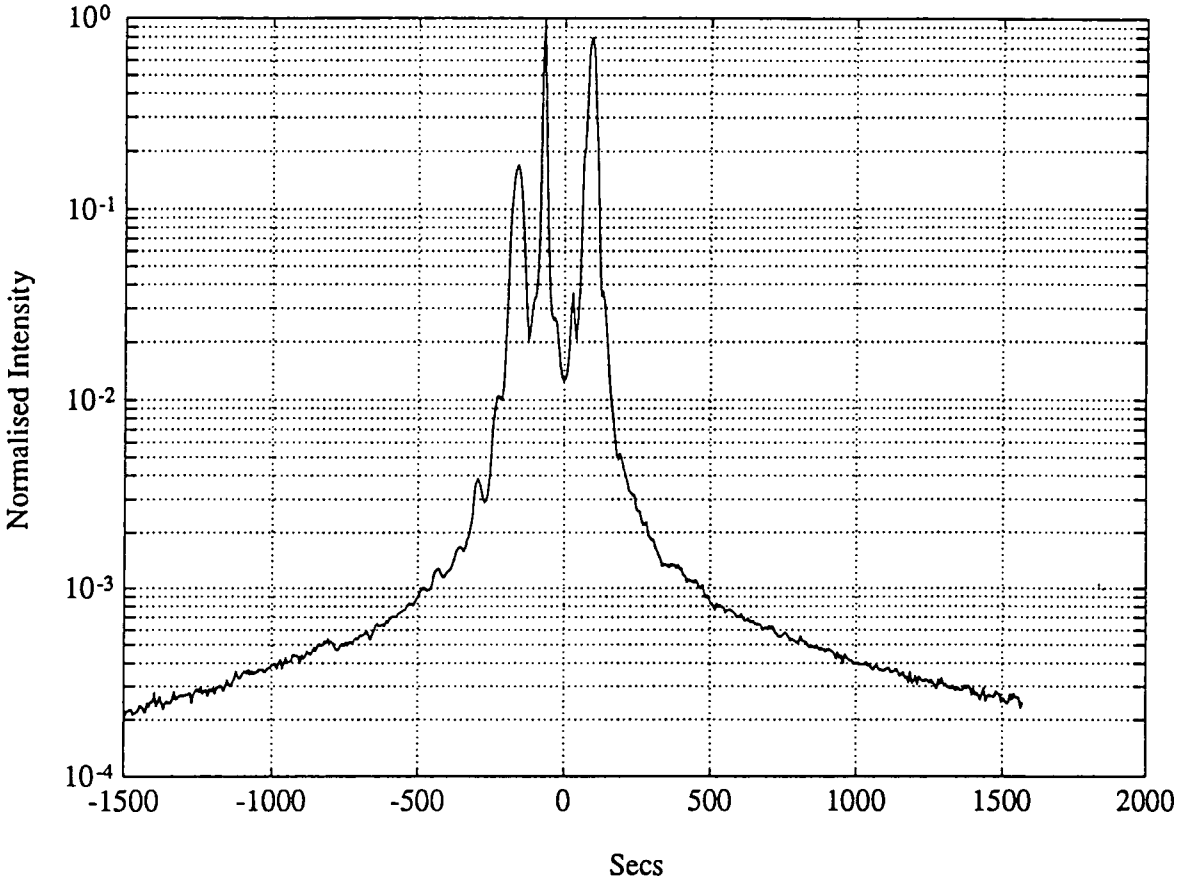

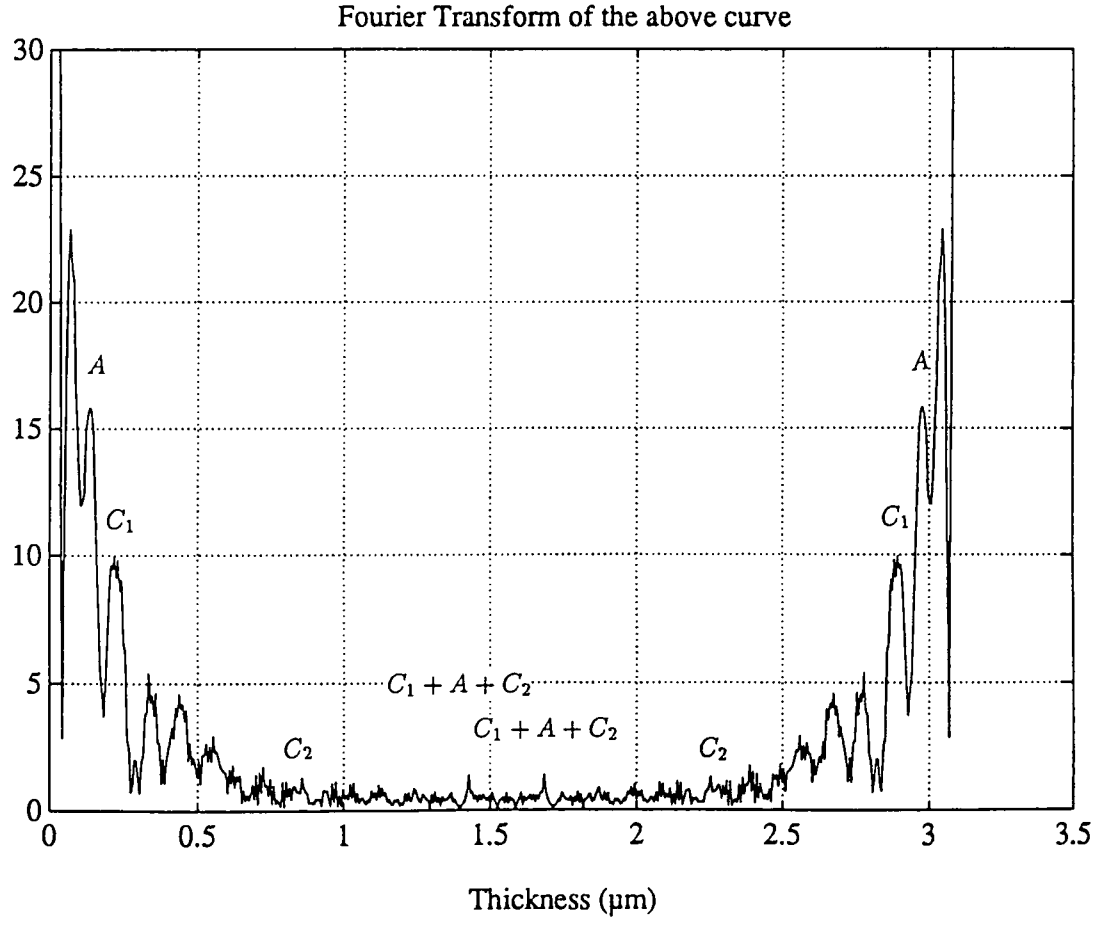

6.5 Summary and Discussion

Moire fringes in electron microscopy have been reported and their observation has enabled dislocations to be studied. In a similar way, Moire fringes have also been observed in Laue (transmission) X-ray topography, where two crystals overlap, and in interferometers where two interfering beams fall on a third analysing crystal. At present the observation of Bragg (reflection) case Moire fringes has not been reported. The reasons for this are principally due to the fact that the upper crystal needs to be very thin and the construction of a Bragg case interferometer by conventional methods is impossible.

The construction of commercial laser structures consisting of a thin active layer sandwiched between two layers of identical composition allows the simultaneous diffraction of two wave fields to be made. The possibility then exists for Moire fringes to be observed in the Bragg geometry.

Two samples were studied, these consisted of an AlGaAs sample on GaAs and an InGaAs sample on InP. The layer thicknesses and exact structural characteristics of these two samples were then made by matching the experimental rocking curves with simulated curves.

Topography at 1.5 $\AA$ radiation using the 004 reflection showed fringes present on the AlGaAs sample but none were observed on the InGaAs sample. The fringes present on the AlGaAs sample were located on the confining layer peak and on the pendellosung fringes located between this peak and the buffer layer peak. No fringes were seen on the buffer layer or the substrate peaks. This observation implies that the origin of the fringes is from the confining layers and not the surface or the buffer layer. The spacing of the fringes allows the assumed Moire dilation or tilt to be calculated. Assuming a pure dilational Moire fringe in which the fringes are produced from a consistent difference in the lattice parameter of the confining layers the mismatch may be calculated using equation 6.17. Using the measured fringe spacing of $60\mu m$ the mismatch between layers is 53ppm. In a similar manner assuming a pure tilt Moire fringe and using equation 6.19, the tilt angle between the confining layers is 2 arc secs.

In order to determine if the fringes were fixed in the surface plane of the crystal

or dependent on the angle of the incident X-ray beam, a series of topographs at different rotations about the sample surface were performed. These results indicated that the fringes did rotate with the sample and were therefore independent of the incident beam angle. The spacing of the fringes was also found to be independent of rotation about the sample surface.

Topography at $1.0\mathring{A}$ using the 004 on the AlGaAs sample revealed a much reduced fringe intensity but with a very similar fringe spacing, while the fringes could not be resolved using the 224 asymmetrical reflection at 1.54 $\mathring{A}$. Since the 004 topograph taken a $1.0\mathring{A}$ showed fringes of a similar spacing to the fringe observed from the 004 topographs taken at $1.5\mathring{A}$ the fringes are not produced from a uniform thickness variation in the active layer.

From the theoretical study it was shown that a uniform variation in thickness or mismatch could produce fringes. To investigate a variation in thickness or mismatch across the sample, rocking curves were recorded along a line over the samples. The results indicated in the AlGaAs sample a variation in either thickness or mismatch of the active layer was present. A similar line scan of the InGaAs sample revealed no detectable variation in the active layer thickness or mismatch. The variation across the AlGaAs sample matched the simulated rocking curves for a $0.07 \pm 0.01\mu m$ variation in thickness or a $4 \pm 0.5\%$ mismatch change. Using equation (6.24) this gives a fringe spacing of $27 \pm 5\mu m$, the error assessment is difficult since one is assuming a uniform variation across the whole sample, which from topographs is strictly not true. However this does support the conclusion that these fringes are not thickness fringes.

The results of the feasibility study into the use of pendellosung fringes for the determination of layer thickness in the samples studied indicated that this should be possible. The complications of a large number of contributing layer frequencies dictates the need for a high (5 orders of magnitude) ratio of signal to noise. Once this has been achieved the fourier transformation should reveal the required layer thickness. The experimental rocking curves obtained on the InGaAs and AlGaAs samples did not have a high enough ratio of signal to noise and therefore the layer thicknesses could not be reliably determined. Recently, this procedure has been

shown to be much more sensitive to layer thickness in highly strain systems (Green et al 1991).

6.5.1 Conclusion

This study has shown that, in theory, Bragg case Moire fringes may be present in X-ray topographs taken from laser structures. These fringes originate from small differences in lattice parameter and/or mismatch between the confining layers of these structures. The possibility of the fringes being produced from a uniform variation in the active layer has also been discussed, but experiments indicate that this is not the case since the fringe spacing appears to remain unchanged at a different wavelength. It is therefore concluded that the fringes may be Bragg case Moire produced from a combination of layer dilation and tilt between the confining layers. However because of difficulties in observing the fringe spacing under different diffraction geometries, this has not been proven definitely.

Chapter VII

The measurement of non-stoichiometry in gallium arsenide and indium antimonide using quasi-forbidden Bragg reflections

7.1 Introduction

Compound semiconductor materials suffer from a higher dislocation and point defect density than silicon. Mounting theoretical and experimental evidence suggests a link between these defects and non-stoichiometry. GaAs is the most widely studied and developed III-V semiconductor material. Promised performance and reliability has, however, been hindered by non-uniform characteristics. Studies using photoluminescence techniques have shown these defects to be complexes of non- stoichiometric origin (Weber et al, 1982). This is consistent with a theoretical analysis carried out by Logan and Hurle (1971). These workers used a thermodynamic model and data taken from lattice parameter measurements of Potts and Pearson (1966) and showed the probability of an existence region during growth of up to 1×10^{19} defects per cm^3, figure 7.01.

The main problem in producing stoichiometric crystals of GaAs is the maintenance of the correct arsenic over- pressure while pulling the seed from the melt. This is because, as the crystal is pulled, the volume of the melt decreases and the temperature varies. Methods of maintaining the melt at the correct temperature for constant growth are therefore required. Automatic computer controlled schemes using buoyancy and empirical corrections allow, with the use of high temperature gradients, a diameter control to within 2%. However, high temperature gradients result in penalties such as a high probability of dislocation generation due to increased thermal stresses. For crystals with a high resolved shear stress, such as Si having a value of 60-150 g mm^2, this is only of secondary concern, while in GaAs the lower value of 4- 40g mm^2 is of major importance. The thermal conductivity of GaAs is low, being $0.54 W cm^{-1} K^{-1}$ compared to that of Si which is $1.4 W cm^{-1} K^{-1}$. As a result large diameter (4-5 inch) Si crystals can be grown

Figure 7.01

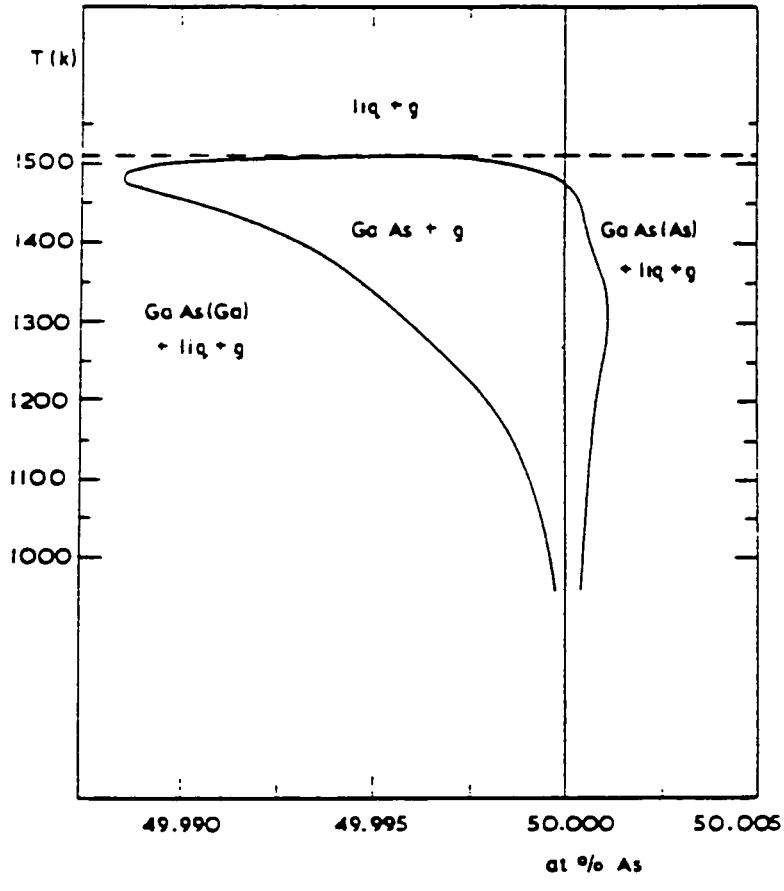

Calculated existence region for GaAs, after Logan and Hurle (1981).

essentially dislocation free, while only small (less than 0.5 inch) GaAs crystals can be grown with comparable perfection (Grabmaier et al, 1972; Steineman et al, 1966). The reduction of thermal gradients in GaAs therefore presents a considerable challenge, particularly in the growth of large diameter wafers. Most of the published work on low dislocation material therefore concentrates on small (less than 0.5 inch in diameter) LEC and HB crystals. Dislocation distributions, as determined by etching, exhibit several features which include:

(1) a minimum in the etch pit density (EPD) observed within a wide annular ring between the centre and edge of the wafer, and;

(2) intermediate EPD values at the wafer centre ,and;

(3) maximum EPD observed at the wafer edge.

Measurements of the dislocation densities then follow a typical 'W' shaped profile.

Morphology studies indicate that at high dislocation densities, typically above 1×10^5 defects cm^{-2}, the distribution of dislocations is an interconnecting cellular network, while at low densities for example below 1×10^5 defects cm^{-2}, the cellular network is not seen (Reed-Hill, 1973). The relationship between dislocation density and melt stoichiometry is still not known, however there is evidence to suggest that the EPD may be minimised provided that the melt stoichiometry is kept within 0.505% and 0.535 $\%As$. Vechten et al (1975) showed that in III-V materials the energy needed to replace atom A with atom B is relatively low so that antisite defects such as an arsenic atom on a gallium site (Ga_{As}) and a gallium on an arsenic site (As_{Ga}) may be readily created. These antisite defects are believed to play a role in the deep level donor EL2 but the exact structure of the defect is still unknown.

Experimental measurements of the carrier concentration of GaAs reveals a delicate balance between defect density populations (Morrow, 1987; Elliott et al, 1984). Investigations of the effect of a variable melt composition on the carrier concentration has revealed that a critical melt composition exists. Below this composition the material is n-type and above this composition the material is p-type becoming semi- insulating in the midpoint, figure 7.02. In the semi-insulating

Figure 7.02

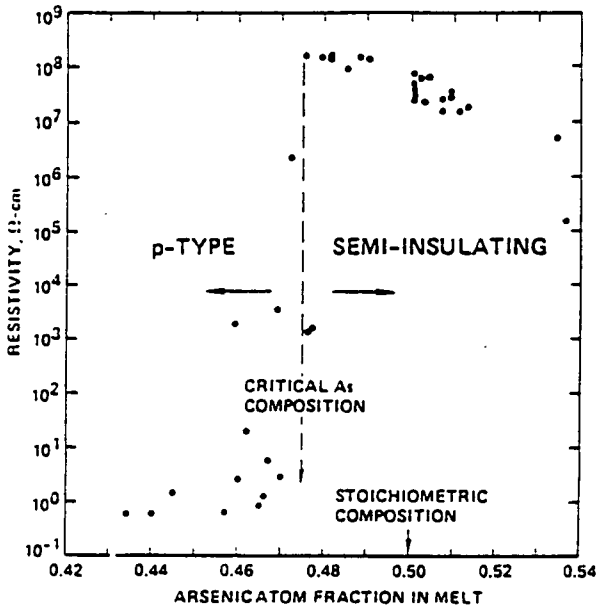

The transition between p-type and semi-insulating GaAs, after Gilmore (1976).

Figure 7.03

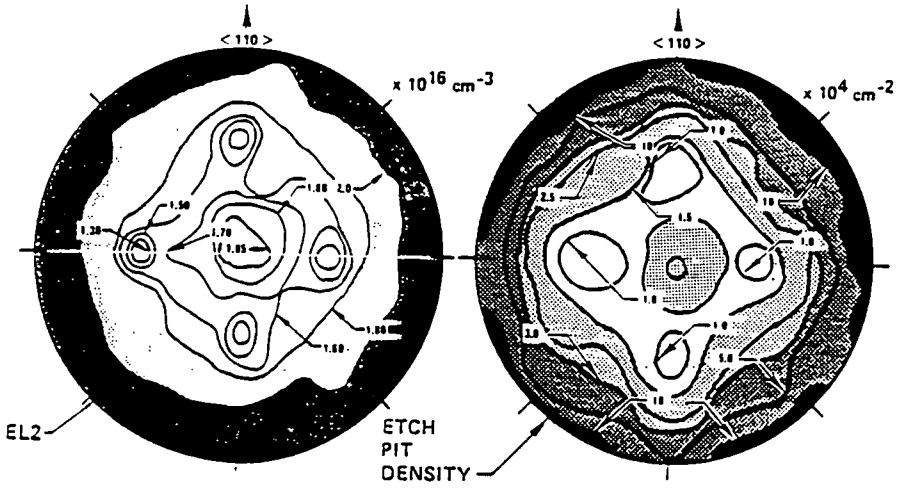

This figure illustrates the distribution of the deep electron trap, labelled EL2 in GaAs, as determined by photoluminescence. The EL2 trap is believed to be made up of a combination of antisite defects and interstitials, after Gilmore (1976).

and p-type region the conductivity is dominated by the deep level donor EL2 and a shallow carbon acceptor, while in the n-type region the carrier concentration is dependent on an unknown acceptor believed to be made up of a boron atom and an antisite defect Ga_{As} (Holmes et al, 1982). It is well established that the composition of the melt is fundamental in determining the concentration of EL2 in the crystal (Holmes et al, 1982). If the melt is too deficient in arsenic, EL2 is not found while in arsenic rich melts it is abundant. The production of semi-insulating GaAs is achieved in the "classically" grown arsenic rich material by compensation of the EL2s by shallow carbon acceptors. It appears that the amount of carbon present in the crystal is determined by the amount of water content in the B_2O_3 liquid encapsulant.

Experiments indicate that the principle energy level of EL2 is E_c -0.77eV, with a second level at E_v +0.45eV (Weber et al, 1982) in semi-insulating material while in p- type material this level is E_v +0.54eV. The radial distribution of EL2 has also been investigated by Martin et al (1980). It has been observed that the EL2 profile follows a characteristic 'W' pattern, similar to the dislocation distribution, figure 7.03. While the defect EL2 is of major importance in semi- insulating material, equal importance has to be given to an unknown dominant acceptor concentration in p-type material. The composition of this acceptor is again not known. However, work undertaken by Elliott (1983) has indicated energy levels of E_v +0.0078eV and E_v +0.1002eV in p-type material. From photoluminescence studies this acceptor is believed to consist of a boron atom and an arsenic antisite at the low energy level, and a gallium on an arsenic site at the higher energy level. The production of substrate material with a required carrier concentration depends on the amount of each type of defect present. While the structures of many of these defects remain unknown the reduction of defect densities can not be readily achieved. The delicate balance between EL2 and acceptor concentrations in semi- insulating material must be maintained if the expansion of this material in the integrated circuit market is to be achieved.

7.2 Characterisation of non-stoichiometry

From the above discussion it is clear that the ability to measure the concentration of gallium and arsenic in GaAs, as well as the concentration of antisite and

vacancy defects, would be of significant importance in understanding defects in this material. Several methods have been developed with this objective in mind. These include coulombic titration, lattice parameter measurements, ion beam scattering and electron probe micro analysis (EPMA).

7.2.1 Coulombic titration

Jordan et al (1974) have investigated the concentrations of group III and group V elements in semiconductor compounds using coulombic titration techniques. This technique measures the mole fraction of one of the elements by dissolving that element in a solution and then applying a reagent which produces a measurable amount of charged ions, these ions being then detected by a potentiometer. Experiments undertaken on gallium phosphide (GaP) have indicated an existence region similar to that predicted by Logan and Hurle (1971) for GaAs during growth, figure 7.04. Coulombic titration has a number of limitations which include the destruction of the sample and the lack of information obtained on the structural nature of the defects as only the relative percentages of the constituent atoms can be determined.

7.2.2 Lattice parameter measurements

The fact that variations in composition lead to variations in lattice parameter has led to attempts to measure accurately the lattice parameters of III-V materials. Using powder X-ray diffraction methods, Straumanis and Kim (1965) noted that the lattice parameters obtained from samples of GaAs grown under various gallium and arsenic over pressures were different. These measurements indicated that an arsenic rich region of width 0.01 % As exists in the crystalline material suggesting that many of the defects calculated theoretically are present in the solid. Similar lattice parameter variations have also been determined by the Kossel Line and Bond techniques used by Potts and Pearson (1966). From these measurements the largest variations in stoichiometry where found to exist in samples annealed at the maximum melting point. Following subsequent annealing a decrease in the lattice parameter was observed and this took place in two stages. The first was a rapid stage thought to be associated with the recombination of arsenic vacancies and the second much slower stage could be described by arsenic vacancy

Figure 7.04

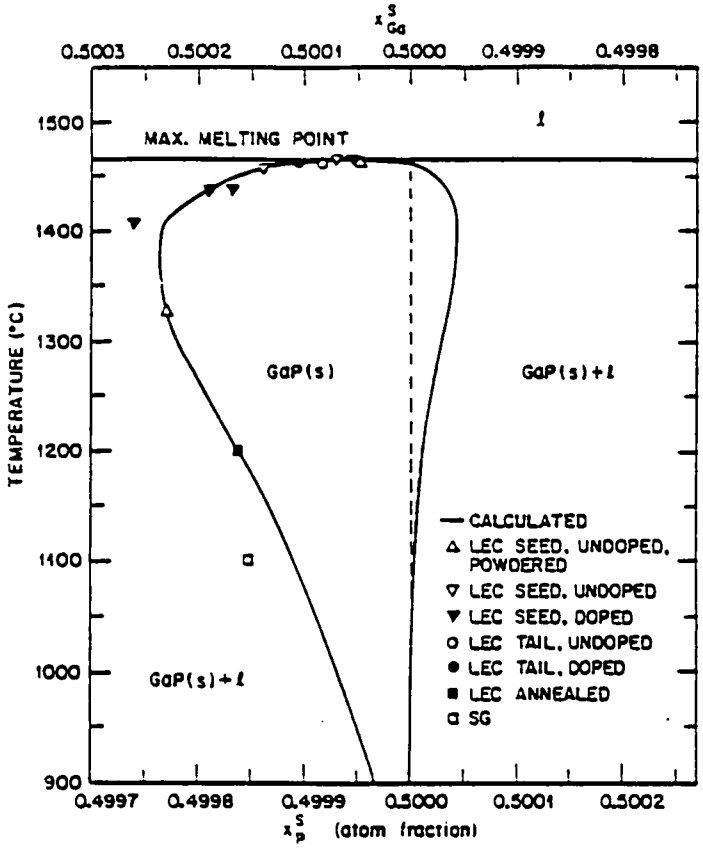

This figure illustrates the solidus of GaP. The data represents the growth or annealing temperature of GaP crystals vs the Ga concentration found by coulombic analysis, after Jordan et al (1964).

diffusion. The Bond method employed in these measurements requires an X-ray Bragg diffraction peak to be recorded at two positions; from the difference in these two positions the lattice parameter can be calculated. This requires an accuracy of 0.25 arc sec to detect a lattice parameter variation of 0.1ppm (Bond, 1960). Willoughby et al (1971) have produced results on lattice parameter variations of both HB and LEC grown crystals, these measurements indicate variations of 1ppm across typical HB material and up to 10ppm in LEC samples in arsenic rich material. Adaptations of the Bond method have been described recently which allow lattice parameter determinations to be made much more quickly and over a smaller angular range (Fukumori et al, 1982; Fatemi, 1989). The measurement of the lattice parameter of a material does not, however, give a direct insight into the range of non-stoichiometry. Variations in dislocation density are also accompanied by a variation in the lattice parameter and therefore point defect densities can not be related directly to lattice parameter measurements.

7.2.3 Ion beam scattering

Kudo et al (1979) has studied stoichiometry in GaAs using 15MeV He^{++} ion beam backscattering. A detected loss in the arsenic concentration could only be measured following heating of the sample. Results indicate a constant departure from stoichiometry at temperatures higher than 200-300^oC increasing gradually until the sublimation point of arsenic is reached at 610^oC. This technique is limited in accuracy relying on precise determination of the differential scattering cross sections of gallium and arsenic.

7.2.4 Electron probe micro analysis (EPMA)

Electron probe micro analysis (EPMA) techniques have been employed to study stoichiometry in GaAs polycrystalline films (Kudo et al, 1979). This technique uses an electron beam with an energy typically in the range 5-30KeV to excite characteristic X-rays when incident on the surface of a material. Energy dispersive X-ray analysis (EDX), in which the output signal from the detector is proportional to the energy of the incident X-rays, is required to measure a variation in stoichiometry. A semi-quantitative measurement of stoichiometry can then be made by measuring the integrated intensity of the peaks obtained. Detection

limitations imposed by counting statistics allow measurement of trace elements to 100ppm yet the relative amounts of these materials can only be determined to between $1-2\%$. The measurement of two large concentrations such as the amount of gallium and arsenic in GaAs cannot therefore be made accurately enough in crystalline material.

7.2.5 Summary

From the previous discussion of the main techniques currently available for non-stoichiometry determination, it is clear that the study of an existence region 0.01% wide presents major difficulties. Lattice parameter and coulombic measurement allow an indication of the ratio of the constituent atoms to be made, while EPMA and backscattering allow the concentration of impurities to be determined. However there is no relatively straight forward method of characterisation with sufficient accuracy. Fujimoto (1984; 1987) has described a technique measuring the stoichiometry of GaAs using quasi-forbidden Bragg reflections. In the following study this approach will be developed and an investigation into the behaviour of the integrated intensity with wavelength made using the synchrotron source at Daresbury, U.K. Measurements on LEC and HB grown GaAs have been made and the study has also been extended to include indium antimonide (InSb).

7.3 Stoichiometry measurements using Bragg reflections

The integrated intensity of a Bragg reflection is dependent on its structure factor. The structure factor is a phase relationship between atomic scattering factors of the constituent atoms. In principle then, departures from the perfect crystal are reflected in the scattered intensity. In practice however, this intensity is dependent on several other factors including the wavelength at which diffraction takes place and whether it can be regarded as kinematical or dynamical.

In perfect crystals the intensity of a Bragg reflection can vary greatly depending on the proximity to an absorption edge. Close to an edge this can have the effect of making a strong reflection weak, resulting in a transition from dynamical to kinematical diffraction. It is also important to realise that although the integrated intensity of a reflection can be independent of global small changes in the lattice parameter, it can be very strongly dependent on the mosaic distribution within the

crystal. Therefore care is required in ascribing absolute changes in the integrated intensity to variations in the crystal lattice.

The integrated intensity of a Bragg reflection may be calculated according to the dynamical diffraction theory of Ewald and von Laue (James, 1948; Zachariasen, 1945). The integrated intensity of a reflection is then given by

$$I_H = \frac{\partial\theta}{\partial y} R_H^y \tag{7.01}$$

where θ is the angle between the Bragg planes and the incident X-ray beam and R_H^y is the integrated intensity on the y scale and θ_b is the Bragg angle. The parameter y is given by

$$y = \frac{[\frac{1}{2}(1-b)\psi_0' + b(\theta_b - \theta)\sin 2\theta_b]}{|b|^{1/2} C |\psi_H'|} \tag{7.02}$$

where ψ_o' is the real part of the susceptibility and ψ_H' is the real fourier component ofthe susceptibility. The factor b is a factor dependent on the geometry of the reflection; for a symmetric reflection $b = -1$. C is the polarisation factor and is equal to 1 if the electric vector is perpendicular to the plane of incidence or to $|cos2\theta_b|$ for the other state. For a symmetric Bragg reflection

$$\frac{\partial\theta}{\partial y} = \frac{C}{sin2\theta_b}\left(\frac{e^2}{mc^2}\right)\frac{N\lambda^2}{\pi}|F_H'|. \tag{7.03}$$

where F_H' is the real part of the structure factor and N is the number of atoms per unit cell. There is some difficulty in evaluating R_H^y, but for the case of a centrosymmetric crystal a very close approximation is given by

$$R_H^y = ((\pi/4)[1+\kappa^2]/|g|) + exp\left(-(1+\kappa^2)^2[|g| + K]\right) \tag{7.04}$$

where

$$|g| = \frac{\mu/\lambda}{2K(e^2/mc^2)N|F_H'|} \tag{7.05}$$

and μ is the linear absorption coefficient and K is equal to $ln(32\pi)$. If there is no absorption (i.e. $\mu = 0$) then $|g| = 0$ and the equation reduces to

$$I_H = \left(\frac{e^2}{mc^2}\right)\left(\frac{1+|cos2\theta|}{2}\right)\frac{N\lambda^2}{sin2\theta}\frac{8}{3\pi}|F_H'| \tag{7.06}$$

which is the Darwin-like formulation for a perfect, non- absorbing crystal.

If $|g|$ is large we have

$$I_H = \left(\frac{e^2}{mc^2}\right)^2 \left(\frac{1+|cos^2 2\theta|}{2}\right) \frac{N^2\lambda^3}{sin2\theta} \frac{|F_H|^2}{2\mu} \tag{7.07}$$

where F_H is the full complex structure factor. This formula represents the integrated intensity from a mosaic crystal.

It can therefore be seen that the strong reflections of a perfect crystal become weaker close to an absorption edge and diffract like a mosaic crystal when $|g|$ is large. The diffracted intensity for strong reflections from a perfect crystal therefore depend on $|F'|$ whereas weak reflections from the same crystal depend on $|F|^2$. For an imperfect crystal, the integrated intensity is proportional to $|F|^2$ for all reflections. The intensity of a weak reflection is therefore much less sensitive to the structural perfection of the crystal than that of a strong reflection. Freund et al (1980) studied the integrated intensity of the 222 reflection from Cu single crystals of various dislocation densities with wavelengths ranging from 0.03 -1.66$\mathring{A}$. Using the 222 reflection it was shown that real crystals diffract varying from near dynamic to near kinematic across the wavelength range with a reflecting power dependent on the dislocation density. The variation of the integrated intensity with wavelength for a particular value of g can only therefore be interpreted as variations in stoichiometry and not dislocation density if the choice of reflection is made so that the crystal diffracts independently of dislocation density. This can be interpreted from dynamical theory as choosing a reflection which has an extinction distance much larger than the thickness of the sample under study. Table 7.01 gives the extinction distances for the 002 and 004 reflections for gallium arsenide.

In the region of an atomic absorption edge, the scattering factor of that atom is highly wavelength dependent. Corrections due to this anomalous dispersion must be taken into account when calculating the structure factor of a reflection at wavelengths close to an absorption edge of any of the atoms present in the crystal.

7.4 Calculations of anomalous dispersion corrections

In chapter 2 anomalous dispersion corrections were briefly introduced as cor-

Wavelength $\AA$	Extinction distances μm in GaAs	
	004	002
1.54	12	468
0.70	26	1000

Table 7.01. This table gives the extinction distances for the 004 and 002 reflections, assuming an 001 surface and sigma polarisation.

rections to the free atomic scattering factor expression. In the work that follows these corrections are used extensively and as such require a detailed discussion, which is given in appendix B .

The classical theory of anomalous dispersion was developed in the 1930's by Honl. This model was later extended to allow higher electron shells to be considered. The approach taken by Parratt and Hempsted (1954) related the real anomalous dispersion correction to the absorption cross section by an empirical expression. Fundamentally new calculations of anomalous dispersion corrections were made by Cromer and Liberman (1970) using the calculations of Brysk and Zerby (1968). Comparison of experimental anomalous dispersion corrections have been made by a number of workers. Studies on LiF undertaken by Creagh and Hart (1970) interferometrically and by Hart and Siddons (1981) on zirconium and niobium have aided the development of Cromer and Lieberman calculations. Figure 7.05 shows the experimentally determined real anomalous dispersion corrections of zirconium (Hart and Siddons, 1981) together with the values calculated theoretically using the Honl and Cromer-Lieberman models. In the Honl model at very long wavelengths the real part of the scattering factor, f' approaches the value of$-g_k$, (where g_k is the oscillator strength) while the imaginary contribution is zero and at very short wavelengths the scattering factor has only very small anomalous dispersion corrections. The classical picture corresponds to the oscillators undergoing forced oscillations with a frequency much smaller than any natural frequency. As the wavelength increases from zero the real correction decreases very slowly at first and then much more rapidly as the absorption edge is approached. In this region the equations given are not valid as damping has not been taken into account. This can be corrected and has been discussed by Parratt and Hempsted (1954). For wavelengths less than the absorption edge the scattering factor is less than f_o (where f_o is the value of the scattering factor far from the region of an absorption edge).. For wavelengths just greater than the absorption edge f' is again large and negative and rises rapidly approaching the oscillator strength. The imaginary part of the scattering factor, f'' rises gradually from very short wavelengths and then undergoes a very sharp transition to zero. This transition is attributed to the discrete nature of the energy level. That is as the energy level is approached absorption will only occur for energies larger than a certain value given by the energy level of the K shell. The Honl model gives values of the real

Figure 7.05. The Honl and Cromer and Liberman (1981) models, compared to the experimental values measured using interferometry by Hart (1970).

Triangles indicate experimental values of Hart.

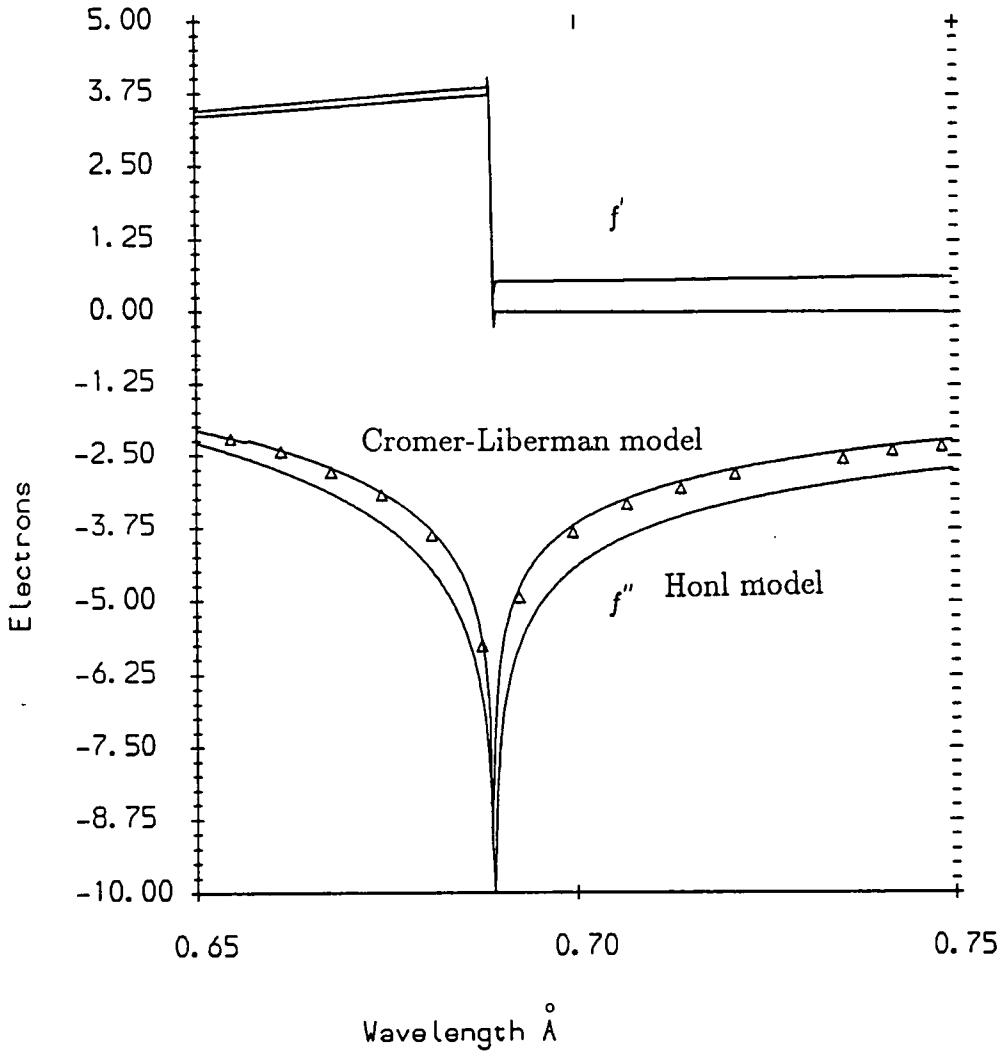

part of anomalous dispersion correction which are larger than the experimentally determined ones for both zirconium and niobium. The discrepancy is substantially worse in the region of the absorption edge. The Cromer and Liberman model is considerably closer to the experimental values over the whole wavelength range.

7.4.1 The Cromer-Liberman program

A copy of the Cromer-Liberman program, referenced in the international tables, was acquired from Professor M.Hart, University of Manchester. This program required modification to accommodate a larger number of data points and so that it could be run on the AMDAHL system at Durham. A full program listing is given in appendix D and it has been modified to accommodate 500 wavelength steps. The theory used in the program can be found in Cromer amd Liberman (1970). In this approach the full relativistic equation of the scattering of a bound electron is considered. This expression is then broken down into the components, which allows those terms which are regarded as small to be evaluated in a non-relativistic way. The remaining relativistic terms are evaluated using the absorption cross sections of Brysk and Zerby (1968). In the following work the calculated anomalous dispersion corrections for GaAs and InSb are used. Figures 7.06, 7.07, 7.08 and 7.09 show the real and imaginary anomalous dispersion corrections for gallium, arsenic, indium and antimony respectively and these are listed in appendix C.

The calculation of the intensity of a Bragg reflection requires the structure factor to be considered, in which the atomic scattering factors are related to the phase of the given reflection. Using the anomalous dispersion corrections discussed above the expressions for the structure factor of both weak and strong reflections will now be discussed.

7.5 The structure factor for strong and weak reflections

The calculation of the structure factor of compound materials is usually achieved by taking the values of the free atomic scattering factors of the constituent atoms. This approach however ignores the effect of the change in the electronic distribution in the compound material. To consider this contribution, the electronic density must be evaluated and the degree of ionicity determined. Once this has

Figure 7.06

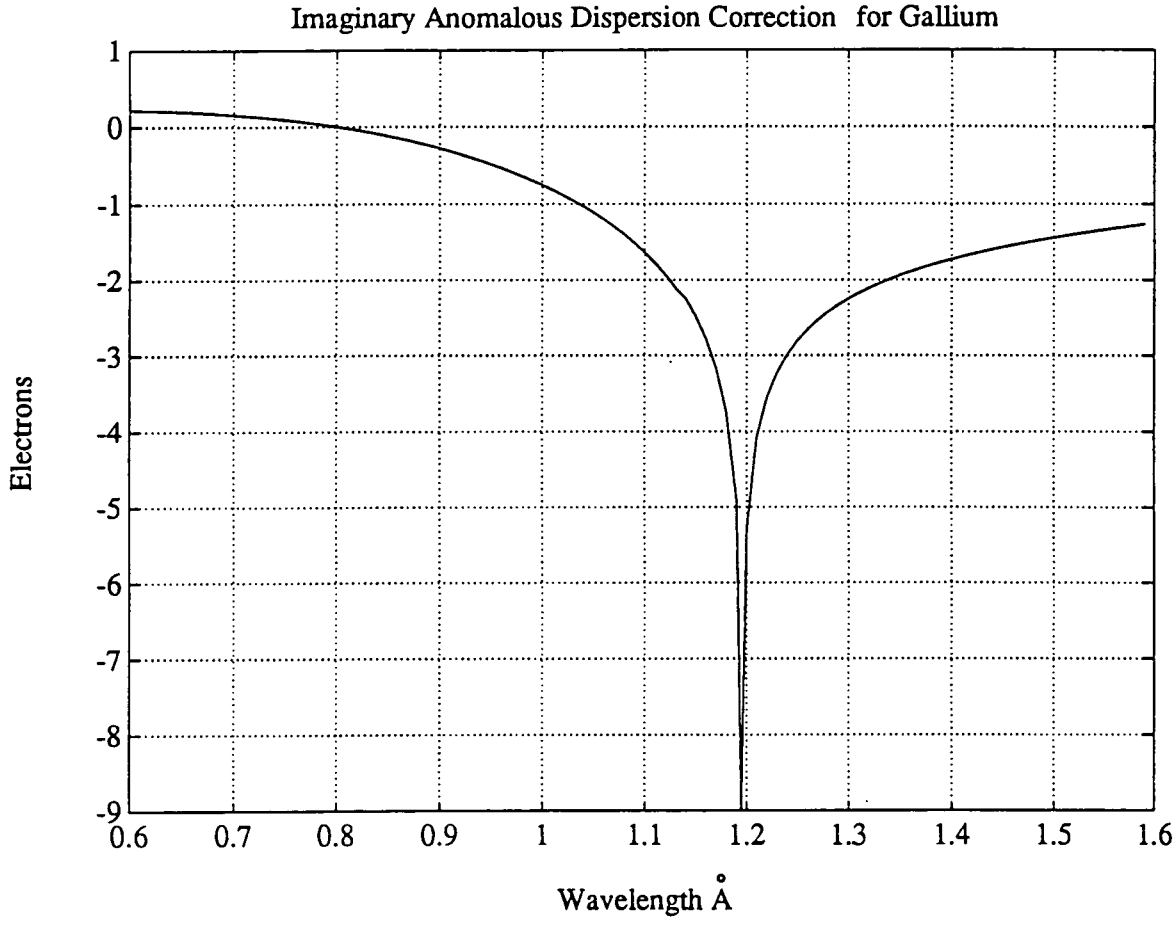
Imaginary Anomalous Dispersion Correction for Gallium
Electrons
1
0
-1
-2
-3
-4
-5
-6
-7
-8
-9
0.6
0.7
0.8
0.9
1
1.1
1.2
1.3
1.4
1.5
1.6
Wavelength Å

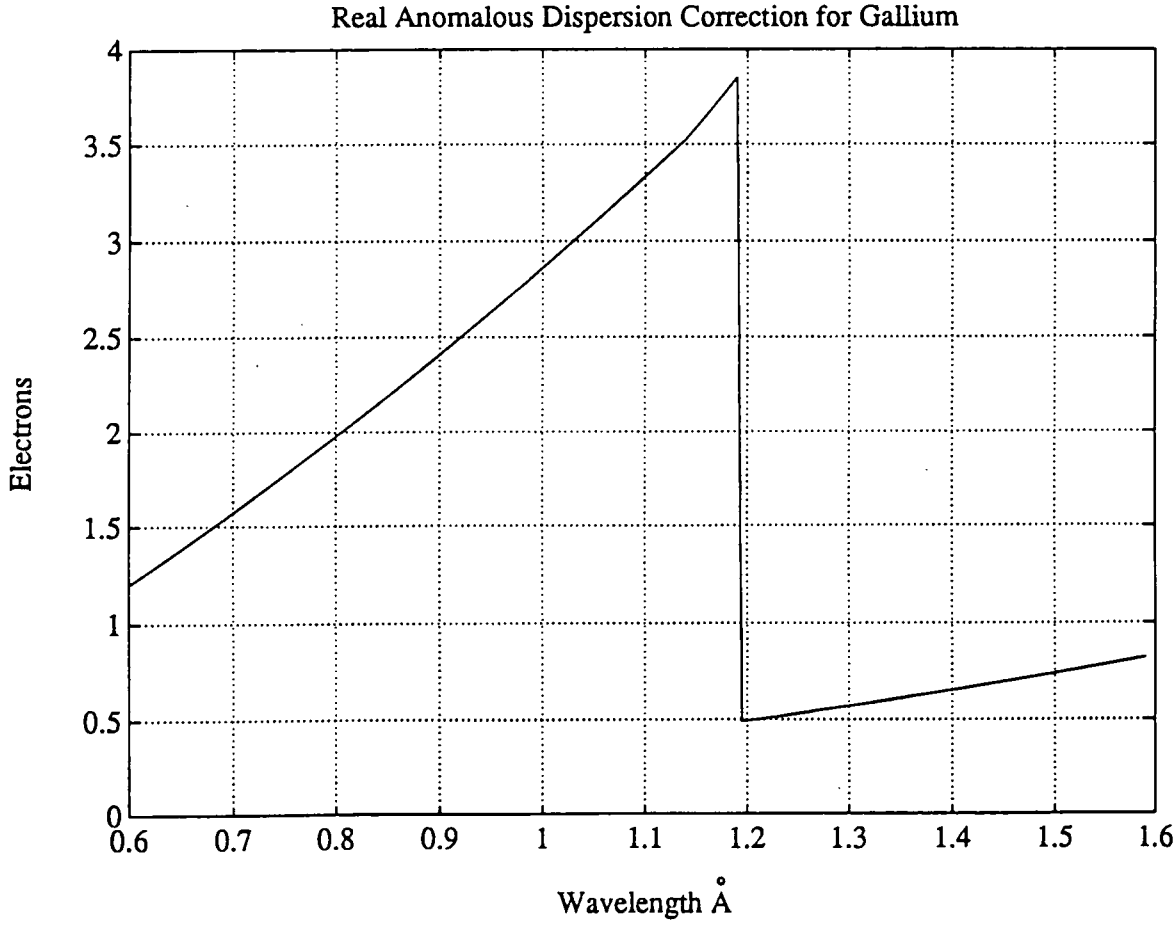
Real Anomalous Dispersion Correction for Gallium
Electrons
4
3.5
3
2.5
2
1.5
1
0.5
0
0.6
0.7
0.8
0.9
1
1.1
1.2
1.3
1.4
1.5
1.6
Wavelength Å

Figure 7.07

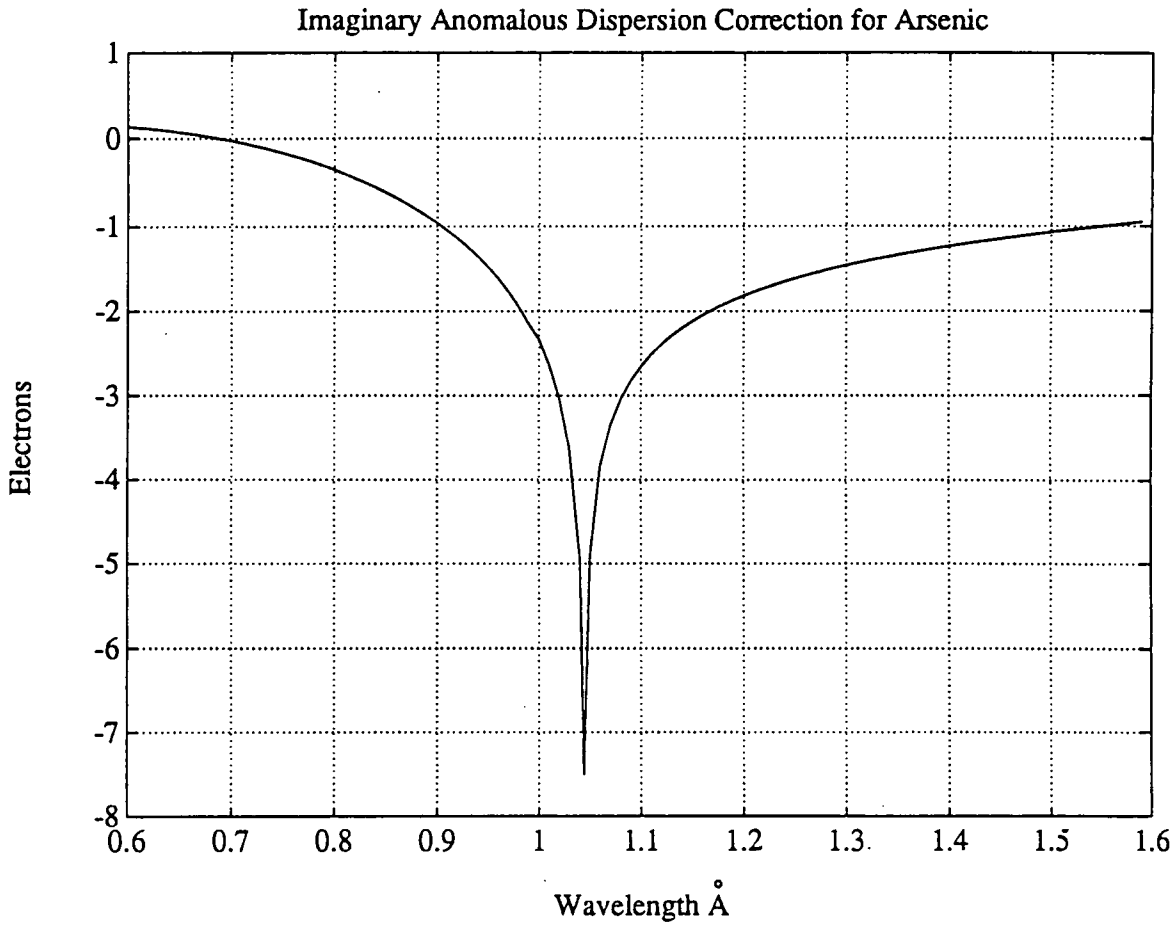
Imaginary Anomalous Dispersion Correction for Arsenic
Electrons
1
0
-1
-2
-3
-4
-5
-6
-7
-8
0.6
0.7
0.8
0.9
1
1.1
1.2
1.3
1.4
1.5
1.6
Wavelength Å

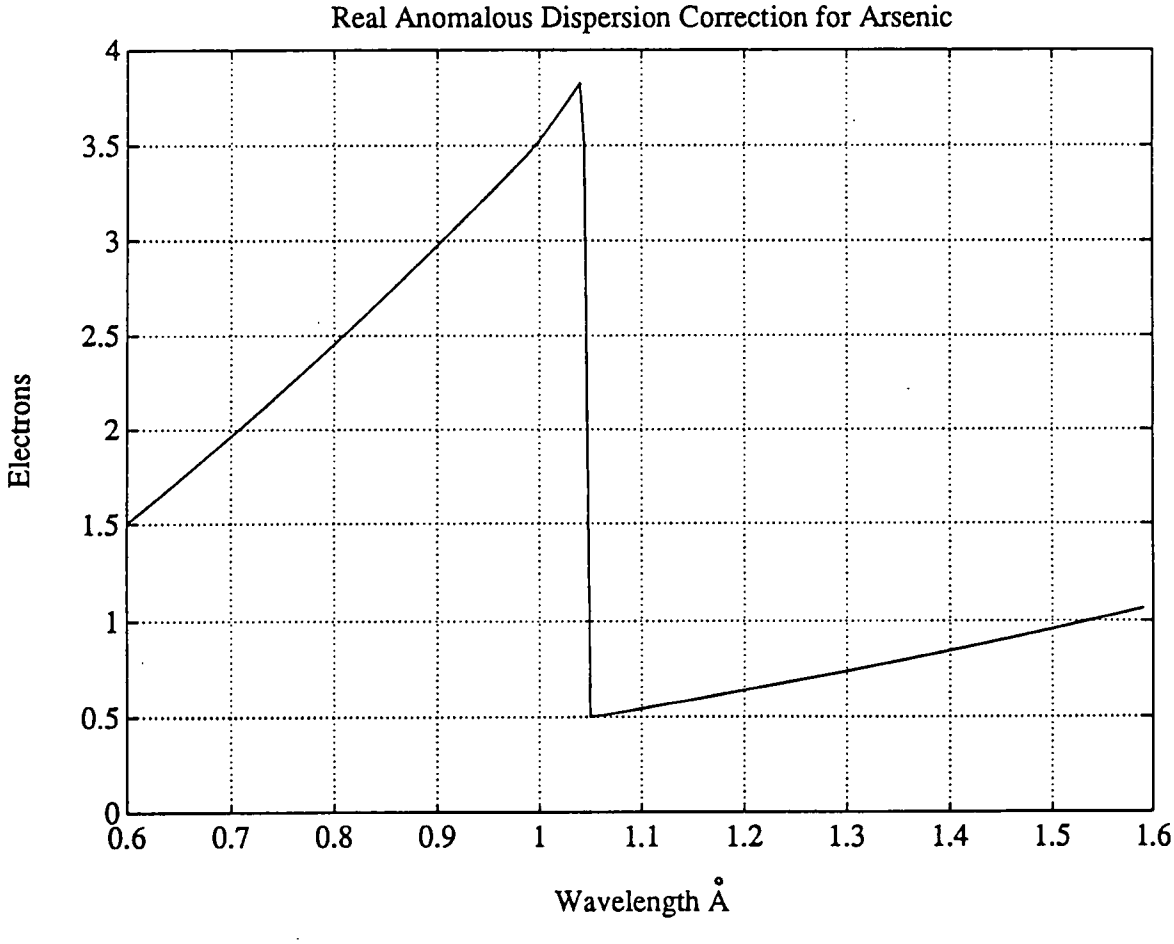
Real Anomalous Dispersion Correction for Arsenic
Electrons
4
3.5
3
2.5
2
1.5
1
0.5
0
0.6
0.7
0.8
0.9
1
1.1
1.2
1.3
1.4
1.5
1.6
Wavelength Å

Figure 7.08

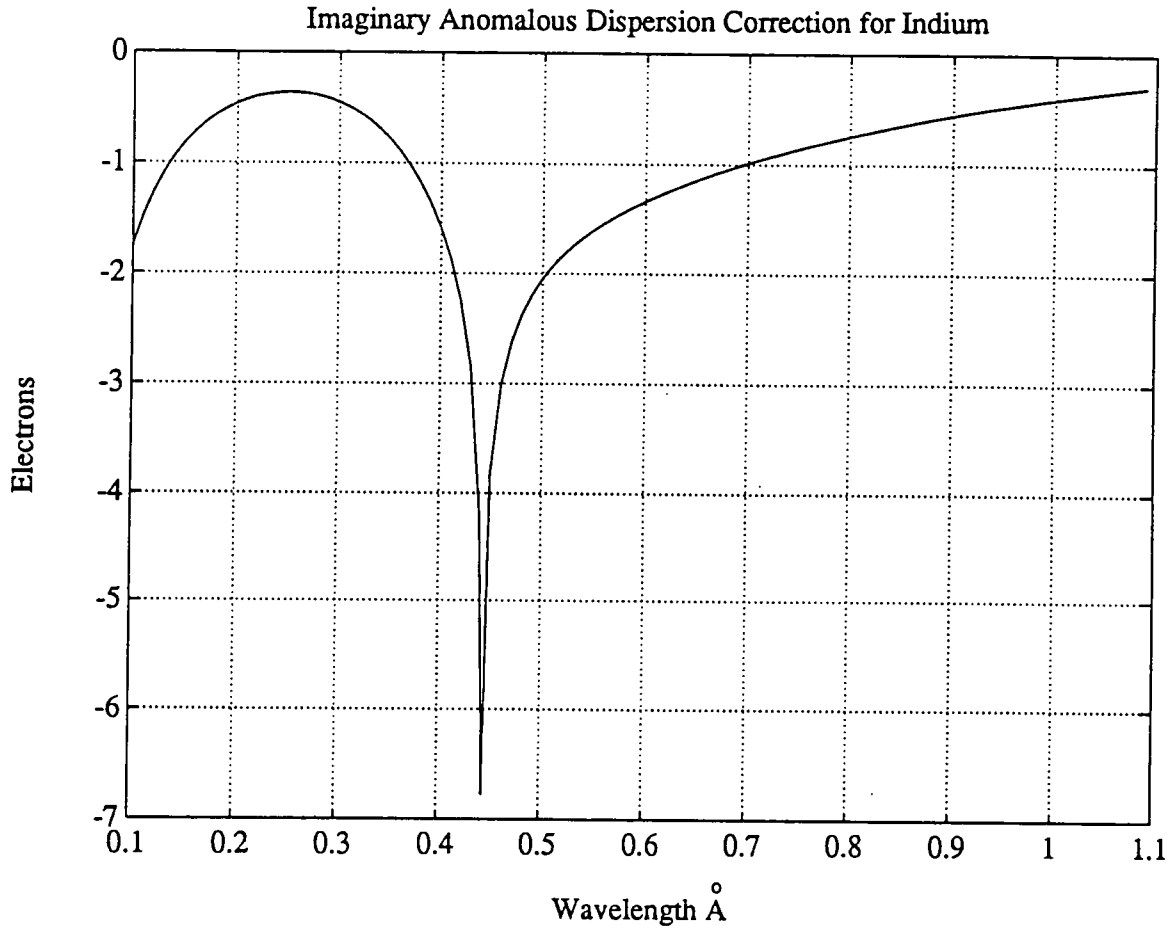
Imaginary Anomalous Dispersion Correction for Indium
Electrons
0
-1
-2
-3
-4
-5
-6
-7
0.1
0.2
0.3
0.4
0.5
0.6
0.7
0.8
0.9
1
1.1
Wavelength Å

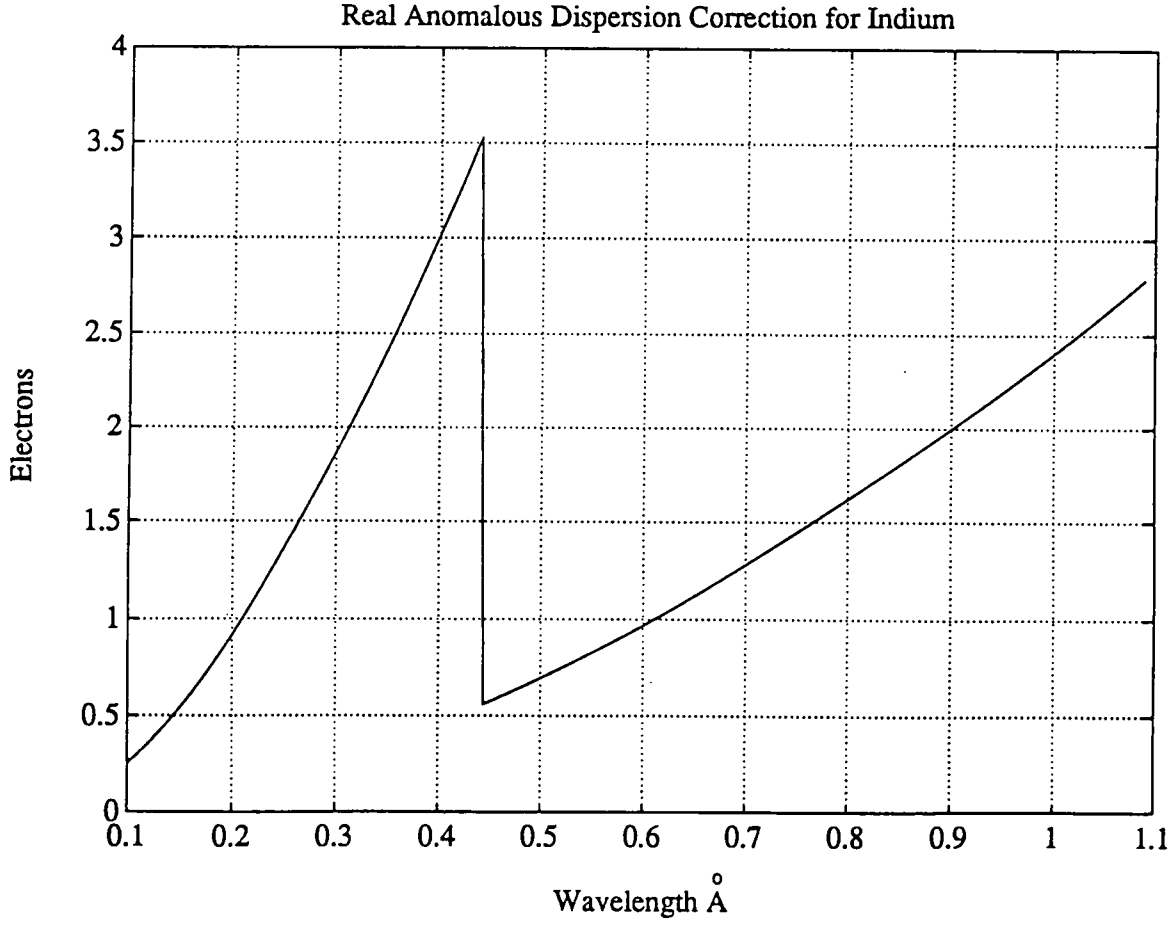
Real Anomalous Dispersion Correction for Indium
Electrons
4
3.5
3
2.5
2
1.5
1
0.5
0
0.1
0.2
0.3
0.4
0.5
0.6
0.7
0.8
0.9
1
1.1
Wavelength Å

Figure 7.09

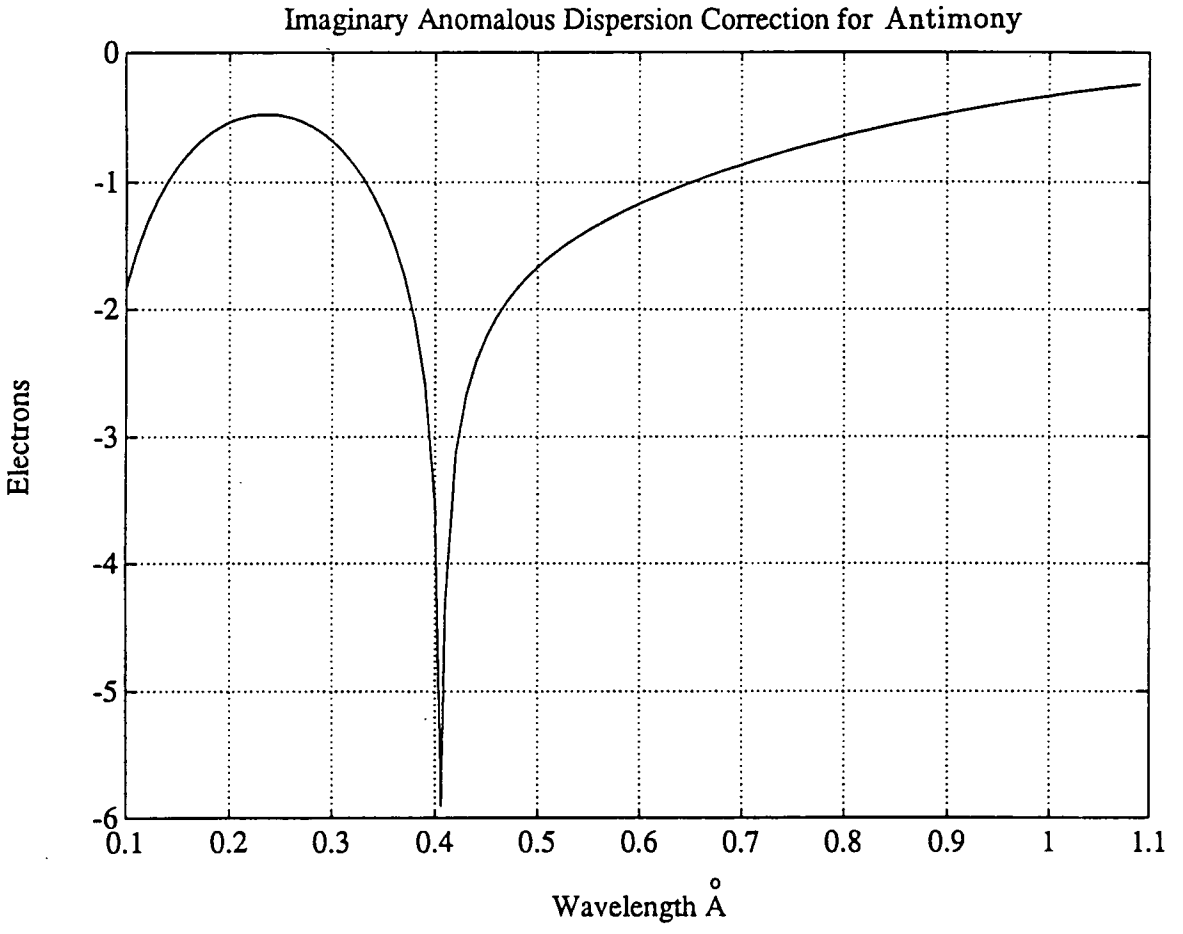
Imaginary Anomalous Dispersion Correction for Antimony
Electrons
0
-1
-2
-3
-4
-5
-6
0.1
0.2
0.3
0.4
0.5
0.6
0.7
0.8
0.9
1
1.1
Wavelength Å

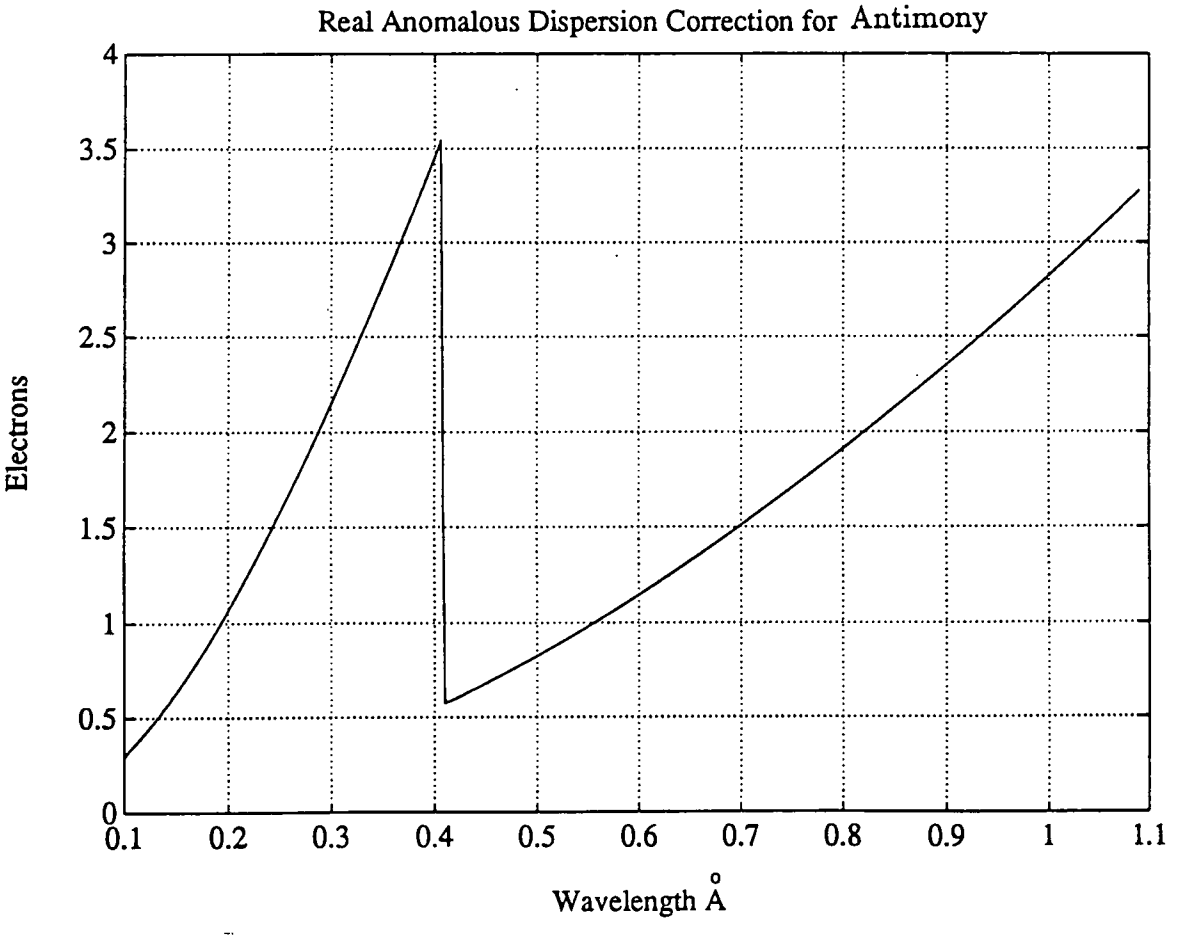
Real Anomalous Dispersion Correction for Antimony
Electrons
4
3.5
3
2.5
2
1.5
1
0.5
0
0.1
0.2
0.3
0.4
0.5
0.6
0.7
0.8
0.9
1
1.1
Wavelength Å

been achieved the ratio of the ionic and covalent contributions to the total scattering factor can be calculated. A net charge transfer from the cation to the anion takes place in the case of GaAs and InSb with the result of creating an interstitial concentration of charge along the bond between near neighbours. Such a model originally proposed by Ewald and Honl in 1936 was used to explain non zero intensity in the 222 reflection from diamond. More recently Walter and Cohen (1975) have calculated valency electron charge distribution maps for a number of semiconductor compounds. Figures 7.10, 7.11 and 7.12 show the valency band distributions for Ge, GaAs and InSb respectively. When viewing these figures it is important to realise that these zincblend structures have 4 nearest neighbours arranged tetrahedrally with a total of 8 electrons per primitive cell. The most noticeable feature is the piling of charge on the cation and the reduction in tetragonal symmetry when going from Ge to GaAs or InSb.

Bilderback and Colella (1976) have studied the non- symmetrical nature of the bonding in III-V semiconductors by using quasi- forbidden reflections. In this approach the measured structure factors are compared with those calculated via models which included the relativistic model mentioned previously as well as a tetragonal model, the latter having been shown to give good agreement with experimental results. Interestingly the departure from the structure factors calculated using the spherical model is large. Within this work it was pointed out that the intensity difference between the 222 and the $\bar{2}\bar{2}\bar{2}$ is solely due to the asymmetry of the bond. To obtain some quantitative measure of the degree of covalency in these materials Walter and Cohen (1975) deduced values of 0.146 for Ge, 0.080 for GaAs, 0.091 for InSb and 0.027 for CdTe, the larger the number the more covalent the bond.

In the following equations the values of the atomic scattering factor f are those of the free atomic scattering factors.

The structure factor is an expression of the atomic positions and is given by

$$F_{hkl} = \sum_n f_n e^{2\pi i \underline{h}.\underline{r}} \tag{7.08}$$

For the sphalerite type lattice common to many compound semiconductors this reduces to four simple forms, given by:

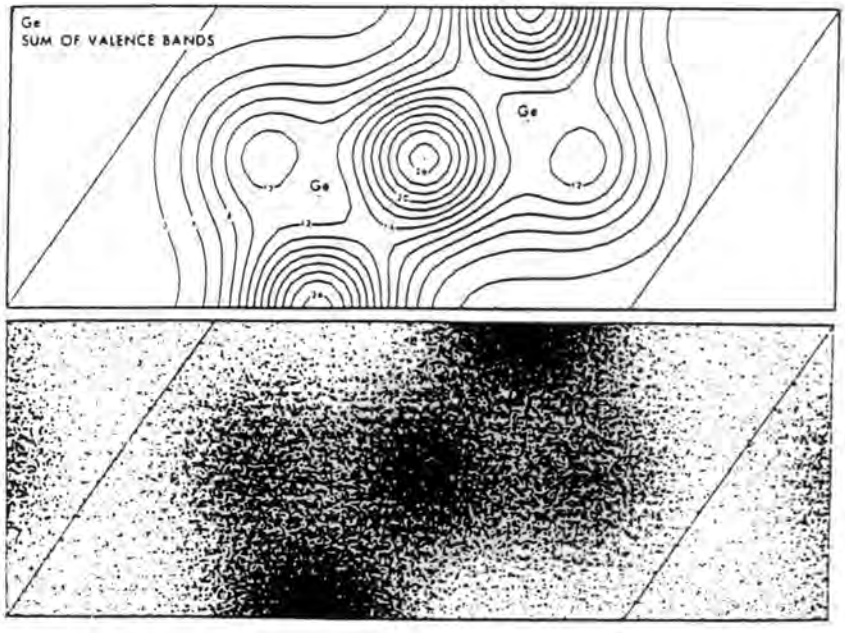

Figure 7.10 Valency charge density map for Germanium. The units are in $\frac{e}{\Omega_e}$ where Ω_e is the volume of a unit cell. After Walter and Cohen (1975).

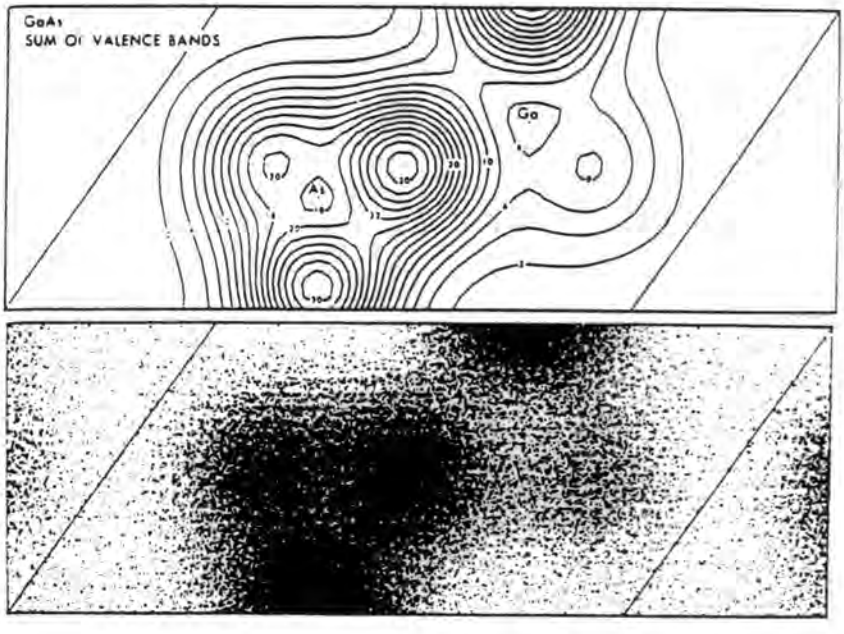

Figure 7.11 Valency charge density map for GaAs. The units are in $\frac{e}{\Omega_e}$ where Ω_e is the volume of a unit cell. After Walter and Cohen (1975).

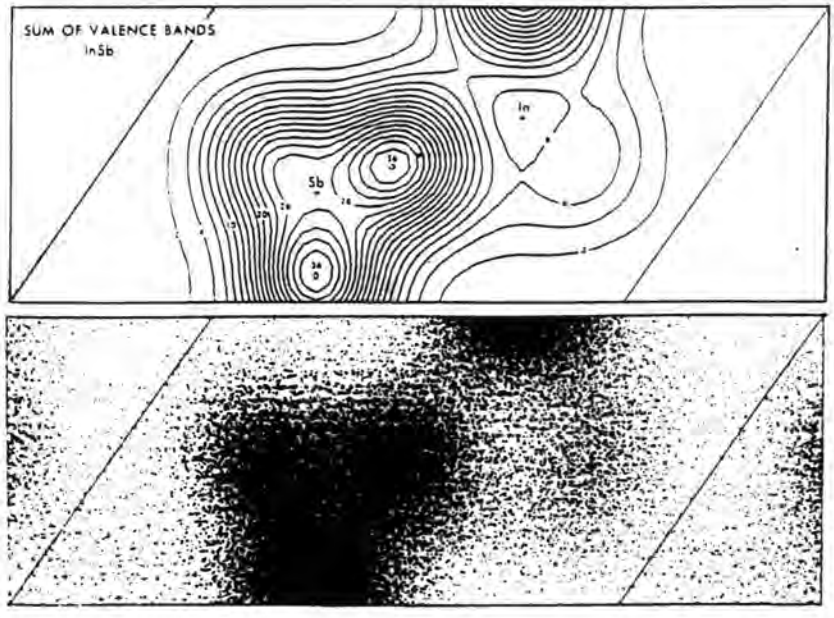

Figure 7.12 .Valency charge density map for InSb. The units are in $\frac{e}{\Omega_e}$ where Ω_e is the volume of a unit cell. After Walter and Cohen (1975).

$$h+k+l=4n \qquad F_{hkl}=4(f_A+f_B) \tag{7.09}$$

$$h+k+l=2(2n+1) \qquad F_{hkl}=4(f_A-f_B) \tag{7.10}$$

$$h,k,l \ \ all\ odd \qquad F_{hkl}=4(f_A^2+f_B^2)^{\frac{1}{2}} \tag{7.11}$$

$$h,k,l \ \ mixed \qquad F_{hkl}=0 \tag{7.12}$$

For a strong reflection such as the 004, the structure factor in GaAs takes the form

$$F=4[f_{Ga}+f_{As}] \tag{7.13}$$

which becomes

$$F=4[f_{Ga}+f'_{Ga}+if''_{Ga}+f_{As}+f'_{As}+if''_{As}] \tag{7.14}$$

when the anomalous dispersion corrections are included. Since the reflection is strong, the integrated intensity is proportional to $|F'|$, and may be written as

$$I \propto 4\left([f_{Ga}+f_{As}+f'_{Ga}+f'_{As}]^2+[f''_{Ga}+f''_{As}]^2\right)^{1/2} \tag{7.15}$$

This expression is represented for a range of wavelengths in figure 7.13 for GaAs and figure 7.14 InSb.

The values of the anomalous dispersion corrections are those calculated previously from the Cromer-Liberman program.

Figure 7.13 004 Reflection From InSb

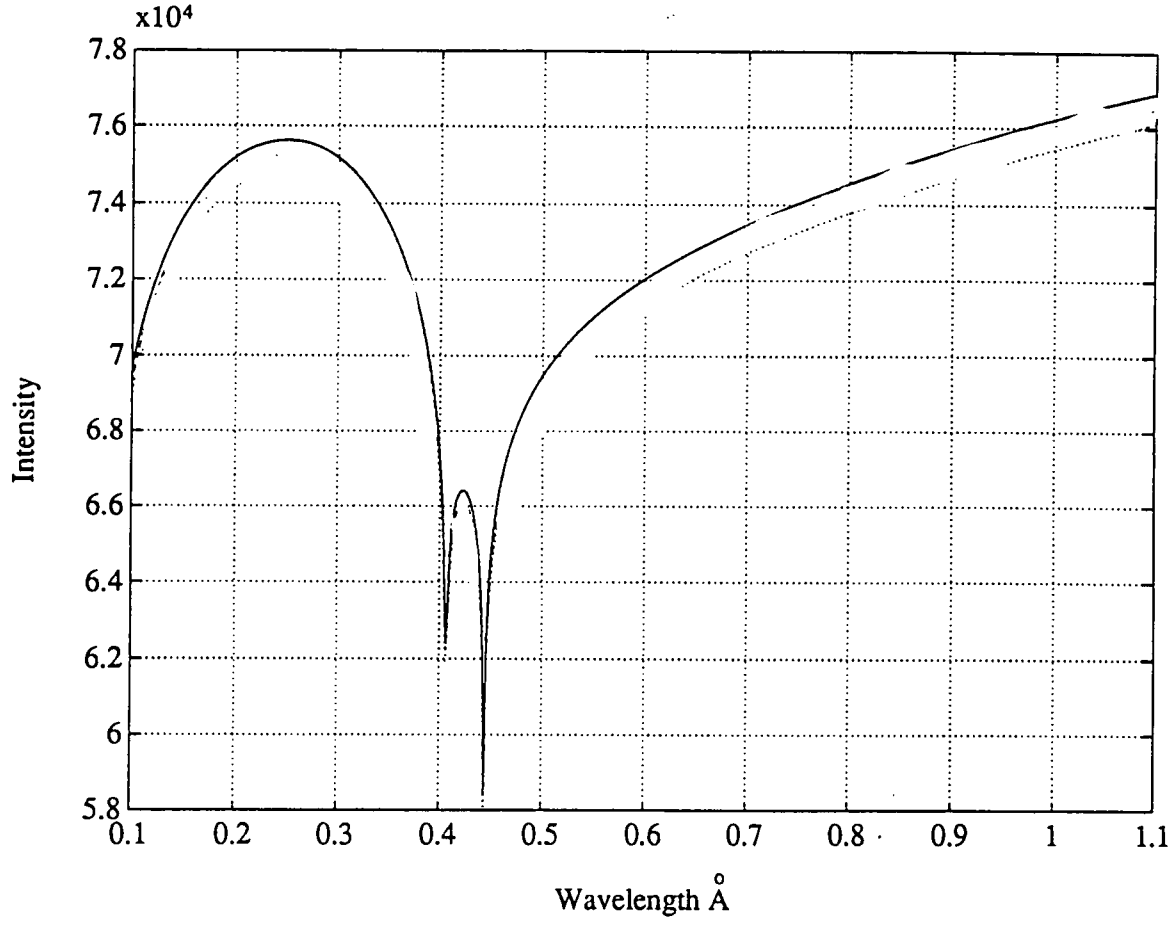

Figure 7.14 004 Reflection From GaAs

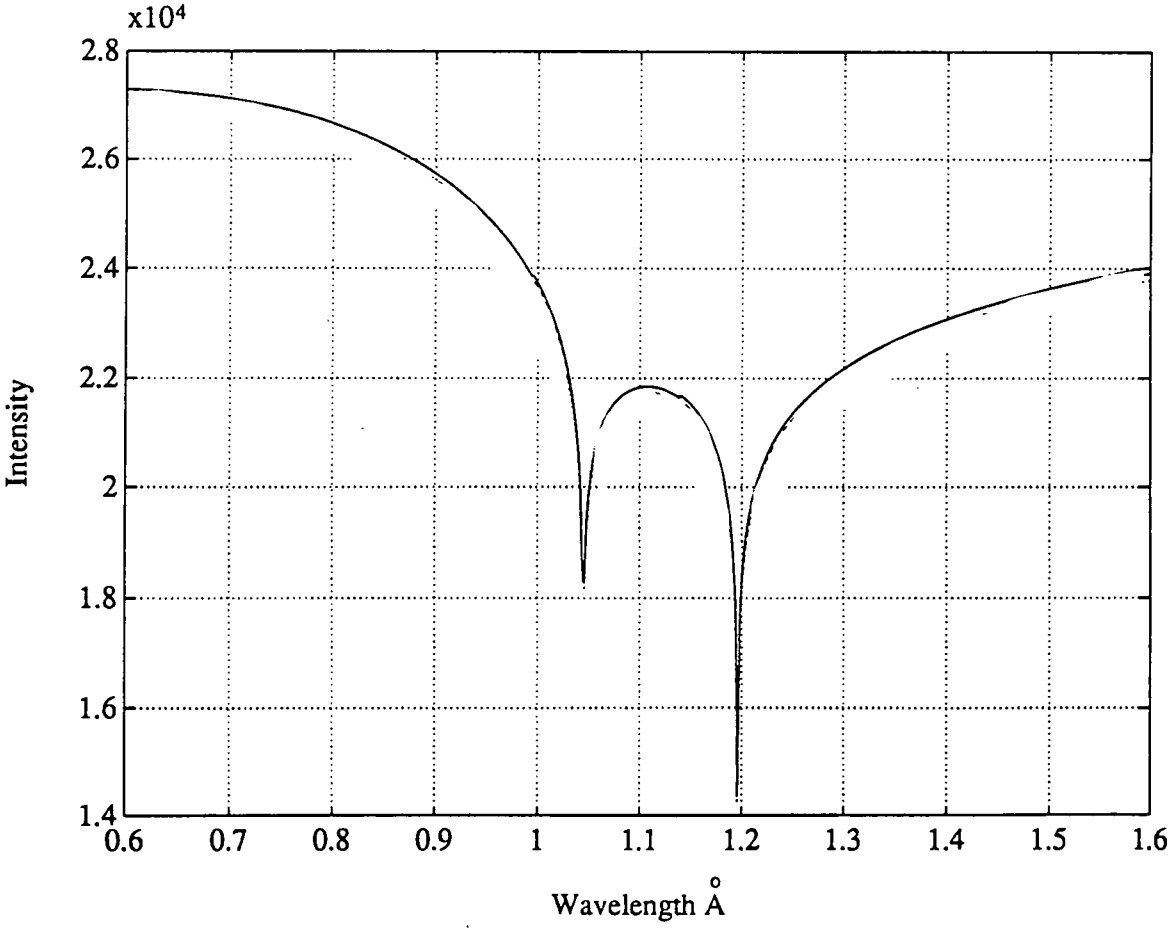

7.5.1 Non-stoichiometry and its effect on the structure factor

Consider now the case of a crystal of non-stoichiometric composition. In particular, we will take as an example a crystal with an arsenic vacancy fraction Δc. The 004 structure factor for this crystal is

$$F = 4[f_{Ga} + (1 - \Delta c) f_{As}] \tag{7.16}$$

and the integrated intensity

$$I \propto 4\left([f_{Ga} + f'_{Ga} + (f_{As} + f'_{As})(1 - \Delta c)]^2 + [f''_{Ga} + f''_{As}(1 - \Delta c)]^2\right)^{1/2}. \tag{7.17}$$

The above expression is represented graphically in figure 7.15 for GaAs and figure 7.16 for InSb with effective arsenic and antimony vacancy concentrations of 0.05%, 0.5% and 1.0%. From the graphs it can be seen that the integrated intensity is relatively insensitive to defect densities of this size.

There are two disadvantages in using the 004 reflection for stoichiometry measurements. Firstly, the intensity variations are very small, and secondly the 004 reflection, being strong, is sensitive to the degree of perfection of the sample. These problems effectively rule out the use of strong reflections for measurements of this kind.

7.6 Quasi-forbidden reflections

Reflections whose indices sum to 4n-2 are forbidden in the face centred cubic system. In 1921 Bragg detected intensities diffracted by the forbidden 222 reflection in diamond and attributed his findings to non-symmetrical binding of the atoms. In compound semiconductor materials the quasi-forbidden reflections exist principally due to differences in the scattering factors of their constituent atoms. The scattering factor of the 002 reflection is then given by;

$$F = 4[f_{Ga} - f_{As}] \tag{7.18}$$

Figure 7.15 004 Reflection From GaAs with a 0.0%,0.5%(--)and 1.0%(..) As Vacancy Concentration

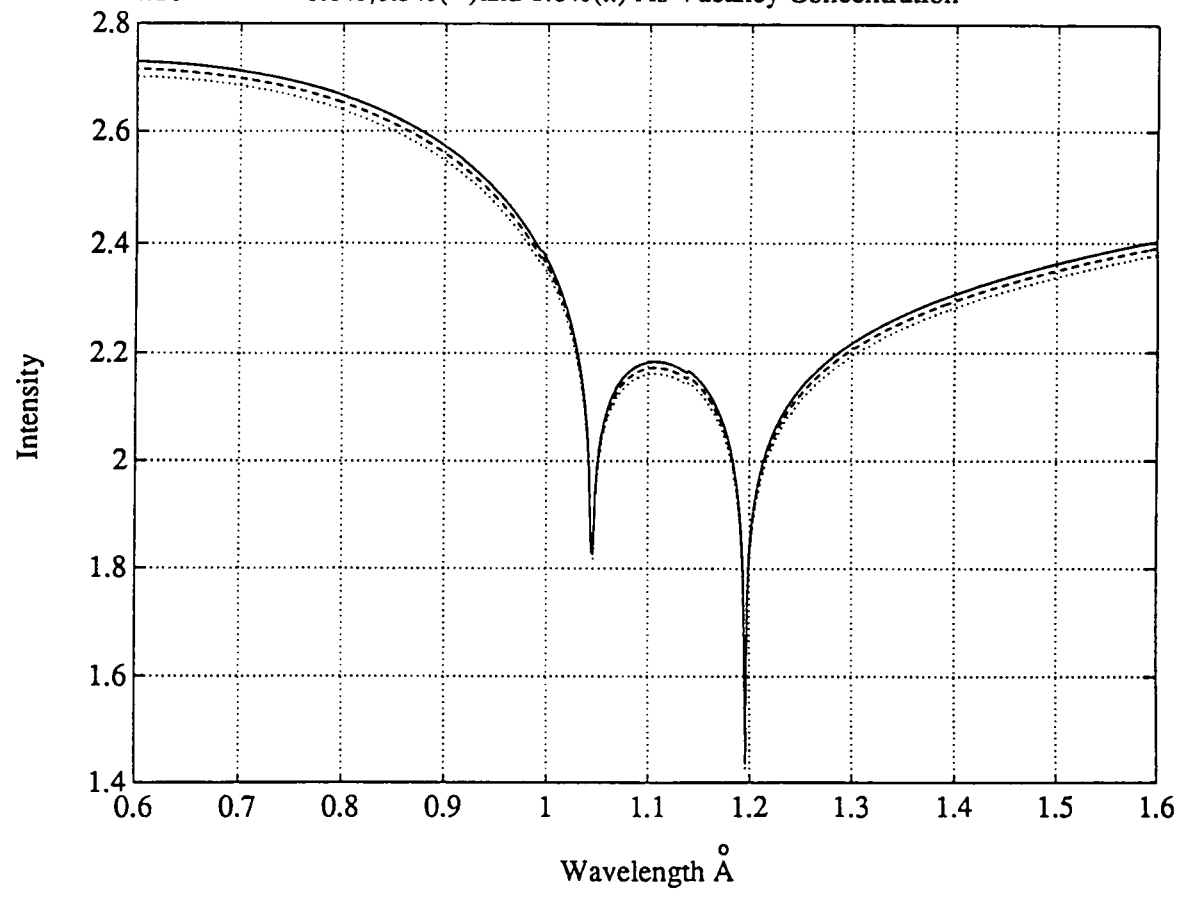

Figure 7.16 004 Reflection From InSb with a 0.0%(_),0.5%(--),and 1.0%(..) Sb Vacancy Concentration

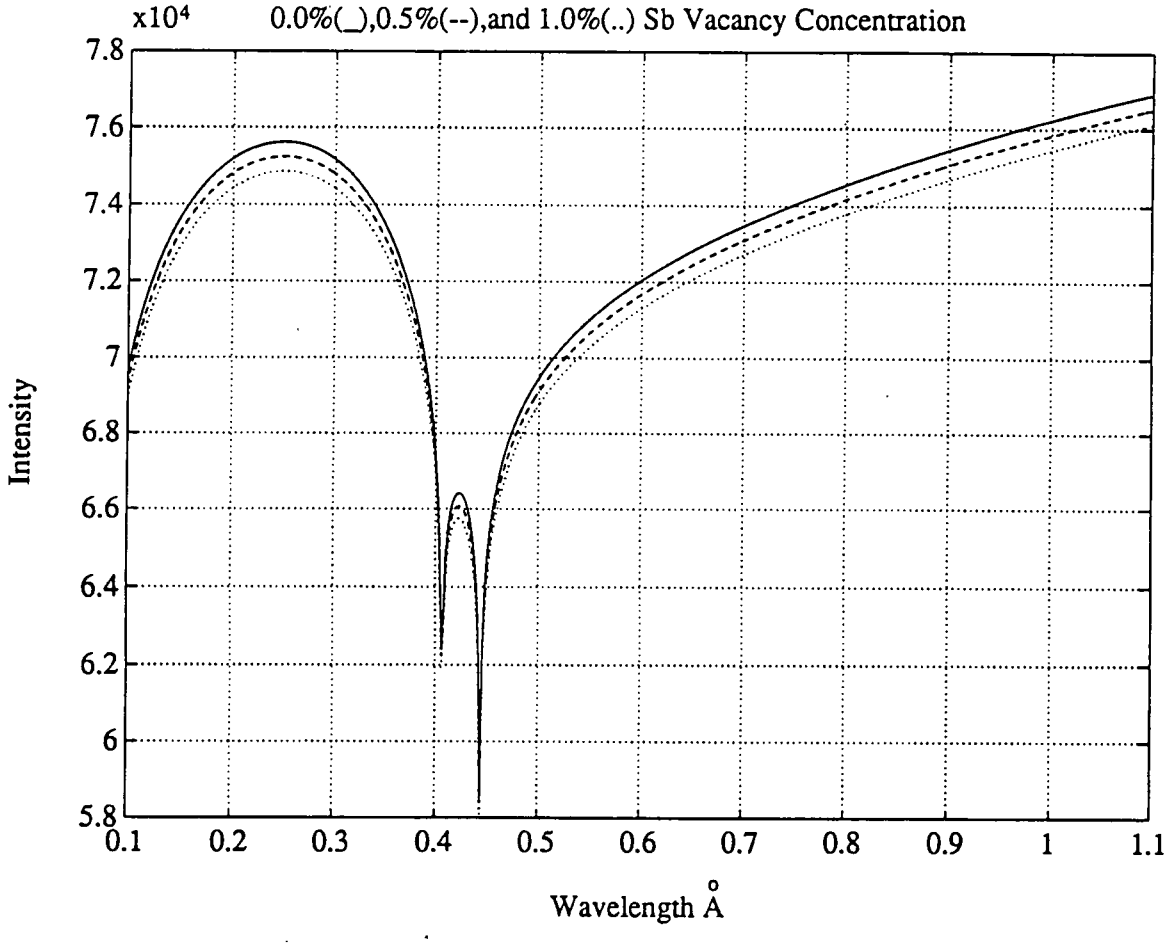

and taking into account the anomalous dispersion corrections of Cromer and Liberman this becomes

$$F = 4[f_{Ga} + f'_{Ga} + if''_{Ga} - (f_{As} + f'_{As} + if''_{As}] \tag{7.19}$$

The 002 reflection is weak, and so the integrated intensity is proportional to $|F|^2$ and may be written as

$$I \propto 16\left([f_{Ga} - f_{As} + f'_{Ga} - f'_{As}]^2 + [f''_{Ga} - f''_{As}]^2\right) \tag{7.20}$$

As before, an arsenic vacancy fraction can be introduced so that the structure factor is

$$F = 4[f_{Ga} - (1 - \Delta c)f_{As}] \tag{7.21}$$

and the integrated intensity is

$$I \propto 16\left([f_{Ga} + f'_{Ga} - (1 - \Delta c)(f_{As} + f'_{As})]^2 + [f''_{Ga} - f''_{As}(1 - \Delta c)]^2\right) \tag{7.22}$$

From this expression it is clear that the large real term which made the 004 reflection relatively insensitive has been significantly reduced, since the two real scattering factors now subtract rather than add. Reflections of this type are considerably more sensitive to composition variations as illustrated in figure 7.17 for GaAs and figure 7.18 for InSb. These figures illustrate two peaks in intensity located at the K absorption edges and a minimum position at the low wavelength side of the absorption edges. The figures also show the effect of increasing the arsenic and antimony concentrations. The position of the minimum can clearly be seen to increase in wavelength with increasing concentration.

Antisite defects produce no change in the minimum position, only a change in the overall intensity of the diffracted beam. This can be seen by considering the following expression, in which Δc is now an antisite defect concentration.

$$F = 4[(1 - \Delta c)f_{Ga} + e^{i\pi}(1 - \Delta c)f_{As} + e^{i\pi}\Delta c f_{Ga} + \Delta c f_{As}] \tag{7.23}$$

Figure 7.17 002 Reflection From GaAs with a
0.0%, 0.5%(--) and 1.0%(..) As Vacancy Concentration

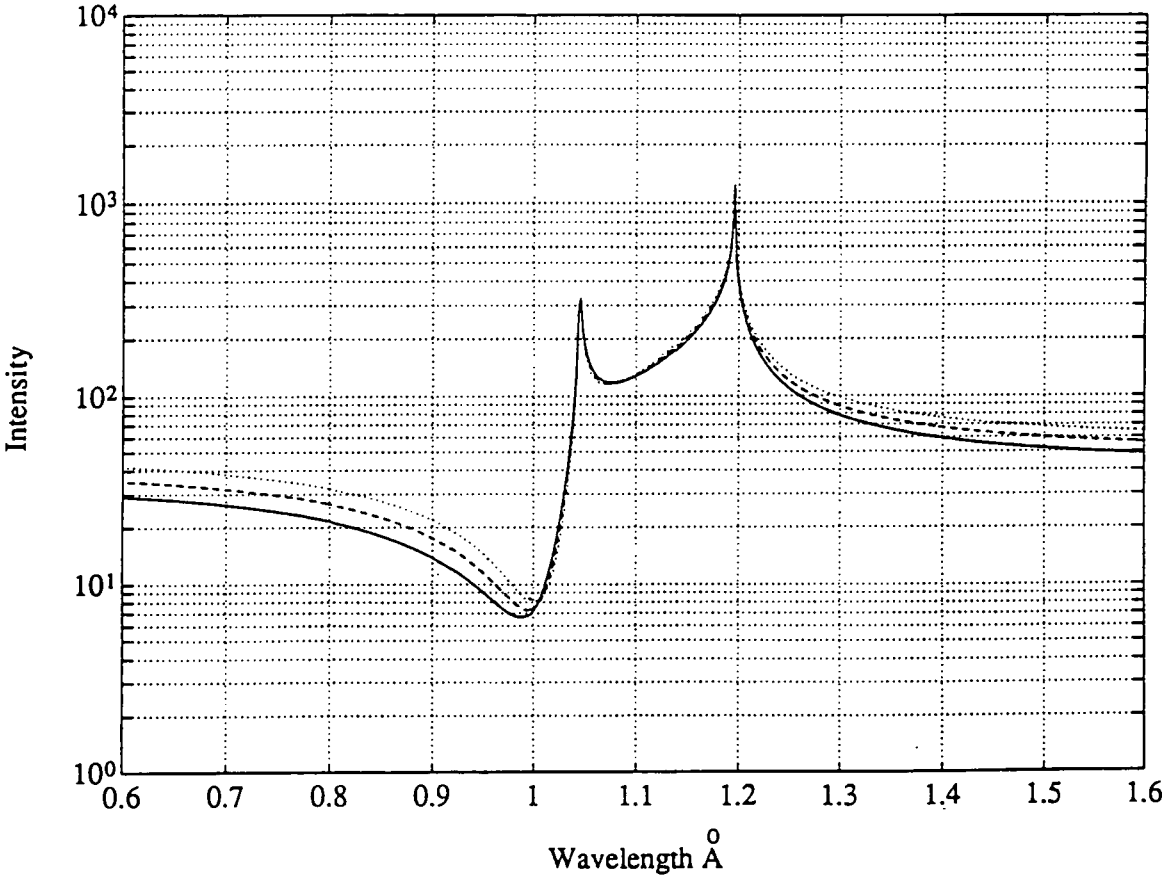

Figure 7.18 002 Reflection From InSb with a
0.0%,0.5%(--) and 1.0%(..) Sb Vacancy Concentration

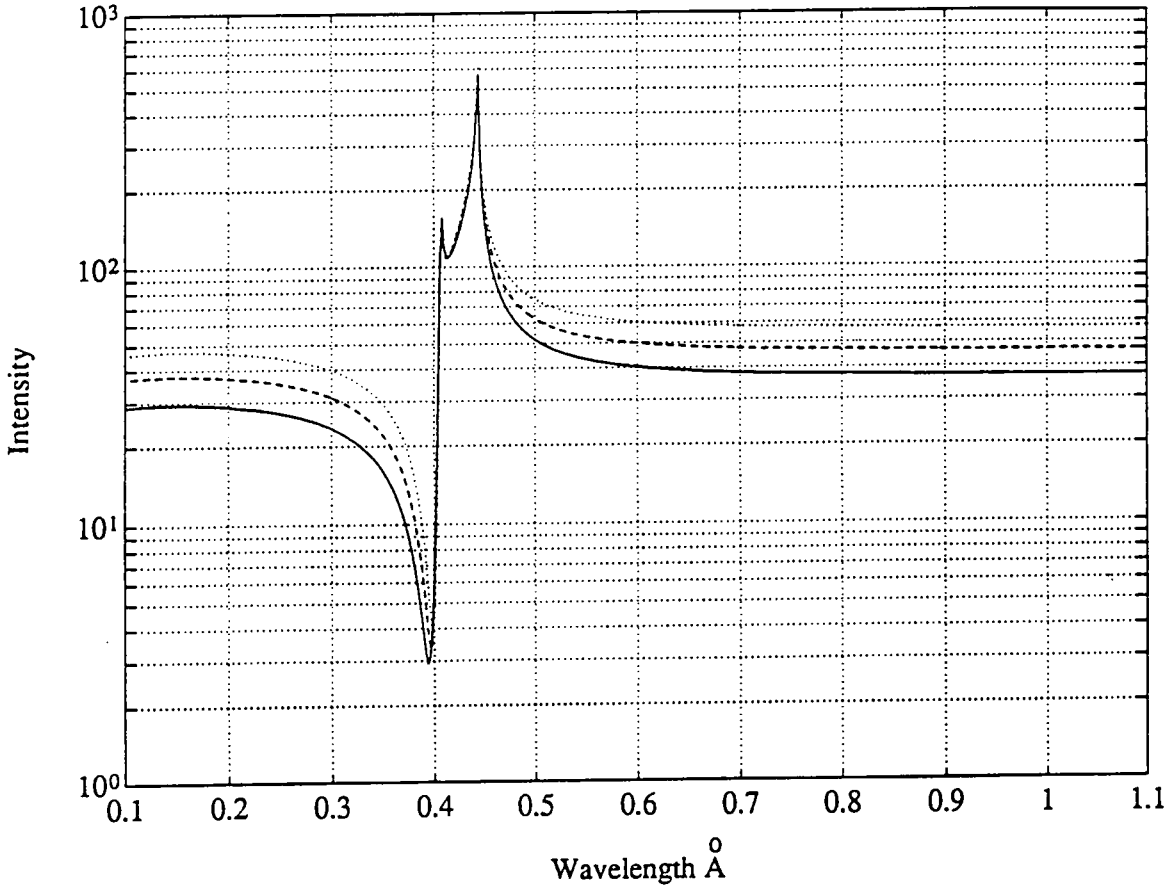

which when simplified becomes,

$$F = 4[(1 - 2\Delta c)(f_{Ga} - f_{As}] \tag{7.24}$$

7.7 Stoichiometry measurements at a single wavelength

Fujimoto and co-workers (1984; 1987) have attempted to study stoichiometry variations in both LEC and HB grown GaAs substrates. Epitaxial layers have also been studied, as well as doped material. Results indicate that the level of stoichiometric and dopant impurities can be determined to 1 part in 1×10^4, measurements being made on the integrated intensity variations at $MoK\alpha$. This wavelength was chosen in preference to the other commonly available sources because the ratio of I(mosaic)/I(perfect) was the smallest, this ratio being calculated by assuming the intensity from a ideally mosaic crystal is proportional to I^2 and the intensity from an ideally perfect crystal is proportional to I. Fujimoto did not discuss the extinction distance in his analysis which would of indicated that by using the 002 reflection one could assume the scattering to be that of a mosaic crystal away from any absorption edges.

The measurements made by Fujimoto and co-workers were made using a singularly diffracted beam, this then could allow the possibility of harmonic contamination. The excitation voltage for the 004 harmonic within a 002 refection is 16.5 kV. Fujimoto et al (1984) reported generator settings of 60kV and 500 mA and as pointed out by Hill and co-workers (1985) these results would suffer from significant harmonic contamination making them sensitive to the dislocation density. The measurement of stoichiometry directly from integrated intensity variations also renders inaccuracies possible due to variations in X-ray generator output and counting electronics.

Harmonic contamination may be reduced by using a double crystal arrangement with suitable reflections. This removal may be achieved, in the case of the 002 reflection from GaAs, by using a first reflection of silicon 111. The strongest harmonic present in the first crystal diffracted beam is then the 333 which can only match with the 006 off the GaAs second crystal. The 006 reflection is also quasi

forbidden and therefore insensitive to dislocation density and mosaic spread. Fujimoto suggested that the sensitivity of the integrated intensity to composition could be improved if a wavelength was chosen near to a characteristic absorption edge of the material. In the previous discussion it has been shown that the anomalous dispersion corrections undergo a sharp change near to the edge. The integrated intensity for a particular reflection has also been shown to depend strongly on the mode of diffraction taking place. Very close to the edge the structure factor for the 002 reflection becomes very large and consequently the assumption that the crystal diffracts kinematically is no longer valid. This in turn implies that the diffracted intensity of the 002 reflection could then be considerably more sensitive to the dislocation density present in the material.

7.8 Measurement of stoichiometry using a minimum position

The simulations of the integrated intensity of the 002 reflection with wavelength show a minimum position together with two peaks corresponding to the positions of the K absorption edges. Introducing a relative change in the arsenic concentration as described above produces a minimum position as a function of composition. Referring to figures (7.17) and (7.18) it can be clearly seen that the minimum position (located at 1.0$\AA$ in the case of GaAs and 0.39 $\AA$ in the case of InSb) is dependent on the arsenic vacancy fraction ΔC in the model. The amount of movement for a range of ΔC was simulated and the results are given in figures 7.19 for GaAs and figure 7.20 for InSb. The ability to characterise non-stoichiometry by using shifts in a minimum position has the advantage of removing the direct dependency on absolute intensity variations and the associated disadvantages discussed above.

7.8.1 Experimental methods

All the experiments were performed at the SRS at Daresbury, U.K. The main requirements of the experiment were,

(1) a continuous X-ray source in the wavelength range 0.3-2.0$\AA$;

(2) the ability to select the wavelength to 0.0001$\AA$ and reduce harmonic contamination;

Figure 7.19 Minimum position movement for a range of As vacancies.

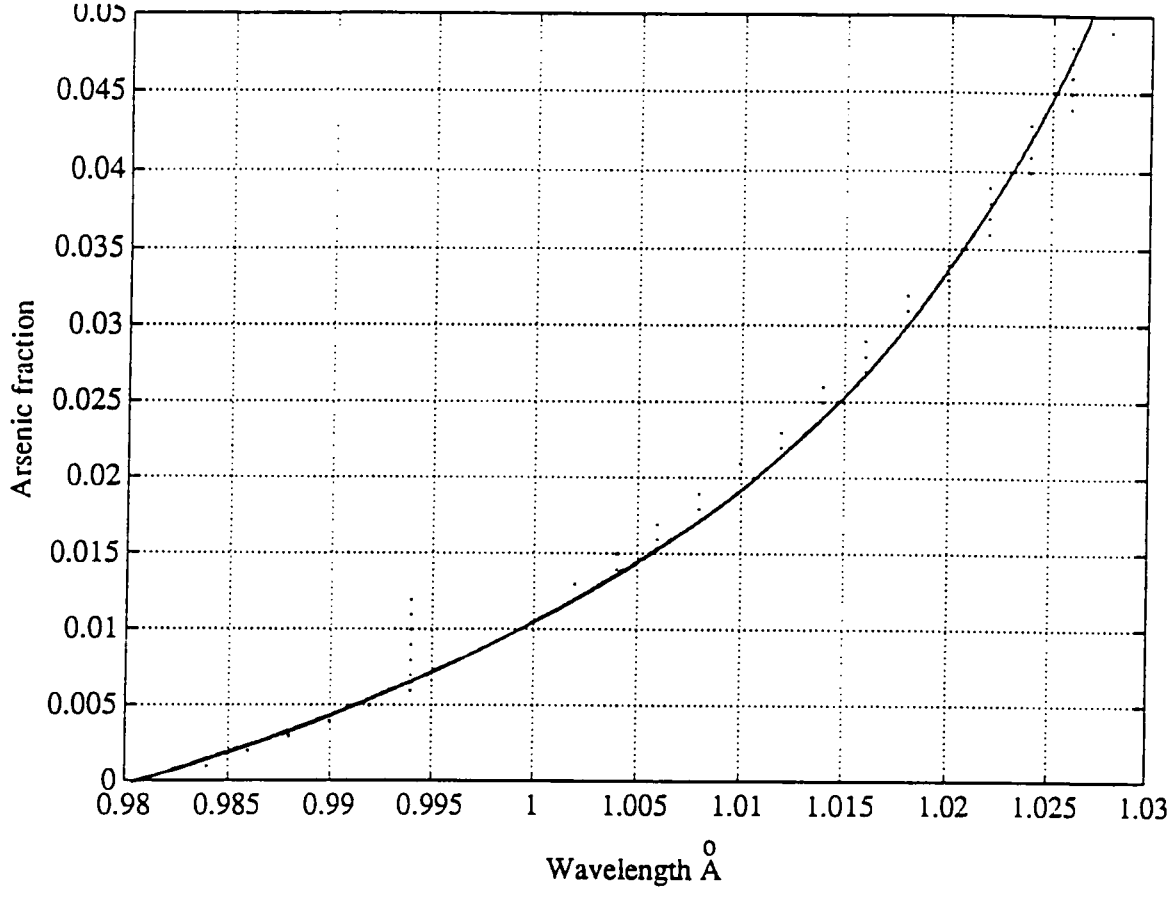

Figure 7.20 Minimum position movement for a range of Sb vacancies.

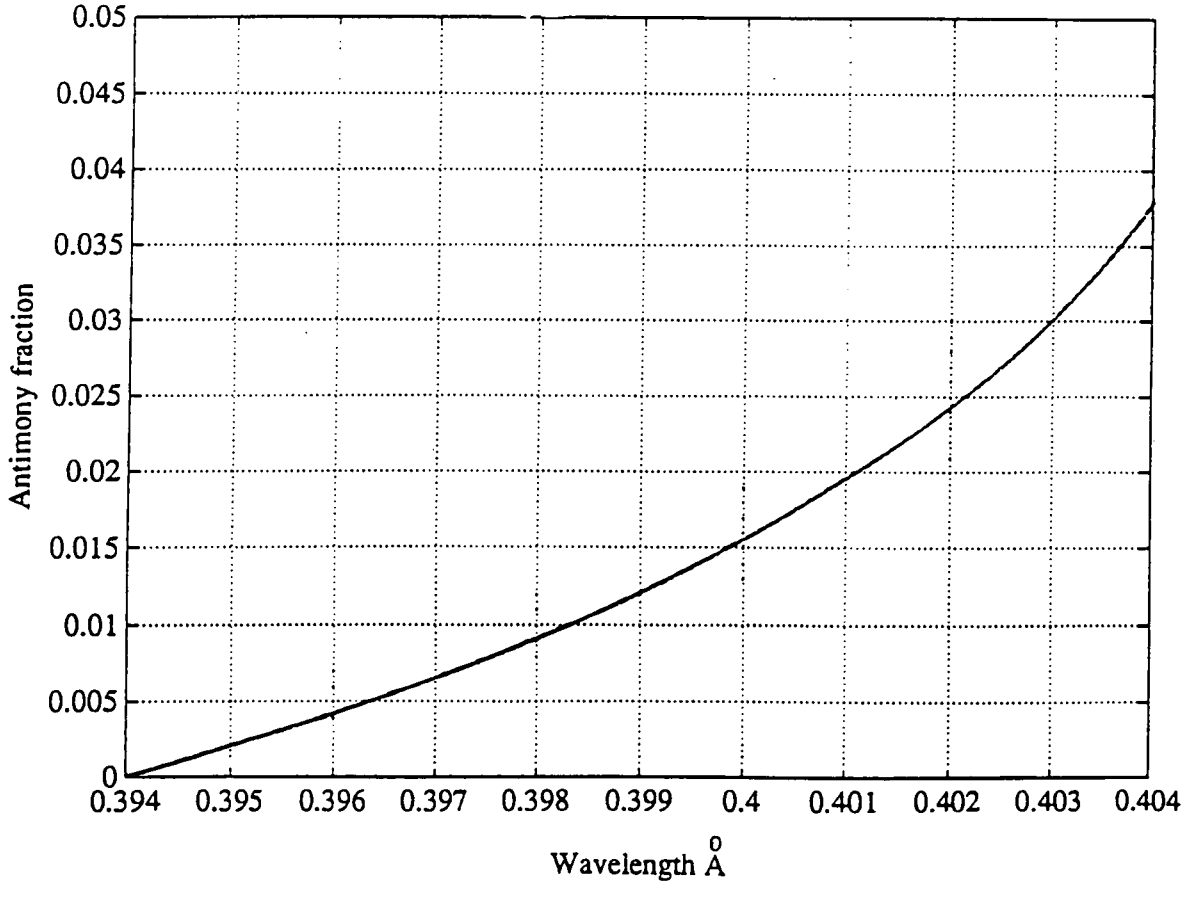

(3) in changing the wavelength the same area of the sample should be illuminated;

(4) reduction of the source size to a minimum to reduce averaging over a large area;

(5) the incident beam and the beam diffracted from the first crystal require monitoring to ensure that variations in the integrated intensity of the second reflection are not variations in the incoming beam.

Changing the wavelength of the incident X-rays can be achieved by simply changing the incident angle on the first crystal or beam conditioner. When a single reflection beam conditioner is used, rotating the beam conditioner results in a shift in the monochromatic beam position and direction. Because the camera has a limited step size (0.02 degrees) this limits the first axis rotation to 36 secs and the wavelength step to $0.001\mathring{A}$. A much more satisfactory approach can be achieved by using a double bounce beam conditioner, reducing the diffracted beam movement to an acceptable level while allowing the camera to remain in a fixed position. Figure 7.21 illustrates the beam conditioners used in this study and table 7.02 gives the vertical beam movement for these beam conditioners as a function of wavelength. It can be seen that the movement of the beam on the sample depends on the gap between the faces of the beam conditioner, the larger the gap the larger the movement. The range of wavelengths allowed through the beam conditioner depends on the length of the faces and the extent of the overlap between them. In order to reduce the movement of the beam on the sample to a minimum the gap between the faces should be as small as possible.

In order to detect variations in the integrated intensity of the beam incident on the sample, the incident beam intensity was monitored with an ion chamber (situated after the large horizontal slits) and the first axis scan was performed. Wavelength calibration was achieved by recording the fluorescence background and noting the position of the K absorption edges. A typical absorption edge fluorescence yield plot for GaAs is given in figure 7.22. In this figure both the Ga and As edges can be clearly seen, an enlarged region of the Ga edge is given in figure 7.23 indicating the calibration limitation defined by resolving the position of the absorption edge. The position of the edge, ± 5 arc seconds, was taken as being in

Table 7.02. This table gives the beam deviation, XY, with wavelength for double bounce beam conditioners with a 1mm and 4mm channel width.

Wavelength $\AA$	Channel width 1mm	Channel width 4mm
0.8	1.978mm	7.912mm
1.0	1.965mm	7.860mm
1.2	1.951mm	7.828mm
1.4	1.932mm	7.728mm
1.6	1.911mm	7.644mm
Beam movement	0.067mm	0.268mm

Figure 7.21 Schematic diagram of a double bounce beam conditioner.

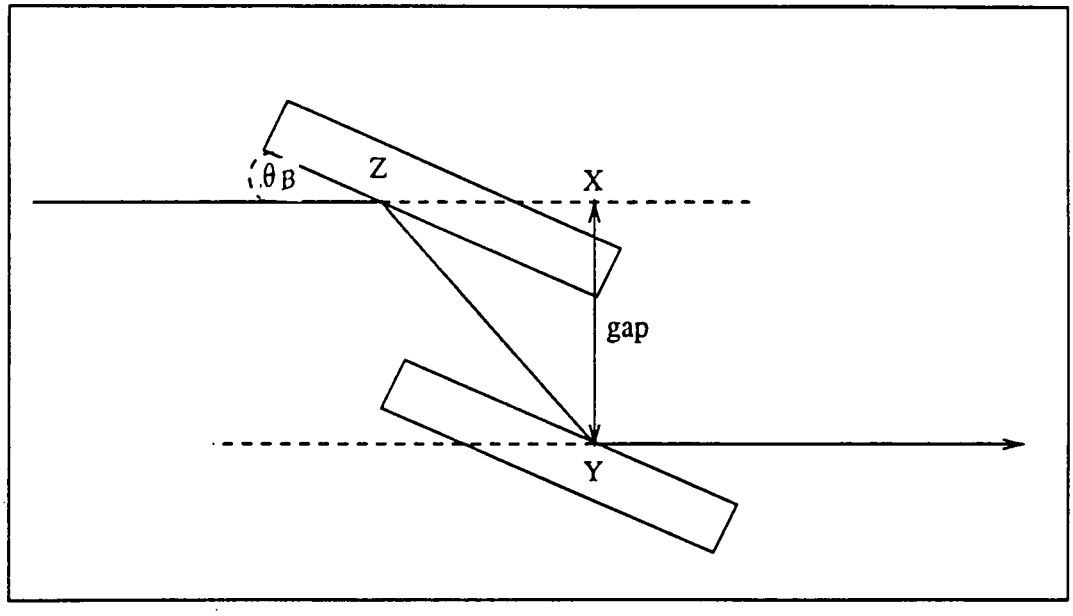

Vertical displacement XY is given by

$$ZX = \frac{gap}{sin\theta_B}$$

$$XY = \frac{sin2\theta_B}{sin\theta_B}.gap$$

Figure 7.22

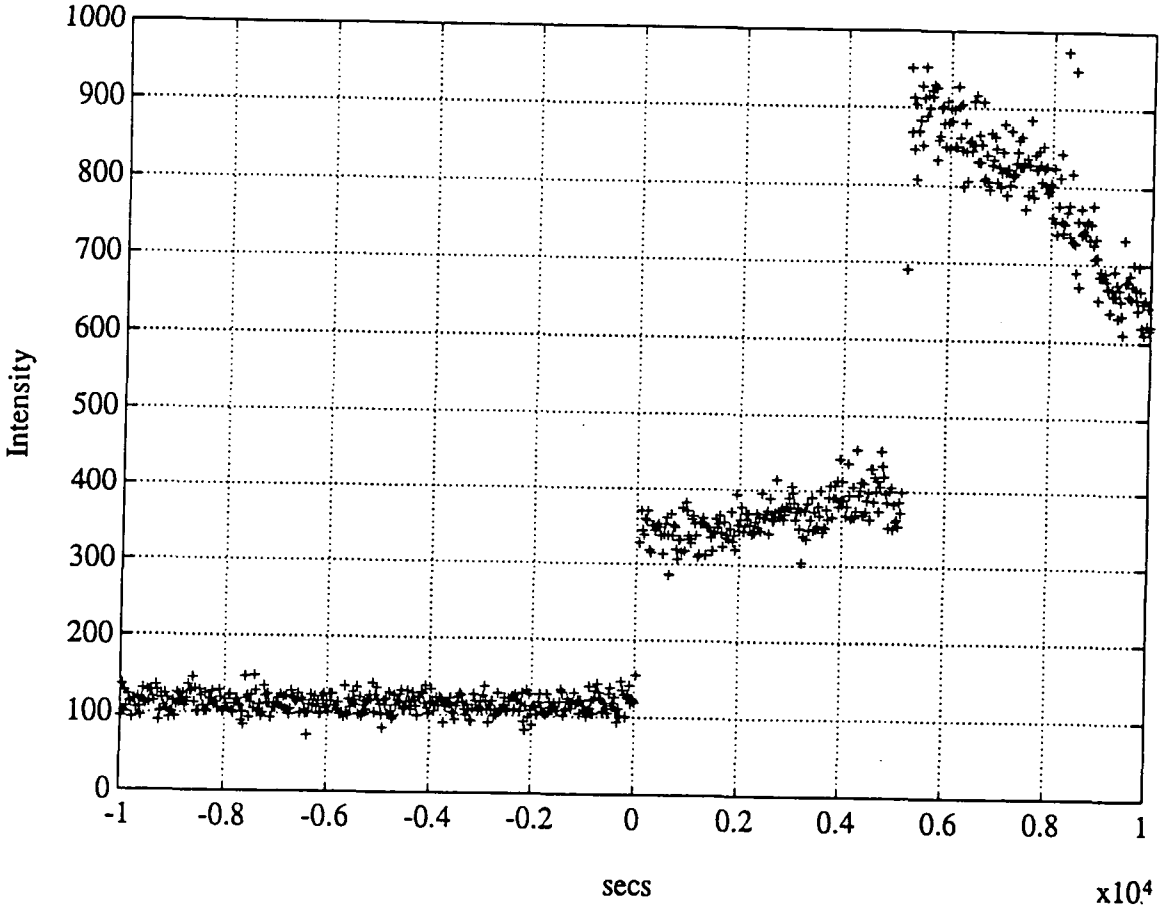

Fluorescence yield around the K absorption edge of arsenic and gallium. The arsenic edge is located on the high angle side corresponding to a region of higher fluorescence. This curve is used as a wavelength calibration.

Figure 7.23

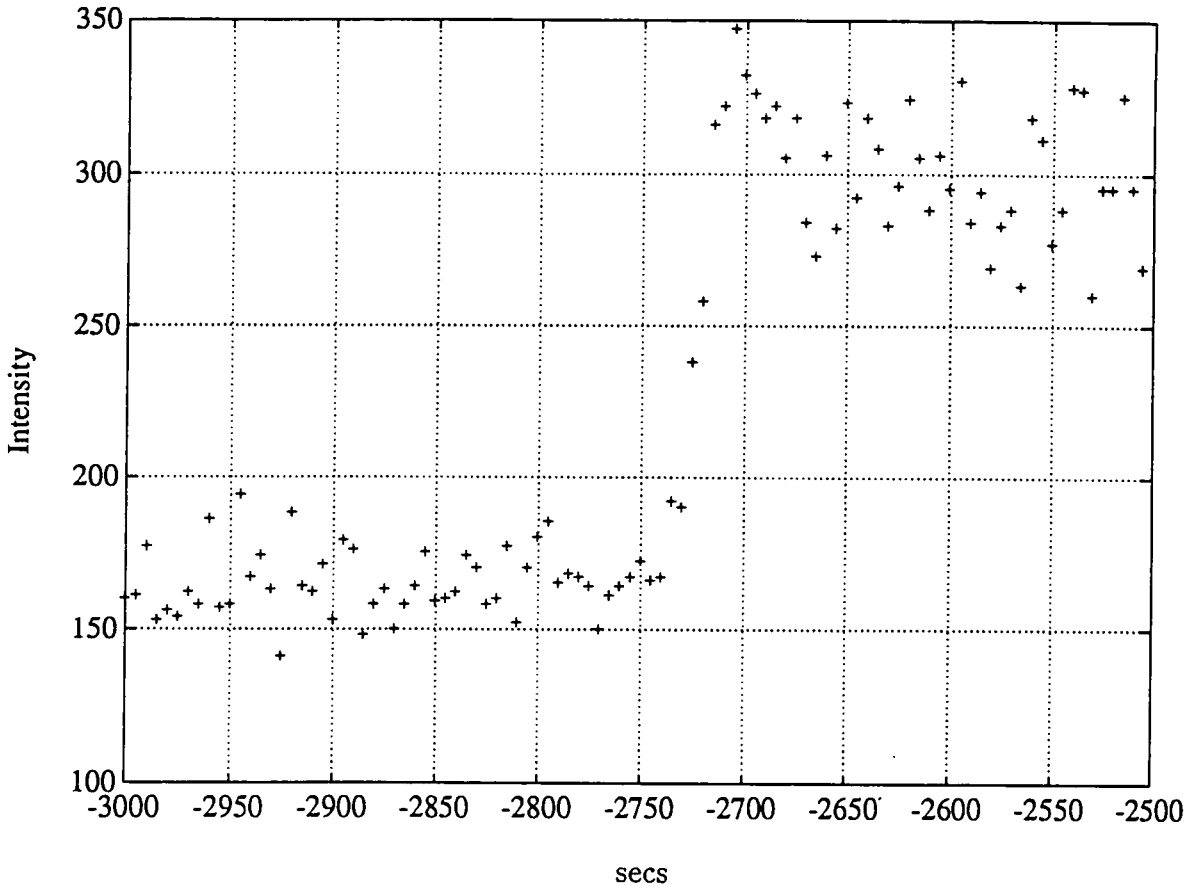

This figure illustrates a close in region around an arsenic edge, showing that the edge can be measured to within 5 secs of arc which corresponds to a wavelength step of 0.00013$\mathring{A}$.

the centre of the ramp, thus defining a wavelength minimum step of 0.0001$\mathring{A}$. The best method found for shielding was the use of a combination of a pair of slits, one placed immediately after the beam conditioner and the second immediately in front of the detector. The beam conditioner was also enclosed in a lead lined steel box with only a small window to allow the beam to pass through.

As mentioned previously, the choice of a suitable combination of reflections can greatly reduce harmonic contamination; for this reason a silicon 111 reflection was used from the beam conditioner. The experimental procedure is then as follows:

(1) align the beam conditioner so that the face is on axis with the incident beam and set to an approximate Bragg angle by eye;

(2) adjust the goniometer to ensure the diffracted beam passes through the centre of the second axis;

(3) construct shielding around the beam conditioner allowing a suitable window to cater for any vertical beam movement;

(4) record a first axis scan with the beam-defining slits set;

(5) mount sample on second axis and adjust the detector angle and position to give a good fluorescent count rate;

(6) scan axis 1 and record the characteristic absorption edges of the material to enable calibration of the experiment;

(7) rotate the sample by hand to the approximate Bragg angle for the required reflection at the wavelength required by the beam conditioner and scan axis 2 to obtain the rocking curve;

(8) change wavelength on axis 1 by rotating the beam conditioner and repeat. It is very important when rotating axis 1 to always move in the same direction as backlash in the gearbox can result in a positional error and hence an error in the value of the wavelength.

Plate 7.01 illustrates the experimental setup of the double crystal camera to achieve good scatter shielding.

Plate 7.01. This plate shows a double crystal experiment inside hutch 7.6. The goniometer (g) is marked together with the optical bench (ob) and the first crystal radiation shielding (rs). The crystal visible is located on the second axis on a sliding holder. The diffracted beam is recorded with the scintillation detector (sd) which rotates about the second crystal (sc) axis.

7.9 Experimental results

Initial studies were made on a Horizontal Bridgman grown sample of GaAs supplied by MCP. These results are published in Cockerton et al (1989) and shows the behaviour of the 002 reflection with wavelength at two positions on the sample.

In the work that follows minimum position measurements were made on two Czochralski grown 3 inch GaAs wafers supplied by Spectrum Technologies and two Czochralski grown InSb samples.

7.9.1 The LEC GaAs samples

Ten 3 inch diameter GaAs wafers were provided by Spectrum Technologies, U.S.A. for evaluation using this technique. Two wafers from this set were chosen, the first taken from the tail end of the boule and the second was from the seed end. These wafers were chosen in an attempt to highlight any variation in non-stoichiometry as a function of crystal growth.

7.9.2 Seed end sample

The ion chamber readings were monitored while varying the first crystal angle over a range of wavelengths from 0.95 to 1.03$\AA$, the result is shown in figure 7.24. The wavelength was then changed to a value estimated to be near to one of the K absorption edges and the sample was placed on the second axis. The absorption edge of arsenic was then recorded, figure 7.25. A wavelength was then selected near to this edge enabling the 002 reflection to be found relatively easily.

Because of the need to undertake many rocking curves to define accurately the minimum position, only two different positions on the sample were studied. Table 7.03 gives the measured integrated intensities together with the peak heights and monitor rates as a function of wavelength. The integrated intensities were then corrected from the first axis scan as well as the beam monitor values. Figure 7.26 illustrates a plot around the minimum position for the central point on the sample. The solid line corresponds to a simulation based on a stoichiometric composition using equation 7.22. It can be seen that the behaviour between 0.95 and 1.03$\AA$ is similar to that predicted from the simulation in general shape. There is difficulty in defining the minimum position, though it seems to be located between 0.98 -1.0$\AA$

Figure 7.24

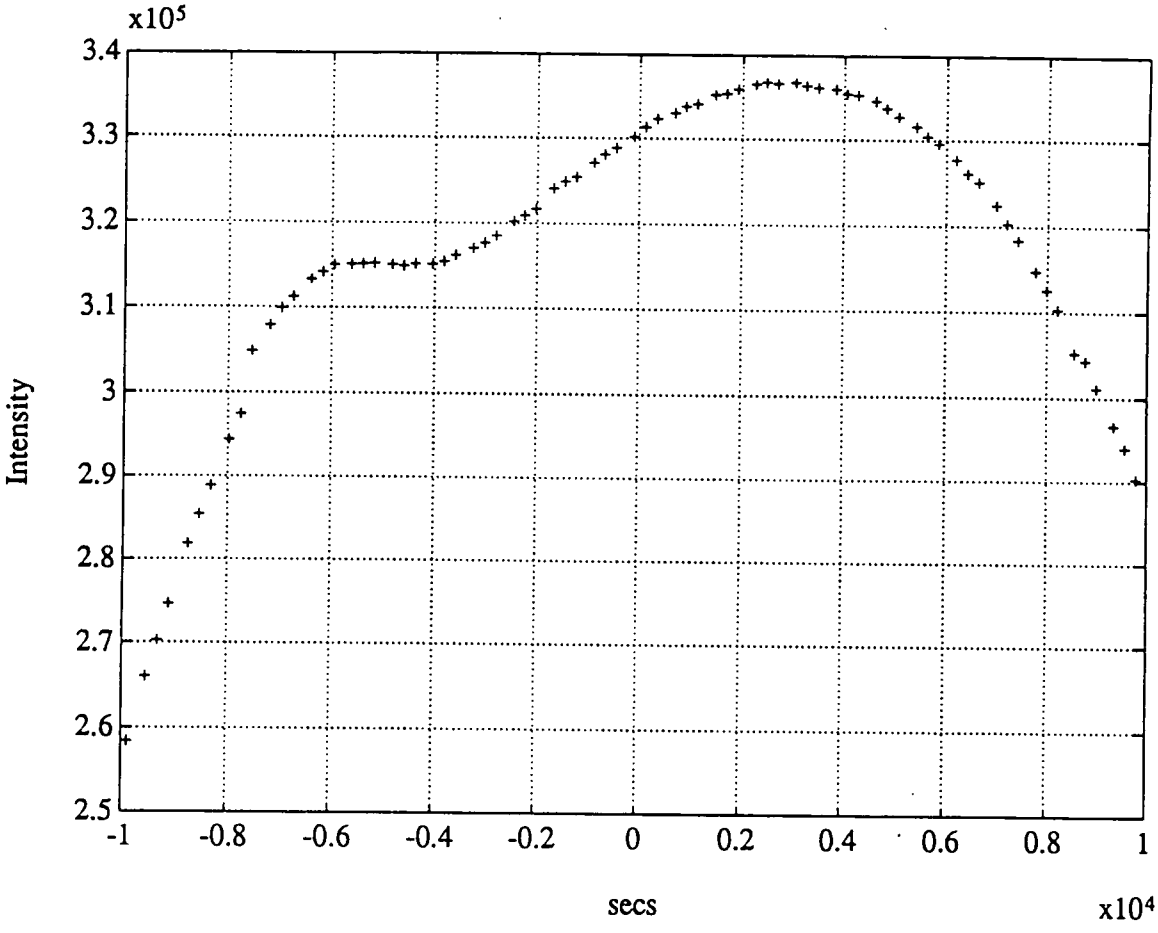

This figure illustrates the first axis scan using the channel cut beam conditioner. The fall off at low and high angles corresponds to the two extremes of incident angles allowed through the channel.

Figure 7.25

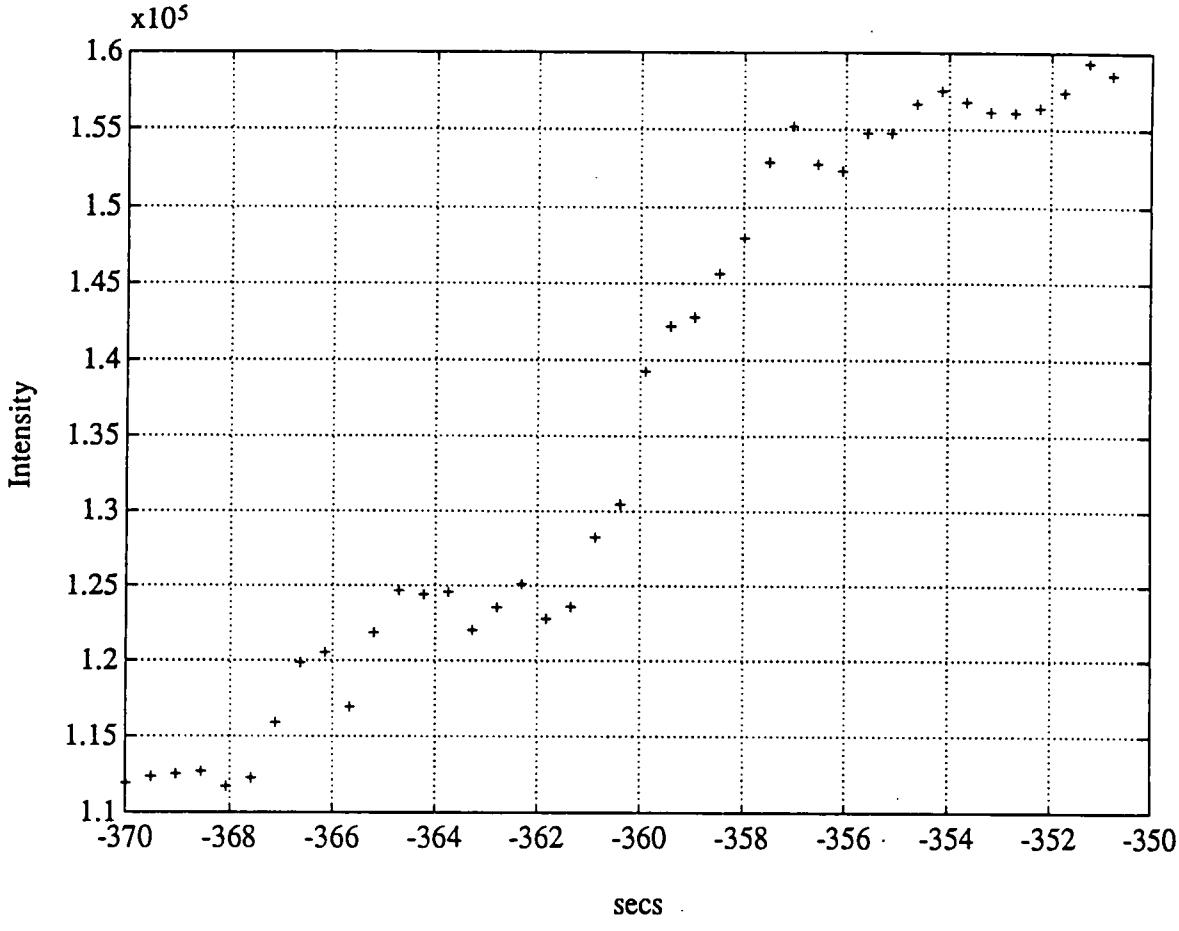

This figure illustrates the fluorescence yield near to the absorption edge of arsenic used to calibrate the LEC sample at the seed end of the boule.

Table 7.03

Run File Number	Axis 1 secs	Wavelength Angstroms	Profile Ref cps	Current Ref cps	Count secs	Expt I.I	Corrected I.I
r2033	150	1.0300	1782322	331314	5	26562± 2745	26562± 2745
r2034	473	1.0200	1779105	332300	5	12970± 2055	12955± 2052
r2035	806	1.0100	1765139	332979	5	6786 ± 1515	6818 ± 1522
r2036	840	1.0090	3501987	333710	10	148268±2363	7491 8±1194
r2037	1140	1.0000	3541620	334034	10	17079± 2457	8525 ± 1226
r2038	1473	0.9900	3601964	335078	10	16827± 2476	8233 ± 1211
r2039	1806	0.9800	3609041	335772	10	17082± 2495	8324 ± 1215
r2041	2139	0.9700	3605425	336385	10	18760± 2538	9134 ± 1235
r2042	2472	0.9600	3592737	336627	10	20748± 2663	10130± 1200
r2043	2805	0.9500	3583368	336460	10	15111± 2257	7401 ± 1105
r2044	3137	0.9400	3574339	336288	10	15073± 2209	7405 ± 1085
r2045	4467	0.9000	3549307	334511	10	12915± 2083	6423 ± 1036
r2046	840	1.0090	3521691	332500	10	17977± 2671	9066 ± 1347
r2047	873	1.0080	3518173	332700	10	32064± 5115	7931 ± 1280
r2048	906	1.0070	3502759	333630	10	31392± 5108	8156 ± 1281
r2049	940	1.0060	3494567	333650	10	32211± 5123	10208± 1294
r2050	973	1.0050	3486625	333670	10	40224± 5657	8461 ± 1471
r2051	1006	1.0040	3476241	333820	10	33268± 5179	8399 ± 1335
r2052	1040	1.0030	3465400	333830	10	32911± 5152	9294 ± 1329
r2053	1073	1.0020	3454772	333835	10	36304± 5283	9331 ± 1304
r2054	1106	1.0010	3445202	333400	10	30465± 4954	7831 ± 1346
r2055	890	1.0075	3433845	333600	10	317148±3066	8174 8±1580
r2056	923	1.0065	3421538	333620	10	30516± 5009	7893 ± 1291

This table illustrates the rocking curves obtained from the central region of the seed end sample.

Figure 7.26. This figure shows the experimental data obtained from the centre of the seed end sample, together with a stoichiometric simulation (solid line)

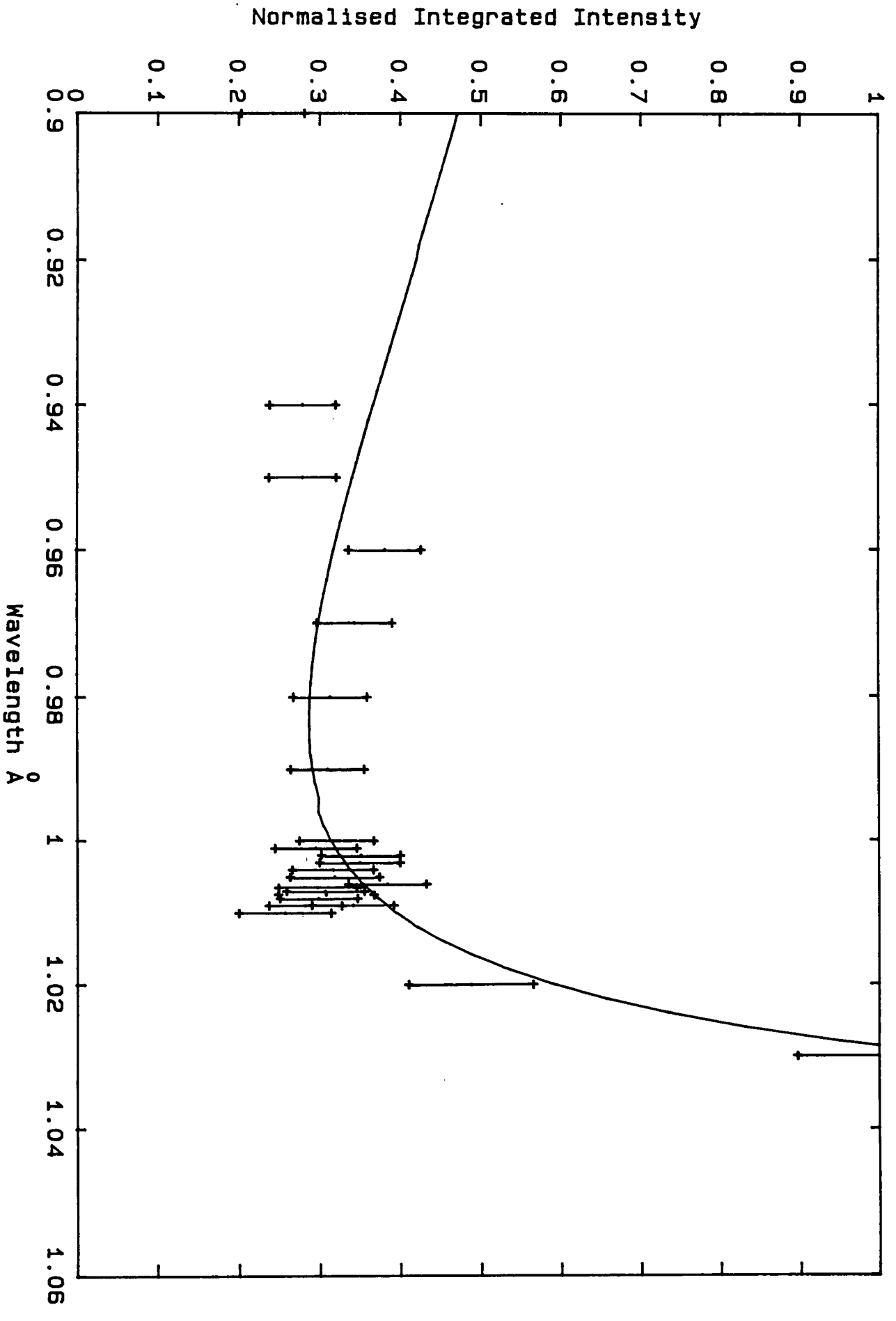

with a very sharp peak corresponding to the K absorption edge of As at 1.044$\mathring{A}$. Identification of a more exact minimum position however can not be made due to the inaccuracy of the fit. The simulation is fitted to the experimental results by normalising the two curves at the same wavelength. Table 7.04 gives the measured integrated intensities and the corrected integrated intensities together with the peak heights and beam monitor rates at the second position corresponding to +25mm away from the central position. The corrected integrated intensities are then displayed in figure 7.27. There appears to be a minimum position located between 0.98$\mathring{A}$ and 1.01$\mathring{A}$, again the curve displays structure making a more exact identification unreliable. The simulation shows a small dip at about 1.0$\mathring{A}$ which appear to be a problem with the simulation program.

7.9.3 Tail end sample

Measurements were again made at positions in the centre of the crystal and at the edge 25mm away. The fluorescence yield near the absorption edge of As for this sample is given in figure 7.28. Table 7.05 gives the measured integrated intensities together with the peak heights and beam monitor rates for the central position on the crystal. Table 7.06 gives the measured integrated intensities together with the corrected values for the position 25mm towards one edge. The corrected integrated intensities are then displayed in figures 7.29 and 7.30 for positions corresponding to the centre of the crystal and 25mm towards one edge, together with a stoichiometric simulation. Figure 7.29 illustrates the close in region around 1.0$\mathring{A}$, the curve displays an enhanced structure compared to the curve obtained from the seed end crystal. This curves also has a sharp minimum at about 1.01$\mathring{A}$ which may be due to a diffraction effect. A minimum position is observed in the range 0.98-1.01$\mathring{A}$. Figure 7.30 shows similar enhanced structure displaying a minimum in the range 0.98-1.01$\mathring{A}$.

7.9.4 InSb samples

Measurements were made on two InSb samples; one provided by McDonald Douglas, St Louis, USA and one supplied by MCP. The first sample was of unknown dislocation density and the second was specified to have no more than 500 dislocations per cm^3. Both samples were nominally 111 surfaces and the 222 quasi-

Table 7.04

Run File Number	Axis 1 secs	Wavelength Angstroms	Profile Ref cps	Current Ref cps	Count secs	Expt I.I	Corrected I.I
r2057	150	1.0300	1820144	331314	5	150894 ± 9377	150894 ± 9377
r2058	473	1.0200	1855083	332300	5	77091 ± 6839	75410 ± 6690
r2059	635	1.0150	1860241	332979	5	140251 ± 8766	136540 ± 8534
r2060	806	1.0100	1864808	333350	5	50469 ± 5839	48960 ± 5664
r2061	840	1.0090	1861463	333420	5	44019 ± 5427	42770 ± 5273
r2062	875	1.0080	1861463	333510	5	50432 ± 5851	48990 ± 5683
r2063	906	1.0070	1860292	333620	5	34850 ± 4758	33860 ± 4623
r2064	940	1.0060	1857180	333730	5	47996 ± 5590	46700 ± 5438
r2065	973	1.0050	1821153	333800	5	41581 ± 5213	41250 ± 5171
r2066	1006	1.0040	1824239	333820	5	41669 ± 5266	41260 ± 5214
r2067	1040	1.0030	1818617	333840	5	39963 ± 5111	39690 ± 5076
r2068	1073	1.0020	1818617	333900	5	46860 ± 5423	46540 ± 5385
r2069	1106	1.0010	1816049	334000	5	41287 ± 5247	41050 ± 5216
r2070	1149	1.0000	1815595	334100	5	42024 ± 5270	41780 ± 5239
r2071	1473	0.9900	1810877	335078	5	41797 ± 5239	41540 ± 5206
r2072	1806	0.9800	1807517	335772	5	37546 ± 4708	37310 ± 4677
r2073	2139	0.9700	1803937	336385	5	54007 ± 5962	53670 ± 5924
r2074	2472	0.9600	1456404	336627	5	47375 ± 5469	58270 ± 6727
r2075	2865	0.9500	1794192	336460	5	46625 ± 5400	46580 ± 5394
r2076	4467	0.9000	1788808	334511	5	39230 ± 4927	39540 ± 4965
r2077	703	1.0130	3527239	332990	5	79122 ± 7306	40620 ± 3751
r2078	740	1.0120	1735144	333100	5	39518 ± 5109	41230 ± 5330
r2079	674	1.0140	1737901	332900	5	28334 ± 4416	29530 ± 4602
r2080	690	1.0135	1737523	333900	5	32443 ± 4646	33720 ± 4829

This table gives the rocking curves obtained from 25mm towards the edge of the seed end sample.

Figure 7.27. This figure shows the experimental data obtained from the edge of the seed end sample, together with a stoichiometric simulation (solid line)

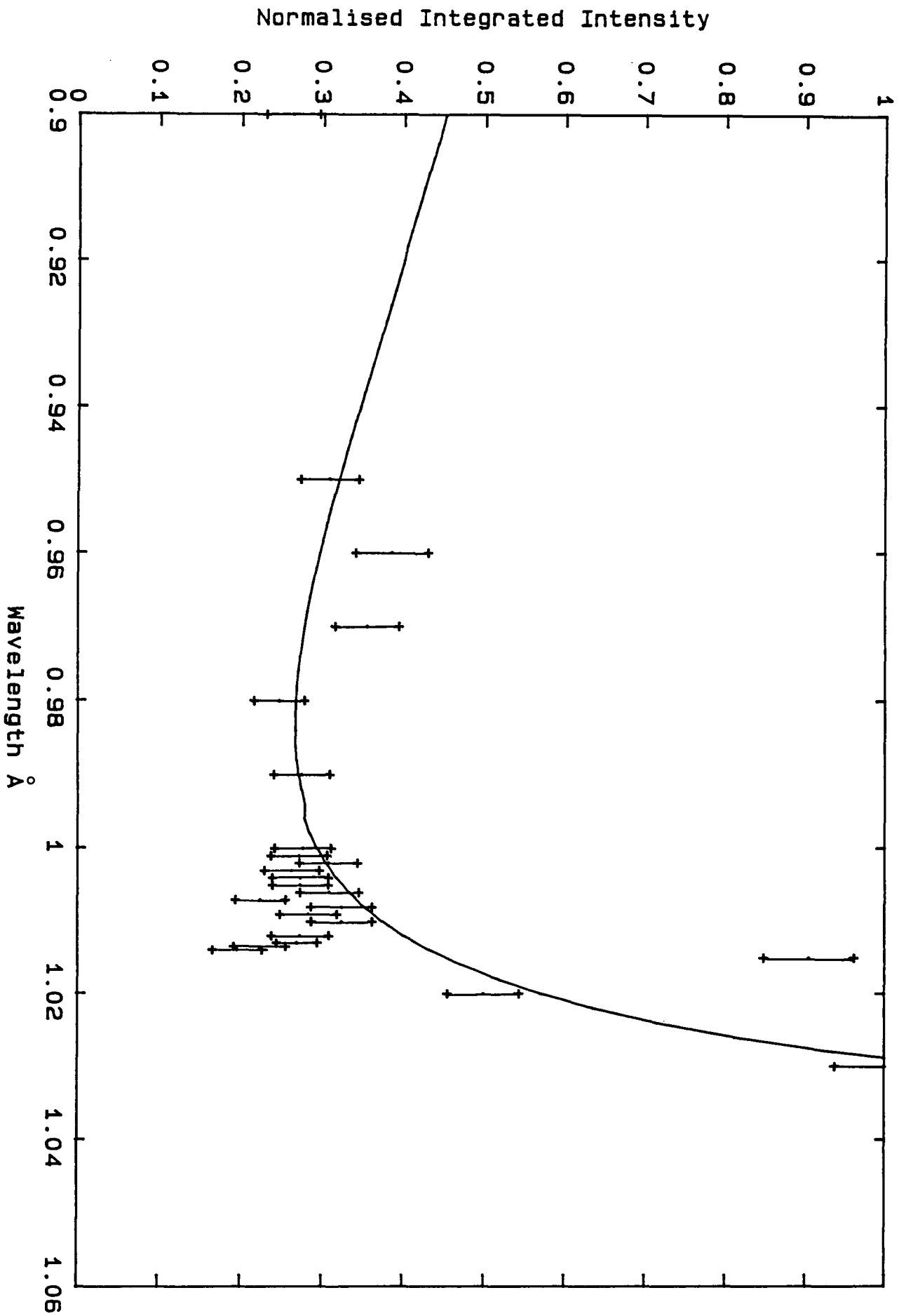

Figure 7.28

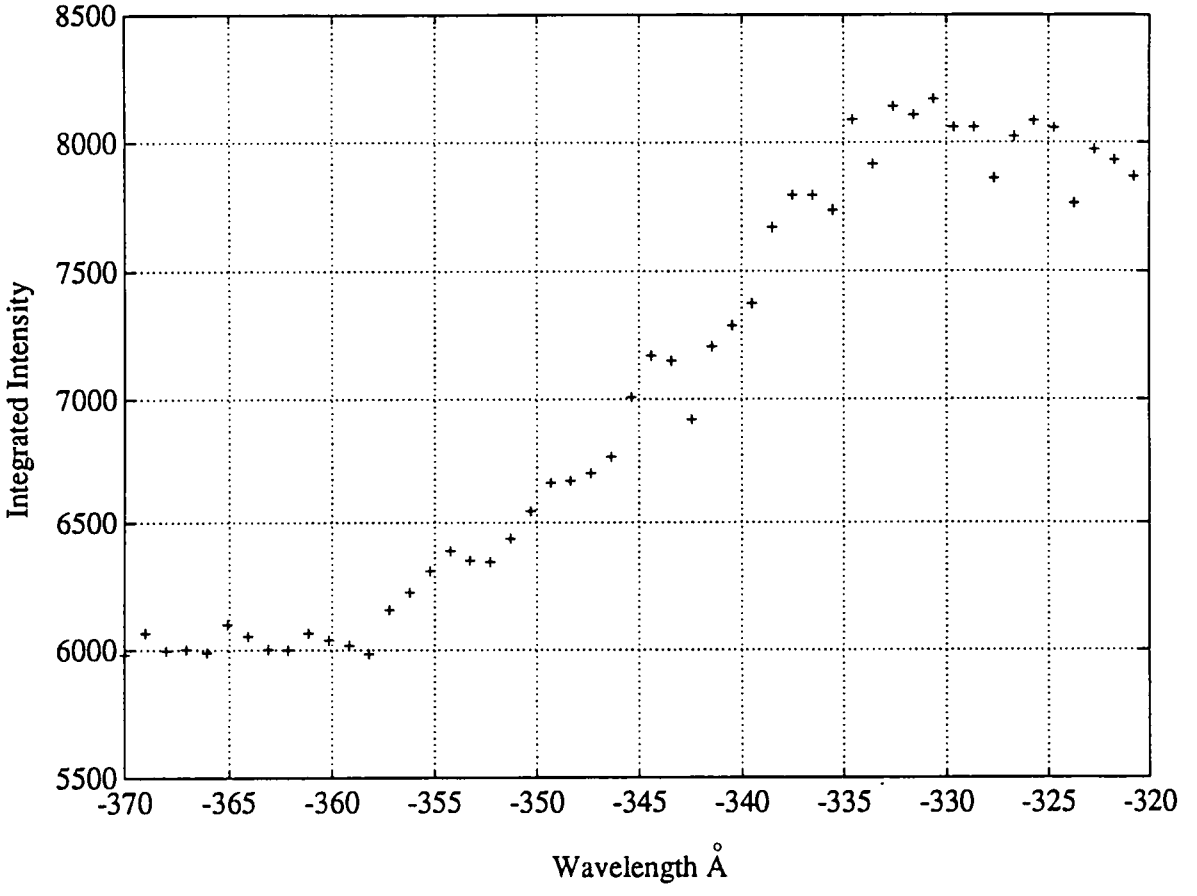

This figure illustrates the fluorescence yield near the arsenic absorption edge obtained from the tail end sample.

Table 7.05

Run File Number	First Axis secs	Wavelength Angstroms	Profile ref cps	Current ref cps	Count secs	Expt I.I	Corrected I.I
r2100	473	1.0200	1643838	332300	5	43397 ±5259	43397± 5259
r2101	572	1.0170	1641244	332800	5	38651 ±5129	38654± 5129
r2102	635	1.0150	1637395	332870	5	42003 ±5319	42096± 5330
r2103	703	1.0130	1636331	332990	5	42091 ±5391	42196± 5404
r2104	806	1.0100	1632633	332979	5	19654 ±3663	19749± 3680
r2105	973	1.0050	1628068	333670	5	30261 ±4581	30429± 4604
r2106	1149	1.0000	1626036	334034	5	27699 ±4406	27857± 4431
r2107	1473	0.9900	1618653	335078	5	26201 ±4319	26388± 4349
r2108	1806	0.9800	1614206	335772	5	27275 ±4456	27488± 4490
r2109	2139	0.9700	1543688	336385	5	21999 ±3681	23142± 3872
r2112	306	1.0250	1708007	332200	5	67114 ±6472	64612± 6230
r2113	373	1.0230	1711861	332300	5	68908 ±6577	66170± 6315
r2114	440	1.0210	1710956	332310	5	66818 ±6561	64192± 6303
r2115	506	1.0190	1706731	332390	5	51311 ±5774	49407± 5559
r2116	773	1.0110	1703473	333000	5	24894 ±4192	23972± 4036
r2117	840	1.0090	1701021	333710	5	36523 ±4994	35146± 4805
r2118	906	1.0070	1698357	333630	5	34270 ±4872	33038± 4696
r2119	1040	1.0030	1694268	333830	5	30380 ±4638	29341± 4439
r2120	790	1.0105	1351010	333200	5	18564 ±3597	22527± 4354

This table gives the rocking curves obtained from the central region of the tail end sample.

Table 7.06

Run File Number	First Axis secs	Wavelength Angstroms	Profile ref cps	Current ref cps	Count secs	Expt I.I	Corrected I.I
r2121	150	1.0300	1681577	331314	5	92058 ± 7761	92058 ± 7761
r2122	306	1.0250	1679091	332200	5	61613 ± 6447	61540 ± 6439
r2123	473	1.0200	1677394	332300	5	46394 ± 5752	46372 ± 5749
r2124	635	1.0150	1674232	332870	5	27152 ± 4357	27144 ± 4355
r2125	806	1.0100	3346090	333350	5	73498 ± 7451	36711 ± 3721
r2126	973	1.0050	1671019	333800	5	27968 ± 4569	27935 ± 4563
r2127	1149	1.0000	1668885	334100	5	26914 ± 4452	26893 ± 4485
r2128	1300	0.9950	1666868	3350780	5	27936 ± 4577	27870 ± 4566
r2129	572	1.0170	1664685	332800	5	34036 ± 4944	34228 ± 4971
r2130	605	1.0160	1662981	332820	5	31672 ± 4724	31851 ± 4755
r2131	674	1.0140	1662274	332900	5	39427 ± 5288	39695 ± 5323
r2132	703	1.0130	1661120	332990	5	38594 ± 5260	38873 ± 5298

This table gives the rocking curves obtained from 25mm towards the edge of the tail end sample.

Figure 7.29. This figure shows the experimental data obtained from the centre of the tail end sample, together with a stoichiometric simulation (solid line)

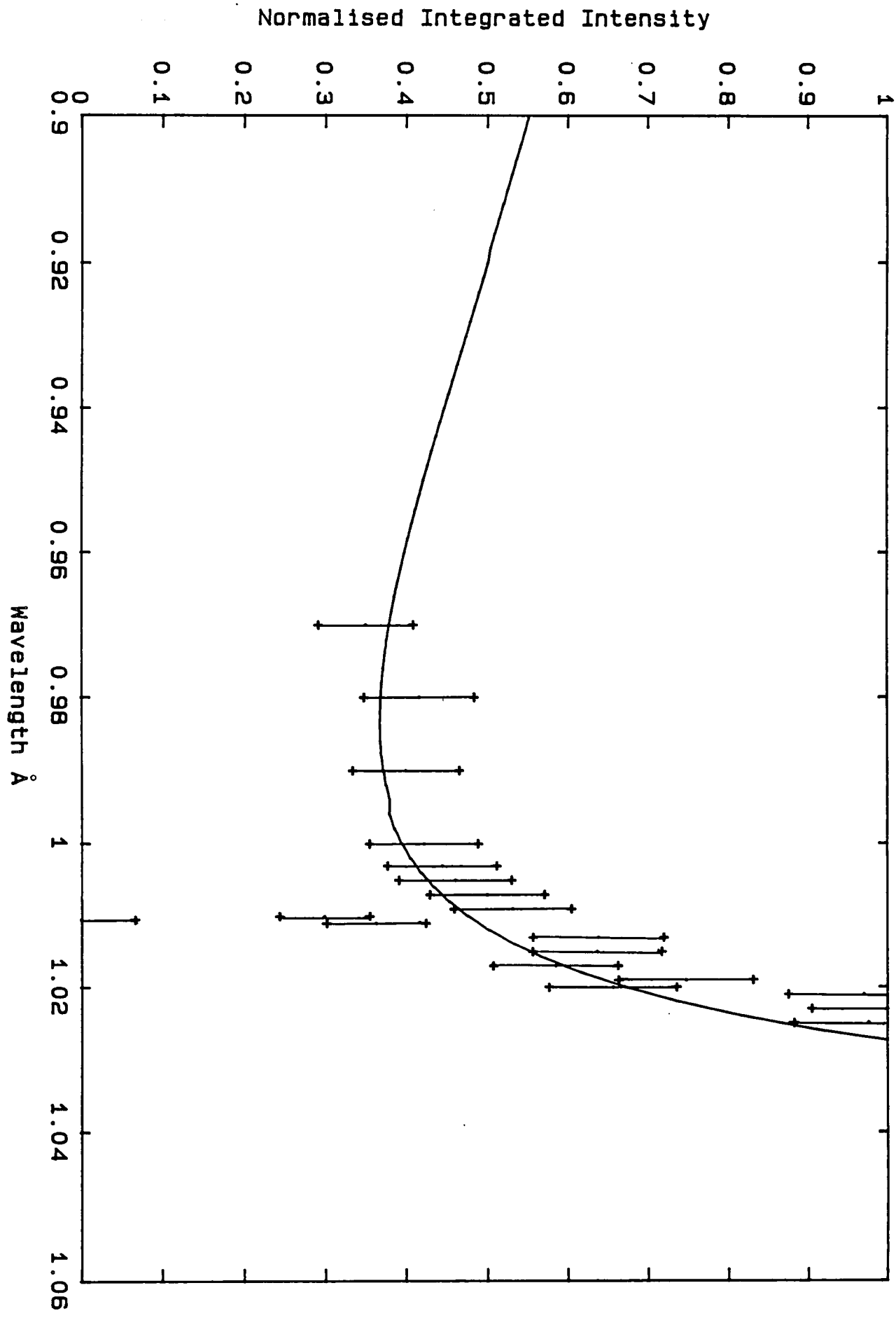

Figure 7.30. This figure shows the experimental data obtained from the centre of the tail end sample, together with a stoichiometric simulation (solid line)

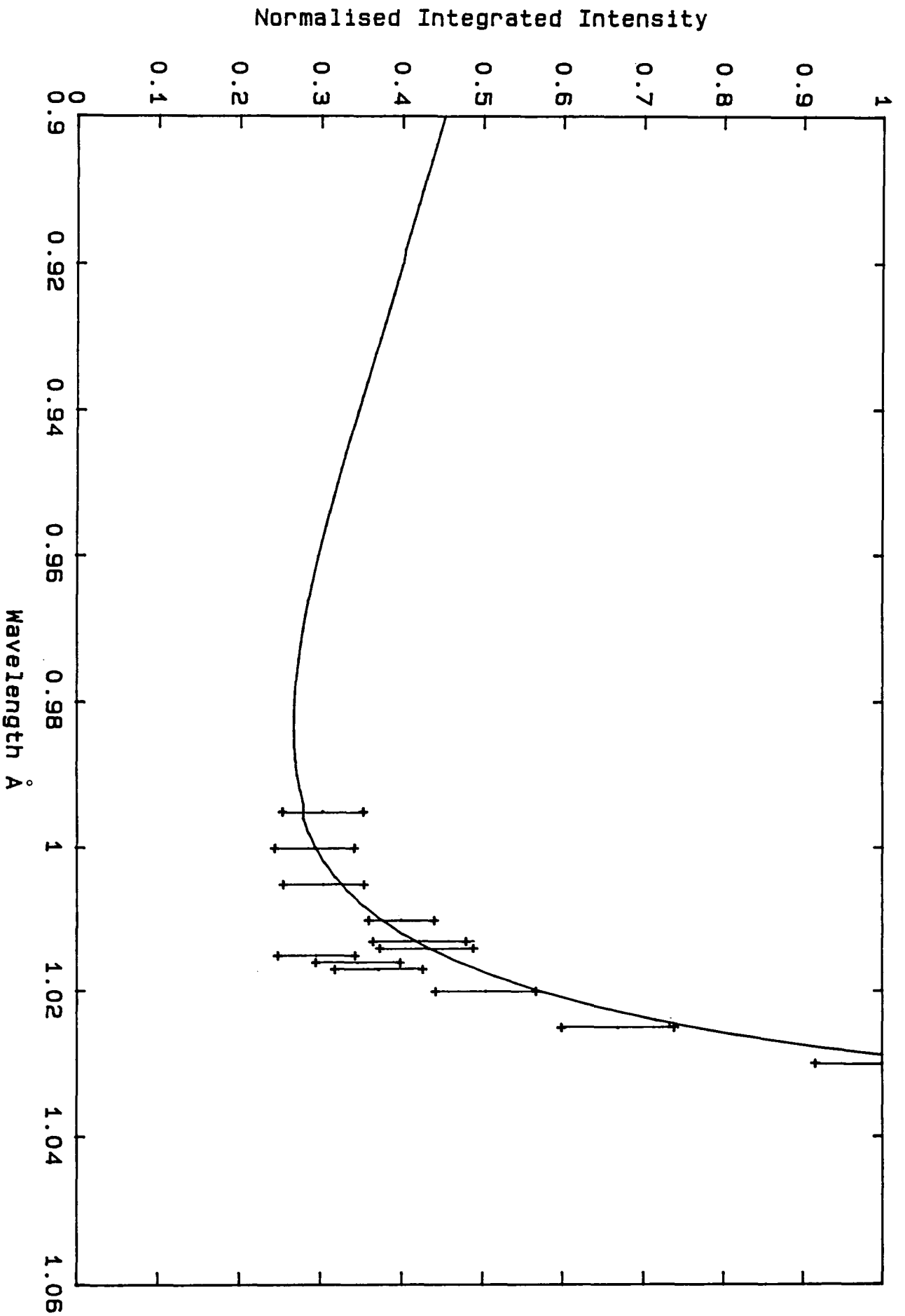

forbidden reflection was used. The K edges of InSb, as discussed previously, are at 0.4447Å and 0.4074Å respectively. The intensity of the Daresbury synchrotron source on line 7 is too low at these wavelengths and the wiggler line at Daresbury was required. These experiments were therefore performed on the wiggler line on station 9.4. The experimental set up and procedure is identical to that described previously except that a separate ion chamber was obtained which could be placed after the first reflection making the first axis scan redundant.

Because of the low angle of incidence for the 222 reflection over the range of wavelengths (0.3-0.5Å) around the K absorption edges and the small size of the samples, approximately 10mm by 10mm, only one position on each sample was studied. The procedure followed is identical to that described previously with the exception that greater care has to be taken in shielding the experiment. This arises because of the higher energy X-rays present and also because of the lower angle of incidence.

Table 7.07 gives the measured integrated intensities together with the peak heights and ion beam monitor rates from the MCP sample. The absorption edge of antimony is shown in figure 7.31, this edge displays much less structure than the As edge of GaAs. Figure 7.32 illustrates the corrected integrated intensity over the range of wavelengths for the MCP sample. It can be seen that the curves display much less structure than those obtained from the GaAs data and the minimum positions are much more clearly defined. The curves rise much more steeply at the lower wavelengths making the minimum range much narrower. Table 7.08 displays the measured integrated intensities together with the beam monitor rates for the McDonell Douglas sample. Figure 7.33 shows the absorption edge plot, while figure 7.34 shows the integrated intensity variation.

The minima obtained from the two samples are in the same range of wavelengths but one minimum is considerably narrower than the other and is at a higher intensity. The width of the minimum position may be interpreted as being dependant on the range of stoichiometry present in the illuminated beam area, the larger the range of composition the wider the minimum. The simulations shown in the two figure correspond to stoichiometric compositions. The fit is not as close

Table 7.07

Run File Number	Axis 1 secs	Wavelength Ångstroms	Profile Ref cps	Count secs	Expt I.I	Corrected I.I
r8218	1090	0.4056	14118	1	161621 ± 9404	161621±.9404
r8219	1170	0.4032	14327	1	73033 ± 4250	71970.±.4188
r8223	1490	0.3934	28768	1	149663 ± 9848	73450.± 4832
r8225	1570	0.3910	14179	2	79230 ± 6962	78890.±.6932
r8228	1650	0.3886	14187	1	86027 ± 7097	85610.±.7062
r8230	1730	0.3862	14178	1	85632 ± 7043	85270.±.7013
r8233	1810	0.3837	13616	1	87848 ± 7048	91090.±.7307
r8237	1890	0.3813	13469	1	95353 ± 7148	99950.±.7492
r8238	1186	0.4027	28285	2	98635 ± 7129	49230.±.3558
r8240	1202	0.4022	75357	5	224190 ± 9717	42000.±.1820
r8250	1169	0.4032	32097	2	124500 ± 7246	54760.±.3187
r8252	1185	0.4027	31893	2	116260 ± 7051	51460.±.3121
r8253	1201	0.4022	31844	2	109809 ± 6903	48680.±.3060
r8255	1217	0.4017	31844	2	104844 ± 6790	46480.±.3010
r8256	1233	0.4012	31549	2	102803 ± 6743	46000.±.3017
r8258	1249	0.4008	31541	2	102230 ± 6729	45760.±.3012
r8259	1265	0.4003	62900	4	200063 ± 9444	44900.±.2119
r8260	1281	0.3998	62202	4	209602 ± 9608	47570.±.2180
r8261	1373	0.3970	61796	4	208551 ± 9564	47650.±.2185
r8262	1297	0.3993	61661	4	208200 ± 9555	47670.±.2187
r8263	1329	0.3983	30674	2	184240 ± 7979	84800.±.3672
r8264	1345	0.3978	61253	4	204437 ± 8804	47120.±.2029
r8266	1361	0.3974	60859	4	220957 ± 9725	51260.±.2256

This table gives the rocking curves obtained from the MCP InSb sample.

Figure 7.31

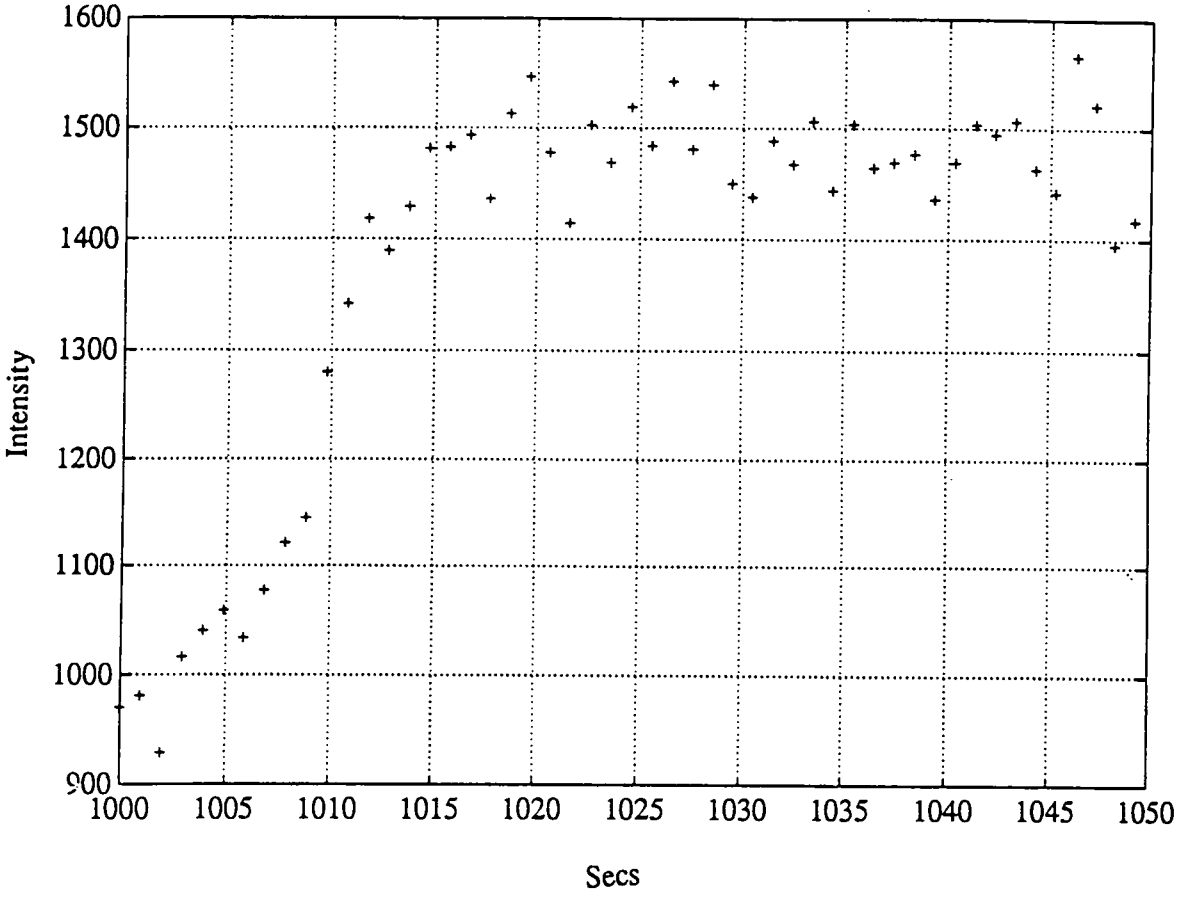

This figure illustrates the fluorescence yield near the K absorption edge of Sb taken from the InSb sample with a high dislocation density.

Figure 7.32. This figure shows the experimental data obtained from the high dislocation density sample, together with a stoichiometric simulation (solid line)

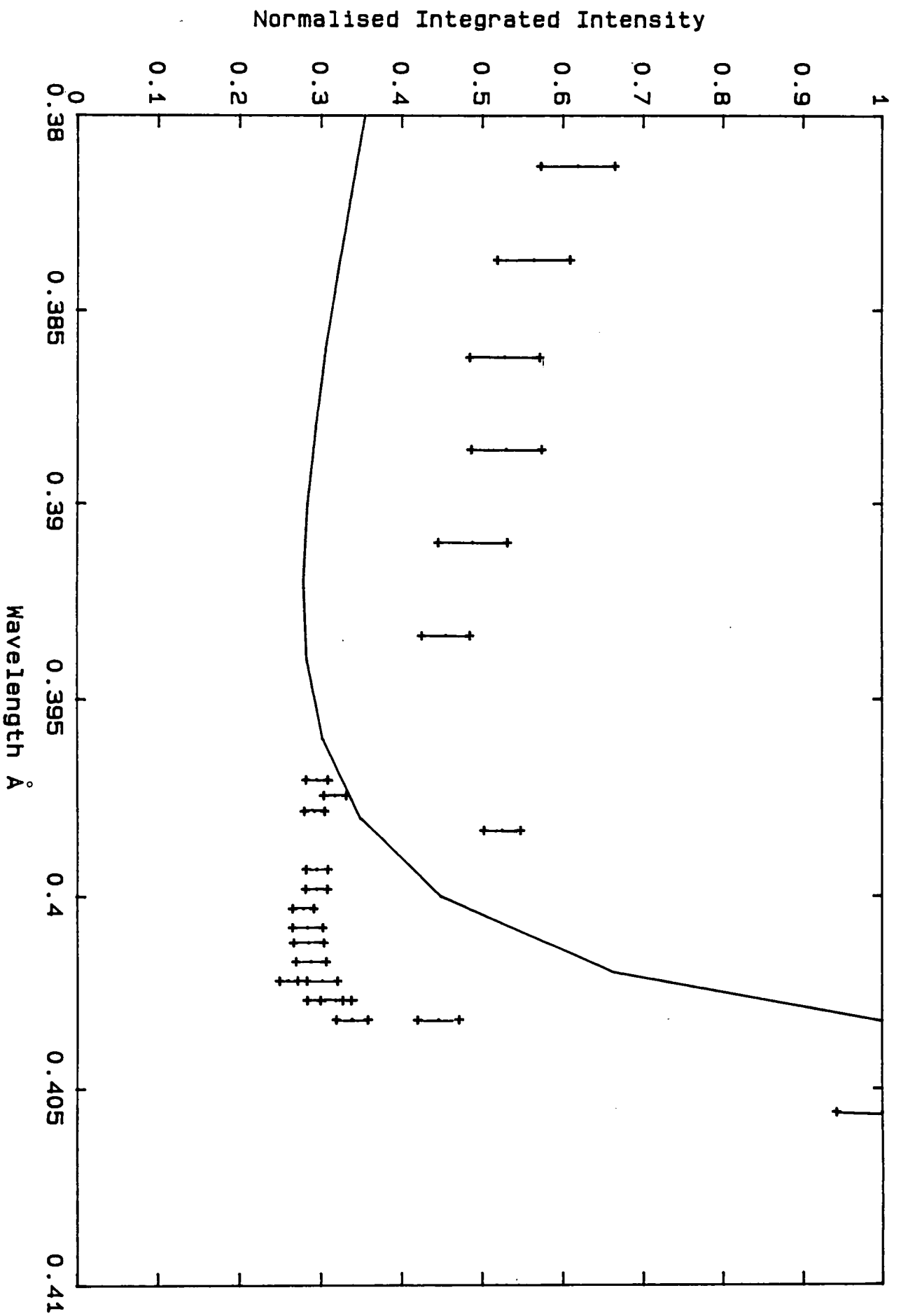

Table 7.08

Run File Number	Axis 1 secs	Wavelength Ångstroms	Profile Ref cps	Count secs	Expt I.I	Corrected I.I
r8175	1067	0.40627	234309	1	279500 ± 10982	279500 ± 10980
r8176	1146	0.40387	233682	1	101649 ± 7696	101650 ± 7700
r8177	1230	0.40127	231996	1	66432 ± 6770	66430 ± 6770
r8180	1473	0.39397	455087	2	119141 ± 9078	59570 ± 4539
r8181	1553	0.39147	453120	2	123353 ± 9139	61680 ± 4569
r8182	1633	0.38907	450760	2	137749 ± 9409	68870 ± 4704
r8183	1713	0.38667	449131	2	147899 ± 9552	73950 ± 4776
r8184	1793	0.38427	447954	2	163021 ± 9839	81510 ± 4919
r8185	1873	0.38177	444593	2	156764 ± 9690	78380 ± 4845
r8186	1970	0.37887	443891	2	174928 ± 9962	87460 ± 4981
r8187	1246	0.40087	912908	2	181657 ± 6322	47850 ± 3161
r8188	1262	0.40037	906365	4	187189 ± 9996	46800 ± 2500
r8189	1278	0.39987	905210	4	179067 ± 9823	44770 ± 2460
r8190	1294	0.39937	902149	4	175209 ± 9730	43800 ± 2428
r8191	1310	0.39887	898747	4	171301 ± 9532	42830 ± 2388
r8192	1326	0.39837	899053	4	232328 ± 13166	58080 ± 2428
r8194	1358	0.39747	894746	4	176679 ± 9739	44170 ± 2420

This table gives the rocking curves obtained from the McDonald Douglas InSb sample.

Figure 7.33

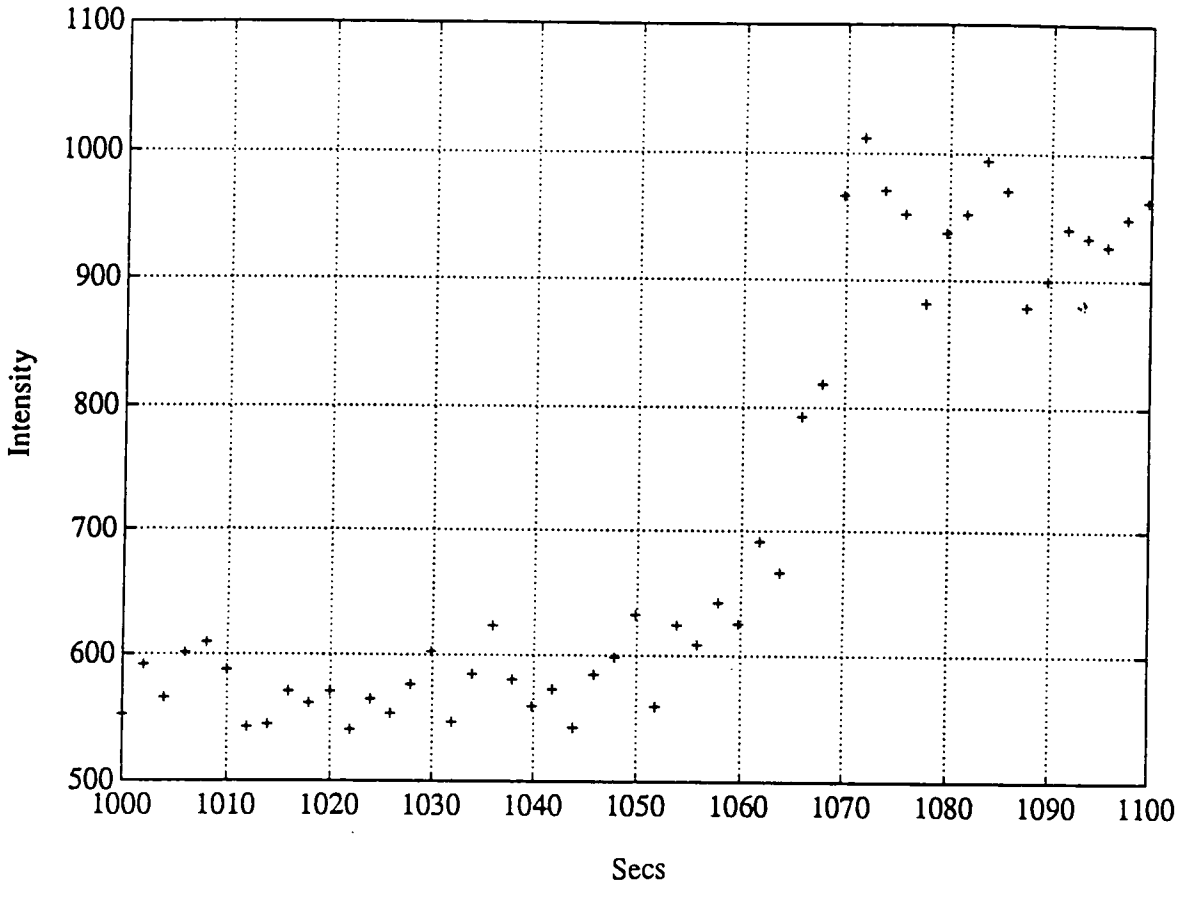

This figure illustrates the fluorescence yield near the K absorption edge of Sb taken from the InSb sample with a lower dislocation density.

Figure 7.34

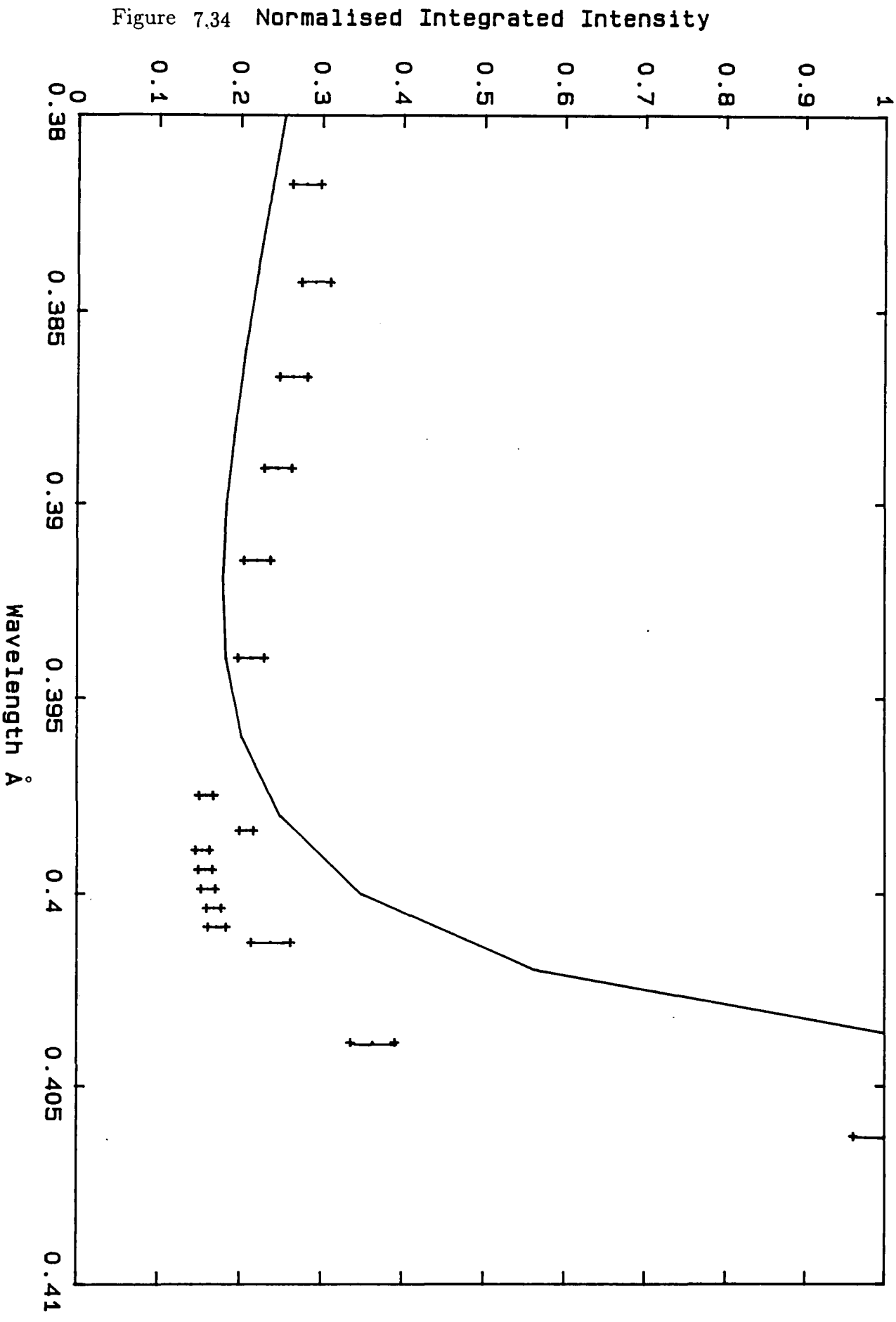
Normalised Integrated Intensity
0
0.1
0.2
0.3
0.4
0.5
0.6
0.7
0.8
0.9
1
0.38
0.385
0.39
0.395
0.4
0.405
0.41
Wavelength Å

as the fit between the GaAs simulation and the GaAs experimental results. The same fitting parameters were used, normalising the simulation and experiment at the same wavelength.

7.9.5 Discussion

The experimental results indicate that the integrated intensity variations close to K absorption edges are not described accurately by a simulation program based solely on the anomalous dispersion corrections of Cromer and Liberman. To account for the discrepancy between the experimental and simulated results one needs to consider possible factors which may affect the scattered intensity. The real scattering factors used in the simulation are those for the classically 'free' atoms. Since we are attempting to describe the behaviour of a crystalline material the atoms can not be regarded as 'free', but must be considered as part of the crystal lattice. Therefore one must consider how variations in the atomic scattering factor values for 'free' and 'bound' atoms affect the simulated results. In the crystal the valency electrons are not distributed evenly around each atom, as would be the case in an ideally covalent compound, but tend to drift towards the group V species. The details of the electronic structure however, are open to speculation and different approaches have led to different models being produced. Edwald and Honl (1936) postulated that the deformation of the outer electron charge was equivalent to an interstitial charge localized midway between nearest neighbours. This work was latter extented by Philips (1963) to include polar semiconductors. Biderback and Colella (1975), using X-ray diffraction data for the 222 and $\bar{2}\bar{2}\bar{2}$ from InSb, found that a more accurate model was a tetragonal distribution of charge. Using this model they determined that the discrepancy between the experimentally measured values and the simulated values was only 2 %. This compared favourably with the discrepancy between the 'free' atomic scattering factors and the experimental value which was 10 %. The effect of non-symmetric bonding or ionicity is therefore to change the values of the scattering factor for the constituent atoms. To study this effect in more detail a number of simulations were performed for InSb. The result of changing the real part of the scattering factor for antimony by ± 0.2 electrons is given in figure 7.35. From these curves it is clear that ionicity is extremely important in determining not only the position of the minimum but also the shape of the curve. Clearly then the simulation equation needs to have appropriate values

Figure 7.35. This figure illustrates the efffect on the curve as a function of ionicity.

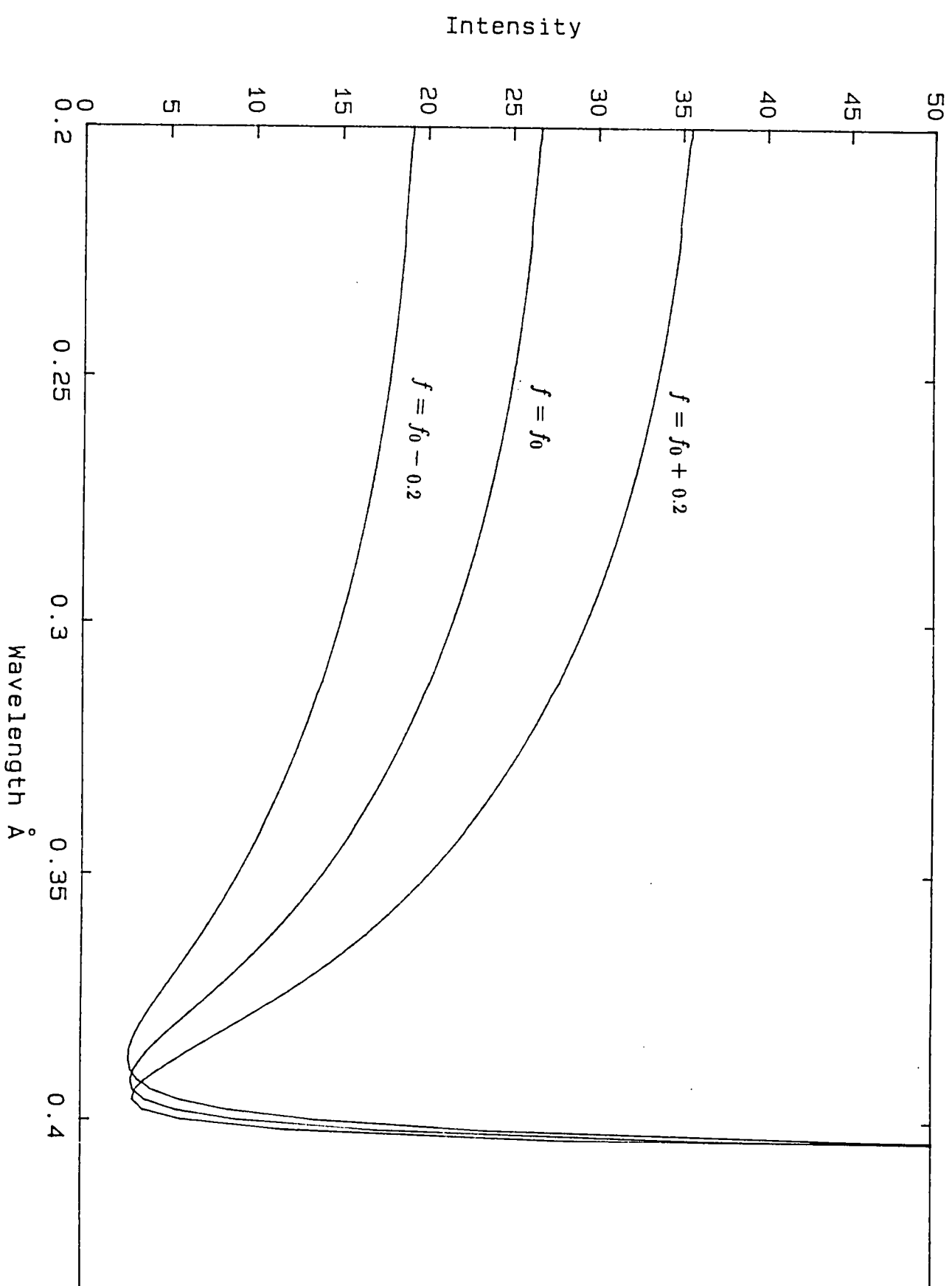

for the scattering factors of the compound atoms, since their effect on the absolute position of the minimum is extremely important. Unfortunately values for the scattering factors of individual atomic species located in a compound material depend on the effect of neighbouring atoms in the material. It is therefore difficult to obtain these values separately but they must be deduced from a correction to the 'free' atomic values.

The development of a model describing the behaviour of a vacancy concentration should also include the effect this vacancy concentration has on the scattering factor values, since the vacancy concentration would produce an equal number of ions with a different scattering factor. Clearly this is a possible cause of error in deducing the values of the scattering factors since the absolute position of the minimum is extremely sensitive to the difference in the real parts of the scattering factors for the group III and group V species.

The scattered intensity is also temperature dependent and this is may be described by the Debye-Waller factor. This calculates the loss in phase of scattered X-rays due to thermal motion and therefore acts to reduce the scattered intensity and is represented by,

$$f = f_o exp(-M) \tag{7.23}$$

where,

$$M = \frac{8\pi^2 u_s^2 sin^2\theta_b}{\lambda^2} \tag{7.24}$$

and u_s^2 represents the mean square displacement of the atoms from their mean positions in a direction perpendicular to the Bragg reflecting planes. This approach is only approximate since each atom should have its own value of M which may also be a function of the reflecting planes used. This function is usually simplified to the form,

$$B = \frac{6hT^2}{mk\Theta^2}(\phi(x) + \frac{x}{4})(\frac{sin\theta_b}{\lambda}) \tag{7.25}$$

where h is Plancks constant, k is Boltzmanns constant ϕ is an integral function of the temperature ratio x which is the ratio of Θ, the Debye temperature and the absolute temperature T. Values of the function ϕ can be found in table 5.2.2B (Vol III of the international tables). Accurate values for the Debye temperature for GaAs and Insb are not published in the international tables, however Bilderback

and Colella (1975) have deduced the Debye temperatures for indium and antimony in InSb using measured X-ray scattering data. These values are 148 ^oK and 158 ^oK for indium and antimony respectively. Using these values in the above expression allows the Debye-Waller factor for indium and antimony to be calculated; 0.9157 and 0.9165 respectively. Using these revised figures in the simulation program allows the effect of the Debye-Waller factor to be simulated. Figure 7.36 shows that there is a shift in the absolute position of the minimum together with a change in its shape. This should also therefore be included in the simulation program.

Together with the problems mentioned above all the curves, particularly the GaAs data, displayed a structural variation in the intensity larger than the statistically calculated variation based on a normal distribution. This statistical variation is indicated by the error bars on the experimental data points at the 3 sigma level. This structure may be accounted for by near edge structure, XANES, since these oscillations extend from the low wavelength side of absorption edges to approximately 300eV or 0.6$\mathring{A}$, which is consistent with the region of study. This structure was clearly seen in all four curves taken from the GaAs samples and to a lesser extent on the InSb samples. Some consistency in the oscillations is also apparent particularly between the curves taken from the centre and edge of the seed end sample. Unfortunately this structure prevents an accurate location of the minimum position to be made and since this was not calculated in the simulation program it was not possible to detect a significant difference in minimum positions between the centre and edge of the GaAs samples. Development of the simulation program to take this into account would clearly be a useful extension to this work. The InSb experimental results displayed a clearly defined minimum position for both the samples studied. Again no significant difference in the minimum positions could be detected, however the curve from the higher dislocation sample did have a steeper rise on the low wavelength side of the minimum. This is consistent with the simulations for a higher degree of non-stoichiometry, however clearly from the previous discussion a more comprehensive simulation program needs to be developed.

7.9.6 Topographic study of GaAs

The previous work used absolute goniometry to attempt to obtain evidence

Figure 7.36. This figure illustrates the effect of temperature using the Debye-Waller correction factor.

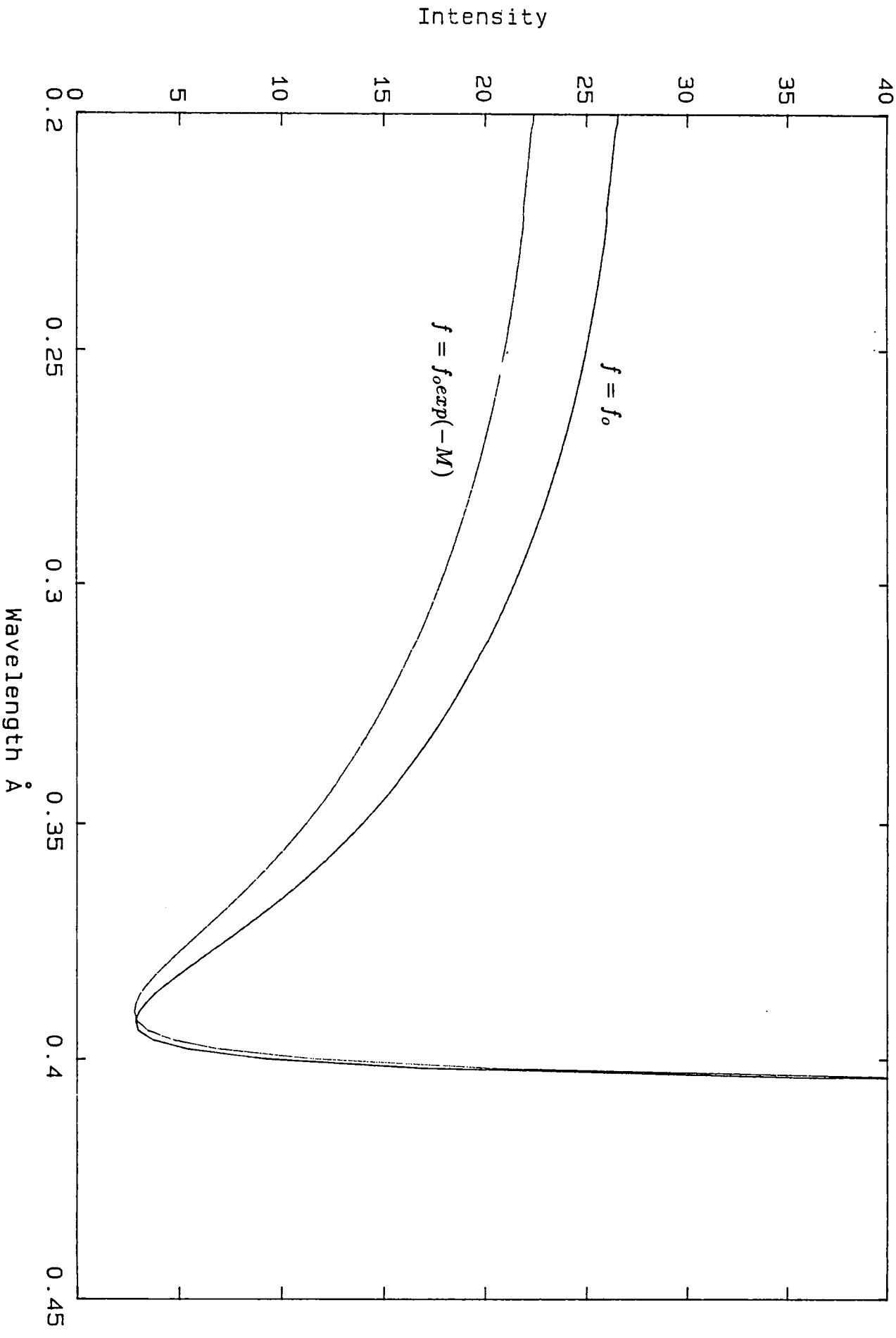

of non-stoichiometry. In the study to follow attempts are made to observe non-stoichiometry from intensity variations. From the theory previously outlined above it may be possible to observe variations in the integrated intensity distributions on a topograph. The basis of this study was to identify, from the simulations, wavelengths at which, in one case the diffracted intensity should be ideally independent of stoichiometry and in the other case that the diffracted intensity should be strongly dependent on stoichiometry. From the simulations of two different GaAs compositions, it was observed that for allowed reflections the diffracted intensity change was small near to the minimum position, and comparatively large at a much lower or much higher wavelength.

A GaAs HB grown sample was studied at two wavelengths using the 002 reflection one at 1.0$\mathring{A}$ (close to the minimum position) and a second at 0.7$\mathring{A}$. To compare two topographs with the objective of observing a change in the diffracted intensity requires carefully controlled exposure and development times. To achieve the same exposure for each topograph the exposure time was scaled to the peak height of the rocking curves and the development time was kept constant for both topographs.

The experimental procedure was firstly to identify the minimum position by successively changing the wavelength until the minimum diffracted intensity was obtained. The rocking curve peak height was then noted and the slits opened to expose a large area of the sample, the resulting topograph is given in plate 7.02. The wavelength was then changed to 0.7 $\mathring{A}$ and the rocking curve recorded. Following correction for the exposure time a topograph was taken and the result is given in plate 7.03. Plate 7.04 shows the output from the double bounce beam conditioner.

It was hoped that comparison of two topographs would reveal long range variations in the diffracted intensity from the centre to the edge of the sample, although this was not observed. There did appear to be some local variation in the diffracted beam intensity, however there are inherent problems in making comparisons of local variations in intensity of two topographs taken at two different wavelengths and hence two different angular positions. These difficulties include ensuring the topographs are taken at exactly the same positions on the rocking curve as the

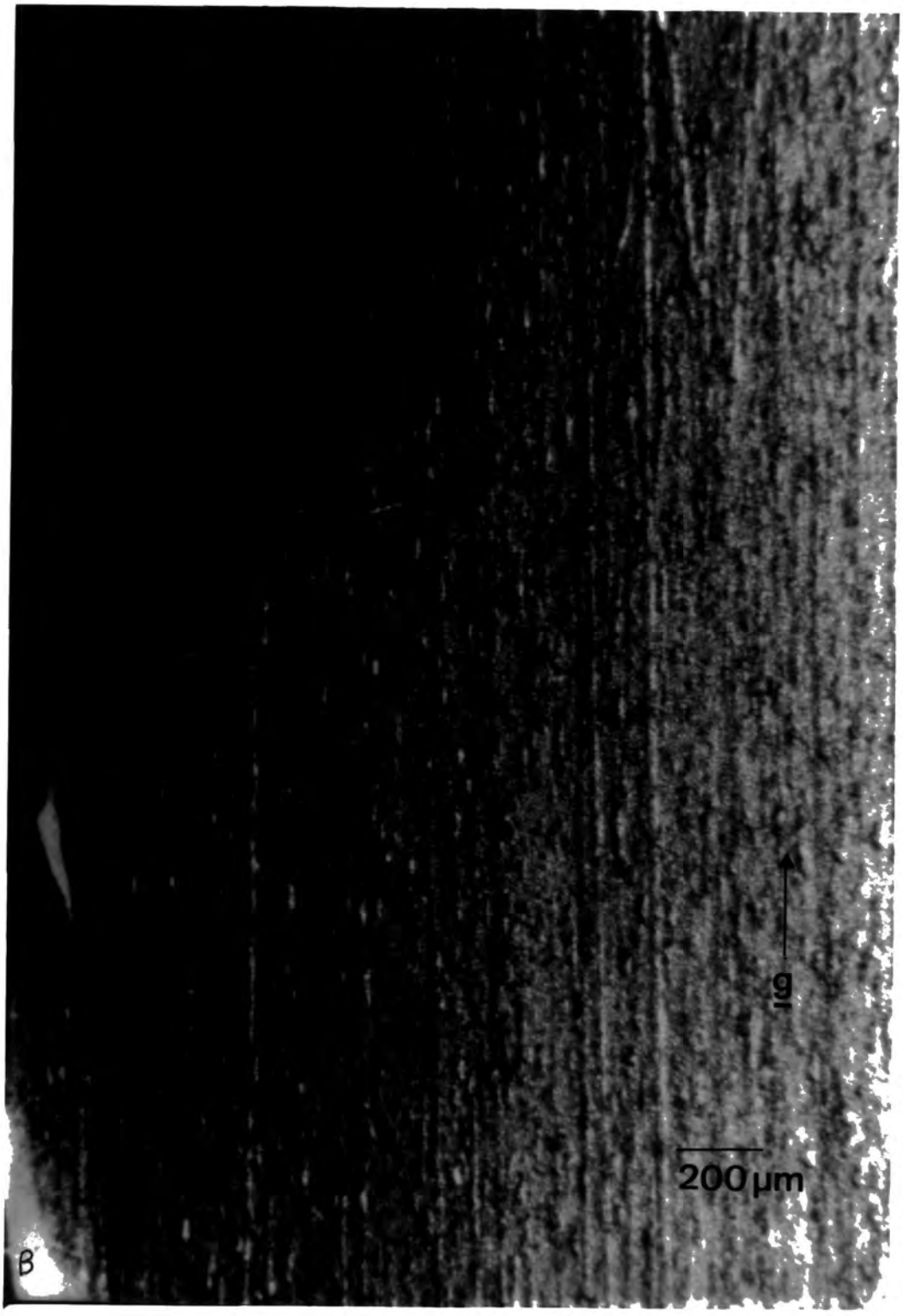

Plate 7.02 The 00 2 topograph at 1.0 Å from the HB grown crystal.

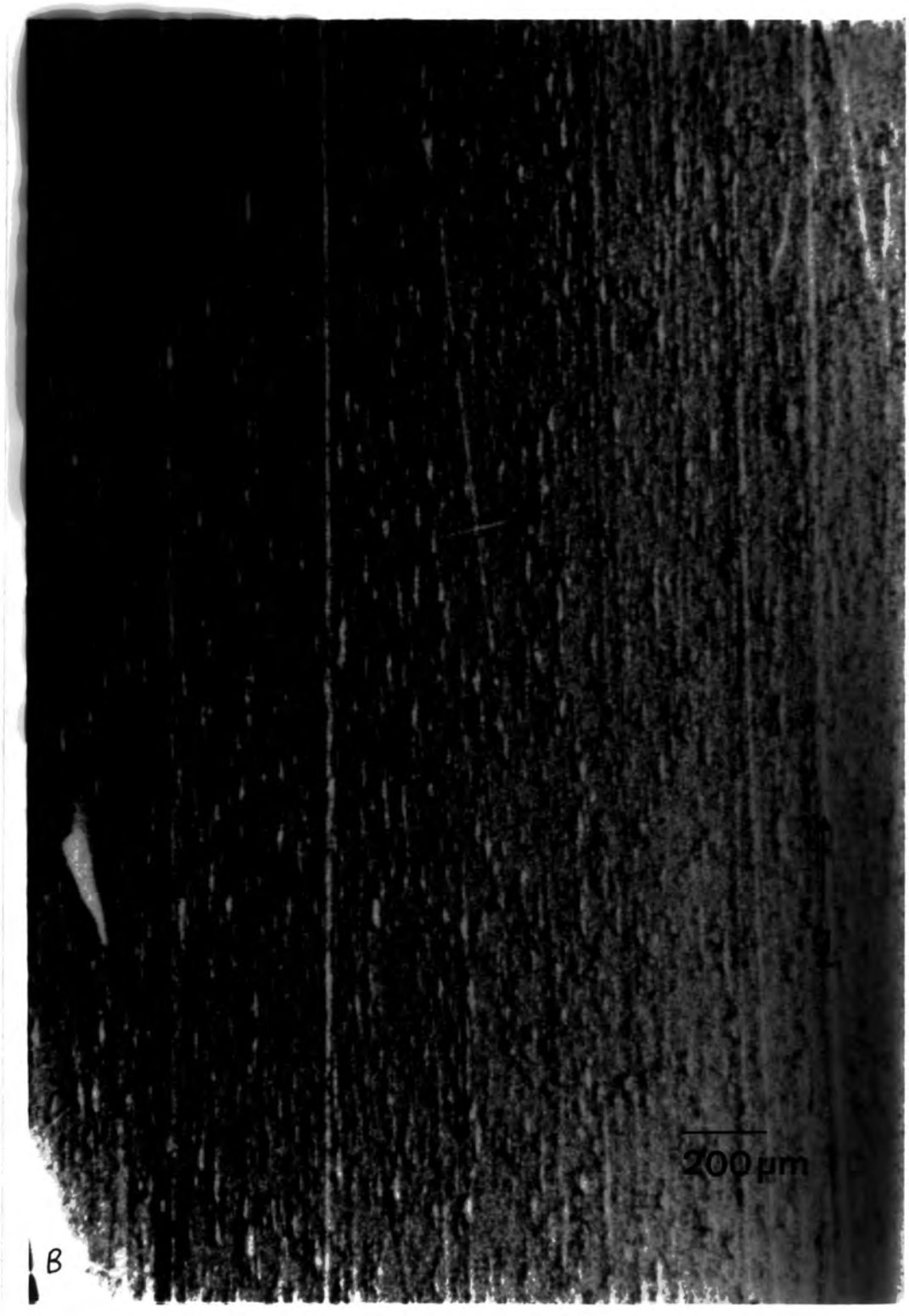

Plate 7.03. The 002 topograph at 0.7 Å from the HB grown crystal.

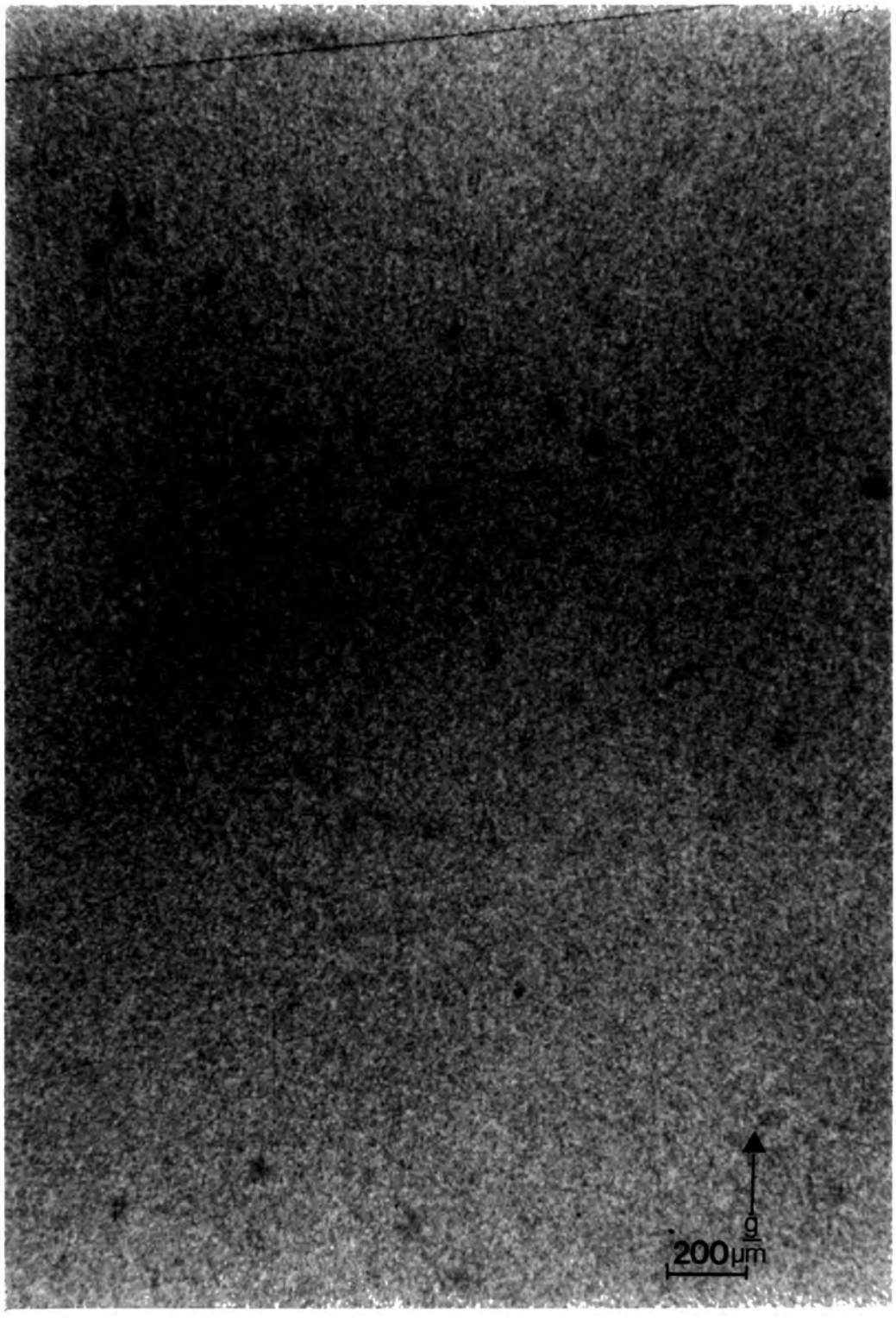

Plate 7.04 The 111 reflection from the double bounce beam conditioner.

strain sensitivity is very different from the peak of the rocking curve to the flank, and there is also the need to ensure that exactly the same area of the sample is illuminated. However, visual interpretation of the topographs suggests that all features visible are present in both topographs and are strain related. Since the double crystal technique is sensitive to strains even under conditions of kinematical diffraction, this is quite reasonable. In both topographs a region of enhanced scattering is observed corresponding to scattering at the peak of the rocking curve. Strain in the crystal results in a loss of intensity away from this region. Scratches are also seen running vertically together with an area of damage to the emulsion marked with the letter B. The defect contrast observed consists of groups of dislocations arranged in a cellular and linkage structure. Contrasts in these features is higher towards the area of enhanced intensity, since this region is more sensitive to strain being produced from the peak and flanks of the rocking curve.

7.10 Summary and conclusions

From the introductory discussion it can be seen that there is a need to develop non-destructive techniques to determine stoichiometry variations in III-V semiconductor materials. Existing non-destructive techniques such as ion beam scattering and EPMA allow very small impurity concentrations to be detected but do not allow an exact (greater than 2%) measurement of their concentration to be made. Destructive techniques such as coulombic titration do allow concentrations of elements to be determined with accuracies of 100ppm, but suffer from the limitations which include destruction of the sample and defect non-identification. From the discussion of Fujimoto's technique of relating non-stoichiometry directly to measured integrated intensity variations it was shown that this technique suffers from a number of difficulties. These include careful monitoring of the stability of the X-ray source and counting electronics together with predicting the behaviour of the intensity as a function of wavelength and the presence of harmonic contamination. Harmonics are of major importance since the integrated intensity of strong reflections are dependant on the mosaic spread in the crystal and therefore are sensitive to dislocation density. By using only a single reflection, higher order harmonics may be present. In this study it has been shown that by using a channel cut beam conditioner with a suitable choice of reflections from the conditioner and the sample that it is possible to eliminate harmonic contamination while suffering only a

small loss in intensity. Following the simulated study of the behaviour of Bragg reflections near to K absorption edges using the anomalous dispersion corrections of Cromer and Liberman (1989), it was shown that the dependence of strong and weak reflections were considerably different in the region of the absorption edges. Anomalous dispersion effects are larger and as such are fundamental in determining the integrated intensity of reflections. The simulations of the 004 reflection from GaAs and InSb around the K absorption edges showed a greatly reduced intensity indicating that the structure factor is greatly reduced at the absorption edges. Simulations of the 002 reflection again revealed distinct changes in the intensity at the absorption edges, since in quasi-forbidden reflections the atomic scattering factors subtract rather than add. The curve also displayed a minimum position located on the low wavelength side of the edges. Following simulations in which a vacancy model was developed, this minimum was found to depend, both in position and shape, on the degree of non- stoichiometry. Simulations indicated that the effect of a change in vacancy concentration is to move the minimum position to a higher wavelength and also to reduce its width. The amount of movement for GaAs and InSb was studied and the results indicated that a vacancy concentration of the order of that predicted by Logan and Hurle (0.01%) should be detectable. This therefore allows the stoichiometry to be studied without the major limitations of a direct comparison with intensity variations since the measurement of the minimum is solely dependent on the wavelength calibration of the goniometer.

To investigate the behaviour of the integrated intensity with wavelength there is a need for a high intensity over a wide range of wavelengths. It was therefore necessary to use the Daresbury SRS. Experiments were undertaken on line 7 for the GaAs work and line 9, the wiggler line, for the InSb work. The wiggler line was required since the K absorption edges of InSb are located at a lower wavelength beyond the useful range of the standard beam line. The development of the procedure required to perform these experiment was only achieved after many days of experiments and many hours of careful planning.

Experiments were performed on two GaAs (001) wafers and two InSb (111) crystals using the quasi- forbidden reflections (002) and (222) respectively. It was shown that the experimental minimum positions and the shape of the diffracted intensity curve differed consistently from the simulated results. To account for the

discrepancies between the experimental and simulated results one needs to consider both experimental errors and factors excluded from the simulation process which could influence the intensity of the scattered beam. These factors were discussed in the previous section and high lighted the need for a more sophisticated simulation program and the difficulties encountered in this study such as the limitations imposed by available flux and the structure found in the minimum position. The GaAs results showed no detectable differences in either the minimum position or shape from the centre and edges of the crystal studies. However the InSb data was much more promising with a more sharply rising minimum position being obtained from the crystal of known high dislocation density. The discrepancies between the simulated results and the experimental results were larger for InSb than for GaAs which is consitent with the exclusion of ionicity from the simulation program since InSb is more ionic. The possiblity of making ionicity measurements using the minimum position technique has also been discussed in the previous section. This technique would allow a more detailed study of how ionicity affected the minimum position and its role in non-stoichiometry measurements.

Appendix A

Discussion and suggestions for further work

Double crystal topography and diffractometry have been used to develop novel approaches for the study of the structural and compositional uniformity of III-V semiconductor compounds.

The effect of interface abruptness has been modelled by comparing in detail the experimental rocking curves with simulations. This work has shown that double crystal rocking curves of very different structures are difficult to distinguish in the asymmetric glancing incidence geometry and that scattering far from the Bragg peak is extremely important in distinguishing between rival structures. In order that this can be achieved, lengthy exposure times and careful shielding are required. The development of this work to include structures of varying layer thicknesses and degrees of abrupt interfaces would be useful, together with the possibility of inspecting more than one layer.

In the study of $LiNbO_3$, synchrotron radiation has been shown capable of imaging a large single crystal, resolving grain and sub grain boundaries at the arc sec level.

The importance of laser structures in the semiconductor industry is clear, existing double crystal techniques have been shown capable of detecting variations in the active layer by interference effects present on the confining layer Bragg peak. In the present topographic study fringes have been observed which may be Moire fringes. These fringes have been shown to be independent of the rotations about the sample surface and are only observed on the confining layer peaks and adjacent pendellosung fringes. The possibility of these fringes being due to a constant variation in the active layer thickness or composition has also been studied. Although a variation in the AlGaAs sample was observed, the measured fringe spacing on the topographs was inconsistent with the fringes being thickness fringes. The fringes were therefore concluded to be Bragg case Moire fringes. The spacing of the fringes is defined solely by the difference in the mismatch and/or rotation of one confining layer relative to the other. This has the potential of resolving differences in one

layer relative to another at the atomic level. Clearly more work using a greater number of samples with a range of active layer thicknesses, grown by different techniques, would be constructive.

The stoichiometry study has shown both the importance and variety of experiments that may be performed using synchrotron radiation. The behaviour of the reflections close to absorption edges has shown that dramatic changes occur in both the intensity of the diffracted beam and the mode of diffraction taking place, demonstrating that strong reflections may become weak and weak reflections may become strong. The dependence on the anomalous dispersion corrections is fundamental in determining the diffracted intensity. The development of the minimum position method of detecting variations in stoichiometry was hampered by structure in the minimum area, making the exact position of the minimum difficult to detect. However measurements taken from the centre of the crystal seem to have a narrower range than those taken from the edge and comparison between a seed end crystal and a tail end indicate a larger range of stoichiometry may be present in the tail end crystal. The study of two samples of InSb revealed a dramatic difference in the shape and width of the minimum position, (a larger width corresponding to a larger range in stoichiometry) corresponding to the narrower width being produced from the lower dislocation density material.

This study has also highlighted a number of other applications of the minimum position method for detecting variations in the structure factor, without the dependence on absolute intensity measurements. One possible application may be in the determination of the degree of asymmetric bonding in partially covalent materials.

Appendix B

Anomalous dispersion theory

The introduction to classical anomalous dispersion theory outlined below follows James (1948). This theory attempts to describe the behaviour of the atomic scattering factor, f, when the wavelength of the incident X-ray is no longer assumed to be large in comparison with the atomic spacing.

An electron may be considered as a dipole oscillator of charge $-e$ and mass m and having an absorption frequency ω_s. An incident X-ray of wave vector $\underline{k}$ and frequency ω, generates forced simple harmonic motion with a damping factor proportional to its velocity. The amplitude, A of the resulting scattered wave is given by,

$$A = (\frac{e^2}{mc^2})\frac{\omega^2 E_0}{\omega_s^2 - \omega^2 + ik\omega} \qquad (B.01)$$

By definition the scattering factor is then given by

$$f = \frac{\omega^2}{\omega^2 - \omega_s^2 - ik\omega} \qquad (B.02)$$

The change in sign associated with the denominator is significant as it indicates that the scattered wave from a "free" electron is opposite in phase to the incident beam. Suppose now that a plane wave passes through a medium in which there are N dipole oscillators per unit volume each of which scatter a wave in phase with the primary beam. This requires the value of the scattering factor to be negative. Following the recombination of the waves associated with each dipole the resultant wave is $\frac{\pi}{2}$ behind the primary beam. This has the effect of producing a refractive index ,n, given by,

$$n = 1 - \frac{2\pi N e^2 f}{m\omega^2} \qquad (B.03)$$

In the above case the scattering factor is negative corresponding to the condition $\omega << \omega_s$ and refractive index is greater than unity. Similarly for positive values of the scattering factor $\omega >> \omega_s$ and the refractive index is then less than unity, in neither case is there any appreciable absorption. However when $\omega = \omega_s$ then both the amplitude and phase of the scattered wave is strongly dependent on the frequency of the incident radiation. The scattering factor is then complex and is given by,

$$f = f' + if'' \tag{B.04}$$

This notation highlights the imaginary term as corresponding to an absorption component which lies $\frac{\pi}{2}$ out of phase with the scattered wave.

The real and imaginary terms can be written as

$$f' = \frac{\omega^2(\omega^2 - \omega_s^2)}{(\omega^2 - \omega_s^2)^2 + k^2\omega^2} \tag{B.05}$$

and

$$f'' = \frac{k\omega^3}{(\omega^2 - \omega_s^2)^2 + k^2\omega^2} \tag{B.06}$$

The imaginary term can be related to the absorption coefficient per dipole by Darwin's optical absorption theorem giving rise to equation B.07.

$$\mu(\omega) = \frac{4\pi N e^2 f''}{m\omega c} \tag{B.07}$$

Extension to an atom containing $g(1)$ oscillators of frequency ω_1 to $g(s)$ oscillators of frequency ω_s is made by considering there to be zero absorption allowing the real part of the scattering factor to be given by,

$$f' = \sum_s \frac{g(s)\omega^2}{w^2 - w_s^2} \tag{B.08}$$

which may be written as,

$$f' = \sum_s g(s) - \sum_s \frac{g(s)\omega_s^2}{\omega_s^2 - \omega^2} \qquad (B.09)$$

where $g(1)$ is the oscillator strength associated with the frequency ω_1. In order to extend our model further one needs to deduce the distribution of oscillators within an atom. This may only be achieved by considering a quantum mechanical approach originally discussed by Waller (1927). Using quantum mechanics it is no longer valid to consider the concept of predicting the exact position and velocity of an electron. These quantities can only be expressed in terms of a probability and Waller considered the scattering process as a small perturbation of the atomic wave function periodic with time. In this approach the frequency of the incident radiation is assumed to be large in comparison with the orbital dimensions, this assumption allows the real part of the scattering factor to be given by

$$f = f_{n,m} - \sum_k \frac{2\hbar}{m\omega_{kn}} B^0_{nk}(B^*_{nk})_R \left[\frac{w_{kn}^2}{\omega_{kn}^2 - \omega^2}\right] \qquad (B.10)$$

where $f_{n,m}$ is the atomic number, B^0_{nk} is the Bohr frequency associated for the transition from state n to a second state k.

This then allows the real part of the scattering factor to be expressed in a more general way as,

$$f = f_0 + f' \qquad (B.11)$$

where f_o corresponds to the free atomic scattering factor.

In deducing equation B.11, no allowance has been made for energy loss; hence this term corresponds to the real part of the scattering factor. Inspection of equation B.10, reveals that for each classical oscillator there is a term in equation B.10 corresponding to the transition probability from a state n to a higher state k. The oscillator strength is then represented by,

$$g(k,n) = \frac{2\hbar B^0_{nk}(B^*_{nk})_p}{m\omega_{kn}} \qquad (B.12)$$

To each natural oscillator in the classical approach there is a corresponding frequency, ω_{kn}, which is the Bohr frequency associated with the transition from an energy state k to an energy state n. The density of energy states is given by $\frac{dg}{d\omega}$ and the total number of states in an interval $d\omega$ is given by summing from the absorption frequency to infinity, that is over the continuum of energy states. The oscillator strength is then given by,

$$g_K = \int_{\omega k}^{\infty} \frac{dg}{d\omega_k} \quad d\omega \qquad (B.13)$$

this then allows f' to be given by

$$f' = \sum_k \int_{\omega k}^{\infty} [\frac{dg}{d\omega_k}] \frac{\omega^2 d\omega}{\omega_i^2 - \omega^2} \qquad (B.14)$$

where

$$\frac{dg}{dw_k}$$

is the oscillator density at frequency ω corresponding to the summation over the k continuum and ω_i is the frequency of the incident radiation.

7.10.1 Oscillator strength calculations

The determination of the oscillator strength requires the atomic wave functions to be calculated from quantum mechanical wave functions. Before this approach is considered a simplified method is discussed in which the connection between the oscillator strength and the absorption coefficient is considered.

Let $E(\omega)d\omega$ be the energy passing per square cm per second in an incident wave train between frequencies ω and $\omega + d\omega$. Each dipole absorbs energy equal to

$$E(abs) = \int_{\omega 1}^{\omega 2} \mu_a(\omega) E(\omega) d(\omega) \qquad (B.15)$$

and since μ_a represents the absorption per dipole,

$$\mu_a(\omega) = \frac{4\pi N f'' e^2}{m\omega c} \tag{B.16}$$

then the energy is given by

$$E(abs) = E(\omega_s)\frac{4\pi e^2 k}{mc}\int_{\omega_1}^{\omega_2} \frac{\omega^2 d\omega}{(\omega^2 - \omega_s^2)^2 + k^2\omega^2} \tag{B.17}$$

The limits of the integration may be replaced by 0 and ∞ since the range of summation is not important as long as it includes ω_s and the integral can then be shown to have the value

$$E(abs) = \frac{2\pi^2 e^2}{mc} E(\omega_s) \tag{B.18}$$

That is each dipole absorbs a fraction

$$\frac{2\pi^2 e^2}{mc} \tag{B.19}$$

of the incident energy. Then the number of oscillators in the neighbourhood of ω is given by $\frac{dg}{d\omega}d\omega$ and the absorption coefficient is given by taking the fraction of the energy absorbed per atom over the energy incident per square metre. It follows that,

$$\mu_a = \frac{2\pi^2}{mc} E(\omega)/E(\omega)d\omega \tag{B.20}$$

and

$$\frac{dg}{d\omega} = \frac{mc}{2\pi^2 e^2}\mu_a(\omega) \tag{B.21}$$

This implies that the oscillator strength and the absorption coefficient are related by only a numerical factor and the value of $\frac{dg}{d\omega}$ may be determined from the absorption coefficient. To allow the calculation of the oscillator strength from the absorption coefficient, Parratt and Hampstead (1954) used the relation

$$\mu(\omega_a) = (\frac{\omega_a k^n}{\omega})\mu(\omega_k) \tag{B.22}$$

for

$$\omega > \omega_k$$

and

$$\mu_a(\omega) = 0$$

for

$$\omega < \omega_k$$

n is a value approximately equal to $\frac{7}{3}$, $\frac{5}{2}$, $\frac{11}{4}$ for the K, L, M absorption edges respectively and ω_k refers the K absorption frequency. This then allows the total oscillator strength for the k continuum to be expressed as

$$g_K = \int_{\omega K}^{\infty} \frac{mc}{2\pi^2 e^2} \mu_a(\omega) d\omega \qquad (B.23)$$

and

$$g_K = \frac{mc}{2\pi^2 e^2} \mu_a(\omega_k) d\omega \int_{\omega K}^{\infty} (\frac{\omega_k}{\omega})^n d\omega \qquad (B.24)$$

which can be evaluated as

$$g_K = \frac{mc}{2\pi^2 e^2 (n-1)} \omega_k \mu(\omega_k) \qquad (B.25)$$

which therefore allows the real scattering factor to be given by

$$f'_k = \frac{mc}{2\pi^2 e^2} \mu(\omega_k) \omega_k^n \int_{\omega K}^{\infty} \frac{\omega^2 d\omega}{(\omega_i^2 - \omega^2)\omega^n} \qquad (B.26)$$

This equation has been integrated for the general case by Parratt and Hampstead (1954). These authors give values of f' for various values of n as a function of g_k and x is the ratio of $\frac{\omega_i}{\omega_k}$.

7.10.2 Calculation of the oscillator strength using wave functions

Honl calculated oscillator strengths using hydrogen like wave functions which he used to model the K electron shells. Extensions to the L and M shell can not

therefore be readily made and Honls calculations can only be regarded as approximations for the heavier elements. In this approach Honl used the calculations of Sugiura (1927) in which the oscillator density is given by

$$\frac{dg}{dz} = \frac{2^7 g(z)}{3z^4} \tag{B.27}$$

where

$$g(z) = \frac{e^{-4/\sqrt{z-1}(tan^{-1}\sqrt{z-1})}}{[1 - e^{-2\pi\sqrt{z}-1}]} \tag{B.28}$$

where z is the ratio of $\frac{\omega}{\omega_o}$ Honl showed that in the limit $1 < z < 4g(z)$;

$$\bar{g}(z) = \frac{e^{-4}}{3}(4z - 1) \tag{B.29}$$

This results in a value of the oscillator strength per electron of 0.434. Following a study of the best experimental data at the time, Honl indicated two main areas of error in these calculations. Considering in more detail the electron environment in the K shell, corrections were introduced which resulted from the screening effect of the first electron on the second and the effective modification of the Coulombic field due to the higher energy orbital electrons. Following these terms Honl deduced an expression for the oscillator strength, which is given in equation B.30 and from this expression the real and imaginary terms which can be calculated as a function of wavelength. These are given in B.31 and B.32.

$$g_K = \frac{2^8 e^{-4}}{9}\left(\frac{2}{(1-\delta k)^2} - \frac{1}{3(1-\delta k)^3}\right) \tag{B.30}$$

$$\delta k = \frac{(A - \frac{911}{\lambda_t})}{A} \tag{B.31}$$

$$A = (z - 0.3)^2 + 1.33 \times .10^{-5}(z - 0.3)^4 \tag{B.32}$$

$$f' = \frac{2^7 e^{-4}}{9}[\left[\left(\frac{4}{(1-\delta k)^2}\right)x^2 log_e|x^2-1| - \frac{1}{(1-\delta k)^3}[\frac{2}{x^2} + \frac{1}{x^3} log_e\left|\frac{x-1}{x+1}\right|\right] \quad (B.33)$$

$$f''_k = \frac{2^7 e^{-4}}{9}\pi\left(\frac{4}{x^2(1-\delta k)^2} - \frac{1}{x^3(1-\delta k)^3}\right) \quad if \quad x > 1 \qquad (B.34)$$

$$f''_k = 0 \qquad if \qquad x < 1$$

7.11 Relativistic model of anomalous dispersion

In 1965 Cromer developed a relativistic approach to calculations of oscillator strength. In his approach Cromer used self-consistent field Dirac wave functions; that is the wave functions derived are discrete states. Using these wave functions dispersion corrections were calculated using the assumed variation of photoelectric absorption coefficient of Parratt and Hempsted (1954). Calculated values for f' and f'' were made for elements 10 to 98 at a few common wavelengths.

In 1970 Cromer and Liberman focused their attention on the basic flaw in their previous calculations, ie the use of the Parratt and Hempsted (1954) power law, and developed (following relativistic calculations of photoelectric absorption cross sections by Brysk and Zerby (1968)) an approach based on a more general relativistic quantum theory. This theory is summarised below. The scattered amplitude for light by a bound electron is given by equation B.34 were f is given by equation B.35.

$$S_{i\rightarrow f} = -2\pi i\delta(\epsilon + \hbar\omega_1 - \epsilon_2 - \hbar\omega_2)[4\pi(e\hbar c)^2/2mc^2\hbar(\omega_1\omega_2)^{\frac{1}{2}}]f \qquad (B.34)$$

$$f = mc^2 \sum_{n+}\left(\frac{< 2|\underline{e}_2.\underline{\alpha}exp(-i\underline{k}_2.\underline{r})|n^+ >< n^+|\underline{e}_1.\underline{\alpha}exp(i\underline{k}_1.\underline{r})|1 >}{\epsilon_1 - \epsilon_{n+} + \hbar\omega_1} + \right.$$

$$\frac{< 2|\underline{e}_1.\underline{\alpha}exp(-i\underline{k}_1.\underline{r})|n^+ >< n^+|\underline{e}_2.\underline{\alpha}exp(i\underline{k}_2.\underline{r})|1 >}{\epsilon_1 - \epsilon_{n+} + \hbar\omega_2}\Bigg)$$

$$+mc^2\sum_{n-}\Bigg(\frac{< 2|\underline{e}_2.\underline{\alpha}exp(-i\underline{k}_2.\underline{r})|n^- >< n^-|\underline{e}_1.\underline{\alpha}exp(i\underline{k}_1.\underline{r})|1 >}{\epsilon_2 - |\epsilon_{n-} + \hbar\omega_2}$$

$$+\frac{< 2|\underline{e}_1.\underline{\alpha}exp(-i\underline{k}_1.\underline{r})|n^- >< n^-|\underline{e}_2.\underline{\alpha}exp(i\underline{k}_2.\underline{r})|1 >}{\epsilon_2 + |\epsilon_{n-}| - \hbar\omega_1}\Bigg) \qquad (B.35)$$

where f is the desired scattering factor, ϵ_1 and ϵ_2 are the polarization states, $\underline{k}_1$ and $\underline{k}_2$ are the incident and scattered wave vectors and ω_1 and ω_2 are the corresponding angular momentum. This equation can be simplified by rewriting the scattering factor in the normal non-relativistic manner. The terms can then be identified with those in the expression above. The assumption is then made that all but one of these terms is small and can therefore be solved in a non-relativistic manner. The principal term is then evaluated using the calculations of Brysk and Zerby (1968).

Appendix C

Anomalous corrections for gallium, arsenic, indium and antimony

Anomalous Dispersion Corrections for Gallium

Wavelength Å	f'	f''
0.60000	0.21517	1.20019
0.61000	0.21248	1.23581
0.62000	0.20906	1.27179
0.63000	0.20490	1.30813
0.64000	0.19999	1.34482
0.65000	0.19431	1.38186
0.66000	0.18784	1.41925
0.67000	0.18056	1.45697
0.68000	0.17246	1.49502
0.69000	0.16350	1.53341
0.70000	0.15368	1.57212
0.71000	0.14296	1.61116
0.72000	0.13133	1.65051
0.73000	0.11875	1.69018
0.74000	0.10520	1.73015
0.75000	0.09065	1.77044
0.76000	0.07507	1.81102
0.77000	0.05843	1.85191
0.78000	0.04068	1.89308
0.79000	0.02180	1.93455
0.80000	0.00174	1.97631
0.81000	-0.01954	2.01836
0.82000	-0.04209	2.06068
0.83000	-0.06595	2.10328
0.84000	-0.09118	2.14616

Wavelength Å	f'	f''
0.85000	-0.11783	2.18931
0.86000	-0.14598	2.23273
0.87000	-0.17568	2.27641
0.88000	-0.20701	2.32035
0.89000	-0.24005	2.36456
0.90000	-0.27488	2.40902
0.91000	-0.31161	2.45373
0.92000	-0.35481	2.49869
0.93000	-0.39578	2.54340
0.94000	-0.43895	2.58831
0.95000	-0.48445	2.63343
0.96000	-0.53246	2.67875
0.97000	-0.58313	2.72426
0.98000	-0.63668	2.76998
0.99000	-0.69331	2.81588
1.00000	-0.75329	2.86198
1.01000	-0.81691	2.90826
1.02000	-0.88452	2.95473
1.03000	-0.95651	3.00138
1.04000	-1.03334	3.04821
1.05000	-1.11559	3.09521
1.06000	-1.20394	3.14239
1.07000	-1.29920	3.18974
1.07999	-1.40240	3.23726
1.08999	-1.51485	3.28495

continued

Wavelength Å	f'	f''
1.09999	-1.63823	3.33281
1.10999	-1.77474	3.38082
1.11999	-1.92740	3.42899
1.12999	-2.10053	3.47733
1.13999	-2.24297	3.52610
1.14999	-2.48070	3.58819
1.15999	-2.77612	3.65178
1.16999	-3.16555	3.71691
1.17999	-3.73896	3.78359
1.18999	-4.87442	3.85186
1.19999	-5.34358	0.49266
1.20999	-4.07808	0.50023
1.21998	-3.55248	0.50786
1.22998	-3.22357	0.51553
1.23998	-2.98672	0.52326
1.24998	-2.80312	0.53104
1.25998	-2.65408	0.53886
1.26998	-2.52921	0.54674
1.27998	-2.42213	0.55467
1.28998	-2.32868	0.56265
1.29998	-2.24598	0.57068
1.30998	-2.17194	0.57876
1.31998	-2.10504	0.58689
1.32998	-2.04410	0.59507
1.33997	-1.98821	0.60330

Wavelength Å	f'	f''
1.34997	-1.93664	0.61159
1.35997	-1.88883	0.61992
1.36997	-1.84428	0.62830
1.37997	-1.80261	0.63673
1.38997	-1.76349	0.64521
1.39997	-1.72661	0.65364
1.40997	-1.69177	0.66207
1.41997	-1.65874	0.67055
1.42997	-1.62737	0.67908
1.43997	-1.59749	0.68764
1.44997	-1.56898	0.69626
1.45997	-1.54172	0.70491
1.46997	-1.51561	0.71361
1.47996	-1.49055	0.72236
1.48996	-1.46647	0.73115
1.49996	-1.44328	0.73998
1.50996	-1.42094	0.74886
1.51996	-1.39936	0.75778
1.52996	-1.37851	0.76674
1.53996	-1.35834	0.77575
1.54996	-1.33880	0.78480
1.55996	-1.31985	0.79389
1.56996	-1.30147	0.80303
1.57996	-1.28360	0.81221
1.58996	-1.26622	0.82143

Anomalous Dispersion Corrections for Arsenic

Wavelength Å	f'	f''
0.60000	0.13380	1.50511
0.61000	0.12341	1.54894
0.62000	0.11185	1.59319
0.63000	0.09909	1.63785
0.64000	0.08510	1.68292
0.65000	0.06984	1.72840
0.66000	0.05325	1.77427
0.67000	0.03530	1.82053
0.68000	0.01593	1.86717
0.69000	-0.00491	1.91420
0.70000	-0.02728	1.96160
0.71000	-0.05124	2.00937
0.72000	-0.07686	2.05750
0.73000	-0.10421	2.10599
0.74000	-0.13338	2.15484
0.75000	-0.16446	2.20404
0.76000	-0.19754	2.25359
0.77000	-0.23273	2.30347
0.78000	-0.27015	2.35369
0.79000	-0.30994	2.40425
0.80000	-0.35223	2.45513
0.81000	-0.40113	2.50602
0.82000	-0.44904	2.55701
0.83000	-0.49995	2.60828
0.84000	-0.55411	2.65981

Wavelength Å	f'	f''
0.85000	-0.61177	2.71161
0.86000	-0.67323	2.76367
0.87000	-0.73884	2.81599
0.88000	-0.80900	2.86855
0.89000	-0.88421	2.92137
0.90000	-0.96503	2.97443
0.91000	-1.05216	3.02772
0.92000	-1.14645	3.08126
0.93000	-1.24894	3.13502
0.94000	-1.36098	3.18902
0.95000	-1.48428	3.24324
0.96000	-1.62114	3.29768
0.97000	-1.77467	3.35234
0.98000	-1.94934	3.40721
0.99000	-2.15180	3.46230
1.00000	-2.33343	3.52418
1.01000	-2.63433	3.59641
1.02000	-3.03554	3.67072
1.03000	-3.63858	3.74712
1.04000	-4.92066	3.82567
1.05000	-4.90744	0.50046
1.06000	-3.83721	0.50925
1.07000	-3.35468	0.51810
1.07999	-3.04672	0.52702
1.08999	-2.82300	0.53601

continued

Wavelength Å	f'	f''
1.09999	-2.64869	0.54507
1.10999	-2.50674	0.55419
1.11999	-2.38755	0.56338
1.12999	-2.28517	0.57263
1.13999	-2.19570	0.58195
1.14999	-2.11642	0.59134
1.15999	-2.04537	0.60079
1.16999	-1.98110	0.61032
1.17999	-1.92250	0.61990
1.18999	-1.86871	0.62955
1.19999	-1.81903	0.63927
1.20999	-1.77291	0.64905
1.21998	-1.72990	0.65890
1.22998	-1.68963	0.66882
1.23998	-1.65178	0.67880
1.24998	-1.61608	0.68884
1.25998	-1.58232	0.69895
1.26998	-1.55029	0.70912
1.27998	-1.51984	0.71936
1.28998	-1.49081	0.72967
1.29998	-1.46309	0.74003
1.30998	-1.43656	0.75047
1.31998	-1.41112	0.76096
1.32998	-1.38669	0.77153
1.33997	-1.36318	0.78215

Wavelength Å	f'	f''
1.34997	-1.34054	0.79284
1.35997	-1.31870	0.80359
1.36997	-1.29760	0.81441
1.37997	-1.27720	0.82529
1.38997	-1.25745	0.83624
1.39997	-1.23822	0.84711
1.40997	-1.21953	0.85799
1.41997	-1.20135	0.86892
1.42997	-1.18367	0.87991
1.43997	-1.16646	0.89095
1.44997	-1.14968	0.90205
1.45997	-1.13331	0.91321
1.46997	-1.11734	0.92443
1.47996	-1.10173	0.93570
1.48996	-1.08648	0.94703
1.49996	-1.07156	0.95841
1.50996	-1.05696	0.96985
1.51996	-1.04265	0.98134
1.52996	-1.02864	0.99289
1.53996	-1.01490	1.00450
1.54996	-1.00142	1.01616
1.55996	-0.98818	1.02787
1.56996	-0.97519	1.03964
1.57996	-0.96243	1.05147
1.58996	-0.94988	1.06335

Anomalous Dispersion Corrections for Antimony

Wavelength Å	f'	f''
0.10000	-1.83153	0.29628
0.11000	-1.54229	0.35408
0.12000	-1.31693	0.41657
0.13000	-1.13747	0.48370
0.14000	-0.99235	0.55541
0.15000	-0.87395	0.63164
0.16000	-0.77698	0.71146
0.17000	-0.69717	0.79430
0.18000	-0.63193	0.88074
0.19000	-0.57942	0.97068
0.20000	-0.53834	1.06404
0.21000	-0.51008	1.16029
0.22000	-0.48992	1.25935
0.23000	-0.47931	1.36127
0.24000	-0.47811	1.46597
0.25000	-0.48636	1.57334
0.26000	-0.50432	1.68331
0.27000	-0.53241	1.79580
0.28000	-0.57125	1.91074
0.29000	-0.62173	2.02805
0.30000	-0.68503	2.14767
0.31000	-0.76271	2.26954
0.32000	-0.85865	2.39317
0.33000	-0.97225	2.51866
0.34000	-1.10919	2.64610

Wavelength Å	f'	f''
0.35000	-1.27546	2.77542
0.36000	-1.48047	2.90659
0.37000	-1.74023	3.03954
0.38000	-2.08582	3.17422
0.39000	-2.58514	3.31177
0.40000	-3.54750	3.45539
0.41000	-4.32870	0.57216
0.42000	-3.13370	0.59836
0.43000	-2.68176	0.62509
0.44000	-2.40651	0.65237
0.45000	-2.21091	0.68018
0.46000	-2.06024	0.70853
0.47000	-1.93791	0.73703
0.48000	-1.83494	0.76574
0.49000	-1.74617	0.79491
0.50000	-1.66811	0.82454
0.51000	-1.59838	0.85463
0.52000	-1.53530	0.88518
0.53000	-1.47762	0.91619
0.54000	-1.42441	0.94765
0.55000	-1.37496	0.97956
0.56000	-1.32871	1.01192
0.57000	-1.28521	1.04472
0.58000	-1.24409	1.07797
0.59000	-1.20507	1.11166

continued

Wavelength Å	f'	f''
0.60000	-1.16790	1.14579
0.61000	-1.13360	1.18034
0.62000	-1.09964	1.21528
0.63000	-1.06702	1.25063
0.64000	-1.03561	1.28641
0.65000	-1.00530	1.32261
0.66000	-0.97736	1.35919
0.67000	-0.94910	1.39615
0.68000	-0.92170	1.43351
0.69000	-0.89512	1.47128
0.70000	-0.87081	1.50940
0.71000	-0.84578	1.54790
0.72000	-0.82142	1.58678
0.73000	-0.79769	1.62605
0.74000	-0.77457	1.66570
0.75000	-0.75202	1.70573
0.76000	-0.73002	1.74615
0.77000	-0.70854	1.78694
0.78000	-0.68757	1.82810
0.79000	-0.66709	1.86964
0.80000	-0.64708	1.91154
0.81000	-0.62753	1.95382
0.82000	-0.60974	1.99644
0.83000	-0.59112	2.03942
0.84000	-0.57293	2.08276

Wavelength Å	f'	f''
0.85000	-0.55516	2.12646
0.86000	-0.53779	2.17052
0.87000	-0.52260	2.21490
0.88000	-0.50610	2.25963
0.89000	-0.48999	2.30471
0.90000	-0.47426	2.35014
0.91000	-0.45892	2.39591
0.92000	-0.44395	2.44202
0.93000	-0.42935	2.48847
0.94000	-0.41513	2.53527
0.95000	-0.40127	2.58240
0.96000	-0.38778	2.62986
0.97000	-0.37466	2.67766
0.98000	-0.36190	2.72579
0.99000	-0.34951	2.77425
1.00000	-0.33747	2.82304
1.01000	-0.32580	2.87216
1.02000	-0.31450	2.92160
1.03000	-0.30355	2.97136
1.04000	-0.29297	3.02144
1.05000	-0.28275	3.07185
1.06000	-0.27290	3.12257
1.06999	-0.26341	3.17361
1.07999	-0.25429	3.22497
1.08999	-0.24554	3.27664

Anomalous Dispersion Corrections for Indium

Wavelength Å	f'	f''
0.10000	-1.74110	0.25268
0.11000	-1.46337	0.30231
0.12000	-1.24652	0.35602
0.13000	-1.07322	0.41376
0.14000	-0.93222	0.47548
0.15000	-0.81607	0.54112
0.16000	-0.71976	0.61004
0.17000	-0.63937	0.68177
0.18000	-0.57217	0.75670
0.19000	-0.51627	0.83475
0.20000	-0.47036	0.91582
0.21000	-0.43347	0.99985
0.22000	-0.40495	1.08676
0.23000	-0.38720	1.17591
0.24000	-0.37463	1.26745
0.25000	-0.36950	1.36143
0.26000	-0.37180	1.45777
0.27000	-0.38163	1.55641
0.28000	-0.39921	1.65727
0.29000	-0.42488	1.76031
0.30000	-0.45914	1.86545
0.31000	-0.50259	1.97264
0.32000	-0.55606	2.08184
0.33000	-0.62059	2.19299
0.34000	-0.69753	2.30603

Wavelength Å	f'	f''
0.35000	-0.79027	2.42051
0.36000	-0.89793	2.53665
0.37000	-1.02524	2.65445
0.38000	-1.17675	2.77389
0.39000	-1.35928	2.89491
0.40000	-1.58373	3.01749
0.41000	-1.86930	3.14157
0.42000	-2.25512	3.26712
0.43000	-2.83947	3.39694
0.44000	-4.18898	3.53018
0.45000	-3.83412	0.57383
0.46000	-3.01133	0.59791
0.47000	-2.62211	0.62209
0.48000	-2.37085	0.64642
0.49000	-2.18727	0.67114
0.50000	-2.04349	0.69626
0.51000	-1.92570	0.72177
0.52000	-1.82612	0.74767
0.53000	-1.73990	0.77396
0.54000	-1.66388	0.80064
0.55000	-1.59584	0.82771
0.56000	-1.53422	0.85516
0.57000	-1.47785	0.88299
0.58000	-1.42583	0.91120
0.59000	-1.37749	0.93979

continued

Wavelength $\AA$	f'	f''
0.60000	-1.33228	0.96875
0.61000	-1.28977	0.99809
0.62000	-1.24961	1.02781
0.63000	-1.21151	1.05789
0.64000	-1.17523	1.08834
0.65000	-1.14057	1.11916
0.66000	-1.10737	1.15035
0.67000	-1.07548	1.18190
0.68000	-1.04653	1.21377
0.69000	-1.01700	1.24596
0.70000	-0.98846	1.27851
0.71000	-0.96083	1.31140
0.72000	-0.93405	1.34464
0.73000	-0.90978	1.37820
0.74000	-0.88460	1.41206
0.75000	-0.86011	1.44626
0.76000	-0.83625	1.48079
0.77000	-0.81494	1.51563
0.78000	-0.79236	1.55074
0.79000	-0.77032	1.58618
0.80000	-0.74883	1.62194
0.81000	-0.72780	1.65802
0.82000	-0.70724	1.69442
0.83000	-0.68714	1.73113
0.84000	-0.66747	1.76816

Wavelength $\AA$	f'	f''
0.85000	-0.64822	1.80550
0.86000	-0.62938	1.84315
0.87000	-0.61093	1.88111
0.88000	-0.59286	1.91938
0.89000	-0.57517	1.95796
0.90000	-0.55784	1.99684
0.91000	-0.54087	2.03602
0.92000	-0.52424	2.07551
0.93000	-0.50796	2.11530
0.94000	-0.49200	2.15538
0.95000	-0.47817	2.19574
0.96000	-0.46294	2.23639
0.97000	-0.44803	2.27734
0.98000	-0.43344	2.31857
0.99000	-0.41916	2.36010
1.00000	-0.40747	2.40189
1.01000	-0.39389	2.44396
1.02000	-0.38062	2.48631
1.03000	-0.36765	2.52894
1.04000	-0.35500	2.57185
1.05000	-0.34264	2.61505
1.06000	-0.33059	2.65852
1.06999	-0.31884	2.70227
1.07999	-0.30740	2.74630
1.08999	-0.29625	2.79060

Appendix D

The Cromer Liberman program

PROGRAM TO INTERPOLATE CROSS SECTIONS
AND COMPUTE ANOMALOUS SCATTERING FACTORS

QUESTIONS CONCERNING THIS PROGRAM SHOULD BE ADDRESSED TO
DON T. CROMER MST-5
MAIL STOP G730
LOS ALAMOS NATIONAL LABORATORY
LOS ALAMOS, NEW MEXICO 87545

THIS PROGRAM WAS WRITTEN IN SIMPLE FORTRAN FOR
A CDC MACHINE. FOR AN IBM SYSTEM CERTAIN CHANGES
WERE MADE. THE IBM SPECIFIC STATMENTS ARE COURTESY OF
PAUL MOEWS OF THE INSTITUTE OF MATERIALS SCIENCE,
UNIVERSITY OF CONNECTICUT.

Adapted for the IBM PC by Lieselotte Templeton, U.C.Berkeley.

INPUT CARDS

THREE CARDS ARE READ FROM FILE "FORT.10" (called IN in the
Fortran listing).

CARD 1. NATOM(ATOMIC SYMBOL) AND IZ(ATOMIC NUMBER)
IN FORMAT (A2,3X,I5). NATOM IS LEFT ADJUSTED

CARD 2 HAS FORMAT 3I5. NW=NUMBER OF XRAY WAVELENGTHS
(10 MAXIMUM). NORD=INTERPOLATION TYPE(SEE BELOW) .

NORD=0 INTERPOLATION IS BY FITTING THREE CLOSEST POINTS
TO A QUADRATIC
NORD=1,2,3 ETC. USE AITKEN'S INTERPOLATION METHOD AND NORD
IS THE INTERPOLATION ORDER. NORD=2 IS PROBABLY THE BEST
VALUE TO USE

CARD 3 HAS NW VALUES OF XRAY LAMBDA IN 10F8.0

CROSS SECTIONS ARE READ FROM FILES "fprm1.dat to fprm11.dat"
depending on the element. The program will prompt you for the
name of this file (called IS in the Fortran listing).

OUTPUT IS ON FILE "FPRIME.PRT" (called IO in the Fortran listing).

*********NOTE********

THREE CONTRIBUTIONS TO FPRIME ARE LISTED SEPARATELY
IN THE OUTPUT.

1. P.E. PHOTOELECTRIC CONTRIBUTION
2. ETERM TERM DEPENDENT ON THE TOTAL ENERGY OF
THE ATOM. CROMER AND LIBERMAN J. CHEM. PHYS.
53,1891-1898(1970).
3. JENSEN TERM DEPENDENT ON THE XRAY ENERGY.
JENSEN, PHYSICS LETTERS,74A,41-44(1979)

THE CROSS SECTION FILE WILL HAVE A NUMBER OF ORBITALS
FOR EACH ATOM FROM ATOMIC NUMBER 3-95
THE FIRST MX CARDS (MX=5 FOR THIS XSECTION FILE AND IS SET IN
PROGRAM)
FOR EACH ORBITAL WILL HAVE CROSS SECTIONS AT MX VALUES OF ENERGY
FROM ABOUT 1 TO 80 KEV APPROXIMATELY EQUALLY SPACED IN LOG(ENERGY)

```
C     THE NEXT FIVE RECORDS WILL BE CROSS SECTIONS AT ENERGIES SELECTED
C     BY GAUSS INTEGRATION SCHEME. IF THE FUNCTION TYPE IS 0 (IF=0)
C     ( FUNCTION TYPE GIVEN IN CROMER AND LIBERMAN
C         J. CHEM. PHYS. 53,1891-1898(1970)     )
C     A SIXTH VALUE IS READ IN FOR AN ENERGY=1.001*(BINDING ENERGY).
C     IF THE XRAY ENERGY IS LESS THAN BINDING ENERGY, FUNCTION SIGMA3
C     WILL BE USED (CROMER AND LIBERMAN ACTA CRYST. A37,267-268(1981))
C
C
C**********WARNING*************
C
C
C     IF AN XRAY ENERGY IS VERY CLOSE TO ONE OF THE ENERGIES
C     USED IN THE GAUSS INTEGRATION AN #ANOMALOUS# ANOMALOUS SCATTERING
C     FACTOR MAY RESULT. THERE IS NO EASY WAY OUT OF THIS PROBLEM. A
C     SUGGESTED WAY IS TO COMPUTE SEVERAL VALUES AT NEARBY ENERGIES
C     AND DRAW A SMOOTH CURVE. THIS METHOD SHOULD WORK PROVIDED
C     THE POINTS DO NOT PASS THROUGH AN EDGE
C
C
      IMPLICIT REAL*8(A - H,O - Z), INTEGER*4(I - N)
      CHARACTER*12 FPRDAT,FIL1,FIL2
      EXTERNAL  SIGMA0,SIGMA1,SIGMA2,  SIGMA3, LGNDR
      DIMENSION XK(500),XR(500),FP(500,240),FPP(500,240),ABS(500,240)
      DIMENSION EW(540),SIG(540),EL(540),SL(540)
      DIMENSION M1(540), M2(540),M3(550)
      DIMENSION CXB(500),SUMFP(500),SUMFPP(500)
      DIMENSION T(320)
      DIMENSION XJENSN(500), ET(500)
      DIMENSION EG(500)
      DIMENSION ETERM(98), WT(98), NORB(98)
      COMMON /GAUS/ CX, BB, SIGG(5), RX, ICOUNT
      COMMON /PLT/ NPLOTL, NAT, NSHEL(2,24)
      COMMON /EDGE/ SEDGE
      DATA ETERM /.0, .0, .001, .001, .002, .003, .005, .007, .009,
     1     .011, .014, .018, .021, .026, .030, .035, .041, .047, .053,
     2     .060, .068, .075, .084, .093, .102, .113, .123, .135, .146,
     3     .159, .172, .186, .200, .215, .231, .247, .264, .282, .300,
     4     .319, .338, .359, .380, .401, .424, .447, .471, .496, .521,
     5     .547, .575, .602, .631, .660, .690, .721, .753, .786, .819,
     6     .854, .889, .925, .962, 1.0, 1.039, 1.079, 1.119, 1.161,
     7     1.204, 1.248, 1.293, 1.338, 1.385, 1.433, 1.482, 1.532,
     8     1.583, 1.636, 1.689, 1.743, 1.799, 1.856, 1.914, 1.973,
     9     2.033, 2.095, 2.157, 2.221, 2.287, 2.353, 2.421, 2.490,
     *     2.561, 2.633, 2.707, 2.782, 2.858, 2.936/
      DATA WT /1.0079, 4.00260, 6.941, 9.01218, 10.81, 12.011, 14.0067,
     1     15.9994, 18.9984, 20.179, 22.98977, 24.305, 26.98154,
     2     28.0855, 30.97376, 32.06, 35.453, 39.948, 39.0983, 40.08,
     3     44.9559, 47.88, 50.9415, 51.996, 54.9380, 55.847, 58.9332,
     4     58.69, 63.546, 65.38, 69.72, 72.59, 74.9216, 78.96, 79.904,
     5     83.80, 85.4678, 87.62, 88.9059, 91.22, 92.9064, 95.94, 98.,
     6     101.07, 102.9055, 106.42, 107.868, 112.41, 114.82, 118.69,
     7     121.75, 127.60, 126.9045, 131.29, 132.9054, 137.33, 138.9055,
     8     140.12, 140.9077, 144.24, 145., 150.36, 151.96, 157.25,
     9     158.9254, 162.50, 164.9304, 167.26, 168.9342, 173.04, 174.67,
     *     178.49, 180.9479, 183.85, 186.207, 190.2, 192.22, 195.08,
     1     196.9655, 200.59, 204.383, 207.2, 208.9804, 209., 210., 222.,
     2     223., 226.0254, 227.0278, 232.0381, 231.0359, 238.0482,
     3     237.0482, 239., 243., 247., 247., 251./
      DATA NORB /0, 0, 2, 2, 3, 3, 4, 4, 4, 4, 4, 4, 5, 6, 7, 7, 7, 7,
     1     7, 7, 7, 7, 8, 9, 9, 9, 9, 9, 9, 9, 9, 9, 9, 9, 9, 9, 9, 12,
     2     12, 13, 13, 14, 14, 14, 14, 14, 14, 14, 14, 14, 14, 14, 14, 14,
     3     14, 17, 17, 17, 18, 18, 18, 18, 18, 18, 19, 19, 19, 19, 19,
     4     19, 19, 19, 20, 20, 20, 21, 21, 21, 21, 21, 22, 22, 23, 23,
     5     24, 24, 24, 24, 24, 24, 24, 24, 24, 24, 24, 24, 24, 24, 24/
      DATA C /137.0367D0/
```

```
      DATA PI /3.14159265D0/
      DATA AU /2.80022D+7/
      DATA C1 /.02721D0/
      DATA XKEV /12.397639D0/
      DATA CXB /500*0.0D0/
      MX = 5
      IPLOT = 0
C*********  SET UP FILE FORT.10 FOR WAVELENGTH RANGE REQUIRED*****
C     WRITE(*,*) 'Range of wavelen
C
C
C*********  SET INPUT, OUTPUT AND X SECTION FILES*****
      WRITE (*,*)'fprime data file name (12ch)'
      READ (*,*) FPRDAT
      IN = 10
      IO = 9
      IS = 1
      FIL1='FPRIME.PRT'
      FIL2='FORT.10'
      OPEN (1,FILE=FPRDAT)
C     OPEN (9,FILE=FIL1,STATUS='NEW')
C     OPEN (10,FILE=FIL2)
C**********
C
C
      READ (IN,280) NATOM, IZ
C*****READ ATOMIC SYMBOL AND ATOMIC NUMBER
      NO = NORB(IZ)
      READ (IN,300) NW, NORD
C
C
C*****READ NUMBER OF XRAY VALUES TO BE INTERPOLATED,
C      INTERPOLATION TYPE, AND IPLOT=0(NO PLOT)
      READ (IN,*) (XR(I),I=1,NW)
C*****READ NW VALUES OF XRAY(ANGSTROMS) AT WHICH INTERPOLATION
C*****   TO BE DONE
C
C*****CHANGE ANGSTROMS TO KEV
      DO 10 K = 1, NW
       XK(K) = XKEV / XR(K)
   10 CONTINUE
      REWIND IS
      DO 20 I = 1, NW
       DO 20 J = 1, NO
        FP(I,J) = 0.0
        FPP(I,J) = 0.0
   20 CONTINUE
      DO 170 J = 1, NO
       DO 40 K = 1, MX
   30   READ (IS,330,END=270) NAT, NJ, NSHEL(1,J), NSHEL(2,J), XW,
     1 EW(K), SIG(K)
      NAT=ATOMIC SYMBOL
      NJ=ORBITAL SEQUENCE NUMBER
      NSHEL=ORBITAL TYPE. 1S1/2 ETC.
      XW=ENERGY IN ANGSTROMS
      EW=ENERGY IN KEV
      SIG=CROSS SECTION IN BARNS
      BE=BINDING ENERGY(KEV)
      IF=0,1,2 FUNCTION TYPE
C*****READ MX ENERGIES AND X SECTIONS FOR ORBITAL J
        IF (NAT .NE. NATOM) GO TO 30
        IF (NJ .NE. J) GO TO 260
   40  CONTINUE
       DO 50 K = 1, 5
        READ (IS,330) NAT, NJ, NSHEL(1,J), NSHEL(2,J), XW, EG(K),
     1 SIGG(K), BE, IF
```

```
C*****READ 5 ENERGIES AND X SECTIONS FOR ORBITAL J
C*****   FOR THE GAUSS INTEGRATION POINTS. BINDING ENERGY
C        AND FUNCTION TYPE ALSO
         IF (NAT .NE. NATOM) GO TO 260
         IF (NJ .NE. J) GO TO 260
         IF (BE .LE. 0.) GO TO 260
         EW(K + MX) = EG(K)
         SIG(K + MX) = SIGG(K)
   50    CONTINUE
         NX = MX + 5
         IF (IF .NE. 0) GO TO 60
         NX = NX + 1
C***** IF=0 SO READ X SEXTION AT ENERGY=1.001*BINDING ENERGY
         READ (IS,330) NAT, NJ, NSHEL(1,J), NSHEL(2,J), XW, EW(NX),
        1 SIG(NX)
         IF (NAT .NE. NATOM) GO TO 260
         EDG = EW(NX)
         SIGEDG = SIG(NX)
   60    CONTINUE
         BB = BE / C1
         DO 70 I = 1, 5
          SIGG(I) = SIGG(I) / AU
   70    CONTINUE
C*****SORT ALL X SECTIONS
         CALL SORT(NX, EW, SIG)
C*****SORT THE FIVE CROSS SECTIONS AT INTEGRATION POINTS
         CALL SORT(5, EG, SIGG)
C*****CHANGE TO LOGS FOR INTERPOLATION
         DO 80 K = 1, NX
          EL(K) = 0.
          SL(K) = 0.
          EL(K) = DLOG(EW(K))
          IF (SIG(K) .EQ. 0.0) GO TO 80
          SL(K) = DLOG(SIG(K))
   80    CONTINUE
         DO 160 K = 1, NW
          MF = 0
          ZX = DLOG(XK(K))
C*****ZX=LOG OF XRAY(KEV) ENERGY
          CX = 0.
          IF (BE .GT. XK(K)) GO TO 130
          IF (NORD .NE. 0) GO TO 90
          CALL XSECT(ZX, EL, SL, CX, NX)
          GO TO 120
   90     DO 100 M = 1, NX
           N1 = M
           IF (SL(M) .NE. 0.0) GO TO 110
  100     CONTINUE
  110     MM = NX - N1 + 1
          CX = AKNINT(ZX,MM,NORD,EL(N1),SL(N1),T)
          CX = DEXP(CX)
*****CX IS THE INTERPOLATED X SECTION IN BARNS
  120     CXB(K) = CXB(K) + CX
        *****CXB IS SUM TO GET MU/RHO
*****CHANGE CX TO ATOMIC UNITS
          CX = CX / AU
  130     ICOUNT = 6
*****RX=XRAY ENERGY IN ATOMIC UNITS
          RX = XK(K) / C1
          IF (IF .NE. 0) GO TO 140
          IF (BE .LT. XK(K)) GO TO 140
*****SEDGE IS XSECTION IN ATOMIC UNITS AT ENERGY=1.001*BE
          SEDGE = SIGEDG / AU
          CX = 0.0
          FP(K,J) = GAUSS(1,SIGMA3,5,LGNDR) * C / (2.0*PI**2)
          MF = 3
```

```
      GO TO 150
  140 CONTINUE
      IF (IF .EQ. 0) FP(K,J) = GAUSS(1,SIGMA0,5,LGNDR) * C / (2.0*PI**
     1 2)
      IF (IF .EQ. 1) FP(K,J) = GAUSS(1,SIGMA1,5,LGNDR) * C / (2.0*PI**
     1 2)
      IF (IF .EQ. 2) FP(K,J) = GAUSS(1,SIGMA2,5,LGNDR) * C / (2.0*PI**
     1 2)
  150 CONTINUE
      FPP(K,J) = 0.
      IF (CX .NE. 0.0) FPP(K,J) = C * CX * RX / (4.0*PI)
      CORR = 0.0
      IF (CX .NE. 0.0) CORR = -CX * RX * 0.5 * DLOG((RX + BB)/(RX -
     1 BB)) * C / (2.0*PI**2)
      IF (MF .EQ. 3) CORR = 0.5 * SEDGE * BB ** 2 * DLOG((-BB + RX)/(-
     1 BB - RX)) / RX * C / (2.*PI**2)
      FP(K,J) = FP(K,J) + CORR
      ABS(K,J) = CX * AU
  160 CONTINUE
  170 CONTINUE
C     WRITE (IO,340) NATOM, IZ, NO, WT(IZ), ETERM(IZ)
C     WRITE (IO,290) NW, NORD
C     WRITE (IO,310) (XR(I),I=1,NW)
C     WRITE (IO,350)
      DO 180 I = 1, NW
       SUMFP(I) = 0.0
       SUMFPP(I) = 0.
  180 CONTINUE
      DO 190 J=  1, NO
      DO 190 K = 1, NW
C      WRITE (IO,320) FP(K,1)
        SUMFP(K) = SUMFP(K) + FP(K,J)
C     WRITE(*,*) FP(K,1)
C     WRITE(*,*) K
C     WRITE(*,*) SUMFP(K)
  190 CONTINUE
C     WRITE (IO,350)
C     WRITE (IO,390) (SUMFP(K),K=1,NW)
      DO 200 K = 1, NW
      XJENSN(K)=-0.5*FLOAT(IZ)*(XK(K)/C1/137.0367**2)**2
  200 CONTINUE
      DO 210 K = 1, NW
  210 ET(K) = -ETERM(IZ)
C     WRITE (IO,400) (ET(K),K=1,NW)
C     WRITE (IO,380) (XJENSN(K),K=1,NW)
      DO 220 K = 1, NW
  220 SUMFP(K) = SUMFP(K) + ET(K) + XJENSN(K)
      WRITE (IO,350)
      DO 225 K=1, NW
      WRITE (IO,370) XR(K),SUMFP(K)
  225 CONTINUE
      WRITE (IO,350)
      DO 230 J = 1, NO
       WRITE (IO,320) FPP(1,J)
       DO 230 K = 1, NW
        SUMFPP(K) = SUMFPP(K) + FPP(K,J)
  230 CONTINUE
      WRITE (IO,350)
      WRITE (IO,410) (SUMFPP(K),K=1,NW)
      DO 240 K = 1, NW
      WRITE (IO,410) XR(K),SUMFP(K),SUMFPP(K)
       CXB(K) = CXB(K) * 0.602472 / WT(IZ)
  240 CONTINUE
      WRITE (IO,420) (CXB(K),K=1,NW)
      WRITE (IO,350)
      WRITE (IO,430)
```

```
      DO 250 J = 1, NO
C      WRITE (IO,440) NSHEL(1,J), NSHEL(2,J), (ABS(K,J),K=1,NW)
  250 CONTINUE
      STOP
  260 CONTINUE
      STOP
  270 STOP ' WRONG OR DEFECTIVE FPRM.DAT FILE'
C
  280 FORMAT (A2, 3X, I5)
  290 FORMAT (' NW=', I5, '  NORD=', I5)
  300 FORMAT (2I5)
  310 FORMAT (' LAMBDA ', 10F10.5)
  320 FORMAT (F10.6)
  330 FORMAT (A4, I4, A4, A2, 1P3E15.8, E15.8, I2)
  340 FORMAT (1X, A4, 2I5, 2F8.3)
  350 FORMAT (' ')
  360 FORMAT (2X, A4, A2, 10F10.3)
  370 FORMAT (10F10.3)
  380 FORMAT (' JENSEN=', 10F10.3)
  390 FORMAT ('    P.E.=', 10F10.3)
  400 FORMAT ('  ETERM=', 10F10.3)
  410 FORMAT (10F10.5)
  420 FORMAT (' MU/RHO=', 10F10.1)
  430 FORMAT (15X, 'CROSS SECTION(BARNS) AT XRAY ENERGY', /)
  440 FORMAT (2X, A4, A2, 1P10E10.3)
  450 FORMAT (' DATA FILE ERROR')
      END
      SUBROUTINE XSECT(ZX, EL, SL, CX, NX)
      IMPLICIT REAL*8(A - H,O - Z), INTEGER*4(I - N)
      DIMENSION EL(14), SL(14)
C*****FIND EL(K) CLOSEST TO ZX
      ER = 1000000.
      DO 10 L = 1, NX
       P = DABS(ZX - EL(L))
       IF (P .GT. ER) GO TO 10
       ER = P
       LL = L
   10 CONTINUE
      LL = LL - 1
      IF (LL .EQ. 0) LL = 1
      IF (LL .EQ. 12) LL = 11
      IF (SL(LL) .EQ. 0.) LL = LL + 1
      DET = EL(LL + 2) ** 2 * (EL(LL + 1) - EL(LL)) + EL(LL + 1) ** 2 *
     1(EL(LL) - EL(LL + 2)) + EL(LL) ** 2 * (EL(LL + 2) - EL(LL + 1))
      A0 = (EL(LL)**2*(SL(LL + 1)*EL(LL + 2) - SL(LL + 2)*EL(LL + 1)) +
     1EL(LL + 1)**2*(SL(LL + 2)*EL(LL) - SL(LL)*EL(LL + 2)) + EL(LL + 2)
     2**2*(SL(LL)*EL(LL + 1) - SL(LL + 1)*EL(LL))) / DET
      A1 = (EL(LL)**2*(SL(LL + 2) - SL(LL + 1)) + EL(LL + 1)**2*(SL(LL)
     1- SL(LL + 2)) + EL(LL + 2)**2*(SL(LL + 1) - SL(LL))) / DET
      A2 = (SL(LL)*(EL(LL + 2) - EL(LL + 1)) + SL(LL + 1)*(EL(LL) - EL(
     1LL + 2)) + SL(LL + 2)*(EL(LL + 1) - EL(LL))) / DET
      CX = DEXP(A0 + A1*ZX + A2*ZX**2)
      RETURN
      END
*****************************************************************************
      DOUBLE PRECISION FUNCTION SIGMA0(K,X)
      IMPLICIT REAL*8(A - H,O - Z), INTEGER*4(I - N)
      COMMON /GAUS/ CX, BB, SG(5), RX, ICOUNT
      ICOUNT = ICOUNT - 1
      SIGMA0 = SG(ICOUNT) * BB ** 3 / X ** 2 / (RX**2*X**2 - BB**2) -
     1BB * CX * RX ** 2 / (RX**2*X**2 - BB**2)
      RETURN
      END
*****************************************************************************
      DOUBLE PRECISION FUNCTION SIGMA1(K,X)
      IMPLICIT REAL*8(A - H,O - Z), INTEGER*4(I - N)
```

```
      COMMON /GAUS/ CX, BB, SG(5), RX, ICOUNT
      ICOUNT = ICOUNT - 1
      SIGMA1 = 0.5 * BB ** 3 * SG(ICOUNT) / (DSQRT(X)*(RX**2*X**2 - BB**
     12*X))
      RETURN
      END
C*****************************************************************************
      DOUBLE PRECISION FUNCTION SIGMA2(K,X)
      IMPLICIT REAL*8(A - H,O - Z), INTEGER*4(I - N)
      COMMON /GAUS/ CX, BB, SG(5), RX, ICOUNT
      ICOUNT = ICOUNT - 1
      DENOM = X ** 3 * RX ** 2 - BB ** 2 / X
      SIGMA2 = 2.0 * BB * SG(ICOUNT) * BB ** 2 / X ** 4 / DENOM - 2.0 *
     1BB * CX * RX ** 2 / DENOM
      RETURN
      END
C*****************************************************
      DOUBLE PRECISION FUNCTION SIGMA3(K,X)
      IMPLICIT REAL*8(A - H,O - Z), INTEGER*4(I - N)
      COMMON /EDGE/ SEDGE
      COMMON /GAUS/ CX, BB, SG(5), RX, ICOUNT
      ICOUNT = ICOUNT - 1
      SIGMA3 = BB ** 3 * (SG(ICOUNT) - SEDGE*X**2) / (X**2*(X**2*RX**2 -
     1 BB**2))
      RETURN
      END
C*****************************************************************************
      SUBROUTINE LGNDR(M, K, AA, Z)
      IMPLICIT REAL*8(A - H,O - Z), INTEGER*4(I - N)
      DIMENSION A(68), X(62)
      DATA X(1) /.06943184420297/
      DATA X(2) /.33000947820757/
      DATA X(3) /.04691007703067/
      DATA X(4) /.23076534494716/
      DATA X(5) /.03376524289992/
      DATA X(6) /.16939530676687/
      DATA X(7) /.38069040695840/
      DATA X(8) /.02544604382862/
      DATA X(9) /.12923440720030/
      DATA X(10) /.29707742431130/
      DATA X(11) /.01985507175123/
      DATA X(12) /.10166676129319/
      DATA X(13) /.23723379504184/
      DATA X(14) /.40828267875217/
      DATA X(15) /.01591988024619/
      DATA X(16) /.08198444633668/
      DATA X(17) /.19331428364971/
      DATA X(18) /.33787328829809/
      DATA X(19) /.01304673574141/
      DATA X(20) /.06746831665551/
      DATA X(21) /.16029521585049/
      DATA X(22) /.28330230293537/
      DATA X(23) /.42556283050918/
      DATA X(24) /.01088567092697/
      DATA X(25) /.05646870011595/
      DATA X(26) /.13492399721298/
      DATA X(27) /.24045193539659/
      DATA X(28) /.36522842202382/
      DATA X(29) /.00921968287664/
      DATA X(30) /.04794137181476/
      DATA X(31) /.11504866290285/
      DATA X(32) /.20634102285669/
      DATA X(33) /.31608425050091/
      DATA X(34) /.43738329574426/
      DATA X(35) /.00790847264071/
      DATA X(36) /.04120080038851/
```

```
DATA X(37) /.09921095463335/
DATA X(38) /.17882533027983/
DATA X(39) /.27575362448178/
DATA X(40) /.38477084202243/
DATA X(41) /.00685809565159/
DATA X(42) /.03578255816821/
DATA X(43) /.08639934246512/
DATA X(44) /.15635354759416/
DATA X(45) /.24237568182092/
DATA X(46) /.34044381553605/
DATA X(47) /.44597252564632/
DATA X(48) /.600374098758E-2/
DATA X(49) /.31363303799647E-1/
DATA X(50) /.75896708294787E-1/
DATA X(51) /.13779113431991/
DATA X(52) /.21451391369574/
DATA X(53) /.30292432646121/
DATA X(54) /.39940295300128/
DATA X(55) /.00529953250417/
DATA X(56) /.02771248846338/
DATA X(57) /.06718439880608/
DATA X(58) /.12229779582250/
DATA X(59) /.19106187779868/
DATA X(60) /.27099161117138/
DATA X(61) /.35919822461038/
DATA X(62) /.45249374508118/
DATA A(1) /.17392742256873/
DATA A(2) /.32607257743127/
DATA A(3) /.11846344252810/
DATA A(4) /.23931433524968/
DATA A(5) /.28444444444444/
DATA A(6) /.85662246189585E-1/
DATA A(7) /.18038078652407/
DATA A(8) /.23395696728635/
DATA A(9) /.06474248308443/
DATA A(10) /.13985269574464/
DATA A(11) /.19091502525256/
DATA A(12) /.20897959183674/
DATA A(13) /.05061426814519/
DATA A(14) /.11119051722669/
DATA A(15) /.15685332293894/
DATA A(16) /.18134189168918/
DATA A(17) /.04063719418079/
DATA A(18) /.09032408034743/
DATA A(19) /.13030534820147/
DATA A(20) /.15617353852000/
DATA A(21) /.16511967750063/
DATA A(23) /.07472567457529/
DATA A(24) /.10954318125799/
DATA A(25) /.13463335965500/
DATA A(26) /.14776211235738/
DATA A(27) /.02783428355809/
DATA A(28) /.06279018473245/
DATA A(29) /.09314510546387/
DATA A(30) /.11659688229599/
DATA A(31) /.13140227225512/
DATA A(32) /.13646254338895/
DATA A(33) /.02358766819326/
DATA A(34) /.05346966299766/
DATA A(35) /.08003916427167/
DATA A(36) /.10158371336153/
DATA A(37) /.11674626826918/
DATA A(38) /.12457352290670/
DATA A(39) /.02024200238266/
DATA A(40) /.04606074991886/
DATA A(41) /.06943675510989/
```

```
      DATA A(42) /.08907299038097/
      DATA A(43) /.10390802376845/
      DATA A(44) /.11314159013145/
      DATA A(45) /.11627577661544/
      DATA A(46) /.01755973016588/
      DATA A(47) /.04007904357988/
      DATA A(48) /.06075928534395/
      DATA A(49) /.07860158357910/
      DATA A(50) /.09276919873897/
      DATA A(51) /.10259923186065/
      DATA A(52) /.10763192673158/
      DATA A(53) /.01537662099806/
      DATA A(54) /.03518302374405/
      DATA A(55) /.05357961023359/
      DATA A(56) /.06978533896308/
      DATA A(57) /.08313460290850/
      DATA A(58) /.09308050000778/
      DATA A(59) /.09921574266356/
      DATA A(60) /.10128912096278/
      DATA A(61) /.01357622970588/
      DATA A(62) /.03112676196932/
      DATA A(63) /.04757925584125/
      DATA A(64) /.06231448562777/
      DATA A(65) /.07479799440829/
      DATA A(66) /.08457825969750/
      DATA A(67) /.09130170752246/
      DATA A(68) /.09472530522754/
      KK = K
      IF ((M .GT. 16) .OR. (M .LT. 4)) KK = 4
      IS = 0
      IH = (M + 1) / 2
      Z = .5
      IF (MOD(M,2) .EQ. 1) IS = -1
      IP = KK
      T = 0.
      IF (IP .LE. IH) GO TO 10
      IP = M + 1 - IP
      T = -1
   10 I4 = M - 4
      IA = (I4*(M + 4) + IS) / 4 + IP
      AA = A(IA)
      IF ((IP .EQ. IH) .AND. (IS .LT. 0)) RETURN
      IA = IA - (I4 + IS) / 2
      Z = -T + DSIGN(X(IA),T)
      RETURN
      END
C*********************************************************************
      DOUBLE PRECISION FUNCTION GAUSS(N,Y,M,LTBL)
      IMPLICIT REAL*8(A - H,O - Z), INTEGER*4(I - N)
      CHARACTER*50 CMT
      DIMENSION M(6), G(6), Z(6)
      DIMENSION A(6)
      DATA CMT /'GAUSS   N NOT IN (1,6).  RESULTS   SET TO ZERO.'/
      IF ((N .GT. 6) .OR. (N .LT. 1)) GO TO 140
      NN = N
      GO TO (110, 90, 70, 50, 30, 10), NN
   10 J = 1
      G(6) = 0.
   20 CALL LTBL(M(6), J, A(6), Z(6))
   30 K = 1
      G(5) = 0.
   40 CALL LTBL(M(5), K, A(5), Z(5))
   50 L = 1
      G(4) = 0.
   60 CALL LTBL(M(4), L, A(4), Z(4))
   70 JJ = 1
```

```
      G(3) = 0.
   80 CALL LTBL(M(3), JJ, A(3), Z(3))
   90 KK = 1
      G(2) = 0.
  100 CALL LTBL(M(2), KK, A(2), Z(2))
  110 LL = 1
      G(1) = 0.
  120 CALL LTBL(M(1), LL, A(1), Z(1))
      G(1) = G(1) + A(1) * Y(1,Z)
      LL = LL + 1
      IF (LL .LE. M(1)) GO TO 120
      IF (NN .EQ. 1) GO TO 130
      G(2) = G(2) + A(2) * Y(2,Z) * G(1)
      KK = KK + 1
      IF (KK .LE. M(2)) GO TO 100
      IF (NN .EQ. 2) GO TO 130
      G(3) = G(3) + A(3) * Y(3,Z) * G(2)
      JJ = JJ + 1
      IF (JJ .LE. M(3)) GO TO 80
      IF (NN .EQ. 3) GO TO 130
      G(4) = G(4) + A(4) * Y(4,Z) * G(3)
      L = L + 1
      IF (L .LE. M(4)) GO TO 60
      IF (NN .EQ. 4) GO TO 130
      G(5) = G(5) + A(5) * Y(5,Z) * G(4)
      K = K + 1
      IF (K .LE. M(5)) GO TO 40
      IF (NN .EQ. 5) GO TO 130
      G(6) = G(6) + A(6) * Y(6,Z) * G(5)
      J = J + 1
      IF (J .LE. M(6)) GO TO 20
  130 GAUSS = G(NN)
      RETURN
  140 CALL LABRT(1, CMT, 1)
      GAUSS = 0.
      RETURN
      END
C*************************************************************
      SUBROUTINE LABRT(ISW, LHOL, INX)
      IMPLICIT REAL*8(A - H,O - Z), INTEGER*4(I - N)
      CHARACTER*50 LHOL
      LOGICAL PS, TS
      IF ((ISW .EQ. 0) .OR. (ISW .GT. 5)) RETURN
      GO TO (10, 20, 30, 40, 50), ISW
      DATA NP /10/, PS / .TRUE. /, TS / .FALSE. /
   10 IF (PS .AND. (NP .GT. 0)) WRITE (*,60) LHOL, INX
      NP = NP - 1
      IF (TS) CALL EXIT
      RETURN
   20 PS = .FALSE.
      RETURN
   30 PS = .TRUE.
      NP = INX
      RETURN
   40 TS = .TRUE.
      RETURN
   50 TS = .FALSE.
      RETURN
   60 FORMAT ('0', 9X, A50, 3X, I6)
      END
      DOUBLE PRECISION FUNCTION AKNINT(XBAR,IN,IM,X,Y,T)
      IMPLICIT REAL*8(A - H,O - Z), INTEGER*4(I - N)
C AITKEN REPEATED INTERPOLATION
C
C    XBAR = ABSCISSA AT WHICH INTERPOLATION IS DESIRED
C    IABS(IN) = NO. OF VALUES IN TABLE
```

```
C               IF IN.GT.0, CHK ORDERING OF X(I).
C               IF IN.LT.0, SKIP PRECEEDING TEST.
C   IM    = DEGREE OF APPROXIMATING POLYNOMIAL
C   X     = VECTOR OF IABS(IN) VALUES OF ABSCISSA
C   Y     = VECTOR OF IABS(IN) VALUES OF ORDINATE
C   T     = TEMPORARY STORAGE VECTOR OF 4*(M+1) LOCATIONS)
C*    REAL*16 T,DXBAR
      DIMENSION T(80), X(9), Y(9)
      DXBAR = XBAR
      N = IABS(IN)
      M = IM
      IF (M .GE. N) GO TO 140
   10 K = N - 1
      IF (N .LT. 2) GO TO 120
      S = X(2) - X(1)
      IF (IN .LT. 0) GO TO 30
C CHK IF ORDER MONOTONIC
      IF (N .EQ. 2) GO TO 30
      DO 20 I = 3, N
       Z = (X(I) - X(I - 1)) * S
   20 IF (Z .LE. 0.) GO TO 100
   30 IF (S .LT. 0.) GO TO 50
C INCREASING ORDER
      DO 40 J = 1, N
   40 IF (XBAR .LE. X(J)) GO TO 70
      J = N
      GO TO 70
C DECREASING ORDER
   50 DO 60 J = 1, N
   60 IF (XBAR .GE. X(J)) GO TO 70
      J = N
   70 K = M
      M = M + 1
      J = J - M / 2
      J = MAX0(J,1)
      J = MIN0(J,N - K)
      MEND = J + K
      DO 80 I = J, MEND
       KK = I - J + 1
       T(KK) = Y(I)
   80 T(KK + M) = X(I) - DXBAR
      DO 90 I = 1, K
       KK = I + 1
       DO 90 JJ = KK, M
        T(JJ) = (T(I)*T(JJ + M) - T(JJ)*T(I + M)) / (X(JJ + J - 1) - X(
     1  I + J - 1))
   90 CONTINUE
      AKNINT = T(M)
      RETURN
  100 CONTINUE
  110 FORMAT (' AKNINT X(I) NOT SEQUENCED PROPERLY')
  120 CONTINUE
  130 FORMAT (' AKNINT N.LT.2 YBAR RETURNED AS Y(1)')
      AKNINT = Y(1)
      RETURN
  140 CONTINUE
  150 FORMAT (' AKNINT WARNING ORDER OF INTERPOLATION TOO LARGE')
      M = N - 1
      GO TO 10
      END
      SUBROUTINE SORT(N, A, B)
      IMPLICIT REAL*8(A - H,O - Z), INTEGER*4(I - N)
      DIMENSION A(1), B(1)
      M = N - 1
      DO 20 I = 1, M
       I1 = I + 1
```

```
      DO 10 J = I1, N
       IF (A(J) .GT. A(I)) GO TO 10
       X = A(J)
       Y = A(I)
       A(I) = X
       A(J) = Y
       X = B(J)
       Y = B(I)
       B(I) = X
       B(J) = Y
10    CONTINUE
20    CONTINUE
      RETURN
      END
```

Appendix E

References

Alavi, K., Petroff, P., Wagner, W. R. and Cho, A. Y. (1983) J. Vac. Sci. Technol. B1(2), 146.

Ambridge, T. and Wakefield, B. (1985) Br. Telecom. Technol. J. 3(1), 47.

Andrews, S. R. and Cowley, R. A. (1986) J. Phys. C: Solid State Phys. 18, 6427.

Authier, A. (1970) In: Advances in Structure Research by Diffraction Methods (ed; Brill and Mason) 3, 1.

Barnett, S. J. (1987) Ph.D Thesis, University of Durham.

Bartels, W. J. and Nijman, W. (1978) J. Cryst. Growth 44, 518.

Bartels, W. J. (1983) J. Vac. Sci. Technol. B1(2), 338.

Bartels, W. J., Hornstra, J. and Lobeek, D. J. W. (1986) Acta Cryst. A42, 539.

Bass, S. J., Barnett, S. J., Brown, G. T., Chew, N. G., Cullis, A. G., Pitt A. D. and Skolnick, M. S. (1986) J. Cryst. Growth 79, 378.

Bates, S., Hatton, P. D., Lucas, C. A., Ryan, T. W., Miles, S. J. and Tanner, B. K. (1988) Adv. X-Ray Anal. 31, 155.

Batterman, B. W. and Cole, H. (1964) Rev. Mod. Phys. 36(3), 681.

Baumbach, T., Rhan, H. and Pietsch, U. (1988) Phys. Stat. Sol. (a) 109, K7.

Bean, J. C., Feldman, L. C., Fiory, A. T., Nakahara, S. and Robinson, I. K. (1984) J. Vac. Sci. Technol. A2, 436.

Bensoussan, S., Malgrange, C. and Sauvage-Simkin, M. (1987) J. Appl. Cryst. 20, 222.

Bilderback, D. H. and Colella, R. (1976) Phys. Rev. 13(6), 2479.

Bond, W. L. (1960) Acta Cryst. 13, 814.

Bond, W. L. and Andrus, J. (1952) Am. Mineralogist 37, 622.

Bonse, U. (1962) Direct Observations of Imperfections in Crystals ,Interscience, 431.

Bonse, U. and Hart, M. (1965) Appl. Phys. Lett. 7, 238.

Bonse, U. and Kappler, E. (1958) Z. Naturforschung 13a, 792.

Bowen, D. K. and Davies, S. T. (1983) Nucl. Inst. Meth. 208, 725.

Bowen, D. K., Hill, M. J. and Tanner, B. K. (1987) Mat. Res. Soc. Symp. Proc. 82, 447.

Bruhl, H. -G., Pietsch, U. and Lengeler, B. (1988) J. Appl. Cryst. 21, 240.

Brysk, H. and Zerby, C. D. (1968) Phys. Rev. 171, 292.

Burgeat, J. and Colella, R. (1969) J. Appl. Phys. 40(9), 3505.

Burgeat, J., Quillec, M., Primot, J., Le Roux, G. and Launois, H. (1981) Appl. Phys. Letts. 38(7), 542.

Byer, R. L., Young, J. F. and Feigelson, R. S. (1970) L. Appl. Phys. 41, 2320.

Capano, M. A. (1989) Ph.D Thesis, MIT, USA.

Chikawa, J.-I. (1965) Appl.Phys. Letts. 7, 193.

Cho, A. Y. (1979) J. Vac. Sci. Technol. 16, 275.

Cho, A. Y. and Arthur, J. R. (1975) Prog. Solid State Chem. 10(3), 1975.

Chu, X. and Tanner, B. K. (1986) Appl. Phys. Lett. 49(26), 1773.

Chu, X. and Tanner, B. K. (1987) Semicond. Sci. Technol. 2, 765.

Cockerton, S., Green, G. S. and Tanner, B. K. (1989) Mat. Res. Soc. Symp. Proc. 138, 65.

Cockerton, S., Miles, S. J., Green, G. S. and Tanner, B. K. (1990) J. Cryst Growth 99, 1324.

Cole, H. and Stemple, N. R. (1962) J. Appl. Phys. 33(7), 2227.

Compton, A. H. (1931) Rev. Sci. Instrum. 2(7) 365.

Compton, A. H. and Allison, S. K. (1936) X-Rays in Theory and Experiment, MacMillon.

Creagh, D. C. and Hart, M. (1970) Phys. Stat. Sol. 37, 753.

Cromer, D. T. (1965) Acta Cryst. 18, 17.

Cromer, D. T. and Lieberman, D. A. (1970a) J. Chem. Phys. 53, 1891.

Cromer, D. T. and Lieberman, D. A. (1970b) Los Alamos Scientific Laboratory Report, LA-4403, 163.

Cromer, D. T. and Lieberman, D. A. (1981) Acta Cryst. A37, 267.

Dapkus, P.D., Manasevit, H. M., Hess, K. L., Low, T. S. and Stillman, G. E. (1981) J. Cryst. Growth 55, 10.

Davey, S. T., Scott, E. G., Wafefield, B. and Davies, G. J. (1987) Semicond. Sci. Technol. 2, 683.

Davies, G. J. and Andrews, D. A. (1985) Br. Telecom. Technol. J. 3(2) 59.

Diebold, A. C., Steinhauser, S. W. and Mariella, R. P. (1989) J. Vac. Sci. Technol. B7(2) 365.

Dorrity, I. A., Grange, J. D.and Wickenden, D. K. (1985) In: Gallium Arsenide; Mataerials, devices and circuits. Eds Howes and Morgan, Wiley and Sons. pp 95.

DuMond, J. W. M. (1937) Phys. Rev. 52, 872.

Elliot, A. G., Wei, C. -L., Farrara, R., Woolhouse, G., Scott, M. and Hiskes, R. (1984) J. Cryst. Growth 70, 169.

Elliott, K. R. (1983) Appl. Phys. Lett. 42, 274.

Estrop, E., Izrael, A. and Sauvage, M. (1976) Acta Cryst. A32, 627.

Fatemi, M. (1989) J. Cryst. Growth 96, 316.

Fewster, P. F. (1986) Phillips J. Phys. 41, 268.

Fewster, P. F. and Curling, C. J. (1987) J. Appl. Phys. 62, 4154.

Fleming, R. M., McWhan, D. B., Gossard, A. C., Wiegmann, W. and Logan, R. A. (1980) J. Appl. Phys. 51(1), 357.

Fontaine, A. and Warburton, W. K. (1985) Phys. Rev. 31(6), 3599.

Frank, F. C. and van der Merwe, J. H. (1949) Proc. Roy. Soc. (A) 198, 205.

Freund, A. (1980) Proc. of the NATO A.S.I. on characterisation of crystal growth and crystal defects (Ed. Tanner and Bowen, Plenum).

Fujimoto, I. (1984) Jpn. J. Appl. Phys. 23, L287.

Fujimoto, I. (1987) In: Defects and Properties of Semiconductors: Defect Engineering (ed; Chikawa, Sumino and Wada), 71, Tokyo.

Fukamachi, T. and Hosoya, S. (1975) Acta Cryst. A31, 215.

Fukuhara, A.and Takano, Y. (1977) Acta Cryst. A33, 137.

Fukui, T. (1984) Japn. J. Appl. Phys. 23(4), L208.

Fukumori, T. and Futagami, K. (1988) Jpn. J. Appl. Phys. 27(3), 442.

Fukumori, T., Futagami, K. and Matsunaga, K. (1982) Jpn. J. Appl. Phys. 21(10), 1525.

Goetz, K. -H., Bimberg, D., Jurgensen, H., Selders, J., Solomonov, A. V., Glinskii, G. F. and Razeghi, M. (1983) J. Appl. Phys. 54(8), 4543.

Grabmaier, B. C. and Grabmaier, J. G. (1972) J. Cryst. Growth 13/14, 635.

Halliwell, M. A. G., Childs, J. B. and O'Hara, S. (1972) Proc, Symp. GaAs Rel. Comp. 98.

Halliwell, M. A. G. (1981) Inst. Phys. Conf. Ser. 60(5) 271.

Halliwell, M. A. G., Juler, J. and Norman, A. G. (1983) Inst. Phys. Conf. Ser. 67(7), 365.

Halliwell, M. A. G., Lyons, M. H. and Hill, M. J. (1984) J. Cryst. Growth 68, 523.

Halliwell, M. A. G., Taylor, M. R. and Ambridge, T. (1985) Br. Telecom. Technol. J. 3(3) 30.

Hart, M. (1968) Sci.Prog, Oxford. 56, 429-447.

Hart, M. (1972) Phil. Mag. 26, 821.

Hart, M. (1975) J. Appl. Cryst. 8, 436.

Hart, M. (1980) In: Characterisation of Crystal Growth Defects by X-Ray Methods (ed; Tanner and Bowen), Plenum Press, 216 and 483.

Hart, M. and Siddons, D. P. (1981) Proc. R. Soc. Lond. A376, 465.

Hart, M. and Siddons, D. P. (1982) Nuclear Inst. Meth. 204, 219.

Hartwig, J. (1978) Kristall Techn. 13(9), 1117.

Hashizume, H., Iida, A. and Kohra, K. (1975) Japn. J. Appl. Phys. 14, 1433.

Hill, M. J. (1985) Ph.D. Thesis, University of Durham.

Hill, M. J., Tanner, B. K. and Halliwell, M. A. G. (1985) Mat. Res. Soc. Symp. Proc. 37, 53.

Holmes, D. E., Chen, R. T., Elliott, K. R. and Kirkpatrick, (1982) J. Appl. Phys. Lett. 40, 46.

Hornstra, J. and Bartels, W. J. (1978) J. Cryst. Growth 44, 513.

James, R. W. (1948) The Optical Principles of the Diffraction of X-rays, Bell, London.

Jeong, J., Schilesinger, T. E. and Milnes, A. G. (1988) J. Cryst. Growth 87, 265.

Jordan, A. S., Von Neida, A. R., Caruso, R. and Kim, C. K. (1974) J. Electrochem. Soc. 121(1), 153.

Jusserand, B. J., Alexandre, D. P and Roux, G. (1985). Appl. Phys. Letters 47 (1985) 301.

Kudo, H., Ochiai, Y., Takita, K., Masuda, K. and Seki, S. (1979) J. Appl. Phys. 50, 5034.

Lang, A. R. and Muiskov, V. F. (1965) Appl. Phys. Letts. 7, 214.

Larson, B. C. and Barhorst, J. F. (1980) J. Appl. Phys. 51(6), 3181.

Logan, R. and Hurle, D. (1971) J. Phys. Chem. Solids 32, 1739.

Lucas, C. A., Hatton, P. D., Bates, S., Ryan, T. W., Miles, S. J. and Tanner, B. K. (1988) J. Appl. Phys. 63(6), 1936.

Lyons, M. H. (1989) J. Cryst. Growth 96, 339.

Macrander, A. T. and Strege, K. (1986) J. Appl. Phys. 59(2), 442.

Macrander, A. T., Dupuis, R. D., Bean, J. C. and Brown, J. M. (1986) In: Semiconductor-based Heterostructures: Interfacial Structure and Stability, 75, The Metallurgical Soc.

Macrander, A. T., Lau, S., Strege, K. and Chu, S. N. G. (1988) Appl. Phys. Lett. 52(23), 1985.

Malgrange, C. and Authier, A. (1965) C. R. Acad. Sci. Paris 261, 3774.

Martin, G. M., Farges, J. P., Jacob, G. and Haalais, J. P. (1980) J. Appl. Phys. 51, 2840.

Martin, G. M., Mitonneau, A. and Mircea, A. (1977) Electron. Lett. 13, 191.

Matthews, J. W. (1966) Phil. Mag. 13, 1207.

Midwinter, J. E. (1967) Appl. Phys. Letts. 11, 128.

Miles, S. J. (1989) Ph.D Thesis, University of Durham.

Miles, S. J., Green, G. S., Tanner, B. K., Halliwell, M. A. G. and Lyons, M. H. (1989) Mat. Res. Soc. Symp. Proc. 138, 539.

Morrow, R. A. (1987) J. Mater. Res. 2(5), 680.

Mullin, J. B., Straughan, B. W. and Brickell, J. (1965) Appl. Phys. Lett. 40, 46.

Nahory, R. E., Pollock, M. A., Johnston, W. D. and Barns, R. L. (1978) Appl. Phys. Letts. 33(7), 659.

Nanishi, Y., Ishida, S., Honda, T., Yamazaki, H. and Miyazawa, S. (1982) Jpn. J. Appl. Phys. 21, L335.

Nassau, K., Levinstein, H. J. and Loiacono, G. M. (1966) J. Phys. Chem. Solids 27, 983.

Nelson, H. (1963) RCA Rev. 24, 603.

Olsen, G. H. and Smith, R. T. (1975) Phys. Stat. Sol. (a) 31, 739.

Olsen, G. H. and Zamerowski, T. J. (1979) Prog. Cryst. Growth Charact. 2, 309.

Osbourne, G. C. (1982) J. Appl. Phys. 53, 1586.

Panish, M. B., Hayashi, I. and Sumski, S. (1969) J. Quantum Electronics, QE-5, 210.

Panish, M. B. and Ilegems, M. (1972) Prog. Solid State Chem. 7, 39.

Parratt, L. G. and Hempsted, C. F. (1954) Phys. Rev. 94(6), 1593.

Parsey, J. M., Naminski, Y., Lagowski, J. and Gatos, H. C. (1981) J. Electrochem. Soc. 128, 936.

Parsey, J. M. and Thiel, F. A. (1987) J. Cryst. Growth 85, 327.

Petroff, P. and Hartman, R. L. (1973) Appl. Phys. Lett. 23, 469.

Pinsker, Z. G. (1978) Dynamical Scattering of X-Rays in Crystals, Springer-Verlag, Berlin.

Potts, H. R. and Pearson, G. (1966) J. Appl. Phys. 37, 2098.

Reed-Hill, R. E. (1973) In: Physical Metallurgy Principles, Princetown, NJ, Von Nostrand, pp274.

Renninger, M. Von (1955) Acta Cryst.8, 597.

Riglet, P., Sauvage, M., Petroff, J. F. and Epelboin, Y. (1980) Phil. Mag. A42(3) 339.

Roedel, R. J., VonNeida, A. R., Caruso, R. and Dawson, L. R. (1979) J. Electrochem. Soc. 126, 637.

Rupprecht, H. (1967) Gallium Arsenide, Inst. Phys. Conf. Ser. 3, London, Institute of Physics, pp57.

Ryan, T. W. (1989) Private Communication.

Ryan, T. W., Hatton, P. D., Bates, S., Watt, M., Sotomayor-Torres, C., Claxton, P. A. and Roberts, J. S. (1987) Semicond. Sci. Technol. 2, 241.

Schwarzschild, M. M. (1928) Phys. Rev. 32, 162.

Scott, E. G., Davey, S. T., Halliwell, M. A. G. and Davies, G. J. (1988) J. Vac. Sci. Technol. B6(2), 603.

Shaffner, T. J. (1986) Scan. Elect. Microsc. 1, 11.

Shinoyama, S. (1987) In: Defects and Properties of Semiconductors: Defect Engineering. Ed Chikawa, Sumino and Wada, KTK Scientific Publishers, Tokyo, pp87.

Skolnick, M. S., Tapster, P. R., Bass, S. J., Pitt, A. D., Apsley, N. and Aldred, S. P. (1986) Semicond. Sci. Technol. 1, 29.

Sugiura, Y. (1927) Jour.de Physique et le Radium, 8, 113.

Steinemann, A. and Zimmerli, U. (1966) Proc. Int. Crystal Growth Conf. (Boston, MA) Oxford, Pergamon, pp81.

Straumanis, M. and Kim, C. (1965) Acta Cryst. 19, 256.

Sugii, K., Iwasaki, H., Miyazawa, S. and Niizeki, N. (1973) J. Cryst. Growth 18, 159.

Sugimara, A., Daikoku, K., Imoto, N. and Miya, T. (1980) IEEE J. Quantum Elect. QE-16(2), 215.

Takagi, S. (1962) Acta Cryst. 15, 1311.

Takagi, S. (1969) J. Phys. Soc. Japn. 26(5), 1239.

Tanner, B. K. (1990) In Press

Tanner, B. K. (1976) X-Ray Diffraction Topography, Pergamon, Oxford.

Tanner, B. K. and Hill, M. J. (1986) J. Phys. D: Appl. Phys. 19, L229.

Tanner, B. K., Chu, X. and Bowen, D. K. (1986) Mat. Res. Soc. Symp. Proc. 69, 191.

Tanner, B. K. and Halliwell, M. A. G. (1988) Semicond. Sci. Technol. 3, 967.

Tapfer, L. and Ploog, K. (1986) Phys. Rev. B33, 5565.

Taupin, D. (1964) Bull. Soc. Franc. Miner. Crist. 87, 469.

Tomizawa, K., Sassa, K., Shimanuki, Y. and Nishizawa, J. (1987) In: Defects and Properties of Semiconductors: Defect Engineering. Ed Chikawa, Sumino and Wada, KTK Scientific Publishers, Tokyo, pp25.

Tuomi, T., Naukkarinen, K. and Rabe, P. (1974) Phys. Stat. Sol. 25, 93.

Vechten, Van. A. (1975) J.Electrochem. Soc. 122,419 and 423.

Waller, I. (1927) Phil. Mag. 4, 1228.

Walter, J. P. and Cohen, M. L. (1972) Phys. Rev. B5, 3101.

Wang, X. R., Chi, X. Y., Zheng, H., Miao, Z. L., Wang, J., Zhang, Z. S. and Jin, Y. S. (1988) J. Vac. Sci. Technol. B6(1) 34.

Warren, B. E. (1969) X-Ray Diffraction, Addison Wesley.

Weber, E. R., Ennen, H., Kaufmann, U., Windscheif, J., Schneider, J. and Wosinski, T. (1982) J. Appl. Phys. 53(9), 6140.

Wie, C. R. (1989) J. Appl. Phys. 65(3), 1036.

Willoughby, A. F. W., Driscoll, C. M. H. and Bellamy, B. A. (1971) J. Mat. Sci. 6, 1389.

Wilson, J. and Hawkes, J. F. B. (1983) Optoelectronics:An Introduction. Prentice/Hall International.

Yoshimura, J. (1984) J. Appl. Cryst. 17, 426.

Zachariasen, W. H. (1945) Theory of X-ray Diffraction in Crystals, Wiley, New York.